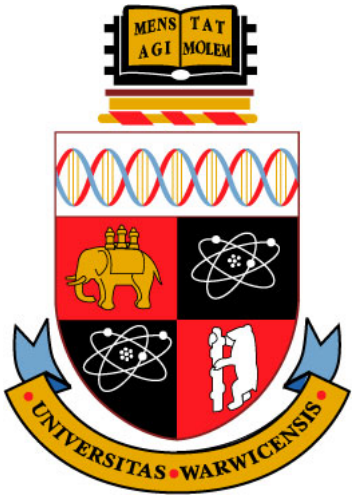

THESIS FOR EXAMINATION FOR THE DEGREE OF
DOCTOR OF PHILOSOPHY

A study of the interaction of end-binding proteins with microtubules

By:
Ben FITTON

Supervised by:
Dr. Anne STRAUBE

University of Warwick, MOAC-DTC

March 24, 2016.

Contents

List of Figures

List of Tables

List of Abbreviations

+TIP	a microtubule plus end tracking protein
CH	EB protein calponin homology domain
CLASP1	Cytoplasmic linker associated protein 1
CLASP1	Cytoplasmic linker associated protein 2
CV	Column Volume
DD	EB protein dimerisation domain
E-site	Exchangable nucleotide site on the β-tubulin
EB	Member of the End Binding protein family
EB1	End Binding Protein 1
EB1ΔT	EB1(1-139)-GCN4-GFP-His
EB2ΔN	EB2(43-326)-GFP-His
EB2ΔT	EB2(1-179)-GCN4-GFP-His
EB3ΔT	EB3(1-137)-GCN4-GFP-His
EB2	End Binding Protein 2
EB3	End Binding Protein 3
EB223	EB2-EB3 Chimera, EB2(1-185)-EB3(144-281)-GFP-6xHis
EB232	EB2-EB3 Chimera, EB2(1-90)-EB3(49-143)-EB2(186-326)-GFP-6xHis
EB233	EB2-EB3 Chimera, EB2(1-90)-EB3(49-281)-GFP-6xHis
EB322	EB2-EB3 Chimera, EB3(1-48)-EB2(91-326)-GFP-6xHis
EB323	EB2-EB3 Chimera, EB3(1-48)-EB2(91-185)-EB3(144-281)-GFP-6xHis
EB332	EB2-EB3 Chimera, EB3(1-143)-EB2(186-326)-GFP-6xHis
GDP	Guanosine Di-Phosphate

GEF	Gaussian Error Function
GFP	Green Fluorescent Protein
GMP-CPP	Extremely slowly hydrolysing analogue of GTP
GTP	Guanosine Tri-Phosphate
GTP-γS	Non-hydrolysable analogue of GTP
MAP	Microtubule Associated Proteins
MT	Microtubule
MTOC	Microtubule Organising Center
N-site	Non-exchangable nucleotide site on the α-tubulin
OD	Optical Density
PBS	Phosphate Buffer Saline
PSF	Point Spread Function
SAXS	Small angle x-ray scattering
SNR	Signal to Noise Ratio
STD	Standard Deviation
TIRF	Total Internal Reflection Fluorescence

Acknowledgement

First and foremost I must thank my supervisor Dr. Anne Straube for her guidance, support and wisdom throughout my PhD. I am thankful for her patience through troubled times and for my numerous mistakes, and occasional moments of stupidity. I thank her for turning me from a mathematician with an interest in biology, to an interdisciplinary scientist with a background in mathematics and knowledge of bio-chemistry, image analysis and programming. I extend my thanks to my second supervisor, Dr. Nasir Rajpoot through the early years for his frank advice and critique in an unfamiliar research area. I thank Dr Stefan Grosskinsky for agreeing to take over from Nasir during his secondment in Qatar.

I'd like to thank my Advisory Committee; Dr. Nick Carter, Dr. Sara Kalvala, and Dr. Magnus Richardson for their time and guidance.

I would like to thank all past and present members of the Straube lab that I have met throughout my PhD. Especially Daniel Roth and Ulrike Thiesen. Daniel for his quiet calm, helpful observations and our invaluable conversation on the state of european football. Ulrike for her love of coffee breaks and cake that gave a half hour of tranquility to every day, and her advice in surviving a PhD.

I would like to thank the cake club for providing that weekly sugar dose to power through the numerous late nights. For allowing me to experiment in a completely different field and humour at my liquid cheesecake failures (to name one). I would like to thank the early morning coffee club for that relaxed start to the morning (when I wasn't purifying proteins) and being friends both inside and outside of work.

I would like to thank the member of my cohort in MOAC for providing an outlet away from the lab with a similar background and drive. For our random conversations, our MSc year of little sleep, for napkin head, and for our away days. I have some fond memories and hope that we will continue to see each other on a regular basis. Special thanks must go to Steve for his patience in sharing a house with me for 18 months.

I thank Jess for her patience, and support through the most difficult times of my PhD. Without her this document may not exist, and for that she will have my eternal thanks and gratitude.

Special thanks must go to my parents without whom I would not be here. For the knowledge that they support me without understanding what it is that I have been doing for the past five years. Similar thanks goes to my sister Olivia, and the rest of my family.

Declarations

This thesis is submitted to the University of Warwick in support of my application for the degree of Doctor of Philosophy. It has been composed by myself and has not been submitted in any previous application for any degree. The work presented (including data generated and data analysis) was carried out by the author except in the cases outlined below:

Tubulin purification was a lab effort (Ben Fitton, Daniel Roth, Ulrike Thiesen, Nida Siddiqui, and Anne Straube).

Imaging of the EB comet shape and the mixed nucleotide lattice experiments were conducted by Anne Straube.

Dynamic microtubule chambers for: EB comet shape; EB position at the microtubule tip in relation to each other; EB localisation relative to the microtubule tip; mixed nucleotide lattice; and the EB shortened and chimeric construct experiments were created by Daniel Roth.

Immunoblotting of endogenous EB concentrations in cells, and negative binding effect of EB1 and EB3 on EB2 *in vitro* was carried out by Charlotte Carroll.

Abstract

Dynamic microtubules control cell shape, cell locomotion and the proper segregation of chromosomes. End Binding (EB) proteins are the key components of the microtubule (MT) plus tip (+TIP) protein network. EBs bind to the MT plus end and regulate microtubule dynamics. EBs localise to the microtubule tip by recognising the nucleotide state of tubulin. Mammalian cells express three members of the EB family (EB1, EB2 and EB3) that localise to spatial distinct sites on the microtubule in cells. Perturbation experiments in cells and *in vitro* reconstitution experiments have shown that EB1 and EB3 accelerate MT assembly and increase catastrophe frequency. This is a paradoxical effect, as an increase in growth speed should increase the size of the GTP cap thus decreasing the probability of catastrophe. To study this paradoxical effect an image analysis routine was developed to gain insight into any structural re-arrangement at the microtubule tip. An algorithm was developed to extract fluorescence intensity data along the length of a microtubule from time-lapse images. Curve fitting to these data allowed determination of the MT end position with sub-pixel resolution, the measurement of taper (i.e. the length difference of protofilaments at the microtubule end) and the quantitative analysis of the comet-shaped distributions of EB proteins at microtubule ends. The method was verified using synthetic images of MTs and then applied to time lapse movies of dynamic MTs from in vitro experiments where either the tubulin concentration or the EB3 concentration was varied. It was discovered that EB3 may increase microtubule taper, thereby de-stabilising the microtubule tip structure.

Binding of the three EB proteins to spatial distinct sites at the MT tip was carefully re-investigated in-vitro by pair-wise comparison, and in relation to the MT tip. All three EB proteins were found to localise to distinct sites with EB3 found to bind closest to the MT tip and EB2 being the furthest from the MT tip. Based on structural data that became available during the course of the project, and additional evidence of different nucleotide preferences between EB1/EB3 and EB2, a dual nucleotide recognition model was conceived to explain these spatially distinct locations. The model assumes that an EB protein is sensitive to the nucleotide state at both E-sites close to its binding site at the interface of 4 tubulin dimers. All three EB proteins showed evidence of dual nucleotide recognition in mixed nucleotide lattice experiments designed to directly test the model.

EB proteins recognise spatial distinct sites by recognising the pairwise nucleotide state of tubulin. As EB3 binds closest to the MT tip, it is best placed to affect microtubule dynamics by increasing taper, promoting a quicker growth phase and destabilising the microtubule. Within cells this is a useful concept as it can be up regulated to increase the dynamicity of MTs ensuring more efficient re-organisation of the cytoskeleton during cell differentiation or neuronal elongation.

Chapter 1

Introduction

The cytoskeleton is a highly specialised dynamic network of protein filaments that is an important component of all cells (Kaverina and Straube, 2011). Its ability to restructure itself to the requirements of the cell is vital for many processes such as cell division, intracellular transport, cell growth and cell motility (Komarova et al., 2002). In eukaryotic cells, the cytoskeleton consists of three macro-molecular protein assemblies: actin, intermediate filaments and microtubules (MTs) (Huber et al., 2015). This thesis focuses on microtubules and how proteins of the mammalian end binding family bind to and control properties of dynamic microtubules.

1.1 Microtubules

1.1.1 Overview

Microtubules are hollow dynamic protein filaments with a diameter of $\sim$25 nm (Mandelkow et al., 1991). Within cells one end of the microtubule is usually anchored in the microtubule organising centre (MTOC), the opposite end is dynamic (Mimori-Kiyosue et al., 2005; Vicente and Wordeman, 2015). Ordinarily the MTOC is the centrosome, which is located adjacent to the nucleus (Vicente and Wordeman, 2015). Microtubules grow from the MTOC towards the cell periphery (Komarova et al., 2002). Microtubules

have important roles in many cellular processes (Komarova et al., 2002; Vicente and Wordeman, 2015; Lakämper and Meyhöfer, 2006; Straube et al., 2003): Microtubules give the cell rigidity and provide the network for intracellular transport (Bachmann and Straube, 2015). They ensure that organelles are properly arranged and maintain a cell tail providing persistence during cell motility (Theisen et al., 2012). During mitosis, the MTOC is duplicated and separated by the formation of the mitotic spindle (Vicente and Wordeman, 2015). The microtubule cytoskeleton connects each pair of chromosomes to both MTOCs and provides the force required to separate the chromosomes (Vicente and Wordeman, 2015; Bancroft et al., 2015). Microtubules are the major structural component of cilia/flagella (Renaud et al., 1968; Lakämper and Meyhöfer, 2006; Stepanova et al., 2003). Together with microtubule motors they provide the force for swimming in some single cell eukaryotes, or for moving extracellular material in multicellular organisms (Lakämper and Meyhöfer, 2006). Within axons, microtubules provide the structure and stability allowing stable connections to be formed between neurons (Stepanova et al., 2003).

1.1.2 Basic Microtubule Structure

Microtubules (MTs) were first clearly identified in electron microscopy (EM) images in the early 1950's (Fawcett and Porter, 1954; Manton and Clarke, 1952). Microtubules were observed as long, thin filaments in flagella (Fawcett and Porter, 1954). It wasn't until 1963 that EM techniques had advanced enough through the addition of glutaraldehyde to the EM fixation media that these filaments were observed to be hollow (Ledbetter and Porter, 1963; Sabatini et al., 1963). This coined the term "microtubules", to represent that they were very small (micro) tubes (tubules) (Ledbetter and Porter, 1963). A year later Ledbetter and Porter (1964) observed that the walls of microtubules in plants were formed of long filaments. Subsequent experiments from different groups confirmed that microtubules in most cell types were formed of thirteen equally spaced parallel filaments that associated along their length, Figure 1.1 A (Phillips, 1966; Tilney et al., 1973). These same experiments also demonstrated that doublet microtubules (those found in cilia and flagella) had eleven protofilaments in its B tubule (Tilney et al., 1973). The B tubule is a

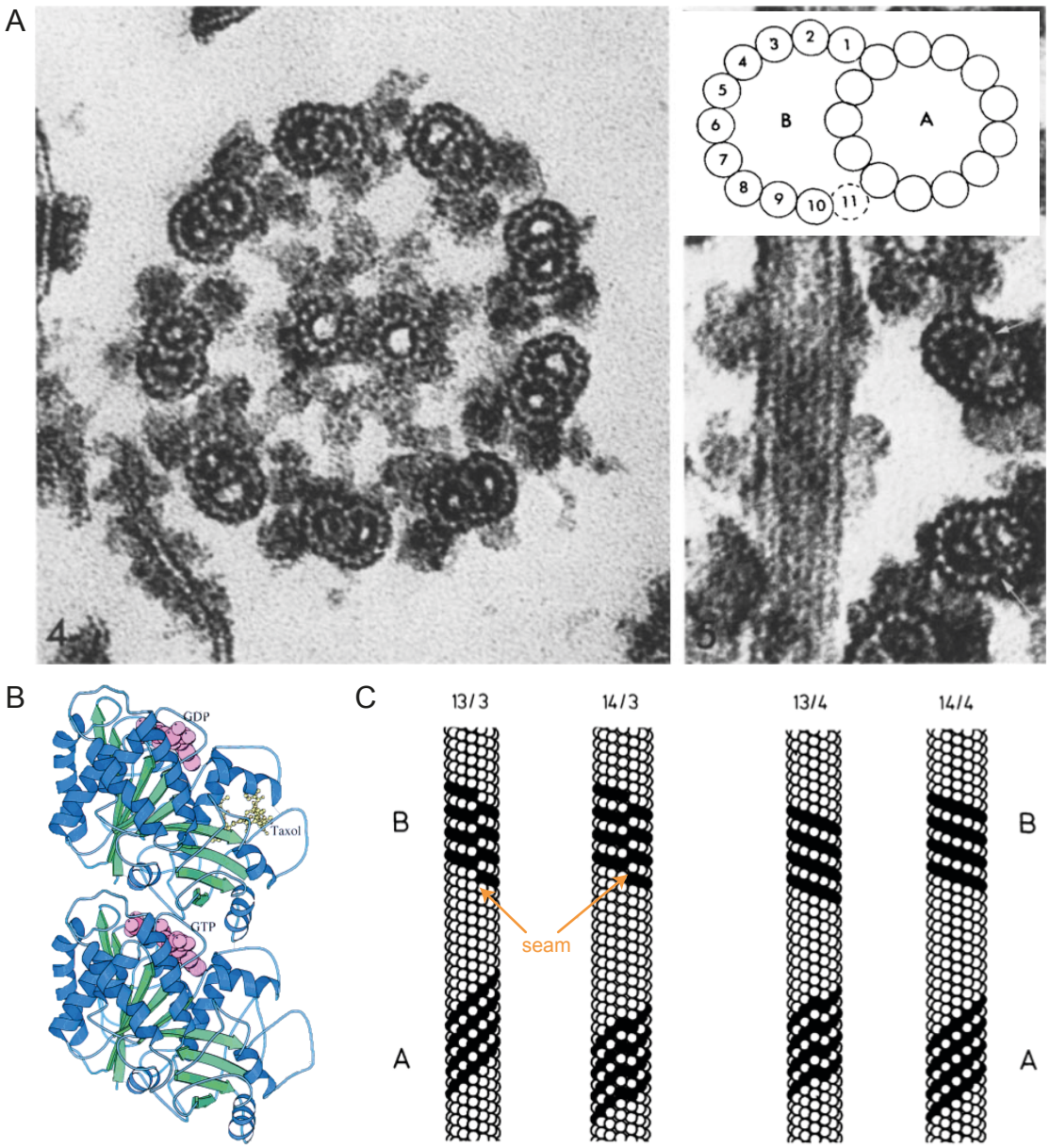

Figure 1.1: **Basic Microtubule Structure:** (A) End on EM images showing how microtubules are arranged in cilia. Right: demonstrates the nine outer doublet microtubules with the two central single microtubules. Left: zoomed in image of a doublet microtubule and Inset: cartoon representation of the structure of a doublet microtubule showing the 11 protofilaments that make up a B-tubule of a doublet microtubule and the 13 protofilament that is found in a single microtubule and the A-tubule of a doublet microtubule. Images taken from Tilney et al. (1973). (B) Ribbon model of the structure of α and β tubulin with GTP in the N-site and GDP in the E-site. Nucleotide is shown in pink. Blue ribbons represent α helices and green ribbons represent β sheets. Taken from Nogales et al. (1998). (C) Cartoon representation showing how the lattice structure of a microtubule is expected to change with different protofilament numbers and the size of the offset in a helix start. Microtubules with 13 or 14 protofilaments were considered, and with either a 3-start helix or a four start helix. Microtubules are coloured to represent either an A-lattice arrangement or a B-lattice arrangement. Taken from Schultheiss and Mandelkow (1983). Annotated to show microtubule seam (orange arrows).

part of a microtubule bound to the side of a full microtubule such that a second tube is formed, Figure 1.1 A (Tilney et al., 1973; Fawcett and Porter, 1954).

Meanwhile, experiments into colchicine (an anti-inflammatory drug used in the treatment of gout) had identified a specific interaction with a protein within cells (Borisy and Taylor, 1967b,a; Shelanski and Taylor, 1967). Borisy and Taylor (1967b) further hypothesised that the interacting protein was a subunit of microtubules. This hypothesis was due to; (i) colchicine having a higher binding affinity to cells rich with microtubules and, (ii) its disruptive effect on mitosis (Borisy and Taylor, 1967b,a; Shelanski and Taylor, 1967). Further experimentation identified the compound as having a molecular weight of around 110 kDa, which could be further decomposed to two molecules, each with a molecular weight of 55 kDa (Renaud et al., 1968). This decomposition was determined to be composed of two similar but different proteins (Adelman et al., 1968; Mohri, 1968; Shelanski and Taylor, 1967). These similar but different proteins were named as α-tubulin and β-tubulin (Adelman et al., 1968; Mohri, 1968). The two proteins were found to exist in a one-to-one ratio (Bryan and Wilson, 1971). This led to the conclusion that a tubulin dimer was likely a heterodimer of α-tubulin and β-tubulin (Bryan and Wilson, 1971).

The first structural models combining the knowledge of heterodimers of tubulin and protofilaments were proposed in the early 1970's (Bryan and Wilson, 1971; Weisenberg, 1972; Tilney et al., 1973; Chasey, 1972; Erickson, 1974; Amos and Klug, 1974). It was established that α-tubulin and β-tubulin were globular proteins with roughly a 4 nm diameter, Figure 1.1 B (Chasey, 1972; Erickson, 1974; Amos and Klug, 1974). The tubulin heterodimer associates head to tail to form a protofilament (Tilney et al., 1973; Amos and Klug, 1974; Erickson, 1974). Protofilaments associate laterally with a small longitudinal offset between adjacent tubulin dimers (Amos and Klug, 1974; Erickson, 1974). The offset between adjacent protofilaments meant that following a ring of laterally associating tubulin subunits around the microtubule, the subunit rose by 12 nm for every complete rotation of the microtubule. The 12 nm increase in height, or three tubulin subunit increase is referred to as a three-start helix (Amos and Klug, 1974; Erickson, 1974). The offset between adjacent protofilaments is consistent with the protofilament to the left starting 0.9/,nm higher than the protofilament to the right when looking from the

outside of the microtubule. This arrangement is known as a left-handed twist or helix, Figure 1.1 C.

It was not until roughly 10 years later that the arrangement of α and β tubulin subunits were resolved within the lattice. The lateral association of two subunits could be identical with the α-tubulin subunit interacting with another α tubulin subunit (β-tubulin laterally associating with a β-tubulin). Alternatively the two interacting subunits could alternate with α-tubulin associating with β tubulin, Figure 1.1 C. The lateral interaction of two identical subunits creates a B-lattice, whilst the lateral interaction of alternative tubulin subunits creates an A-lattice, Figure 1.1 C (Schultheiss and Mandelkow, 1983; des Georges et al., 2008). Various different combinations of the number of protofilaments, helix starts, and subunit associations were considered (Schultheiss and Mandelkow, 1983). Experimental evidence, as discussed above, alludes to a thirteen protofilament, three start helix microtubule. Experimental evidence also appeared to suggest that the majority of microtubules were formed of B-lattice microtubules, (Schultheiss and Mandelkow, 1983; Chrétien et al., 1995; Nogales et al., 1998). A thirteen protofilament, 3 start helix, B-lattice microtubules must contain an A-lattice join. The A-lattice join, or seam, was considered to be a weak point within the microtubule lattice and has been the subject of much discussion, Figure 1.1 C (Katsuki et al., 2014; des Georges et al., 2008; Chrétien et al., 1995; Schultheiss and Mandelkow, 1983; VanBuren et al., 2002). A lot of the disparity came from microtubules *in vitro* being observed with 10 -16 protofilaments, however in cells microtubules are heavily regulated and in mammals always form 13 protofilaments microtubules (des Georges et al., 2008; Chrétien et al., 1995, 1992).

Meanwhile biochemical experiments had shown that guanosine-5'-triphosphate (GTP) associated with a 1:1 relationship with α-tubulin and β-tubulin (Carlier and Pantaloni, 1981; Weisenberg et al., 1976). Upon incorporation into the microtubule lattice the GTP bound to the β-tubulin underwent hydrolysis to guanosine-5'-diphosphate (GDP), releasing a phosphate ion (Pi), Figure 1.1 B (Carlier and Pantaloni, 1981). The GTP binding site on the β-tubulin is referred to as the exchangeable site (E-site) as the bound GTP is able to exchange in solution, and undergo hydrolysis when the tubulin heterodimer is incorporated into the microtubule lattice, Figure 1.1 B (Carlier and Pantaloni, 1981; Carlier et al., 1989; Nogales et al., 1998). The GTP binding site on α-tubulin is buried

between the α-tubulin and β-tubulin within the stable tubulin heterodimer, and the GTP molecule is therefore not able to undergo exchange (Melki et al., 1989; Nogales et al., 1998). Tubulin heterodimers associate head-to-tail, with the β-tubulin subunit from one tubulin heterodimer binding to the α-tubulin subunit from another tubulin heterodimer (Kerssemakers et al., 2006; Chrétien et al., 1995; Tran et al., 1997). This head-to-tail binding of the tubulin subunits gives both the protofilaments and the microtubule an intrinsic polarity. Within cells the α-tubulin end of the microtubule is usually capped by γ tubulin whilst the β-tubulin end is exposed within the cell body (Caplow and Shanks, 1996; VanBuren et al., 2002).

1.1.3 Microtubule Dynamics

Early biochemical experiments found that in order to re-polymerise microtubules in vitro from brain homogenate a number of conditions were essential (Weisenberg, 1972). Firstly, that the solution had to be warmed; that GTP had to be present; that there needed to be free Magnesium ions in solution; that there needed to be a Calcium chelator; and finally that there was a minimum homogenate concentration below which microtubules would not form (Weisenberg, 1972). It was not until the mid 1980's that dynamic microtubules were observed by live darkfield and differential interference contrast microscopy for the first time (Horio and Hotani, 1986; Walker et al., 1988). The live microscopy images showed populations of microtubules that were growing and shrinking (Walker et al., 1988; Horio and Hotani, 1986). Single microtubules were observed switching stochastically between a growth state and a shrinkage state (Horio and Hotani, 1986). Either end of a microtubule is capable of both growth and shrinkage (Horio and Hotani, 1986; Walker et al., 1988, 1991). However the two ends of the microtubule exhibit very different dynamic properties, Figure 1.2 A. One end of the microtubule (the plus-end) grows more rapidly, and switches between growth and shrinkage more rapidly than the opposite end (the minus-end) (Horio and Hotani, 1986; Walker et al., 1988). The microtubule plus-end has the β-tubulin subunit exposed whilst the minus end as the α tubulin subunit exposed (Nogales et al., 1998; Caplow and Shanks, 1996). The change in the end of a microtubule from a growth state to a shrinkage state was termed a catastrophe, and the change from a shrinkage state to a growth state

was termed a rescue (Walker et al., 1988; Gardner et al., 2011). The stochastic switching of the microtubule from a growth state to a shrinkage state is known as dynamic instability (Mitchison and Kirschner, 1984; Walker et al., 1988; Horio and Hotani, 1986).

Walker et al. (1988) undertook the first comprehensive study into dynamic instability of microtubules in vitro, studying the dynamics of both the plus-end and the minus-end whilst varying the concentration of tubulin. Walker et al. (1988) found that there was a critical concentration required for the microtubule to start to grow (nucleate) from a seed, and that the critical concentration was similar for both ends of the microtubule. The rate of growth of the microtubule was proportional to the tubulin concentration and that the association constant at the plus-end was twice that of the minus end. Both the plus-end and the minus-end shrank at roughly the same rate, which was independent of the tubulin concentration. The frequency of catastrophe was inversely proportional to the tubulin concentration, and the frequency of catastrophe at the plus-end was greater than the rate of catastrophe at the minus end. Conversely the frequency of rescue of the microtubule was proportional to the tubulin concentration, and the frequency of rescue was greater at the minus-end.

The explanation for microtubule dynamic instability comes from the observation that a tubulin dimer binds GTP (Carlier and Pantaloni, 1981). Upon incorporation into the microtubule the bound GTP undergoes hydrolysis after a short time lag (Carlier and Pantaloni, 1981). One GTP molecule is hydrolysed for each tubulin dimer incorporated into the microtubule (Carlier and Pantaloni, 1981; Weisenberg et al., 1976). Dynamic instability is explained by GTP-tubulin heterodimers stochastically associating and dissociating from the microtubule tip, Figure 1.2 B (Carlier and Pantaloni, 1981; Walker et al., 1988; Mitchison and Kirschner, 1984). An increase in tubulin concentration increases the tubulin association rate, which causes a greater possibility of there being more GTP-tubulin incorporated at the tip of the microtubule (Walker et al., 1988, 1991; Hyman et al., 1992). With a constant rate of hydrolysis of the incorporated GTP-tubulin to GDP-tubulin, the amount of the GTP-tubulin incorporated at the microtubule tip (GTP cap) is greater (Walker et al., 1991; Tran et al., 1997). A larger GTP cap reduces the possibility of the GDP-tubulin lattice being revealed due to the stochastic loss of GTP-tubulin from the microtubule tip (Walker et al., 1988, 1991; Hyman et al., 1992). Should the GTP cap

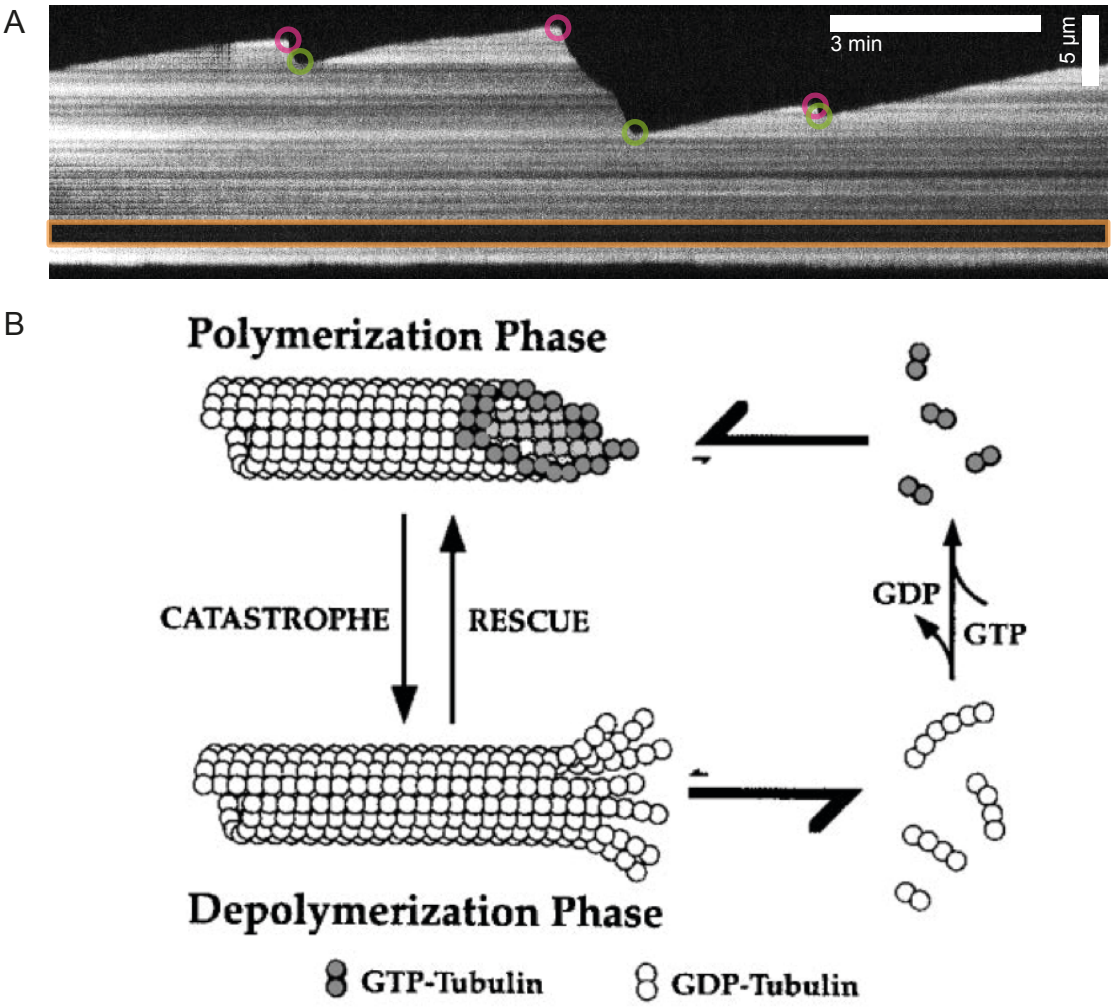

Figure 1.2: **Overview of MT Dynamics:** (A) Kymograph, spatial temporal image displaying the differing dynamics of the plus and minus ends. The orange box surrounds the seed of the MT with the minus end growing to downwards and the plus end upwards. During the fifteen minutes timeframe of the kymograph the minus ends shows almost no change, whilst the plus end undergoes three catastrophe events (magenta circles) and three rescue events (green circles). (B) Schematic of MT polymerisation/depolymerisation. During growth (polymerisation phase) GTP-tubulin dimers are stochastically added to MT tip. When the GTP cap is lost catastrophe occurs, and the MT undergoes rapid shrinkage (depolymerisation). When the GDP-tubulin dimers are released from the MT lattice, the GDP in the E-site on the β tubulin is exchanges with free GTP in solution. If a rescue occurs and the GTP cap is regained GTP-tubulin is incorporated into the lattice and the process repeats. Diagram taken from Desai and Mitchison (1997).

be lost and the GDP-tubulin lattice being revealed, the microtubule would undergo sudden shrinkage, Figure 1.2 B (Schek et al., 2007; Gardner et al., 2013; Walker et al., 1988). If during shrinkage the GTP cap is somehow regained the microtubule switches from shrinkage to growth (Schek et al., 2007; Gardner et al., 2013; Walker et al., 1988).

1.1.4 The GTP cap and tubulin conformational changes

The GTP cap is the stabilising structure preventing a microtubule from undergoing catastrophe (VanBuren et al., 2002; Hyman et al., 1992; Gardner et al., 2013). The size of the GTP cap required to stabilise the microtubule has been reported to be as little as a single layer of GTP (Caplow and Shanks, 1996). When a GTP-tubulin dimer is incorporated into the microtubule, hydrolysis cannot happen immediately as the E-site is left exposed at the plus-end of the microtubule (Caplow and Shanks, 1998). For hydrolysis to occur a composite α-tubulin β-tubulin bond was required (Caplow and Shanks, 1996). When a new protofilament capping tubulin dimer binds it was the previous capping GTP-tubulin dimer of the same protofilament that can now undergo hydrolysis. It is the α-tubulin of the new protofilament capping tubulin dimer that is the GTPase. The GTP-tubulin hydrolyses into the intermediary compound GDP+Pi-tubulin. The GDP+Pi-tubulin dimer undergoes phosphate release to form GDP-tubulin (Melki et al., 1990). Both of these reactions, nucleotide hydrolysis and phosphate release are thought to occur with first order kinetics (Carlier et al., 1989; Tran et al., 1997). Until recently it was thought that a conformation difference between GTP-tubulin (straight) and GDP-tubulin (kinked) causes the different stability (VanBuren et al., 2002; Nogales et al., 1998). Loss of the GTP cap would expose the GDP-tubulin lattice, which naturally prefers a curved orientation causing sudden shrinkage as protofilaments peel away from the microtubule (Mandelkow et al., 1991; Chrétien et al., 1995). However, it has now been shown that both GDP-tubulin and GTP-tubulin have a curved orientation when free in solution (Nawrotek et al., 2011; Rice et al., 2008). Upon hydrolysis and phosphate release different conformational changes were reported to occur within the microtubule lattice using cryo-EM techniques. (Alushin et al., 2014; Yajima et al., 2012). Yajima et al. (2012) compare guanosine-5'-(α,β)-methyleno-triphosphate (GMP-CPP), a slowly hydrolysable analogue of GTP, to GDP-microtubules stabilised with taxol (a drug that prevents

microtubule catastrophe). They discovered that GMP-CPP microtubules have two lateral interactions between adjacent β-tubulins whilst the taxol stabilised GDP microtubules only had a single lateral interactions between two adjacent β-tubulins. The reduction in the number of lateral interactions would increase the chance of loss of GDP-tubulin dimers. Alushin et al. (2014) compared GMPCPP-microtubules to GDP-microtubules and suggested that upon GTP hydrolysis the longitudinal-longitudinal interactions (the bond between two tubulin dimers in the same protofilament) become compacted. This compaction is thought to generate strain in the microtubule lattice that is released when the GTP cap is lost causing the microtubule to undergo catastrophe.

In-vitro imaging experiments on dynamic microtubules show that GTP-tubulin and GMP-CPP-tubulin dissociates from the growing microtubule plus end (Schek et al., 2007; Gardner et al., 2011). Dissociation was first shown at the plus-end via experiments using optical tweezers, Figure 1.3 A (Schek et al., 2007). Optical tweezers work by holding a bead in the centre of a focused beam. In this case the bead was attached to a GMP-CPP stabilised microtubule seed. Microtubules nucleated from the stabilised seed were positioned using the bead so that the plus end grew into a specially fabricated barrier, Figure 1.3 A. By moving the laser beam such that the displacement of the bead within the laser beam is kept constant, the force applied to the microtubule in contact with the fabricated barrier is kept constant. The correction of the laser beam to keep the force on the bead constant is the growth occurring at the microtubule tip, Figure 1.3 A. Under these experimental conditions it was discovered that microtubules regularly shrunk by 40 nm (5 tubulin layers) without catastrophe occurring (shortening excursion) (Schek et al., 2007; Gardner et al., 2011). A similar result was also obtained using fluorescent tubulin in total internal reflection fluorescence (TIRF) microscopy. Images of labelled microtubules were analysed using a novel routine that fitted a Gaussian Error Function (GEF, based on the cumulative distribution function of the standard normal distribution) along the lattice of the microtubule (Demchouk et al., 2011; Gardner et al., 2011). This increased the accuracy of measurements (15 nm error at the microtubule tip), compared to using kymographs, from TIRF microscopy of microtubule length. Additionally the function outputs a measure that relates to the amount of taper a microtubule has.

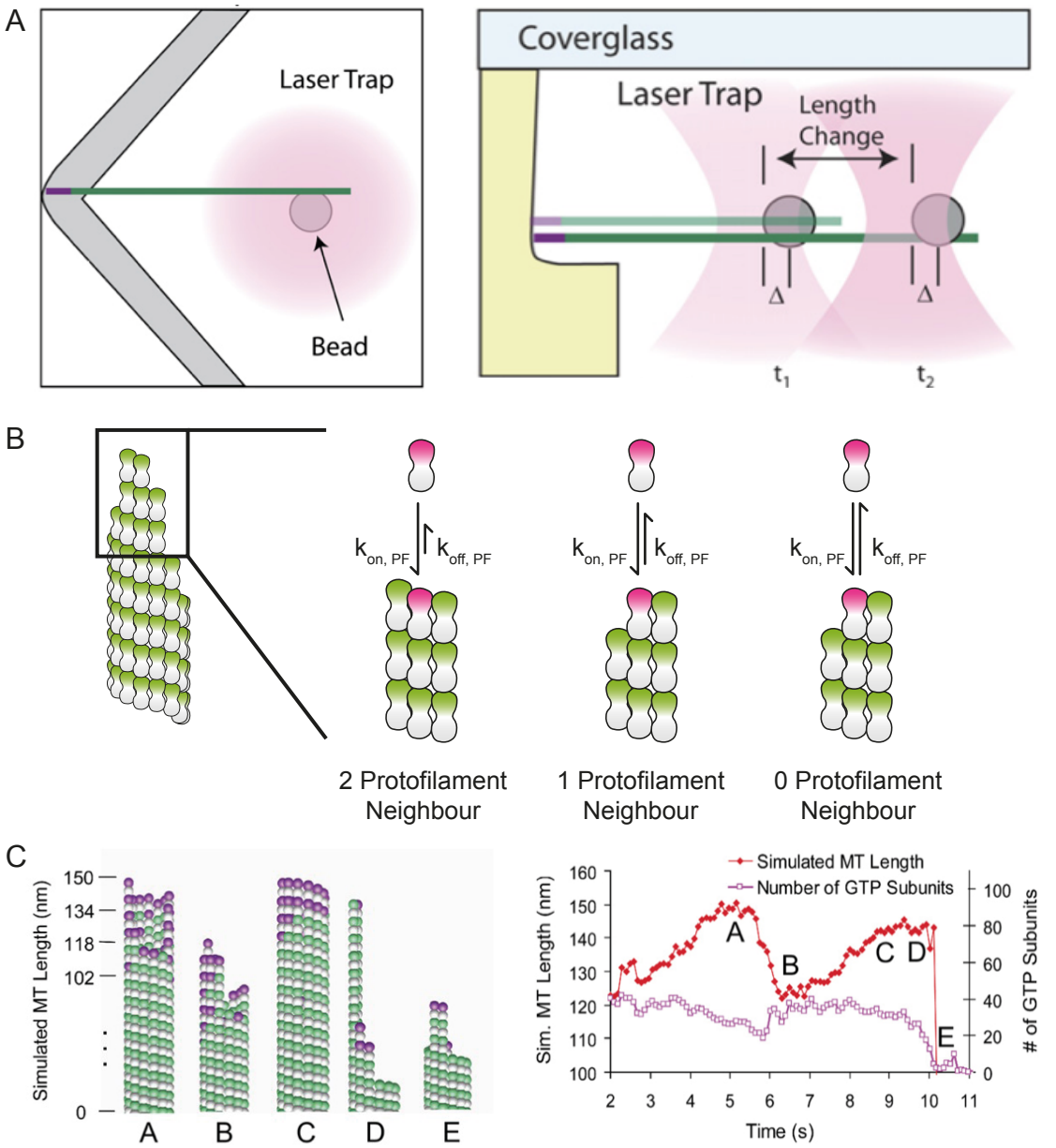

Figure 1.3: **2D Model as proposed by Gardner et al. (2011)** (A) Left: Top view and Right: side view of a schematic of the laser tweezers experiment. The bead dark pink circle is attached to the minus of a MT. The growing end is position into the corner of the prefabricated chamber. Under growth the MT forces the bead away from the corner, and by keeping the distance, Δ between the centre of the laser beam and the centre of the bead constant, the MT length change of time can be recorded. Taken from Schek et al. (2007). (B) Showing the three different combinations of neighbourhoods at the MT tip. As the number of bonds a dimer makes with its neighbour increases the disassociation rate decreases (up arrow), while the association rate does not change (down arrow). Recreated from Gardner et al. (2011). (C) Computer simulated data of the model presented in Schek et al. (2007) and Gardner et al. (2011) used to explain shortening excursions. GTP tubulin (purple) tops protofilaments, if the GTP cap is lost from the leading protofilaments, they shrink. GTP around the lagging protofilament re-stabilises the MT. This has little effect on the number of GTP tubulin with the lattice. If the number of GTP tubulin dimers in the latticed is reduced below a threshold the MT undergoes catastrophe. Taken from Schek et al. (2007).

Microtubule taper is defined as the distance between the longest (leading) protofilament and the shortest (lagging) protofilament (Demchouk et al., 2011).

As microtubules were measured losing several layers of tubulin when grown in the presence of either GTP or GMP-CPP, this removed the possibility that these shortening excursions were mini catastrophes and rescues. Shortening excursions being observed using TIRF microscopy excludes the possibility that these shortening excursions were due to force being applied to the microtubule tip. Gardner et al. (2011) also showed that with increasing tubulin concentration, the magnitude and the proportion of large (32 nm) shortening excursions also increased. Gardner et al. (2011) concluded that this increase in shortening excursions was due to the tubulin subunit dissociation rate being proportional to the tubulin concentration. This is inconsistent with the 1-D model of microtubule dynamics proposed by Walker et al. (1988) and presented above, where the dissociation constant is independent of the free tubulin concentration. To explain the relationship between tubulin dissociation rate and tubulin concentration, Gardner et al. (2011) considered the 2-dimensional geometries of different bindings sites at the microtubule tip, Figure 1.3 B. A tubulin dimer arriving at the microtubule tip could bind to the longest protofilament. In this scenario there is no neighbouring tubulin dimer for the arriving tubulin dimer to form a lateral bond with so a single longitudinal bond is formed. If an arriving tubulin dimer were to bind to a shorter protofilament then one of two scenarios is possible. Firstly, one of the neighbouring protofilaments might be longer, and one shorter. In this scenario the arriving tubulin dimer would form one lateral bond and one longitudinal bond. Secondly, both neighbouring protofilaments are longer. In this scenario the arriving tubulin dimer would form two lateral bonds and one longitudinal bond. The probability of dissociation depends on the number of binds, while the association rate is assumed to be the same in all three configurations. This scenario was modelled computationally to study the distribution of zero, one and two lateral neighbours as a function of tubulin concentration/growth rate (Gardner et al., 2011). The simulation showed that the distribution of binding sites was dependent on the growth rate. The percentage of zero neighbour binding sites was the same in all cases. However, as tubulin concentration increases the number of one neighbour binding sites increased and

the number of two neighbour binding sites decreased. This indicates that the dissociation rate of tubulin dimers during growth is dependent on tubulin concentration/growth speed. It also shows that the shape of the microtubule tip is affected by tubulin concentration. At low tubulin concentrations there are more two neighbour binding sites implying that the deviation between the lengths of protofilaments within a microtubule is less. Microtubules that have little or no difference between the leading and lagging protofilament (taper ~ 0) are called blunt microtubules. As tubulin concentration increases there is an increase in the number of one neighbour binding sites, so the taper of the microtubule increases. High tubulin concentration therefore has two effects, an increase in growth speed giving a larger GTP cap, and a microtubule with longer taper. This allows the magnitude of shortening excursions to be greater at higher tubulin concentrations; more layers of GTP-tubulin can be lost from the leading protofilaments without revealing the GDP lattice, causing a catastrophe. The finding that the dissociation rate is dependent on the tubulin concentration led to the estimated association rate of tubulin during growth phases being increased 10-fold (Gardner et al., 2011). This model of microtubule dynamics proposed by Gardner et al. (2011) is referred to as the 2D model.

1.2 Microtubule Associated Proteins

1.2.1 Overview

Within cells, a large number of proteins are known to associate with microtubules (MAPs) (Kumar and Wittmann, 2012; Jiang et al., 2012; Vicente and Wordeman, 2015). Many of these proteins are essential in controlling microtubule dynamics, or enabling microtubules to carry out a cellular function. These proteins can broadly be combined into one of three groups based upon binding location or function (Kumar and Wittmann, 2012; Jiang et al., 2012; Vicente and Wordeman, 2015; Wasteneys, 2002). The three groups are the motor proteins, the structural MAPs and the tip trackers.

The microtubule associating “motor” proteins are a MAP group made up of two protein families, kinesin and dynein (Bachmann and Straube, 2015; Goodson et al., 2003). The

group is named as the proteins use adenosine triphosphate (ATP) as an energy source to “walk” along microtubules (Lakämper and Meyhöfer, 2006). The kinesin family can be sub-divided into a number of sub-families, named Kinesin-1, Kinesin-2 etc. (Bachmann and Straube, 2015). The majority of kinesin are plus-end directed motors (they walk towards the plus end), however the Kinesin-14 family has been shown to be a minus-end directed motor (Theisen et al., 2012; Bancroft et al., 2015). Dynein is a complex protein composed of various subunits and is a minus-end directed motor (Carter et al., 2016). Kinesin and Dynein are involved in intracellular transport, transporting cargo throughout the cell (Carter et al., 2016; Bachmann and Straube, 2015; Lakämper and Meyhöfer, 2006). By forming tetramers some kinesin can cross-link microtubules forming anti-parallel microtubule arrays such as those found in the mitotic spindle (Bancroft et al., 2015). As mitosis progresses the kinesin walk towards the microtubule plus-ends forcing the chromosomes further apart (Bancroft et al., 2015). Some kinesin can bundle microtubules, either by forming a tetramer, or by having a second microtubule-binding site in the kinesin tail (Straube et al., 2006). Additionally kinesin are part of the kinetochore-binding complex and ensure that the kinetochore remains attached to the microtubule from metaphase to anaphase (Vicente and Wordeman, 2015). Axonemal dynein links microtubules in flagella and generates the forces to bend them (Venier et al., 1994; Carter et al., 2016). As well as being involved in many cellular processes some kinesins have been shown to have an effect on microtubule dynamics (Bachmann and Straube, 2015; Montenegro Gouveia et al., 2010). The best-known microtubule depolymeriser is the kinesin MCAK, a member of the Kinesin-13 family, which increases the catastrophe rate of microtubules (Montenegro Gouveia et al., 2010).

The structural MAPs associate to either the inside or the surface of the microtubule (Orpinell et al., 2010; Bechstedt and Brouhard, 2012). These MAPs bind to the microtubule and have a role in either stabilising/destabilising the microtubule or ensuring correct formation of the microtubule Wasteneys (2002); Bechstedt and Brouhard (2012). Doublecortin ensures the correct formation of the microtubule by preferentially recognises microtubule with 13 protofilaments and by binding stabilises the microtubule Bechstedt and Brouhard (2012). Other proteins such as Katanin destabilise the microtubule Srayko et al. (2006). Katanin cuts the microtubule in two, causing a catastrophe. There are

proteins that are thought to bind to the inside of the microtubule such as Tau, a MAP associated with stabilising microtubules in neuronal cells, and Tubulin Acetyl-Transferase (TAT) which can acetylate α tubulin Noetzel et al. (2005); Qiang et al. (2006); Orpinell et al. (2010); Soppina et al. (2012); Kar et al. (2003). The acetylation is not thought to have a stabilisation effect, but to increase microtubule stiffness (Soppina et al., 2012).

The last group of MAPs associate to the microtubule tip Kumar and Wittmann (2012); Mimori-Kiyosue et al. (2005); Buey et al. (2012); Slep and Vale (2007). The majority of these proteins associate with the microtubule plus-end and are known as +TIPs Kumar and Wittmann (2012). However, there are some proteins, which are known to selectively bind to the microtubule minus-end (Hendershott and Vale, 2014; Akhmanova and Steinmetz, 2015). The best known of these are γ-tubulin, calmodulin-regulated spectrin-associated proteins (CAMSAPs) and Patronin which are all thought to stabilise the minus end of the microtubule (Hendershott and Vale, 2014; Akhmanova and Steinmetz, 2015). Whilst many proteins are included in the +TIP network, there are only a few families that have been shown to autonomously track the plus-end. XMAP215/chTOG/Stu2p is a TOG (Tumour Overexpressed Gene) domain protein that binds to the very tip of the microtubule (Slep and Vale, 2007; Zanic et al., 2013). XMAP215 is a catalyst and increases both growth speed and shrinkage speed (Zanic et al., 2013). It is formed of six TOG domains (van der Vaart et al., 2012; Slep and Vale, 2007). TOG domains are capable of binding tubulin heterodimers in solution (Nakamura et al., 2012; Ayaz et al., 2014). Cytoplasmic linker-associated proteins (CLASPs) bind both to the microtubule tip and to the microtubule lattice via a TOG domain (Grimaldi et al., 2014). In mammalian cells they rely on EB1 (see below) to localise to the microtubule plus-ends (Mimori-Kiyosue et al., 2005; Akhmanova and Steinmetz, 2015). CLASPs have been shown to promote rescues and are capable of binding tubulin hetero-dimers in solution (Ayaz et al., 2014; Mimori-Kiyosue et al., 2005). The key component of the +TIP network however is the End Binding (EB) family Juwana et al. (1999); Straube and Merdes (2007). They have been implicated in binding to a large range of proteins and are thought of as the master regulator of the microtubule +TIP network Jiang et al. (2012).

1.2.2 EB Family

The EB family of proteins is highly conserved. In mammalian cells there are three members (EB1, EB2 and EB3) and they are encoded by the MAPRE genes (Juwana et al., 1999; Su and Qi, 2001). EB1 is ubiquitously expressed with homologues identified in all other Eukaryotes (Juwana et al., 1999; Tirnauer et al., 1999; Rehberg and Gräf, 2002; Beinhauer et al., 1997). Most widely studied of the EB1 homologues are Mal3 in *S. pombe*, and Bim1 in *S. cerevisiae* (des Georges et al., 2008; Juwana et al., 1999). EB2 and EB3 have been shown to be differentially expressed (Goldspink et al., 2013; Straube and Merdes, 2007; Nakagawa et al., 2000). EB3 is up regulated in differentiating myoblast cells, and has a role in ensuring capture of the microtubule at the cell cortex in forming myotubes (Straube and Merdes, 2007). Down regulation of EB2 during epithelial differentiation has been linked to microtubule bundle formation (Goldspink et al., 2013).

All three mammalian EB proteins are highly similar with a molecular weight of $\sim$35 kDa and naturally form a stable homo-dimer (Su and Qi, 2001; Sen et al., 2013). They have a well-conserved calponin-homology (CH) domain near the N-terminus and a dimerisation-domain (DD) near the C-terminus (De Groot et al., 2010; Hayashi and Ikura, 2003). The structures of the CH and the DD have been solved separately by x-ray crystallography for EB1 and EB3 (Slep and Vale, 2007; De Groot et al., 2010). The CH domain is globular is all that is required for binding to MTs (Slep and Vale, 2007; De Groot et al., 2010; Hayashi and Ikura, 2003; Komarova et al., 2009). The DD is a 4 helix bundle in which there is a pair of two larger α helices connected to a pair of shorter α helices by a short unstructured linker (Honnappa et al., 2005).The DD is followed by a highly acidic region containing an EEY/F motif (Honnappa et al., 2005). The CH domain is connected to the DD domain by an unstructured linker (Honnappa et al., 2005). Small angle x-ray scattering (SAXS) analysis of EB dimers has provided a model to which the crystal structures of the CH and DD domain have been fitted (Buey et al., 2011). As a homo-dimer they are thought to be shaped similar to a golf club, Figure 1.4. The two CH domains form a composite microtubule binding site Maurer et al. (2012).

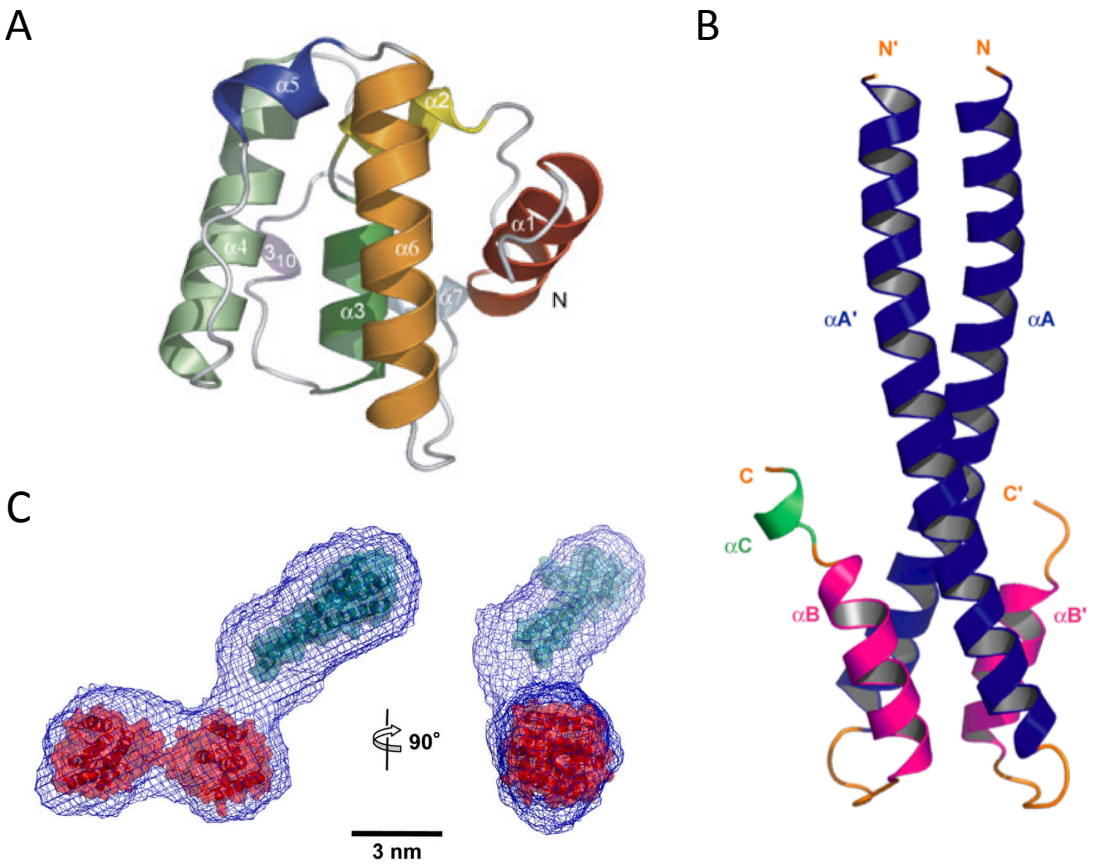

***Figure 1.4:* Cartoon representation of EB Structure** (A) Crystal structure of the CH domain of EB1, showing the six α helices that comprise the CH domain in differing colours. (B) Crystal Structure of the dimerisation-domain of EB1, made up of four intersecting α helices, two from each protein. (C) Model of the expected shape of EB dimer from SAXS analysis (blue mesh) mapped onto the known EB calponin-homology domain (red) and dimerisation-domain (cyan) domain structures. (A) taken from Slep and Vale (2007), (B) taken from Slep et al. (2005) (C) taken from Buey et al. (2011)

Due to the similarity between dimerisation-domains, the existence of hetero-dimers has been investigated and was shown to be possible by the removal of the CH domain (De Groot et al., 2010). Hetero-dimerisation was shown to exist *in vitro* between EB1 and EB3 using fluorescence resonance energy transfer (De Groot et al., 2010). However, with the CH domain intact the EB3 dimer has been shown to be extremely stable over a large range of conditions (Sen et al., 2013). EB2 is the least similar of the three EB family members as it contains an N-terminal extension and a less acidic C terminal tail (De Groot et al., 2010).

The C terminus of EB proteins contains two binding domains that allow it to interact with other proteins (Honnappa et al., 2006, 2005; Weisbrich et al., 2007). The hydrophobic region of the dimerisation-domain binds to proteins containing an SxIP motif (Jiang et al., 2012). The proteins that contain an SxIP domain are structurally and functionally diverse. They include the adenomatous polyposis coli (APC) protein, which has been shown to stabilise microtubules, through to proteins such as MCAK, a kinesin known to be a microtubule depolymerase (Montenegro Gouveia et al., 2010; Bjelić et al., 2012; Honnappa et al., 2005). The acidic region containing the EEY/F motif is a target for proteins containing a CAP-Gly domain (Komarova et al., 2005). CAP-Gly domains are highly conserved and contain a GKNDG motif that has been shown to be being responsible for binding to the EEY/F motif (Honnappa et al., 2006). Known +TIPs with CAP-Gly domains also display a diverse range of functions. Examples include the cytoplasmic linker protein, CLIP 170, which has been shown *in vitro* to decrease catastrophe rate or stimulate rescues. Or the protein p150^{glued} which has been shown to increase processivity of the dynactin complex (Dixit et al., 2009; Honnappa et al., 2006).

The microtubule-binding domain of EB proteins is via the N-terminal CH domain. EB proteins have been shown to bind between protofilaments at the intersection of four tubulin dimers, close to the E-site of the beta subunits (Sandblad et al., 2006; Maurer et al., 2012). There is disagreement over whether EB proteins preferentially recognise the A or B-lattice of the microtubule (des Georges et al., 2008; Sandblad et al., 2006; Maurer et al., 2012). des Georges et al. (2008) and Sandblad et al. (2006) showed Mal3 binding to the A-lattice or seam of a B-lattice microtubule. This gave rise to the idea that EB proteins would bind along the seam (edge of the sheet) and assist in closing the microtubule into a tube (Vitre et al., 2008). This stabilises the microtubule and des Georges et al. (2008) showed that a high concentration of Mal3 on *S. pombe* tubulin formed full A-lattice microtubules. Maurer et al. (2012) reported Mal3 binding between B-lattice protofilaments on GTP-γS tubulin microtubules while the seam was left unoccupied

In the cellular environment both EB1 and EB3 have been shown to autonomously track growing microtubule ends with a distinct comet shape distribution (Komarova et al.,

2009). Additionally EB1 and EB3 have been shown to promote persistent MT growth by suppressing catastrophes (Komarova et al., 2009). Whilst no positional difference was observed between EB1 and EB3 in cells, EB2 does not have such a distinct comet and its localisation is spread along the microtubule lattice Komarova et al. (2009). No single published study has yet directly compared the effect of all three EB family members *in vitro*. A number of studies have looked at the effect of a single EB protein, nominally EB1 or one of its homologues Mal3 and Bim1, alongside a binding partner. *In vitro* experiments show that EB1 and EB3 autonomously track the growing MT end with the distinctive EB comet (Komarova et al., 2005; Zanic et al., 2009; Maurer et al., 2014). Additionally both EB1 (or an EB1 homologue) and EB3 have been shown to increase growth speed (Komarova et al., 2009; Bieling et al., 2007; Tirnauer et al., 1999), and increase catastrophe frequency (Maurer et al., 2014; Komarova et al., 2009).

EB proteins are thought to track the growing tip of microtubules by recognising the nucleotide state of tubulin (Zanic et al., 2009; Maurer et al., 2011). Due to the preference of EB1 and EB3 to bind strongly to microtubules with GTP-γS lattices, or GTP microtubules polymerised in the presence of BeF_3^-, EB proteins are thought to bind to an intermediate state of GTP hydrolysis (Maurer et al., 2012; Zhang et al., 2015). EB1 and EB3 have a weaker preference for GMP-CPP microtubules (Zanic et al., 2009; Maurer et al., 2012), although removal of KCl increases the binding of EB1 to GMP-CPP-tubulin to a similar level to that observed at the MT tip (Zanic et al., 2009).

EB1 has been implicated in affecting the tip structure of the microtubule (Vitre et al., 2008; Maurer et al., 2014). Vitre et al. (2008) show that in electron microscopy images EB1 reduces the amount of protofilament splaying at the microtubule tip. Maurer et al. (2014) report that EB1 accelerates a maturation step on the microtubule, as they observe the peak EB signal approaching the tip of the microtubule with an increase in EB1 concentration.

1.3 Thesis Motivation and Outline

EB3 (and EB1) have been shown to increase microtubule growth speed and to increase microtubule catastrophe rate. Based on the GTP cap model this effect appears to be a paradox. As microtubules grow faster the size of the GTP cap should increase reducing the probability of catastrophe. However, EB3 causes an increase in catastrophe rate. The increase in growth speed can be explained by EB proteins stabilising lateral and longitudinal interactions, thereby reducing the rate of dissociation of tubulin. The reduction in the disassociation rate of tubulin, increases the growth speed of the microtubule. According to the 2D model this would present an increase in taper at the tip of the microtubule. This idea appears to contradict Maurer et al. (2014) who show that EB1 accelerates a maturation step on the microtubule and report no measurable microtubule taper. This leads to the first research question that was investigated:

"How does EB3 simultaneously promote catastrophe and growth of a microtubule?"

To test this, EB3 was chosen as in our hands it has the highest affinity to the microtubule in the hope that any result would be more pronounced. Dynamic fluorescent microtubules were imaged by a total internal reflection fluorescence microscopy. The methods used to detect changes in microtubule taper in Gardner et al. (2011) (based on the paper Demchouk et al. (2011)) were carefully investigated and further developed. The code was then used to measure microtubule tip structure during growth, both in the presence and absence of EB3. This part is described in the first results chapter, Chapter 3

Whilst all Eukaryotes express a homologue of EB1, mammalian cells express three members of the EB protein family. EB1 is ubiquitously expressed whilst EB2 and EB3 are differentially regulated (Straube and Merdes, 2007; Nakagawa et al., 2000). The three EB proteins have been shown to bind to different sites on the microtubule lattice, and whilst EB1 and EB3 have similar binding profiles, EB2 is distinctly different. EB1 and EB3 co-locate with sharp peaks, whilst EB2 is displaced down the lattice with no distinctive peak (Komarova et al., 2005). This leads to the second research question:

"Why do EB family members track the growing microtubule end at spatially distinct sites?"

To test this EB1, EB2 and EB3 distributions were carefully compared against each other in vitro using total internal reflection fluorescence microscopy. The EB comet shape was determined over a range of concentrations. Additionally the peak position was determined for EBs whilst in competition against with other, and alone measured relative to the tip of the microtubule. These results are described in the second results chapter, Chapter 4.

In Chapter 5 I describe a model to explain the differences in localisation of the three EB proteins. Structural function analysis by creating chimeric versions of EB3 and EB2 is presented to begin investigating the mechanism underlying binding preferences.

The results are discussed in detail at the end of each chapter. There is no global discussion at the end of this document.

Chapter 2

Materials and Methods

2.1 Materials

Labelled tubulin was from Cytoskleleton Inc, nucleotides were from Jena Biosciences and all other chemicals were from Sigma unless indicated.

2.2 EB Protein Cloning, Expression and Purification

EB1, EB2 and EB3 ORFs were amplified from random primed cDNA from mouse-myoblast (C2C12) cell line (Straube and Merdes, 2007) introducing NdeI and EcoRI restriction sites. GFP was amplified from pEGFP-C1 to introduce EcoRI and NotI restriction sites. EB and GFP fragments were ligated to pET22b opened with NdeI and NotI. A resulting frameshift was corrected by opening with EcoRI, mung bean nuclease treatment and re-ligation of the vector. This allowed expression of N-terminal EB constructs with a GFP-6xHis C-terminal. GFP was replaced by mCherry to obtain EB-mCherry-6xHis. All plasmid sequences were verified by DNA sequencing.

DNA constructs were transferred into E. coli BL21 (DE3) and grown to OD 0.6 at 18°C in 2xYT broth (1.6% peptone, 1% yeast extract, and 0.5% NaCl) supplemented with Ampicilin. Isopropyl β-D-1-thiogalactopyranodisde (IPTG) was added to 2xYT to a final

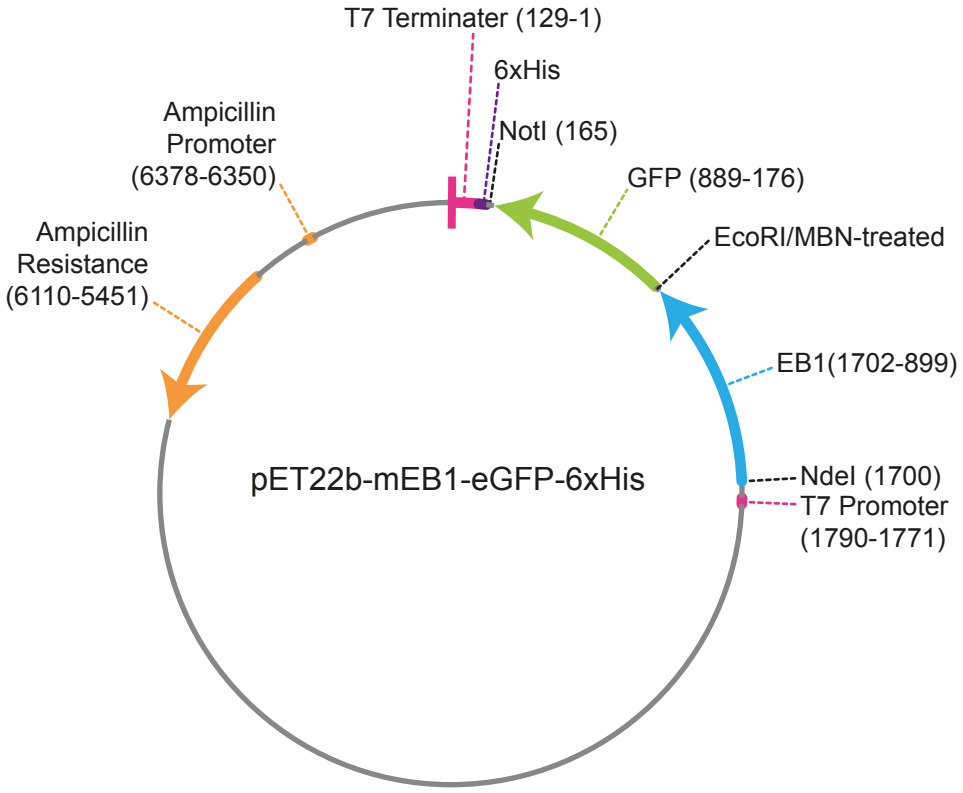

Figure 2.1: **EB1 pET22b vector:** Vector showing the final vector for mouse EB1 with a C-terminal GFP and 6xHis tag. T7 promoter and terminater shown in pink, the GFP in green, mouse EB1 in blue and the ampicillin promoter and resistance in orange. The NotI and NdeI sites are shown in black along with the location of the EcoR1 site before it was mung bean treated.

concentration of 0.8 mM and bacteria were left for 18 hours to express protein. Bacteria were harvested in a Thermo Scientific SLA-3000 rotor at 3,000 rpm, 4°C, for 15 minutes. The supernatant was discarded, and the pellet was resuspended in twice the pellet volume of column buffer (50 mM KPO_4 buffer pH 7.2, 400 mM NaCl, 2 mM $MgCl_2$, 2 mM 2-Mercaptoethanol). The bacteria were then washed by increasing the volume to 10 times the pellet volume with column buffer and pelleting in a Thermo Scientific Sorvall Primo centrifuged at 3000 rpm, 4°C, SLA-3000 rotor for 10 minutes. The pellet was resuspended in twice the pellet volume of column buffer + 20% glycerol and snap frozen in liquid nitrogen and stored at -80°C until required. If used immediately, the glycerol was omitted.

Cell pellets were defrosted on ice. On defrosted bacteria were lysed in binding buffer (column buffer with 12 mM imidazole) supplemented with 0.1% Triton X-100, 1 mg/ml

lysozyme and 1 mM PMSF by sonication. The lysed cells were clarified by two consecutive spins in Thermo Scientific SS-34 rotor at 20,000 rpm, 4°C for 15 minutes, or until clear. The supernatant was incubated for one hour at 4°C with 0.5 ml of Ni-NTA Agarose (Qiagen, 30210) per ml of pellet volume. The Ni-NTA agarose had been equilibrated into binding buffer by being washed with ddH_2O three times. The Ni-NTA agarose was washed by dilution with 5xNi-NTA volume of ddH_2O, resuspension, pelleting via very gentle centrifugation, and careful removal of the waste liquid above the agarose bed volume. To equilibrate Ni-NTA into binding buffer, the washing step was repeated with binding buffer. Following incubation the supernatant was passed through a 5 ml syringe with a glass wool filter, and the resulting agarose bed washed with 5 column volumes of binding buffer and 5 column volumes of wash buffer (column buffer with 20 mM imizadole). The protein was eluted in column buffer supplemented with 400 mM imizadole and collected in 500 μl fractions.

The main EB containing fractions were identified by absorbance at 280 nm (A280) using a Thermo Scientific NanoDrop 2000 Spectrophotometer, and combined. Full length proteins were then purified by size exclusion chromatography using a Superdex200 16/60 column (GE Healthcare) on an AKTApurifier (GE Heathcare) system, controlled by UNICORN software (GE Heathcare). Modified and chimeric versions of full length proteins skipped this step.

All buffers used with the AKTApurifier were filtered using a Millipore Stericup-HV, 0.45 μm, PVDF, 500 ml. The column was removed from storage buffer (20% ethanol) by washing with 2 CV of ddH_2O at 1 ml/min and equilibrated with column buffer by washing with 4 CV of column buffer at 1 ml/min. Protein was loaded using a 2 ml sample loop equilibrated in column buffer, and eluted at 0.3 ml/min and was collect in 0.5 ml fractions. The peak fractions identified by absorbance at 280 nm were combined. The column after use was washed with 2 CV of column buffer. For storage, the column was washed with 2 CV of ddH_2O or until the conductance was stable, and then transferred into 20% ethanol.

Further purification was performed by passing the protein over a HiTrap Q 1 ml ion exchange column followed by a HiTrap SP 1 ml ion exchange column attached to the AKTApurifier. Both columns were removed from 20% ethanol by washing with 5 CV of

ddH_2O at 1 ml/min. They were then equilibrated in modified column buffer (no NaCl, pH 6.8 for the SP column, pH 7.9 for the Q column) by washing with 5 CV at 1 ml/min. Further washings were performed by washing with elution buffer (5 CV modified column buffer with 1 M NaCl, before re-equilibrating with 5 CV of modified column buffer. Protein from the previous step was diluted 1:10 in modified column buffer and loaded by a sample pump at 3 ml/min. The sample pump was washed with 5 ml of modified column buffer at 3 ml/min. The protein bound to the column was washed with 5 CV of modified column buffer at 1 ml/min. The protein was eluted by salt gradient over 15 CV by linear change from modified column buffer to elution buffer at 1 ml/min. Elutions were captured in 250 μl fractions When moving from the Q column to the SP column, the peak fractions ($>$50% of the maximum) from absorbance at 488 nm was combined as the sample to be added to the SP column. After use, the column was washed with a further 5 CV of elution buffer, and re-equilibrated with 5 CV of modified column buffer at 1 ml/min. For storage, the column was washed with 5 CV of ddH_2O or until the conductance was stable, and then transferred into 20% ethanol.

If further concentration was required ($<$25 μM for EB3, or $<$30 μM for EB1 or EB2), The peak fractions were combined and concentrated using vivaspin columns (Sartorius), supplemented with 20% glycerol, snap frozen and stored in liquid nitrogen. Protein concentration was determined by measuring absorption at 280nm and coomassie blue staining of poly-acrylamide gel electrophoresis protein gels.

2.3 Purification of Tubulin from Porcine Brain

Tubulin was prepared from porcine brains according to published protocols (Gell et al., 2011) with a couple of modifications. The brains were extracted immediately after termination of the animal and placed into bags of ice cold PBS containing PBS ice cubes, and transferred to the laboratory. The brains were normally within the laboratory within two hours of termination. Upon arrival the brains were weighed and supplemented with 50% weight to volume crude buffer (100 mM PIPES pH 6.8, 0.5 mM $MgCl_2$, 2 mM EGTA pH 8.0, 0.1 mM EDTA, 1.0 mM MgATP, 0.1 mM NaGTP, 1 mM DTT supplemented with

anti-proteases) homogonised by blending at full power for 30 s (Kenwood Mixer). The slurry was then clarified by centrifugation in SLA-1500 rotor (Thermo Scientific) at 14,500 rpm, 4 °C for 1 hour.

The tubulin was then subjected to its first polymerisation cycle. The supernatant was transferred to a clean vessel and made up to 5 mM $MgCl_2$, 1 mM NaGTP and 50 μl DCI, 33% v/v glycerol. The solution was then raised quickly, under constant swirling, to 37°C and left incubating at 37°C for an hour, with intermittent perturbation, to allow microtubules to form. The microtubules were pelleted by centrifugation in SLA-1500 rotor at 14,500 rpm, 37°C for 3 hours. The supernatant was discarded and at 4°C the pellets were released from the centrifuge pot wall with 10 ml/pellet polymerisation buffer (100 mM PIPES pH 6.8, 0.5 mM $MgCl_2$, 2 mM EGTA pH 8.0, 0.1 mM EDTA, 0.1 mM NaGTP, 4 mM DTT supplemented with anti-proteases and 0.1% β-mercaptoethanol) and homogenised by fifteen strokes of a tight Wheaton homogeniser on ice. The MT's were then left to depolymerise on ice for 40 minutes and the solution clarified by high speed centrifugation in T-865 (Sorvall) at 65,000 rpm, 4°C for 30 minutes.

The tubulin was then subjected to a second polymerisation cycle. The supernatant was transferred to a clean vessel and made up to 5 mM $MgCl_2$, 1 mM NaGTP and 50 μl DCI, 33% v/v glycerol. The solution was then raised, under constant swirling, to 37°C and left to incubate for an hour, with intermittent perturbation, to allow microtubules to form. The microtubules were pelleted by centrifugation in T-865 rotor at 45,000 rpm, 37°C for 1 hour. At this point the supernatant was discarded and the pellet snap frozen, and stored at -80°C.

In general at this point the frozen pellets were split in half and purified in two batches. This was due to reduced capacity in the centrifugal rotas used below to process the whole prep in one step.

The pellets were defrosted on ice and detached using 250 μl of column buffer (50 mM PIPES pH 6.9, 0.2 mM $MgCl_2$, 1 mM EGTA pH 8.0). Each pellet was transfer to a Wheaton homogeniser with an additional 1 ml column buffer per pellet, and homogenised by ten strokes of a tight Wheaton homogeniser on ice. The microtubules were then left to

depolymerise on ice for 40 minutes and the solution clarified by high speed centrifugation in TLA-100.3 (Sorvall) at 50,000 rpm, 4°C for 30 minutes. The clarified supernatant was then loaded onto a phosphocellulose column equilibrated with GTP column buffer (see below). The supernatant was loaded via sample loop at 0.2 ml/min with GTP column buffer. The tubulin was eluted at 0.2 ml/min with GTP column buffer and collected in 1 ml fractions. Following elution the peak fractions were combined, aliquoted and snap frozen in liquid nitrogen.

If required the MAPs can be eluted/ or the column cleaned for a second round by running 2 CV of high salt column buffer at 1ml/min. The column was then equilibrated with GTP column buffer, then ddH_2O, before being dismantled. The AKTA was washed and returned to its storage state by rinsing with 20% EtOH.

2.3.1 Phosophocellulose Column Preparation

The phosphocellulose column was prepared by adding 20 g of phosphocellulose (P11, Whatman) powder to 0.5 L of 0.5 M NaOH to create a uniform slurry. The resin was allowed to settle for 5 minutes before the supernatant was removed. The solution was then neutralised by the addition of 0.5 L of 0.5 M K-phosphate, pH 6.8. Neutralisation was tested by pH paper. After allowing the resin to settle for 5 minutes the clear supernatant was removed and the resin washed with 1 L of ddH_2O. The resin was then acid treated by removing the clear supernatant after 5 minutes and re-suspending into 0.5 L 0.5 M HCl. The resin was allowed to settle for 5 minutes before the clear supernatant was removed. The solution was then neutralised by the addition of 0.5 L of 0.5 M K-phosphate, pH 6.8. Neutralisation was tested by pH paper. After allowing the resin to settle for 5 minutes the clear supernatant was removed and the resin washed with 0.5 L of ddH_2O, this step was repeated once. The clear supernatant was removed after 5 minutes and the resin was resuspended in column buffer. After 5 minutes half of the clear supernatant was removed.

The resin was hand packed into a XK56 AKTA column by gravity flow using column buffer. Once the column has been fully assembled and the resin has settled, the column was

connected to the AKTA, which has been pre-equilibrated into column buffer. The column was further packed under pressure by flowing 1 CV of column buffer at 1 ml/min over, and the column spacing was adjusted as required to ensure the column remained packed. The column was then blocked by loading 30 ml of 30 mg/ml BSA onto the column and chasing with 0.5 CV of column buffer. The BSA was then incubated on the column for two hours before being eluted with 2 CV high salt column buffer (column buffer with 1 M KCl). After elution, the column was equilibrated with 10 CV of column buffer at 1 ml/min. And further equilibrated with 2 CV of GTP column buffer (column buffer plus 0.1 mM NaGTP) at 1 ml/min.

2.4 Sodium Dodecyl Sulfate - Polyacrylamide Gel Electrophoresis (SDS-PAGE)

All gels used in this document are 10% PAA separation gel with a 4% stacking gel on top. The gels were constructed using a standard kit, SDS Gel Preparation Kit (Fluka 08091). Manufactures instructions were followed as per the guidelines.

Samples were prepared by adding 20% v/v laemmli buffer (300 mM Tris-HCl, pH 6.8, 30% Glycerol, 20% SDS, 0.5% Bromophenol-Blue, 15% β-mercapto-ethanol) and boiling at 90°C for 2 mins.

Plates for 1.0 mm thick gels were throughly washed with deH_2O and then wiped over with IMS and left to dry. The back and front plates were assembled in pairs, and placed in the casting frame, before they were placed in the casting module. The separating solution (10%v/v Poly-acrylamide, 33%v/v 3xSeparation Buffer, 64%v/vddH_2O, 2%v/v TEMED and 0.1% Ammonium-persulphate) was then added to within 2 cm of the top and 1 ml of isopropanol added to remove air bubbles. Once set, the isopropanol was removed and the gel washed with ddH_2O; the water was removed and gel was left to dry for 5 minutes. The stacking solution (4%v/v Poly-acrylamide solution, 20%v/v 5x Separation Buffer, 81%v/vddH_2O, 2%v/v TEMED and 0.1% Ammonium-persulphate solution) was then added to the top, and a 1 mm 10 well comb added, taking care not to introduce air

bubbles. Once set, the gel was either used within the hour, or wrapped in damp tissue paper, then cling film, and stored at 4°C for a maximum of 5 days.

The set gels were assembled into the mini-PROTEAN® electrode clamps, using the buffer dam if required and placed into the Tetra tank. SDS running buffer was added to the mini-PROTEAN® Tetra tank, and into the void between gels, as per the manufactures instructions. Samples were loaded into the wells in the gel with one well reserved for the protein ladder. Gels were run at 16 mA/gel for 1 hour 45 minutes. The gels were extracted from between the plates and under went two 5 minute washes in ddH_2O. Each gel was then left to stain overnight in SimplyBlue™ Safe Stain (Life Technologies). For destaining the gels were subjected to several 1 hour washes in ddH_2O, followed by an overnight wash in ddH_2O.

Gels were then imaged, and either dried or discarded.

2.5 In vitro microtubule dynamics and binding assays

2.5.1 Microtubule Seeds

Microtubule seeds were assembled from a 10 μl reaction mix containing a ratio of 85% porcine brain tubulin, 5% biotin-tubulin and 10% labelled tubulin (either rhodamine or HyLite 647™labelled tubulin) with a final concentration of $\sim$30 μM, 1 mM GMP-CPP in MRB80 (80 mM PIPES, pH 6.8 with KOH, 1 mM EGTA, 4 mM $MgCl_2$). The reaction mix was first left on ice for thirty minutes to stimulate nucleotide exchange before being left to polymerise for one hour at 37°C. The polymerised microtubules were then diluted 10-fold with MRB80 containing 2 μM Taxol and stored in the dark at RT.

For creation of pure GTPγS the GMP-CPP in the reaction mix was removed and replaced with GTPγS. For creation of the mixed seeds lattices, two reaction mixes were created, one for GMP-CPP and the other for GTPγS. They were then mixed together on ice at the required ratios before being left to polymerise as above. To distinguish the mixed lattice,

during incubation on ice, GMP-CPP-tubulin was mixed with a fluorescently tagged tubulin, whilst GTP-γS-tubulin was mixed with an alternative fluorescently tagged tubulin.

2.5.2 Glass Coverslip Treatment

Glass coverslips were prepared by placing filling ceramic holders, with coverslips and placing (to cover) in 40% HCl solution overnight at 60°C. The ceramic holders were transferred to a clean beaker containing ddH_2O (enough to cover) and left in a sonicating water bath at 60% for five minutes. The previous step was repeated for a total of four sonications. Following four rounds of sonication the slides are spun dried and stored between lint free tissue paper unit required.

2.5.3 In Vitro Assay Assembly

A 100 μm deep flow chamber was made by fusing a glass slide and a hydrochloric acid-treated coverslip using double-sided tape (Scotch 3M). The surface was passivated with 0.2 mg/ml PLL-PEG-50% biotin (Susos AG, Zurich) by incubation for five minutes, during which the coverslip is underneath the glass slide. The chamber was washed with 200 μl MRB80, and exchanged with 30 μl 1 mg/ml streptadavin and incubated for five minutes, during which the coverslip is underneath the glass slide. The chamber was washed with 50 μl MRB80, and exchanged with 30 μl microtubule seeds, diluted to give a suitable surface density in MRB80 (typically 0.5 μl in 30 ml of MRB80). The seeds were left to attach to the passivated surface, via streptadavin-biotin bonds for five minutes, during which the coverslip is underneath the glass slide. The unattached seeds were then washed out with 50 μl MRB80 and the surface blocked by exchange with 30 μl 1 mg/ml κ-casein for five minutes, during which the coverslip is underneath the glass slide. A reaction mix containing 12 μM tubulin, 50 mM KCl, 1 mM GTP, 0.6mg/ml κ-casein, 0.2% methyl cellulose, 4 mM DTT, 0.2 mg/ml catalase, 0.4 mg/ml glucose oxidase, 50 mM glucose in MRB80, supplemented with EB proteins or buffer was clarified for five minutes at 4°C at 200,000 g in an airfuge (Beckman). The supernatant was added to the flow chamber and the chamber sealed with melted candle wax.

2.5.4 Imaging

Microtubule assembly was observed on an Olympus total internal reflection fluorescence (TIRF) system using a 100x NA 1.49 objective, 1.6x additional magnification, 488 nm, 561 nm and 640 nm laser lines. Images were acquired via a Hamamatsu ImageEM-1k back-illuminated EM-CCD camera under the control of Xcellence software. Resulting spatial resolution of the obtained microscope images were 81 nm/pixel.

2.6 Image Analysis

Images obtained can be separated into two categories, those that contain a labelled microtubule and those that do not. For those that had a labelled microtubule custom code was developed in MATLAB® (2012a, The MathWorks), a full description can be found in Chapter 3. Otherwise kymographs or line scans were obtained from TIRF microscopy images.

Kymographs were created by drawing linear lines onto image stacks and the intensity at every time point extracted using the ImageJ kymograph plugin by Arne Seitz (Seitz). For comet shape, and EB competition experiments, the kymographs were cropped to linear growth regions. The cropped kymographs were created by drawing a rectangular ROI around the linear region and the ROI region duplicated. The resulting images were saved automatically using a ImageJ macro.

For comparative intensity measurements for the EB chimeras, kymographs were examined for linear growth regions with good tip intensity. The average intensity for the tip was obtained by drawing a line through the brightest parts of the tip. The mean intensity was calculated over a 3 pixel wide section centred on the line. Boxes were drawn in front of the tip, behind the tip, and over the seed region to obtain measurements for background, GDP, and GMP-CPP lattice (seed) respectively. Outputs were saved as .txt files and exported to MATLAB® for plotting.

All graphs and higher level analysis was conducted in MATLAB. A detailed description of each of the higher level routines that were developed are described in detail at the relevant parts of this script. Graphs were export to Adobe Illustrator to be made into collated figures.

Chapter 3

Investigation of microtubule tip structure in the presence of EB proteins from TIRF images

3.1 Introduction

Mammalian End Binding (EB) proteins have been shown to have a paradoxical effect on microtubules dynamics (Maurer et al., 2014). EB proteins have been shown to increase the growth speed of microtubules (Komarova et al., 2009; Bieling et al., 2007; Tirnauer et al., 1999). An increase in growth speed would increase the size of the GTP cap, stabilising the microtubule. This stabilisation should reduce the catastrophe frequency of microtubules. However, the EB proteins (EB1 and EB3) have also been shown to increase the catastrophe frequency on dynamic microtubules (Maurer et al., 2014). This raised the question as to how EB proteins are able to have this paradoxical effect? This effect was also in unpublished Straube Laboratory experiments that took place prior to me joining the lab. Dynamic microtubules without and in the presence of 100 nm EB1, EB2 and EB3 were imaged. EB1 and EB3 both exhibited this paradoxical effect. However, for EB3 this effect was much stronger, and EB3 had a much higher affinity to the microtubule tip, Section A.1

Recent improvements in microscope analysis have allowed a more detail analysis of microtubule images. Specifically a routine has been developed to study the end-structure of microtubules, (Demchouk et al., 2011). This was a substantial improvement on previous image analysis routines as it fits to the raw 2D image rather than to kymographs (Smal et al., 2010). Kymographs are a temporal spatial reconstruction of the intensity changes along a single, or several joined, linear region of interest (ROI) through time. Whilst these previous methods are very detailed they rely on the accuracy of a user-defined line. Improvements shown in Demchouk et al. (2011) remove this requirement, as long as the microtubule was linear. This improvement in imaging techniques has allowed a theory to be developed for a 2D model of microtubule assembly, (Gardner et al., 2011). An increase in tubulin concentration causes the rate of tubulin dissociation during growth to increase (Gardner et al., 2011). This was explained by the tip structure of the microtubule changing from a relatively blunt (or flat) end at low concentrations to becoming increasingly tapered at higher concentrations. Taper was defined as the distance between the lagging (shortest) protofilaments and the leading (longest) protofilaments. This changes the neighbourhood of the capping tubulin dimer of each protofilament. As the taper increases there was an increase in the number of tubulin dimers with one lateral neighbour and a decrease in the number of tubulin dimers with two lateral neighbours. Dimers with one lateral neighbour are more likely to dissociate than those with two lateral neighbours hence the tubulin dissociation rate increases.

To study how EB proteins might affect MT dynamics the method presented by Demchouk et al. (2011) was chosen as the starting point. To fully understand the algorithm and to modify the outputs, the algorithm was coded from scratch in MATLAB. This allowed the development of a front-end allowing the selection of multiple microtubules per image. This front-end development allowed automation of fitting to a whole experiment instead of waiting for each microtubule to be fitted before another one could be selected. One of the things noticed was that the method failed to fit to the end of the microtubule on a regular basis due to the fact that microtubules are not always absolutely straight. The method originally tried to fit a linear line to define the microtubule lattice. To overcome this a method was developed to allow a cubic function to be fitted instead of a linear line to take account of the microtubules natural flexibility where appropriate.

The method was also adapted to allow the intensity along a microtubule to be extracted from a second ”channel”, allowing the study of the distribution of a microtubule-associated protein tagged with a suitably spectrally distant fluorophore. Here a full description of the resulting code was presented.

A number of questions were raised as to how accurate this method could be. To test this, and to assist in the optimisation of experimental conditions, synthetic microtubule images were generated to test a number of experimentally variable parameters. This enabled an accurate picture of some of the shortcomings of this method, as well as obtaining a sensible range of error that could be expected.

The method was then applied to image stacks of dynamic microtubules from four different experiments, which vary by tubulin concentration. This was done to verify the previous results presented in Gardner et al. (2011), and see whether microtubule tip structure becomes more elongated with an increase in tubulin concentration. Following this, EB3 was added to dynamic microtubule chambers to see if it has an effect on microtubule tip structure. EB3 was chosen as it has the highest affinity for the microtubule tip out of the EB family of proteins. This makes it a prime candidate for use, as it should give the largest effect on microtubule dynamics.

3.2 Background to Code Development

The code used by Gardner et al. (2011) and presented in Demchouk et al. (2011) to fit to dynamic microtubules was made publicly available. Briefly, the code allows the user to select a single image stack. Within that image stack the code allows the user to select a single microtubule by first clicking at some point along the microtubule lattice and then in close proximity to the tip. Upon the second click the code fits that time slice, which takes in excess of 30 seconds. The fit occurs by the y-axis and x-axis swapping if necessary such that the distance between the two points selected was greatest in y than in x. Scans are then conducted along y-axis, fitting a Gaussian function to the intensity values for each column of values for each point in y. This identifies the microtubule backbone. A linear function was then fitted through these points and extrapolated beyond the tip of the

microtubule. The intensities along the line where then extracted. To these intensities a Gaussian error function was fitted (Section 3.4.1, Equation 3.3) to find the microtubule length, and the microtubule taper length. Following fitting to that time point the code then asks you to click on the microtubule tip in the next time point, or right click to finish.

It was decided that having to click on the end of the microtubule for every time point that was required for analysis, and having to wait for around 30 seconds for each time point to be analysed was not very efficient. Whilst a quick solution would have been to return the position found from the previous time point as the position to fit to in the next time point, it was decided that it would be good to take this opportunity to recode from an understanding view point.

A number of other issues were also thought about. Demchouk et al. (2011) only fit a linear function to the microtubule, in a significant proportion of microtubule images obtained on our microscope the microtubules are not linear. Being only able to select one microtubule at a time for analysis also seems to be inefficient. Additionally our aim was to study the effect of EB (or other MAPs) alongside microtubule dynamics, it might be preferable to extract the intensity along the microtubule tip from more than one colour channel. It was assumed that the image from the second channel would be acquired equally between two consecutive images in the microtubule channel.

From this it was decided that as part of re-coding of the routine, it would also be redesigned into a user-friendlier package. Additionally improvements would be made to allow the selection of all microtubules at the start, followed by complete automation in order to limit the amount of user interaction and therefore input time required by the user. This has the bonus of allowing pre-processing of stacks to also be carried out as part of the package. During fitting the location of the microtubule in the previous time point would be used as the microtubule tip location. Careful consideration would be made to ensure that the right points are being used. Additionally the microtubule backbone would be allowed to undergo a small amount of flexing by fitting a non-linear line to the microtubule tip. The location of the microtubule backbone could be copied to additional image stacks in order to extract the microtubule intensity from those stacks. The general layout of the code can be seen in Figure 3.1.

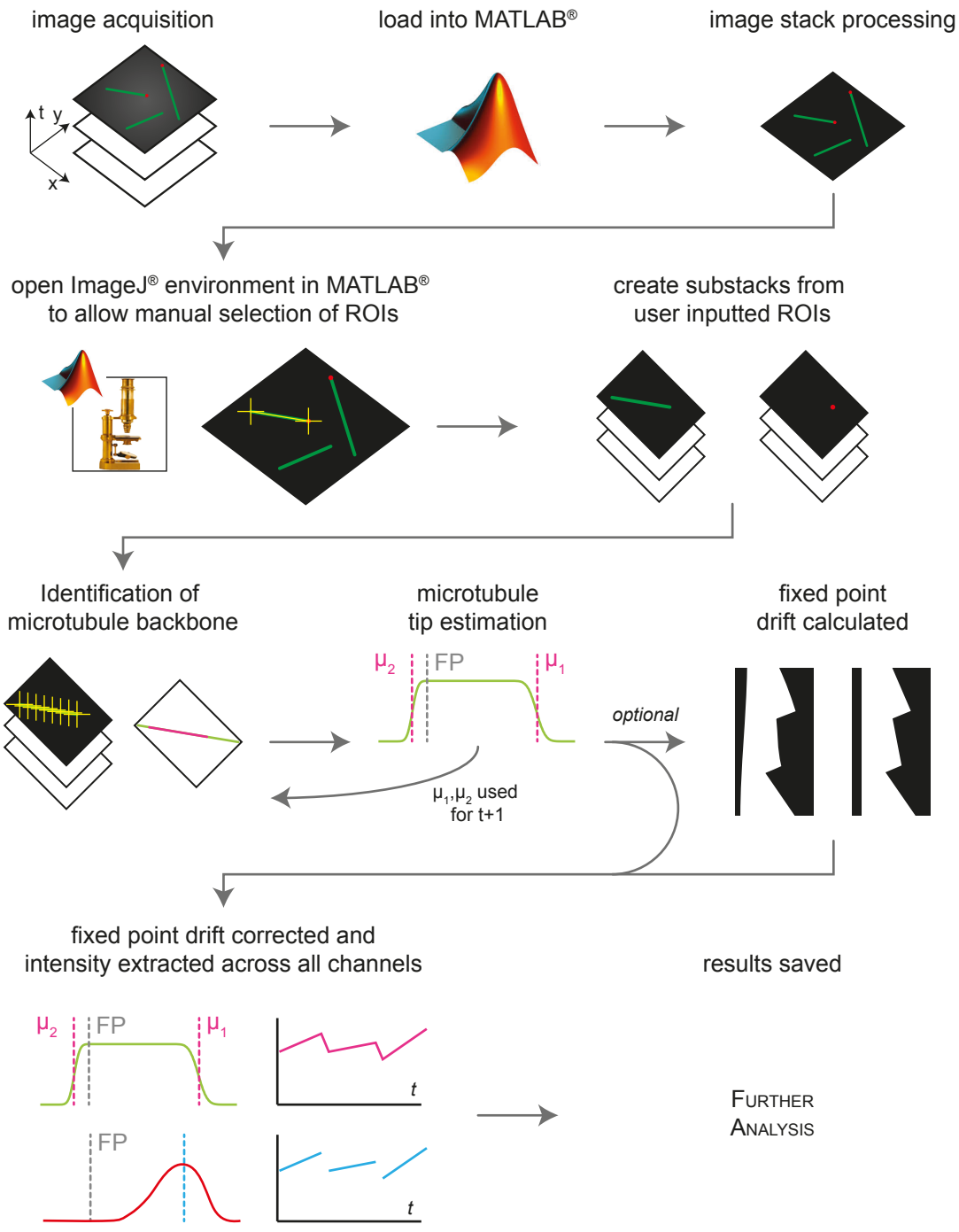

Figure 3.1: **Schema Overview of Microtubule End Fitting Code:** Figure legend continued on the next page.

Figure 3.1: Schema Overview of Microtubule End Fitting Code: Shows how the code fits together from image acquisition to when the results are saved at the end for further analysis. Time series of dynamic microtubules are acquired on the microscope. MATLAB is started and these images loaded in the created algorithm in MATLAB. Basic image stack processing can then take place (background subtraction for example). Following image processing the images are then loaded using ImageJ as it has much better image stack handling than MATLAB. The user can then select a microtubule by drawing a line from the seed end to the plus end of the microtubule. These ROI are copied to image stacks in additional channels and substacks made for each channel. The microtubule channel is then analysed in MATLAB by first identifying the backbone using the user selected points for the first time point. A function is fitted to the extracted backbone to more accurately find the end points. The end points are then used to find the backbone in the next time slice. This is repeated until the backbone has been found in all time slices, the microtubule gets too close to the edge of the sub-stack, or the microtubule becomes too short. Once the microtubule has been found in all time points it can be put through a drift detect routine. If the drift detection routine is skipped, drift is assumed to be zero. Now the microtubule backbone has been found accurately, the intensities are extracted in all channels and saved for all time points. Further analysis can now be carried out.

3.3 Identification of Labelled Microtubules

The method presented in Demchouk et al. (2011) was used as a starting point and has now been rewritten/redeveloped with several major improvements, including packaging into a user-friendly tool. The tool was comprised of two parts. The first part includes the pre-processing of image stacks and manual selection of multiple microtubules. The second part was the fully automated analysis of microtubule dynamics and tip structure. The overall design of the entire package was to enable the automation of this second step and decrease the amount of interaction time during analysis. In addition to automating the process, several improvements were also implemented. Improvements include: allowing for pre-processing; allowing selection of multiple microtubules; full automation of finding of the microtubule lattice; allowing for microtubule backbones that contain a small amount of flexibility; allowing the Gaussian Error Function (GEF, explained in detail later, Section 3.4.1) to be fitted to both ends of the microtubule; and extraction of intensity along the microtubule backbone from a second channel. The first part of the package was discussed in this section and the second half in the next section.

The requirements of the first half of the package are heavily determined by the requirement for total automation of the second half of the code. Crucially, this was the identification of the microtubule lattice. The second half of the package expects a single

microtubule orientated such that the direction of growth of the microtubule lies between 0 – 45 degrees anti-clockwise from the x-axis, Figure 3.2 A. As the second half of the code runs without user interaction, all of the user interaction needs to be in the first part of the package. In addition the output needs to contain all of the image file locations, the location of the microtubules within the images and transformations required to orientate the image correctly.

This part was therefore split into three tasks. The first task was to find the image files for the experiment, and if required extract information pertinent to the experiment conducted. The second task was to conduct any pre-processing of the image files. The third task was for the user to identify the microtubules in the image files. From these selected microtubules, sub-stacks from the original image files are then created automatically. After each task the information collected/extracted was saved.

3.3.1 Finding Image Files

Upon initiation of the process, the user was asked to select the directory where the images are located. It was coded to expect images in the format 'Parent Directory/Image Condition/channel description.tif'. The location provided should be the 'Parent Directory'. Next the user was asked for the number of channels imaged. For each channel it asks for the 'channel description.tif', which it assumes to be the same for the entire experiment. The channel description can be input as a regular expression, i.e. '/*488nm.tif'. Then it searches recursively through the 'Image Condition' directories inside 'Parent Directory'. Every 'Image Condition' needs to contain files matching each 'channel description.tif' for it to be accepted.

Next the user was asked which of three conditions, 'labelled tubulin', '+TIP', or 'other' does each channel represent. Only one channel can be selected as labelled tubulin. The 'labelled tubulin' channel was used as the reference channel to define the region of interest. If no channel was selected as 'labelled tubulin' the code cannot continue. The same relative data gets extracted from every channel labelled '+TIP', as to the channel labelled as 'labelled tubulin'. Therefore all additional images need to be the

same size as the labelled tubulin images (this was checked at a later point). Any images not requiring information to be extracted from them can be chosen as ‘other’. The user inputted information and the identified files are then saved in the structure ’Overview’ to ’Parent Directory/Results/Overview.mat’.

3.3.2 Interpretation and Image Processing

The next stage of the process asks whether information about the experimental conditions (proteins and their concentrations) should be automatically interpreted from the name of the directory ’Image Conditions’. If so it expects the format of the directory name ’Image Conditions’ to be in the form:

‘imaging date _ protein 1 concentration _ protein 1 name _ protein 2 concentration_ .... _ temperature _ chamber imaging number’

i.e.’140618_24uM_12percTub488_100nM_EB1mCherry_T25C_005’.

Due to the above-prescribed format of the image files, the user was asked if they would like the directory names to be automatically deciphered. If yes, then the directory name was separated into parts delimited by an underscore (‘_’). The first and the last two entries in the directory name are automatically assigned. The remainder are paired up in the format concentration-name. There needs to be at least the same number of pairs as the number of channels selected. The user will be asked to assign each channel to a concentration-name pair. If the file name was not right for automatic deciphering, or you decide not to automatically decipher the file names, the fields are still generated but are left blank. If these settings are not the same for all samples, there was an option later on to manually edit each field.

The only image processing required at this point was that which needs to be applied to the original microscope images. The imaging system was checked for chromatic aberration/shift between excitation in the 488 nm and 561 nm channels. Fluorescently labelled beads were imaged and the corresponding images analysed. A 2-Dimensional Gaussian was fitted to each of the brightest points in the 488 nm channel. In the 561 nm

channel, a 2-dimensional Gaussian was fitted to the neighbourhood of each identified point from the 488 nm channel. The offset (distance and direction) was calculated between corresponding Gaussians. There was no discernible pattern detected in the measured offset between the fitted centres of the Gaussians between the two channels. As such it was concluded that the microscope set-up did not suffer from any significant chromatic shift or aberration requiring adjustment. There was no testing done between the 488 nm, or 561 nm channels, and the 640 nm channel. This was because the 640 nm channel is reserved for stabilised seeds and was only used as a generalised reference point. As such a couple of pixels deviation between the imaged position in the 640 nm channel and the observed position with relation to the 488 nm and 561 nm channels was not considered a problem.

Spatial drift through time is occasionally observable in obtained images, especially in the first few minutes a chamber is on the microscope. The main method normally used to correct this type of error is stack registration. Stack registration normally involves whole pixel shifting to minimise the lateral displacement between time points in a temporal stack. More elaborate routines are also capable of dealing with a slight rotational displacement, and sub pixel shifts to better align images. The accuracy of these methods is determined by how well the algorithm can identify key features in each image slice. Due to the lack of fixed features in these images, standard stack registration routines were ignored. Instead each microtubule has it's own fixed control point in the 'dark' seed join. This junction between the GMP-CPP seed and the dynamic microtubule can be used as a fixed point that is independent of temporal drift. By fitting a dual ended GEF (Section 3.4.1, Equation 3.4) it was possible to calculate microtubule length independent of drift.

Obtained microscope images do contain a distinctive background pattern due to uneven illumination. By taking a reference image using a coloured plastic slide, we get a representative image of our background illumination. The raw images are then normalised by the representative background image as follows.

To background correct, the reference image was binned by averaging 16x16 pixel blocks, smoothed and then re-expanded to be 1024x1024 by/using bi-cubic interpolation. As the process was currently being handled by MATLAB, and MATLAB is very efficient at matrix

manipulation, background correction was done in MATLAB. For every image stack, I, the following transformation was applied:

$$I(t) = ((I(t) - 3000) \odot 1/S) * max(S) \qquad \forall t$$

where $\odot$ is the hadamard (or element-wise, point-wise) product, and t is the time slice of the image stack, and S is our reference image. The values of S are sufficiently large that no special case was considered for values of S close to zero.

In situations where the reference image was not obtained, it is constructed from the images available from the experiment. To do this, 10 uniformly spaced time slices are extracted from each image stack. The intensities for each extracted image are normalised to have a mean of 2000 after subtracting the camera offset of 3000. The median is then calculated from all of the normalised images to create the reference image S.

Each transformed image is saved in the same directory as it was loaded from, but it has '_back' appended to its file name. The user inputted information and information for automatic deciphering the image file names are stored in a structure called Image. The structure is saved to 'Parent Directory/Results/Image.mat'.

3.3.3 Manual Selection

The next stage turns each image stack into a series of sub-stacks. Each sub-stack contains a dynamic microtubule. The substacks were obtained by asking the user to identify microtubules of interest from the raw image stacks. There are three possible types of microtubule image. The first are microtubules that have an unlabelled seed and labelled free tubulin. These microtubules are bar code like with two fluorescently labelled parts and a dark centre. The more dynamic plus end extension is selected and the fluorescent end that joins the seed can be used as a static reference point. The second type consists of microtubules that are long enough that they start to intersect with each other. At this point the analysis needs to be restricted to the last few μm as the code can't handle microtubule intersections. There is more error associated with this analysis, as there is no dark seed junction to use as a reference point. Instead a feature (local

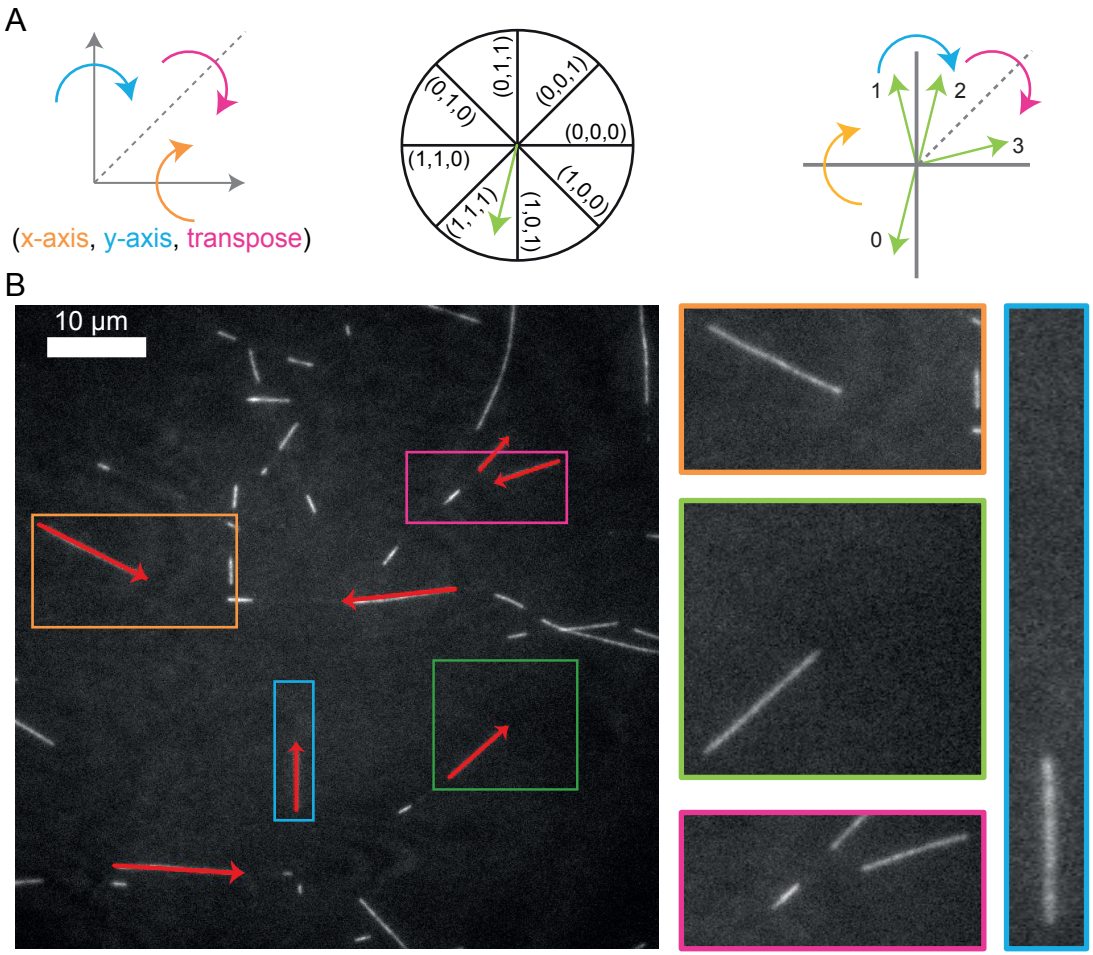

Figure 3.2: **How microtubules are manually selected:** An overview of the process of manually selecting a microtubule and the premise that any microtubule can be considered to be between 0° and 45°. (A) Schematic of how any three transformations can transform a vector (direction orientated line) from being in an orientation to be being orientated between 0° and 45° of the x-axis. Three transformations are reflection in the x-axis, reflection in the y-axis, and transpose. Clock wheel shows the transformations required for each range of angle were the brackets refer to (x-axis reflection, y-axis reflection, transpose). Third image shows all three transformations in action correcting an arrow situated between 225° and 270° to be between 0-45°. (B) Microtubules selected via line ROI in ImageJ (red lines) selection. Coloured boxes showing automatically cropped boxes generated from the initial line ROI.

min/max) of the labelled microtubule lattice needs to be used to align the time points for accurate length change, and velocity measurements. The third type is a microtubule where the seed is labelled similarly to the microtubule lattice. Both ends are dynamic in this case and features of the microtubule lattice need to be used as above for accurate alignment between time points. The user is asked to specify whether it is necessary to fit a dual ended GEF to both ends of a microtubule, and whether both ends are dynamic (Section 3.4.1, Equation 3.4).

As MATLABs visualisation and handling of image stacks is poor (undeveloped) it was necessary to open ImageJ within a MATLAB framework to make use of ImageJ's visualisation and ROI selection properties. For every image stack in the experiment, the stack location is passed to ImageJ and loaded. The user is then asked to define microtubules, one by one, by drawing a line ROI from the seed/stationary/minus end to the microtubule plus tip, Figure 3.2 B. This returns the co-ordinates of two points and the time slice active when the line was drawn, to MATLAB. The first co-ordinate should be away from the microtubule tip at a point on the microtubule backbone that exists for all the time points of interest. The second co-ordinate locates the microtubule tip in the image slice that is active. Once the co-ordinates have been selected, they are returned to MATLAB, MATLAB asks for the image slice number at which to terminate cropping. This creates the vector $(x_0, y_0, x_1, y_1, t_0, t_1)$ that is used for two things.

Firstly the vector is used to obtain the transformations required to orientate the image between 0 and 45 degrees. This is important as the first step of identifying the microtubule is to locate the microtubule backbone, Figure 3.4, Section 3.4, which requires scanning along the x-axis and the accuracy of the algorithm is improved if the microtubule is longer in the x-direction than the y-direction. As such it is simpler to reduce the complexity at this stage rather than, at a later point, having to code for microtubules orientated in all directions. This is achieved by the use of three transformations. Considering the angle between the line, from (x_0, y_0) to (x_1, y_1), and the x-axis, microtubules can have any angle (0 and 360 degrees) once growth direction is taken into account. By performing a combination of: reflection in the x-axis, reflection in the y-axis, and transposition of the image (swapping the x and y axis), it is possible to position any microtubule between

0 and 45 degrees without changing any pixel values in the original image, Figure 3.2 A.

Secondly the vector is used to estimate the maximum likely growth of the microtubule over the time period, and calculate the contribution to the x and y directions (dx, dy). This creates a box around the selected microtubule of interest that should contain the entire growth cycle of the microtubule. The maximum likely growth, $G = v_{max}(t_1 - t_0 + 1)dt$, is the product of maximum average growth (a user provided value), v_{max} nm/s and the time duration of the sub-stack. From Pythagoras it is known that $G^2 = dx^2 + dy^2$. Once x_0, y_0, x_1, y_1 have been transformed following the transformations above, from (x'_0, y'_0) to (x'_1, y'_1), the gradient, m, can be calculated. Solving using the Pythagorean identity to get:

$$dx = \sqrt{\frac{G^2}{m^2 + 1}}$$
$$dy = \sqrt{\frac{G^2 m^2}{1 + m^2}} \tag{3.1}$$

Using this transformation we can get the outline of the box we believe should contain the entire life cycle of the microtubule of interest. If the microtubule is dynamic at both ends then the calculated difference is added to both end points of the microtubule, otherwise it is only added to the second selected point. In order to make sure that there is enough 'empty' space around the microtubule to create accurate fits for the backbone and the tip, we pad the whole image with 15 pixels in each direction. The created box is then used to create a sub-stack, and the sub-stack is saved.

The program then waits for the user to select another microtubule or progress to the next image. Once all the images and microtubules have been selected the code will select any other inputted channels in turn and crop the same regions for each associated image. The outputs are all saved under a new file structure based on the protein names and concentrations used for each image stack.

The user inputted parameters and co-ordinates as well as other calculated values are saved for each microtubule in the structure 'MT'. The structure 'MT' is saved initially to 'Parent Directory/Results/MT_Selection.mat'. After the same transformations

have been applied to the other channels, the structure MT is then saved to 'Parent Directory/Results/MT_selection_C2.mat'.

3.4 Automatic Identification of the microtubule

This algorithm is designed to automatically extract the intensity profile of the microtubule from each channel. Three processes are required for this, all three are applied to the reference channel, and the last process is repeated for the secondary, '+TIP', channels. The processes are 1) location of microtubule backbone in every time slice including a rough fit of a Gaussian Error Function; 2) drift and distance correction (if required); and 3) extracting the intensity profile along the microtubule.

3.4.1 Gaussian Error Function

The basic Gaussian Error Function (GEF) is based upon the cumulative distribution function of the Normal distribution .

$$f_1(x) = \frac{1}{2} E\left(\frac{x}{\sqrt{2}}\right) + \frac{1}{2} \tag{3.2}$$

where $E(x) = \frac{2}{\sqrt{\pi}} \int_0^x e^{-t^2}$.

The GEF is transformed by the addition of variables to model the end of the microtubule. Depending upon whether both ends of the microtubule need to be fitted to, or to just the dynamic end, there are two possible forms of the GEF can take. The first fits a single-ended GEF. A single-ended GEF decays from the lattice to the background.

$$f_1(x) = -\frac{A}{2} E\left(\frac{x-\mu}{\sigma\sqrt{2}}\right) + B \tag{3.3}$$

where $E(x) = \frac{2}{\sqrt{\pi}} \int_0^x e^{-t^2}$.

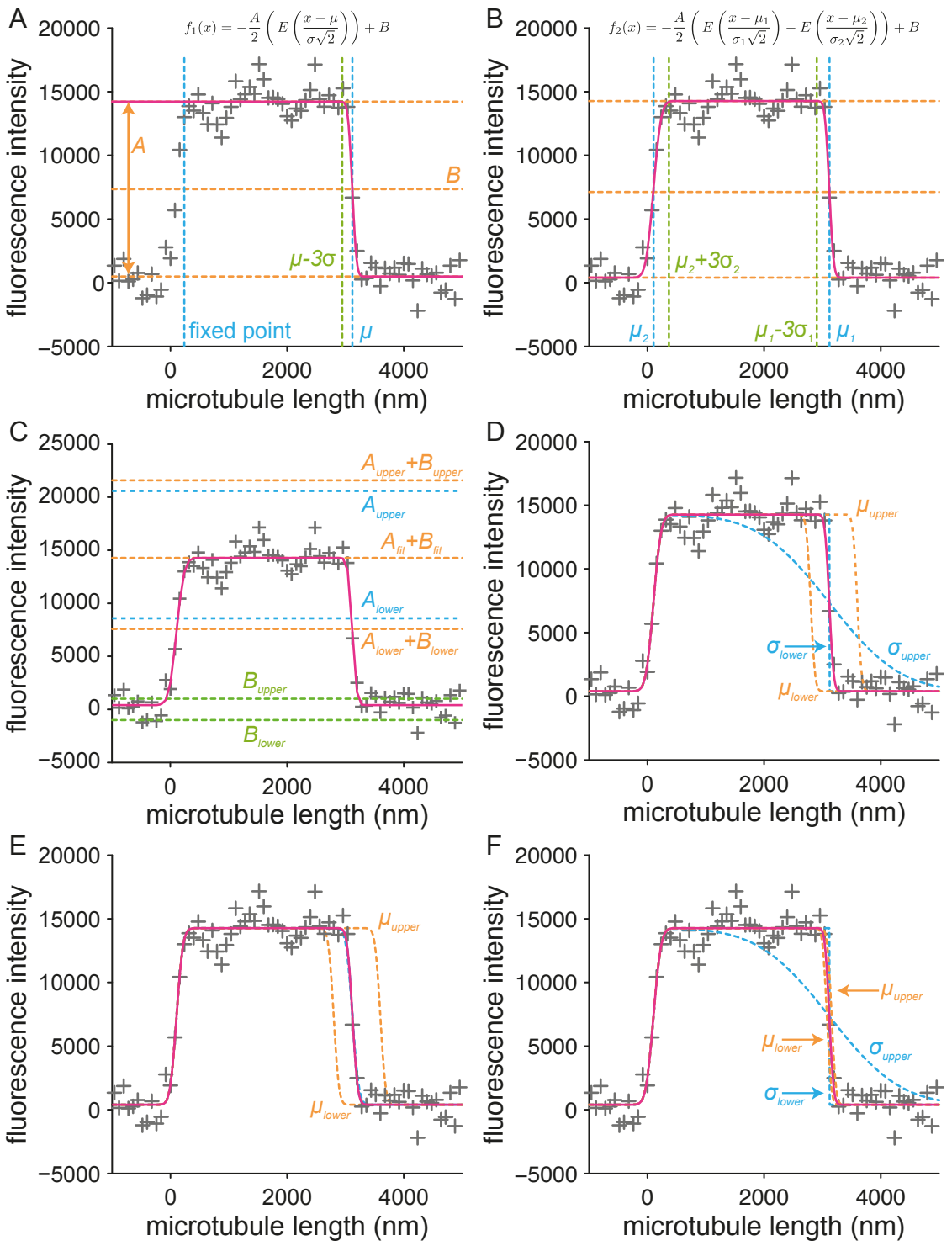

Figure 3.3: **How the parameters differ between single and dual Gaussian error functions:** Continued on next page.

Figure 3.3: How the parameters differ between single and dual Gaussian error functions: (A) how the parameters affect a single sided Gaussian error function, A is the intensity difference between the background intensity, and the MT lattice intensity. B is the intensity value that is halfway between the background intensity and the MT lattice intensity. μ is the value x takes when $f_1(x) = B$. σ is a measure of the distance taken for the lattice signal to decay to the background. Typically $\mu - 3 * \sigma$ to $\mu + 3 * \sigma$ accounts for 99.7% of this change. (B) How the parameters affect a dual sided Gaussian error function, A is the intensity difference between the background intensity, and the MT lattice intensity. B is the value of the background lattice intensity. μ_1 is the first (smallest) solution of $f_2(x) = B$ and μ_2 is the second (greatest) solution. σ_1 and σ_2 is a measure of the distance taken to increase to the lattice intensity and decay to the background intensity, respectively. (C) Shows the range of the upper and lower limits for A and B. (D) Shows the range of the limits when both μ and σ are allowed to vary at the same time for the dynamic end of the microtubule as during a single step fitting. (E-F) Shows the range of the limits first for μ and then for σ for the dynamic end of the microtubule when the two fits are done in consecutive steps as during the dual step fitting.

The parameters dt, A, B, μ and σ relate to the variables in Figure 3.3 A, and x is distance. $-\frac{A}{2}$ reverses the direction of the curve so that it decays from the lattice to the background. A and B change the maximum and minimum vales that the GEF can take. A is the intensity difference between the background and the microtubule lattice. B is the midway point of this difference. μ and σ are linked to the underlying Normal distribution. The subtraction of μ changes the mean of the underlying normal distribution to be centred at μ. Hence μ is the location of the microtubule tip, in this case the x value where $f(x) = B$. The division by σ spreads the standard normal distribution. σ is otherwise the standard deviation of the underlying Normal distribution. σ is therefore a measure of the spread at the microtubule tip. It therefore has a proportional relationship with taper length. Throughout this document σ is referred to as Taper length. It is dependent upon the standard deviation (σ_{PSF}) of the Gaussian approximation to the airy function of our microscope. As such it has been reported that $\sigma^2 = \sigma^2_{PSF} + \sigma^2_{MT}$ where σ_{MT} is the contribution by the microtubule, (Demchouk et al., 2011). However, this assumes that the distribution of the individual protofilament lengths follow a normal distribution, as the identity is drawn from the property that the convolution of two normal distributions is still normal ($N(\mu, \sigma^2) = N(\mu_{MT}, \sigma^2_{MT}) * N(\mu_{PSF}, \sigma^2_{PSF}) = N(\mu_{MT} + \mu PSF, \sigma^2_{MT} + \sigma^2_{PSF})$, where N is the Normal distribution). A more accurate description would be to fit the microtubule as 13 protofilaments, where each protofilament can be fitted by the GEF. Given this discrepancy, only the value of σ is reported in this thesis.

For fitting using a single-ended GEF, the values of x are cropped using a fixed point. Any data before the fixed point is ignored during fitting. The fixed point should be at an x-value on the microtubule lattice.

The second method of fitting a GEF is to fit a dual-ended GEF. A dual-ended GEF rises from the background at one end of the microtubule, to fit to the lattice. It then decays from the lattice to the tip.

$$f_2(x) = -\frac{A}{2}\left(E\left(\frac{x-\mu_1}{\sigma_1\sqrt{2}}\right) - E\left(\frac{x-\mu_2}{\sigma_2\sqrt{2}}\right)\right) + B \tag{3.4}$$

where $E(x) = \frac{2}{\sqrt{\pi}}\int_0^x e^{-t^2}$.

The new equation adds together two GEF. Due to the addition of the second GEF the parameters now align to different points, Figure 3.3 B. A is the difference in intensity between the background and the lattice. B is now the background intensity. μ_1, and μ_2 are the positions of the microtubule tip, and seed end respectively. σ_1, and σ_2 is the standard deviation of the underlying Gaussian distribution function at the microtubule tip and seed respectively.

The two different GEFs have different benefits. The single-ended GEF has less error associated with finding the location of the end in a single time frame. However, as the fixed point remains static the microtubule length measurements are susceptible to drifting of the chamber. It is ideal for use when you wish to align the microtubule tip locations through time (i.e. when change in microtubule length is not the primary concern). It can also be used on extremely long microtubules that intersect with other microtubules. The accuracy in determining microtubule length in this case will be diminished as flexing may occur in the microtubule backbone that is not analysed.

The dual-ended GEF may be preferable for time dependent analysis of microtubule length as it is sensitive to drift of the image chamber. A stable fixed point is created by fitting to a static end, such as the junction of the labelled tubulin microtubule with the stabilised seed. The stable fixed point is used as a reference point to measure the microtubule length from. Fitting to both ends of the microtubule increases the uncertainty of the fit.

Each end will have an inherent error associated with finding the true position of the tip. This error can be exasperated as the microtubule backbone is assumed to have constant intensity, in truth the intensity can vary due to uneven illumination or bleaching.

3.4.2 Locating the Microtubule Backbone

Initially the function loads in the primary image sub-stack, and rotates to the correct orientation using the three basic transformations calculated above: reflection in x-axis, reflection in y-axis, and transposition. The sub-stacks are saved in their original imaged orientation. This aligns the microtubule such that it is between 0 and 45 degrees of the x-axis. A fixed backbone point is now defined. If the microtubule is dynamic at both ends the fixed point is defined as the centre of the image, otherwise the point (15,15) is chosen. Using the transformed user inputted co-ordinates (x_0, y_0, x_1, y_1), from the MT selection step, a series of points, (x_{BB}, y_{BB}), are generated. These points detail the rough microtubule location. The points are found by linearly interpolating between the two user inputted points and rounding to the nearest pixel $\forall x_{BB}$ such that $x_{BB} \in \mathbb{Z}, x_0 \leq x_{BB} \leq x_1$. For the first time point this line is used as guidance to where the microtubule is located. To allow for error a confidence interval ($y_{BB} \pm 2$ pixels) is created around the line. For later time points the confidence interval is created from the linear or cubic fitted line (see below) through the microtubule from the time point before. For every x_{BB} the intensity in the corresponding column in the image matrix is extracted and a 1-dimensional Gaussian fitted to it, Figure 3.4 A. The 1-dimensional Gaussian is restricted in its fitting, with its mean (μ) needing to be within the confidence interval, $y_{BB} \pm 2$.

Next it takes the co-ordinates, (x_{BB}, μ_{BB}) from the fitted 1-dimenisonal Gaussians and fits a linear line through the points, Figure 3.4 B,C. If the average residual error (the squared difference between the observed (μ) and the fitted value of the linear line) is greater than 40 nm then a cubic function is fitted instead. If the average residual error in the 10 pixels closest to either dynamic end is greater than 60 nm, it also fits a cubic. The reason for the extra microtubule tip test is that there is more likely to be deviation or flexibility at the microtubule tip. It is important that this flexibility is identified and fitted to accurately.

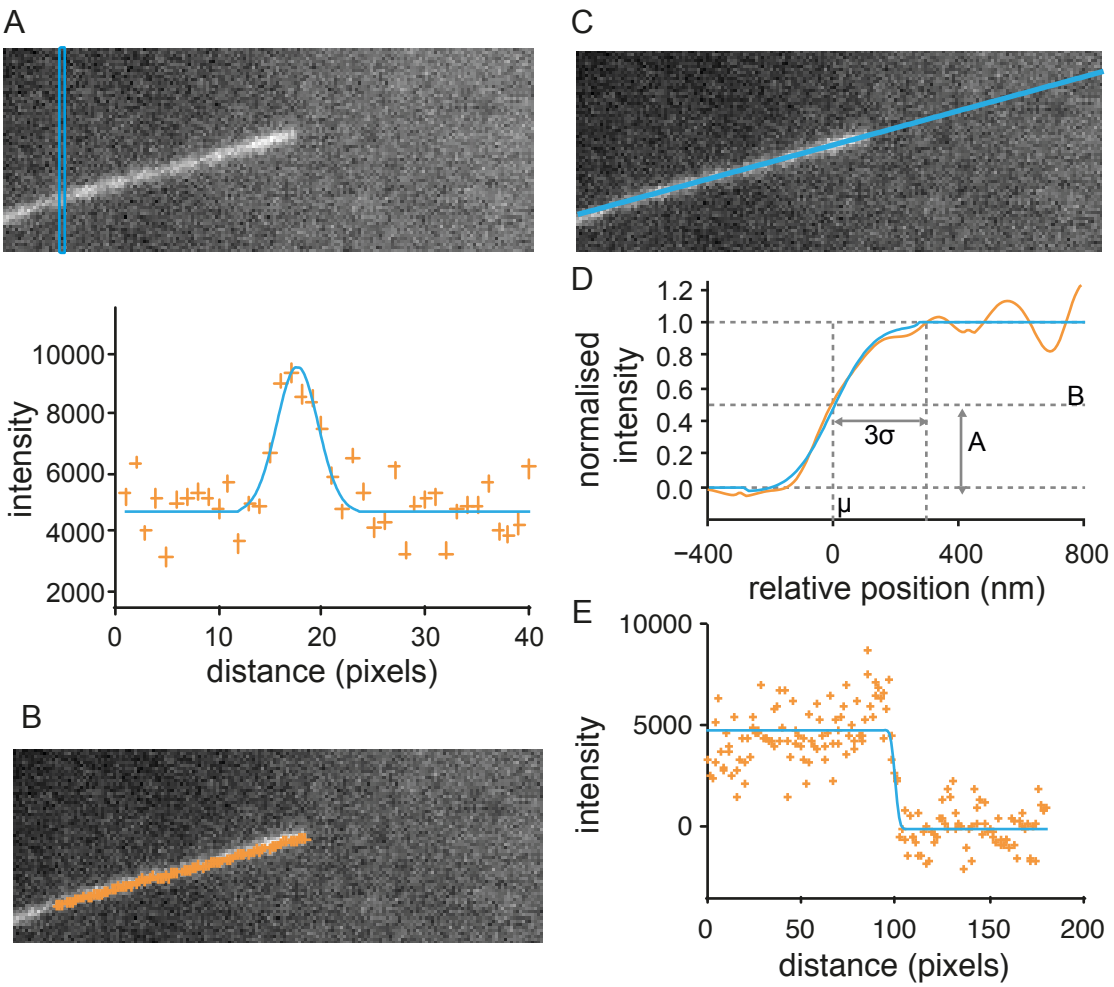

Figure 3.4: **Overview of the process of fitting to the microtubule backbone:** (A-top) Scans along the x-axis fitting a Gaussian to the pixels in y. Pixels within the highlight blue box are extracted and plotted in (A-bottom). Pixel intensity values, gold crosses, from the blue box , are fitted by a Gaussian function and the means extracted and saved for each x. (B) Mean values of the fitted Gaussians from (A) shown superimposed on the microtubule lattice. (C) Superimposed fitted line through the (x,y) co-ordinates of the means of the fitted Gaussians on the microtubule lattice. (D) Extraction of pixel values along the fitted line, fitted using a Gaussian error function to obtain a rough idea of the microtubule end, used to control the extent of the fitting of Gaussians to the next time point. (E) Description of the parameters used to fit the Gaussian error function 3.3. Shows how the fitting parameters have an affect on the look and shape of the curve. The smaller the value of σ becomes the steeper the gradient of the slope from the microtubule lattice to the background intensity. A is half the intensity difference between the background and the microtubule lattice intensity, and B represents the half intensity value. μ is at the intersection of y=B with the GEF curve.

Otherwise the fitted line will not correctly follow the microtubule at the tip so when the GEF is fitted, it will fit to the side of the microtubule, rather than over its tip.

Once the fitted cubic, or linear, line has been obtained, the location of the microtubule backbone is passed to the next time point. To pass the full microtubule location in this time point to the next iteration, it is important to know the location of each end of the microtubule in this time frame, taking account of growth and shrinkage. To find the microtubule end points it is necessary to fit a GEF, Figure 3.4 D,E. For this, the line needs to be extended to the edge of the image, to give us the full range of x so that the image background is included. To extend the fitted curve to the full range of x, the tangent to the curve at each end of the fitted region is calculated, and extrapolated to give us the microtubule reference line (x', y'). For the next step in the process a kymograph is created, Section 3.4.3. For the kymograph to be create the relationship between pixel position and microtubule length needs to be established for each time point. As this step contains a for loop, and for consistence the length of the microtubule is calculate at this point. To calculate the microtubule length the distance between two consecutive points is calculated using Pythagoras. The distance from the fixed point is calculated by summing the individual difference between the fixed point and that point. To increase accuracy in the distance d' measurements the number of data points (x', y') are increased 10 fold before calculating distance values. Corresponding intensity values, z', come from bi-cubic interpolation of the original image grid at (x', y'). The Gaussian Error Function is then fitted to the values (d', z'). If there is a dark seed junction or the microtubule is dynamic at both ends a two sided GEF is fitted, otherwise a one sided GEF is fitted. After fitting x', y' is reduced to contain the points that are within both end points. If not fitting to both ends, the first 15 points are also removed so that we are not fitting to within the padding region. The reduced x', y' are then passed to the next iteration. Should either end of the microtubule come within 10 pixels of the edge of the image, or the microtubule become less than 10 pixels in x long, then the code stops fitting to the backbone at that time point.

3.4.3 Microtubule Drift Correction

As mentioned above the microtubule drift correct element of the algorithm is entirely optional, apart from the first calculation of a fixed point that is used as the reference value in all future calculations. In fact it is not used at all in the thesis, but as it was developed and part of it is required for the next process, Section 3.4.4, it is briefly mentioned here. To calculate the fixed point all of the starting, x_{start}, and end, x_{end}, points are taken from the backbone finding step. It is checked that the $max(x_{start}) < min(x_{end})$. The fixed point is then set to $max(x_{start})$. If this is not true then the fixed point is the rounded down average of the $max(x_{start})$ and the $min(x_{end})$.

The rest of this process is used to correct for drift. This is time intensive and can be skipped if you are not interested in very accurate growth, or microtubule length measurements, and your original image stack does not contain drift. Initially by interpolating at fixed distance values, every 0.5 pixels, along the microtubule backbone, an image resembling a kymograph was created. Using one of MATLAB's inbuilt toolboxes, for mass spectrometry, which contains a function for aligning mass spectra, msalign, the peaks in each row are aligned. As the rows in the kymograph with the background removed, broadly resemble mass spectra outputs, the algorithm works well. In order to fine align the peaks in the kymograph each row is interpolated 10 fold. To align the peaks, the msalign attempts to align the intensity profiles to a generated image based upon provided peak locations. It was found that by passing the whole kymograph to the function msalign, the alignment was flawed. This was because when the microtubule grows new peaks are formed that confuse the algorithm. Instead the kymograph is broken up into smaller chunks each containing 20 rows (time points) and each chunk will overlap with the chunk before it by 10 rows.

The function msalign requires reference points to align each row to. To create reference peaks the first ten rows of each chunk are averaged and the local maxima where found. These local maxima are used to align the chunk and the amount of shift found for each row. For each chunk the gradient of the line of best fit through the shifts per row is recorded along with the associated error. By considering the errors of each fit we can

select the three gradients with the best fit, and take the average of these. The whole kymograph then gets shifted using this gradient. The function returns the gradient and the new kymograph. The whole process gets iterated 10 times as the amount of shifting is limited per go, if the function doesn't converge over this number of iterations it can be ignored. If the drift correction is skipped, or the iterations don't converge the code pretends it returned 0's as the average shift.

3.4.4 Intensity extraction and background normalisation

The goal of this process is to get an accurate average of the intensity along the microtubule backbone in all channels. Additionally, the GEF is fitted in the reference channel. To do this a new image grid, I', is created with the microtubule backbone positioned horizontally down the centre of the image, Figure 3.5 A. For every pixel column in the original image $x(i) = i - x_0, i = (1, ..., x_{len})$ we calculate the corresponding $y(i)$ co-ordinates based on the fitted curve, and the gradient at each point $m(i)$. Then for every point (x, y) we calculate the points $(x'(i, d), y'(i, d))$, lying on the perpendicular to the fitted line at that point, at fixed distances ($d = (-10, ..., -1, 0, 1, ..., 10)$ pixels, where zero is at the point (x, y)). This is done using the inverse of the gradient, $m' = -1/m$ and the equations 3.1. The points (x', y') are then used via cubic interpolation to create the new image matrix $I'(i, d) = I(x'(i, d), y'(i, d))$, Figure 3.5 B,C.

In order to fit the GEF we need to calculate the distance and the intensity values used in the fitting of the function. The distance values d come from calculating the distance along the curve as before, but instead of setting the point (x_0, y_0) to zero, we need to adjust it with the average shift. Using the shifts from the previous step we fit a linear line of best fit with gradient, g. We can now correct our distance values d by using the following transformation to get $d' = d - (d(x_0) + gt)$ for each time point t. The intensity values z come from averaging across the middle three pixels of our new image. These pixels then get background subtracted to take account of any anomalies in this region of the image due to uneven illumination. The background is calculated by averaging the five most extreme pixels on either side of the line, Figure 3.5 B-D. The background subtracted intensities z' versus distance values d' are fitted to the GEF.

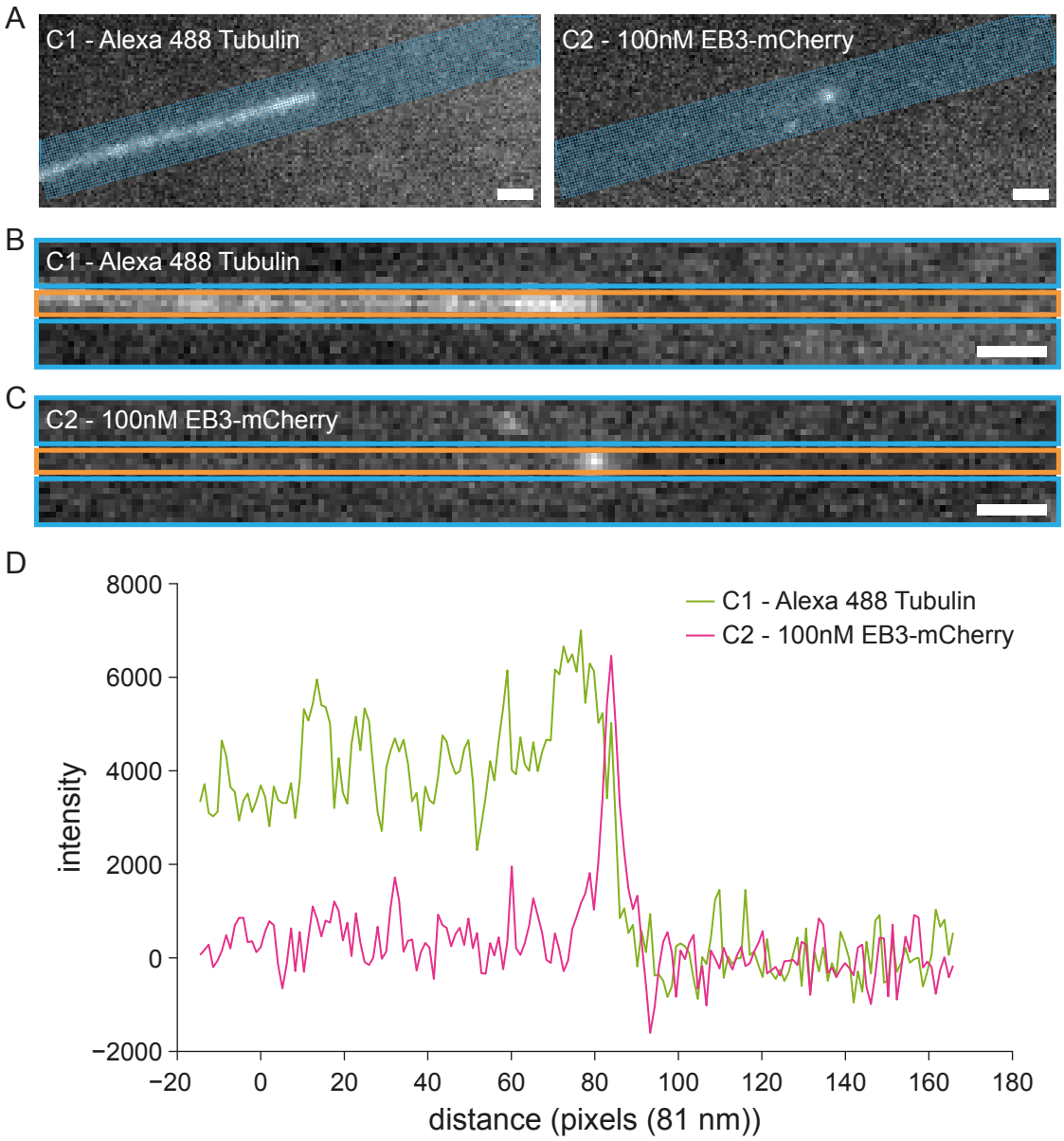

Figure 3.5: **Extracting microtubule backbone intensity in all channels:** Shows the extraction of intensity from a two channel image series. Here 100nM EB3-mCherry is imaged alongside 15μM 18% Alexa 488 labelled tubulin. (A) Same image slice from both channels shown overlayed with a new image grid in blue. New image grid is calculated based on the backbone fitted line, Figure 3.4 C. Perpendiculars are calculated as pixel intervals to create a 21 pixel wide image. (B-C) Extracted new images from channel 1, tubulin, (B) and channel 2, EB, (C). Blue box represents the pixels that are averaged in y to create the background baseline, and the orange box shows the pixels used to generate the lattice signal. The calculated lines Lattice-Background is show in (D) for both channels.

If a multi-channel image has been selected, the above process is repeated for the addition channels, Figure 3.5 C-D.

3.5 Generation of Synthetic Images of Microtubules

In order to estimate the errors expected and the accuracy associated with using the GEF in fitting to the microtubule end it is important that a set of control data against which any developed algorithm and their associated improvements can be tested. For this dynamic microtubules could be imaged and used as a reference for development. However, this would not provide an objective method of deciding the goodness of fit to the data and the errors involved, as the underlying truth is not known. Instead synthetic images of dynamic microtubules can be generated to accurately reflect imaged microtubules.

In order to accurately test and obtain errors associated with fitting a GEF, it is necessary to be able to simulate fluorescently labelled microtubules obtained from a total internal reflection fluorescence microscope. Before an artificial microtubule can be generated it is necessary to decide what parameters are important in accurately simulating a dynamic microtubule. The following list was chosen as the important variables in creating an accurately labelled dynamic microtubule.

Orientation Upon observation of a microscope image it is clear that microtubules can come in all orientations, Figure 3.2 B, as they settle randomly, binding to the cover slip. However, by doing basic matrix manipulations, reflecting in x-axis, y-axis and transposition (swapping x and y co-ordinates) the range of angles to be considered can be reduced to those between 0 and 45 degrees of the x-axis, Figure 3.2 A.

Microtubule Length As microtubules need to be tracked undergoing dynamic instability it is necessary to be able to create image stacks that represent this instability. Microtubule length therefore needs to vary to be able to create a dynamic image stack

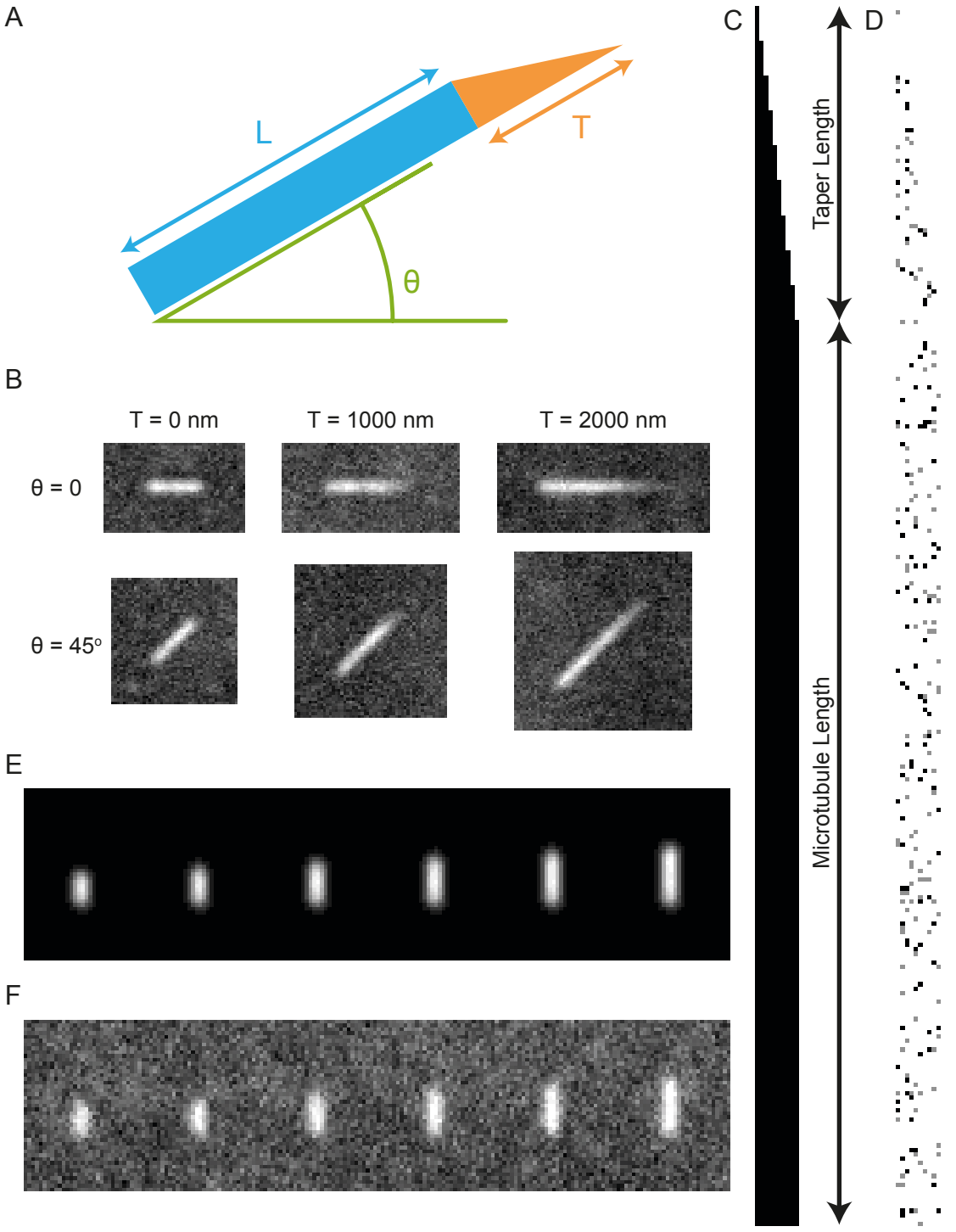

Figure 3.6: **Generation of synthetic images of microtubules:** (A) The microtubule is defined by three key parameters Length, L, Taper, T and Angle, θ. The microtubule length is constructed as a rectangle with length, L and taper is constructed as a right angle triangle with the same width as the length rectangle and length, T. Once constructed the microtubule is rotated through angle θ. (B) examples of microtubules generated with angle = 0° or 45° and taper equal to 0, 100 or 2000. (C) Image of the first step of generating a synthetic microtubule, microtubule is generated at it's greatest extent of L with taper T. (D) The speckle (labelled tubulin dimers) of the microtubule are then defined. (E) A montage of a growing microtubule convolved with the point-spread function and scaled to represent the microtubule lattice intensity. (F) Real image noise is then added after being scaled to represent the values inputted for background intensity and noise levels.

Microtubule Taper One of the chief goals of using this process is to be able to track changes in microtubule taper. We need to be able to represent different microtubule tapers to be able to 1) know at what length we can reliable detect taper; 2) to be able to convert our measured length into a known taper value.

Label Percentage The tubulin we use in our experiments is HiLyte 488™-labelled porcine tubulin, which comes with a labelling efficiency of 1.5 fluorophores per dimer. We can alter the amount of tubulin used in each experiment, and this should have an effect on the speckle pattern observed along the microtubule and how well defined the tip of the microtubule is.

Standard Deviation of the Point Spread Function The observable width (blurring) of the fluorescent microtubule is controlled by the point-spread function of the microscope. Using the correct standard deviation in generating the synthetic image will allow us to create accurate looking images. The amount of blur in the image will affect how sensitive the GEF is to fitting to the end and recognising taper. The greater the standard deviation the greater the microtubule taper will need to be for the increase in taper to be measurable above the point spread function. The point-spread function is dependant upon the optics and the wavelength of light emitted by fluorophores within the sample.

Intensity of the Microtubule Backbone The intensity of the microtubule backbone is the difference in intensity between the background noise and the microtubule itself. The greater this value the better the function should fit, as the distinction between background and backbone increases.

Intensity of the Background The value of average background intensity in the image so that the real and the artificial image match up. This number needs to be high enough so that the Standard Deviation of the background noise (see below) doesn't create negative values.

Standard Deviation of the Background Noise Intensity The standard deviation of the background noise in the image so that the real and the artificial image match up. This value together with intensity of the microtubule backbone decide the signal to noise ratio of the image, this is important as it is expected to have an effect on how well the GEF fits.

The basic method for generating images of synthetic microtubules is based upon that presented in Demchouk et al. (2011) with some improvements. The output is designed to have the same structure as if it had been processed by the microtubule selection routine, Section 3.3.3. Roughly microtubules are generated by the following steps: 1) creation of the microtubule at its greatest length with associated taper and angle on a sub pixel grid; 2) assignment of pixels within the grid containing a label; 3) creation of microtubules with taper for each time slice and convolution with image from step 2; 4) convolve image slices with PSF; 5) sum pixels to create image with the right resolution; and 6) add noise. Each step is based upon the parameters mentioned above. The final microtubule image can be made to present nearly any imaging conditions required, Figure 3.6 B.

Initially the maximal microtubule is defined on a R_1 (simulation grid pixel resolution) pixel grid for the maximum microtubule length, $L_{max} = \max_i L_i$, where L_i is the microtubule length for each time point i. A microtubule has a diameter of 25 nm, so the width of the simulated microtubule is $w = 25/R_1$ pixels (this value is rounded in the code if it isn't a whole number, it is best that R_1 should be a factor of 25). A value of $R_1 = 2.5$ is used for simulation. The main length of the microtubule can therefore be represented as a rectangle, with size $w * l$ where $l = L_{max}/R_1$, and a right-angled triangle extension, with size $w*T/R_1$ where T is the taper, Figure 3.6 A. A binary image is created with the image pixels representing the microtubule are given the value 1, Figure 3.6 C. The image, I_1, is then rotated through an angle, θ, by applying a standard rotational transformation to every $I_1(x_i, y_i) = 1$.

$$x_i' = x_i cos(\theta) - y_i sin(\theta)$$

$$y_i' = x_i sin(\theta) + y_i cos(\theta)$$

This creates the new image, I, where $I_2(x_i, y_i) = 1$.

Next the rotated fully labelled microtubule is turned into a partly labelled speckled microtubule. The amount of speckle, or labelled tubulin (P_{tub}) needs to be converted to represent the altered image grid. For example if we consider a microtubule that is 80 nm long then it will contain 130 tubulin dimers. Over that same distance in our 2.5 nm pixel grid we have 320 (10x32) pixels, so the percentage label needs to change to take account of the value of R_1 that we have chosen. So for our altered percentage label, P_{new}, we generate a random number, r_i drawn from the uniform distribution function for each $I_2(x_i, y_i) = 1$. From this we get

$$I_3(x_i, y_i) = \begin{cases} 0 & \text{if } r_i > P_{new} \\ \textit{Poisson}(1.5) & \text{if } r_i < P_{new} \end{cases}$$

to give a speckled rotated image, Figure 3.6 D.

Now that there is a maximum length rotated speckled microtubule it is necessary to create the image stack containing the dynamic microtubule. To do this step 1 is repeated creating a fully labelled microtubule image stack $J_1(i) = I_2(L(i))$ for all i. The speckled microtubule image stack is then created by $J_2(i) = J_1(i) \odot I_3$, where $\odot$ is the hamamard (or element-wise, point-wise) product.

In order to convolve the image stack with the point spread function of the microscope the image is padded so that the full extent of the Gaussian blur can be seen. To match the microtubule selection cropping algorithm, Section 3.3.3, a padding of 15 full size image pixels is added ($15 \times R_2/R_1$ of the R_1 sized pixels), where R_2 is the image pixel resolution. The padding is added uniformly on every side. The enlarged image is then convolved with a Gaussian blur formed on a R_1 grid. The Gaussian Blur is created on a grid double the pixel length plus one of the amount of the padding required, Figure 3.6 E.

Now the image should look similar to a microtubule from the microscope image stacks except that it lacks noise. Before noise can be added the pixel size need to be changed to that of the microscope. As one of the requirements for an input is that $R_2 = nR_1$, where n is an integer, we simply bin and sum $n \times n$ boxes to create our reduced resolution image, J_3. To change the pixel size from R_1 nm/pixel to R_2 nm/pixel.

The final step is to add noise to our reduced resolution image. Image noise is a difficult thing to quantify exactly as it comes from random diffusion of fluorophores and Poisson noise in the camera chip. One method would have been to randomly add white pixels of differing intensity to each image slice in J_2 to represent fluorophores moving in an out of the field of view. To convolve this image with the 2D Gaussian, bin the pixels and then add Poisson noise to represent the noise from the camera chip. Instead 'real' noise was obtained by placing a standard chamber containing a fluorescent reaction mix on the microscope. This chamber was imaged in different locations and the resulting images temporally joined and used as random noise. From this noise image, a sub-stack, N, is randomly selected of the same size as J_3. N and J_3 are added together to give us our final image which is saved as a TIFF stack, Figure 3.6 B,F.

3.6 Analysis of Synthetic Images of Microtubules

Given the large number of parameters that can be altered it is possible to generate synthetic microtubules that reflect any imaging situation that is encountered. However, it is not known what the direct effect these parameters have on the accuracy of the routine used to extract the microtubule backbone and in fitting the Gaussian error function to the microtubule backbone. This section explores the relationship between some of the parameters and the accuracy of fitting. For the parameters looked at errors in fitting will be determined over a range of values, and a rough cut off decided to maintain a minimum quality of fit. Firstly, however, it was necessary to check that the simulation method itself did not contain any errors. Following this the method employed to best fit the Gaussian Error Function needs to be determined.

3.6.1 Errors associated with Synthetic Microtubule Image Generation

In order to see whether there were any errors in the generation of synthetic images, microtubules were generated without any background intensity, background standard deviation (SNR = ∞), and without convolving with the PSF of the microscope at 100% label. A single microtubule was generated on a 2.5 nm pixel grid with a final pixel size of

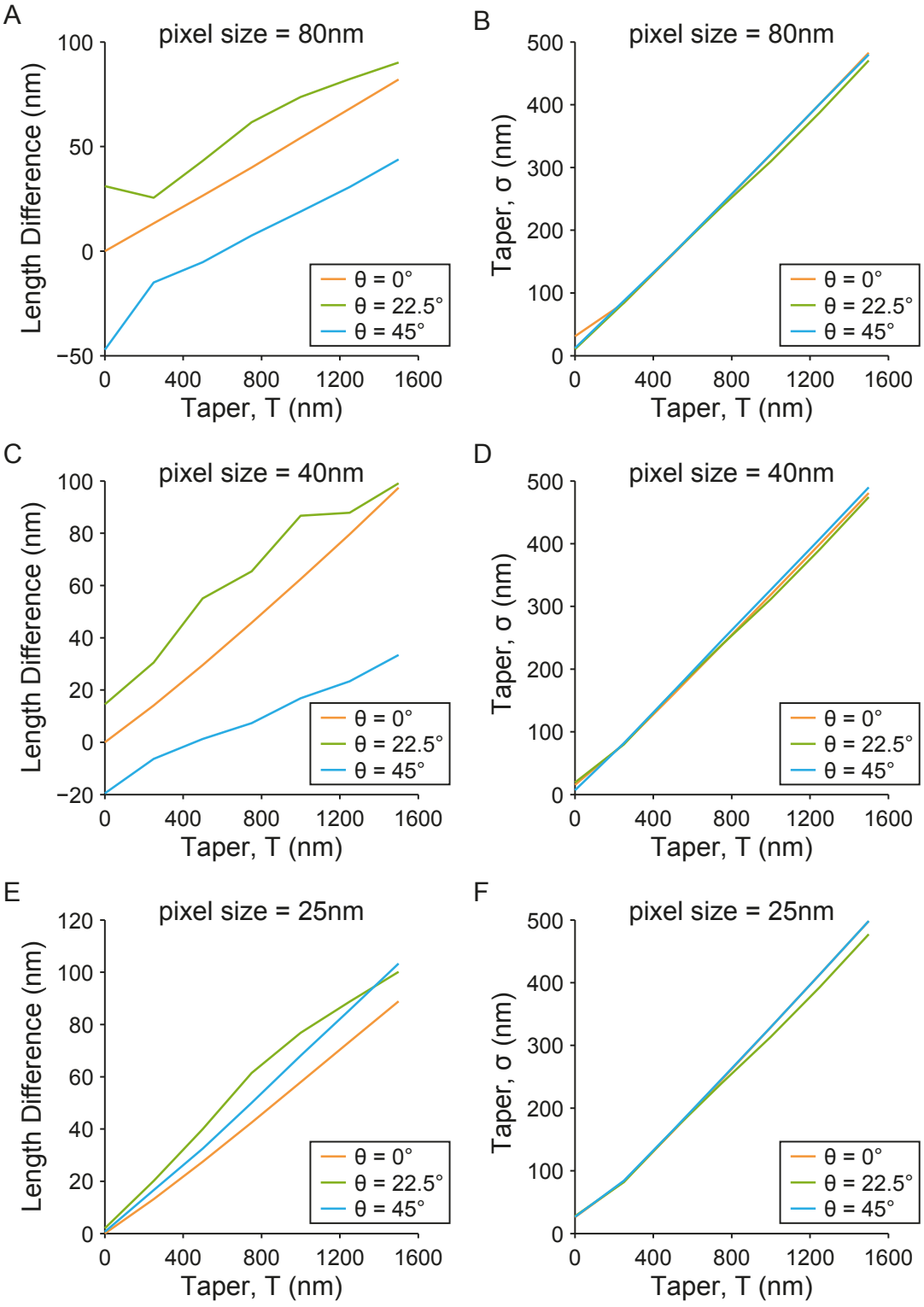

Figure 3.7: **Fitting to an "unconvolved" microtubule:** Twenty-one single images of an unconvolved (PSF = 0 nm), fully-labelled (100% label) microtubule without noise (background intensity = 2,000. background standard deviation = 0, microtubule lattice intensity = 10,000) was generated as taper (T=0, 250, 500, 750, 1000, 1250, 1500 nm) and angle (θ = 0, 22.5 and 45°) where varied. This was repeated three times for three different final pixel sizes; (A-B) 80 nm, (C-D) 40 nm, and (E-F) 25 nm. Images where analysis by: (A,C,E) plotting taper (T) against the length difference between measured via the developed algorithm (μ) and simulated (Ł), calculated as $\mu - L - T/2$; and, (B, D, F) plotting taper, T, against measure taper, σ.

80 nm, for each of the different angles (0°, 22.5° and 45°) over a range of tapers (0, 250, 500, 750, 1000, 1250 and 1500 nm). To each synthetic microtubule image the GEF fitting routine was applied. As there is no probability used in generating these microtubules, the label is 100% so there is no random assignment of pixels, there is no need to calculate multiply images. From the fitting of these routines the raw values for length difference (the difference between the simulate microtubule length (L) and the measured length of the microtubule (μ_1–μ_2)) and measured taper (σ) was plotted against simulated taper length (T), Figure 3.7. The length difference was corrected for expected taper contribution so the calculation is μ_1–μ_2–L–$T/2$. Whilst measured taper shows little deviation between the three angles as simulated taper length is varied, measured lengths between the three angles show different values, Figure 3.7 A,B.

This difference can only be due to underlying errors in the rotation and pixel summing routines. To test this, the final pixel size of the image is reduced by repeating the experiment at 40 nm and 25 nm, Figure 3.7 C-F. For both additional experiments measured taper shows good agreement as the angles change. For length difference the same discourse is apparent. As the lack of agreement is not angle dependent and the differences between the lines reduce as the pixel size reduces the error is likely to do with how the pixels are summed after the image has been rotated. During rotation the destination pixels are identified by apply a rotational transformation as described above and rounding to the nearest pixel. As the pixel is found by rounding, there is an inherent error of half a pixel at both ends of the microtubule. This leads to an error of up to a pixel, which can clearly be seen as the angle increases.

Interestingly, the contribution of taper length to the microtubule length is greater than half the microtubule length as can be seen by the positive gradient for each curve. This is not entirely surprising as the microtubule is generated with a triangular end, being fitted by a function expecting something based upon a Gaussian. This will exaggerate the microtubule length as the fitting of the function looks to minimise error due to the underlying shape being angular rather than curved.

The relationship between simulated microtubule taper length and measured taper length is linear with a ratio of $\sim$3:1 consistent across each pixel size measured. The expected

ratio would be 6:1 as the spread of the fit of the GEF at the microtubule tip is roughly 6σ. This difference is what is influencing the positive gradient for the length difference curves. Whether these differences are an inherent property of fitting the GEF or because of the lack of expect PSF will be determined later. It is useful to know that at a basic level these errors exist to help explain any observed differences later.

3.6.2 How best to fit the Gaussian Error Function

Restrictions can be applied to the upper and lower bounds during fitting of the GEF. However, the best method of applying these restrictions to the upper and lower bound is not known. The method of applying restrictions will be tested on a dual-ended GEF. This is because the majority of experimentally imaged microtubules are short. Additionally, the image chambers contain a small amount of drift. So whilst a dual-ended GEF contains more error per time point, it should give more accurate total length measurements over time.

Two options are considered for restricting the upper and lower bounds of the GEF. Firstly fitting the GEF in one single step (1-step). The background, microtubule lattice signal, microtubule tip location and microtubule taper length is allowed to vary between loose limits, Figure 3.3. Secondly, the GEF is fitted in two steps (2-step). For this, in the first fit the value of the taper is restricted to a very small interval, between 0.9-1.1 pixels ($\sim$73-89 nm). This restriction results in a quick rise from background intensity to lattice intensity. This restriction involves a smaller σ than the experimentally determined σ from raw images of $\sim$125 nm. The second fit fixes the microtubule tip location based on the previous fit and allows the taper length to vary, Figure 3.3. The limits on background and signal intensity are kept the same for all fits.

Initially microtubule images were generated with minimal noise to discover the minimal amount of error that can be expected from this algorithm. Microtubule images were generated with 17% label, a lattice intensity of 12,000, PSF of 125 nm, background intensity of 1 and background intensity standard deviation of 1. The microtubules have

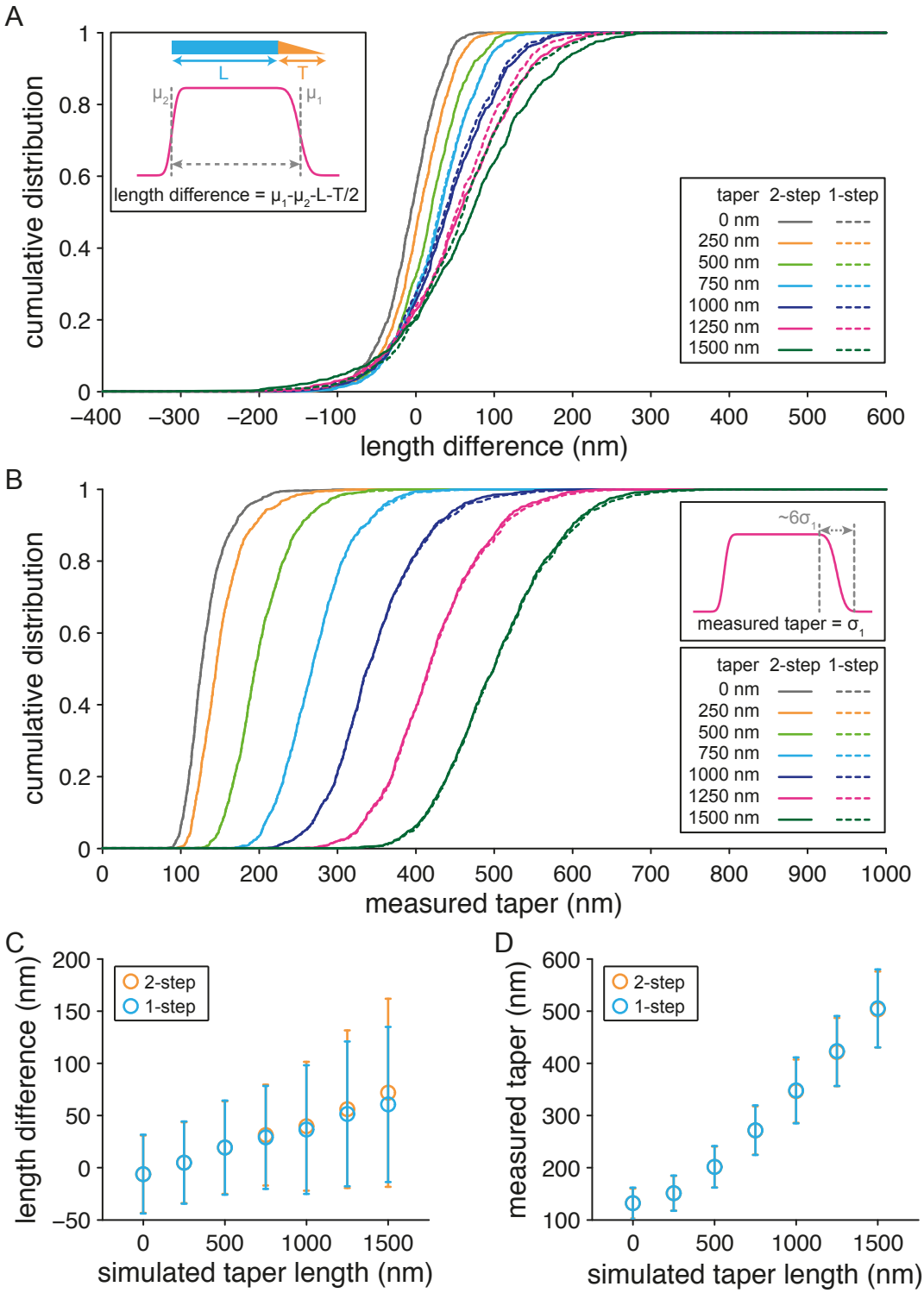

Figure 3.8: **Dual v Single GEF Fit without image noise:** Figure caption is continued on the next page

Figure 3.8: Dual v Single GEF Fit without image noise: 1000 single images were generated with the same conditions (17% label, lattice intensity = 12,000, PSF = 125 nm, background intensity of 1 and background intensity standard deviation of 1. L= 2000 nm, Θ = 0). Each condition was repeated 1000 times for 7 different taper lengths (T = 0, 250, 500, 750, 1000, 1250, 1500). The images were explored for the best way to fit the GEF in two different ways. (A) Cumulative distribution functions of the difference between the simulated and measured lengths plotted for each of the simulated tapers, dotted lines are 1-step fit and solid lines 2-step. Inset shows a cartoon of the values from the GEF fitted to the microtubule image are used with the simulated microtubule length and taper to generate the length difference values. (B) Cumulative distribution functions of the measured tapers plotted for each of the simulated tapers, dotted lines are single fit and solid lines dual. (C) Plot of the mean difference between simulated and measured microtubule length, plotted against the simulated taper length. Error bars are standard deviation. (D) Plot of the mean measured taper STD plotted against the simulated taper length. Error bars are standard deviation.

length 2000 nm and varying taper (0, 250, 500, 750, 1000, 1250, 1500) at angle 0. Each condition was repeated 1000 times.

The microtubules were fitted with a dual-ended GEF. The length was calculated as the difference between the two fitted mean values. From these length measurements the simulated length is subtracted for a blunt microtubule. For non-blunt microtubules the length plus half the taper is subtracted, as above. The analysis of these synthetic microtubule images shows a dependence on the length of taper, Figure 3.8. As taper increase the difference between measured and simulated length increases from -9 nm to 67 nm for a 2-step fitting of the GEF, or -9 nm through to -58 nm for a 1-step fitting of the GEF, Figure 3.8 and Table 3.1. The error, the standard deviation of length difference, associated with these values shows the same dependence on taper, increasing as the simulated taper length increases. The error increases from 37 nm to 90 nm for the 2-step fitting of the GEF and from 38 nm to 74 nm for the 1-step fitting of the GEF, Table 3.1.

Errors using a similar method, Demchouk et al. (2011), have been reported as being as low as 15 nm for a simulated blunt microtubule. This was based on a 42 nm pixel grid size and was fitted using a one-ended GEF. When the algorithm presented here is restricted to fitting to one end, rather than both, the error is reduced to 25 nm. The simulations carried out by Demchouk et al. (2011) used a PSF of 72 nm apposed to the standard deviation approximation of 125 nm used here. Given that 42 nm pixel grid is nearly half the pixel size used in these simulations, and 72 nm PSF is less than 2/3 the size of the PSF used,

a direct comparison cannot be made. Additionally they used a speckle parameter of 5.2 which is assumed to be a label of $\sim$26%. Whilst the SNR was not quoted in the paper, using an image provided in the supplementary information the SNR was calculated to be $\sim$14. Whilst the underlying methods of synthetic microtubule image generation are not the same, using the above parameters a close approximation to these images was calculated. With a SNR of 14, the error at the tip of the microtubule was found to 28 nm, using the dual-ended GEF. When a single-ended GEF was used the error was found to be 18 nm. When the experiment was repeated without noise the error was found to be 22 nm for a dual ended GEF and 13 nm for a single ended microtubule. A comparison can only really be made with the single ended GEF fits as that was the method used by Demchouk et al. (2011). In this case the two values of 13 nm and 18 nm error match closely to the values produced by Demchouk et al. (2011).

Carrying on from the original experiment, the measured taper values were also plotted for the different simulated microtubule taper lengths to compare the differences between fitting a one-step and a two-step fit of the GEF, Figure 3.8 B. The same trend, an increase in measured taper length can be seen as the simulated taper length increases. However there are now distinct differences between the distributions for different lengths of taper, Figure 3.8 B. For both the one-step and the two-step fitting of the GEF, the mean of the measured taper increases from 132 nm to about 500 nm, Table 3.1 B. The differences between the 1-step and the 2-step fit were tested and there was found to be no significant difference between the two methods of fitting. Significance testing was done first by an f-test to test for differences between variances, and then by student's t-test to test for differences between the means. Once taper has reached 500 nm or greater there is roughly a linear relationship between measured taper and simulated taper, Figure 3.8 D. The method returns an average of $\sim$125 nm for both the simulated images of blunt microtubules and for the fitted value of the standard deviation to the fixed seed end. This shows that without noise, it is the PSF of the microscope that is dominating the error in fitting the GEF to the simulated images.

Whilst investigative of which method of fitting a GEF is best, this analysis is not representative of a standard image. To test what the errors in measurement would be for a standard experiment, the parameters for synthetic microtubule image generation

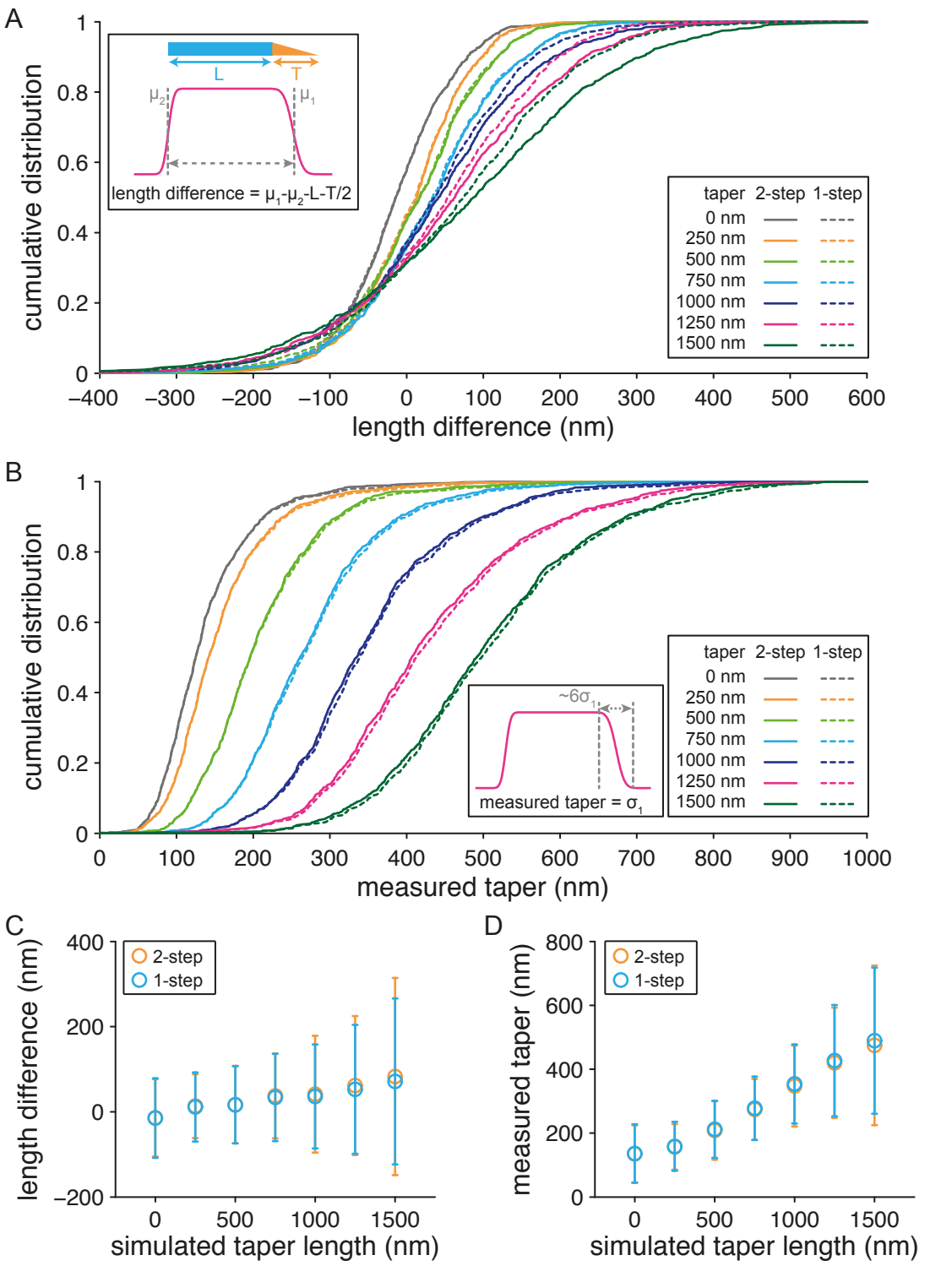

Figure 3.9: **2-step v 1-step GEF fit with image noise:** Figure caption is continued on the next page

Figure 3.9: 2-step v 1-step GEF Fit with image noise: 1000 single images were generated with the same conditions (17% label, lattice intensity = 12,000, PSF = 125 nm, background intensity of 10,000 and background intensity standard deviation of 2,000. L= 2000 nm, Θ = 0). Each condition was repeated 1000 times for 7 different taper lengths (T = 0, 250, 500, 750, 1000, 1250, 1500). The images were explored for the best way to fit the GEF in two different ways. (A) Cumulative distribution functions of the difference between the simulated and measured lengths plotted for each of the simulated tapers, dotted lines are 1-step fit and solid lines 2-step fit. Inset shows a cartoon of the values from the GEF fitted to the microtubule image are used with the simulated microtubule length and taper to generate the length difference values. (B) Cumulative distribution functions of the measured tapers plotted for each of the simulated tapers, dotted lines are 1-step fit and solid lines 2-step fit. (C) Plot of the mean difference between simulated and measured microtubule length, plotted against the simulated taper length. Error bars are standard deviation. (D) Plot of the mean measured taper STD plotted against the simulated taper length. Error bars are standard deviation.

were matched to an experimental chamber. The resulting parameters were: background intensity of 10,000; lattice intensity of 12,000; PSF of 125 nm; and background intensity standard deviation of 2000. As before the microtubules were simulated with length 2000 nm and varying taper (0, 250, 500, 750, 1000, 1250, 1500) at angle 0, each image was generated 1000 times. To calculate the goodness of fit to the microtubule end, the measured microtubule length from a dual-ended GEF was compared to the simulated microtubule length, Figure 3.9. The analysis was carried out as before.

The same relationship holds for data with noise added, as was present for data without noise. As simulated taper increases, the length difference also increases from -12 nm to 85 nm. For the 1-step fit GEF the mean length difference increase from -14 nm to 66 nm, Table 3.1 C. The standard deviation (or error) with these measurements increases from 73 nm to 177 nm for the 2-step fit, and 76 nm to 147 nm for the 1-step fit. This lesser error results in tighter cumulative distributions curves, Figure 3.9 A. An f-test is applied to test for differences between the distributions for 1-step and 2-step fit. If the f-test is not significant a student's t-test is applied. Up to 1000 nm of simulated taper there is no statistically significant difference between the distributions.

The same analysis is applied to taper length measurements. Statistical tests, f-test and student's t-test, were applied to the data and no difference was detectable between the distributions for 1-step or 2-step fitting of the GEF. A visual comparison of the distributions shows that there is a slight difference between the distributions, Figure 3.9 B. The cumulative distribution curves for the 2-step and 1-step GEF fits are distinguishable above 750 nm.

A - Dual v Single GEF, no noise - Length Difference Statistics

	Dual		Single		Statistical Tests	
Taper	mean	std	mean	std	f-test p value	t-test p value
0	-8.62	37.08	-8.86	37.76	0.565	0.886
250	3.25	38.77	3.00	39.39	0.618	0.884
500	16.64	44.38	16.22	45.05	0.635	0.831
750	27.87	48.32	26.45	49.28	0.532	0.515
1000	39.78	61.71	35.44	61.64	0.970	0.116
1250	54.47	75.52	49.12	69.37	0.007 *	0.099
1500	66.96	90.13	57.65	74.26	0.000 ***	0.012 *

B - Dual v Single GEF, no noise - Taper Length Statistics

	Dual		Single		Statistical Tests	
Taper	mean	std	mean	std	f-test p value	t-test p value
0	132.00	28.06	132.21	29.78	0.061	0.874
250	151.16	33.20	151.26	33.71	0.627	0.947
500	201.48	39.12	201.67	39.83	0.570	0.914
750	271.37	46.36	271.87	47.54	0.426	0.815
1000	346.64	60.66	348.08	63.23	0.191	0.602
1250	421.77	65.38	423.65	67.06	0.422	0.527
1500	503.16	72.74	505.29	74.70	0.401	0.518

C - Dual v Single GEF - Length Difference Statistics

	Dual		Single		Statistical Tests	
Taper	mean	std	mean	std	f-test p value	t-test p value
0	-12.21	73.05	-14.05	76.45	0.152	0.584
250	5.78	74.98	2.34	81.15	0.013 *	0.325
500	12.67	85.17	8.09	90.66	0.049 *	0.244
750	31.03	99.64	28.05	102.42	0.384	0.509
1000	38.37	128.96	29.25	117.65	0.004 **	NA
1250	57.23	141.57	44.28	128.41	0.002 **	NA
1500	83.13	176.79	66.23	146.52	0.000 ***	NA

D - Dual v Single GEF - Taper Length Statistics

	Dual		Single		Statistical Tests	
Taper	mean	std	mean	std	f-test p value	t-test p value
0	138.32	64.20	139.39	67.53	0.111	0.717
250	156.94	71.67	158.58	76.55	0.037 *	0.622
500	209.70	83.50	212.10	89.31	0.034 *	0.535
750	274.35	95.32	277.81	99.17	0.211	0.426
1000	350.18	111.28	355.44	116.16	0.175	0.302
1250	428.77	133.30	435.46	134.67	0.748	0.266
1500	504.70	135.88	512.08	137.17	0.766	0.231

Table 3.1: **Values for 2-step v 1-step GEF Fit:** The table caption is continued on the next page

Table 3.1: 2-step v 1-step GEF Fit: 1000 single images were generated with the same conditions (17% label, lattice intensity = 12,000, PSF = 125 nm, L= 2000 nm, Θ = 0) for 7 different taper length measurements. (A-B) The experiment was first conducted with no noise image (background intensity 1, background STD 1) (see also Figure 3.8). (C-D) It was repeated with image noise (background intensity 1, background STD 1) (see also Figure 3.9. (A-D) The statistics for a dual step or singular Gaussian error function fit, mean and standard deviation (STD). The variance of the distributions are tested for significant difference by an f-test and if suitable a t-test to check whether there is significant difference between the means. For the statistical tests * is statistically significant at the 95% level, ** the 99.5% level and *** the 99.95% level.

The length difference and the taper length were plotted against simulated taper length. As observed above, there is a linear correlation between simulated taper length and average difference in microtubule length. The gradient of the two lines are roughly similar with the range between 0-1500 only changing from $\sim$90 nm to 80 nm for the 1-step fitting of the GEF used here. For taper length measurements there is not a linear correlation. This is because unlike above the PSF hides any taper changes under the PSF. Given the rough 3:1 ratio observed early this will equate to $\sim$375 nm.

In general, there is little noticeable difference between fitting the GEF as a 1-step and fitting as a 2-step. The only difference is the tighter distributions in length distribution for 1-step fitting. Given the time penalty for fitting in two steps, there is no benefit to it. Therefore from this point onwards the GEF will be fitted in a one step process.

3.6.3 How label density affects fitting of the Gaussian Error function

To test how the density of microtubule labelling affects the fitting of the GEF to microtubules, blunt (taper = 0 nm) microtubules were simulated with length varying from 2000 nm to 4000 nm and back to 2000 nm at a rate of 50 nm per frame as an image stack. Intensity parameters were kept the same as before: microtubule lattice intensity was set at 12000; background to 10000; and background standard deviation to 2000. The simulation was done at two angles, 0° and 45°. To change label density the label percentage was varied over 6%, 12%, 18%, 25%, 35% and 50% label. Each condition was simulated 10 times.

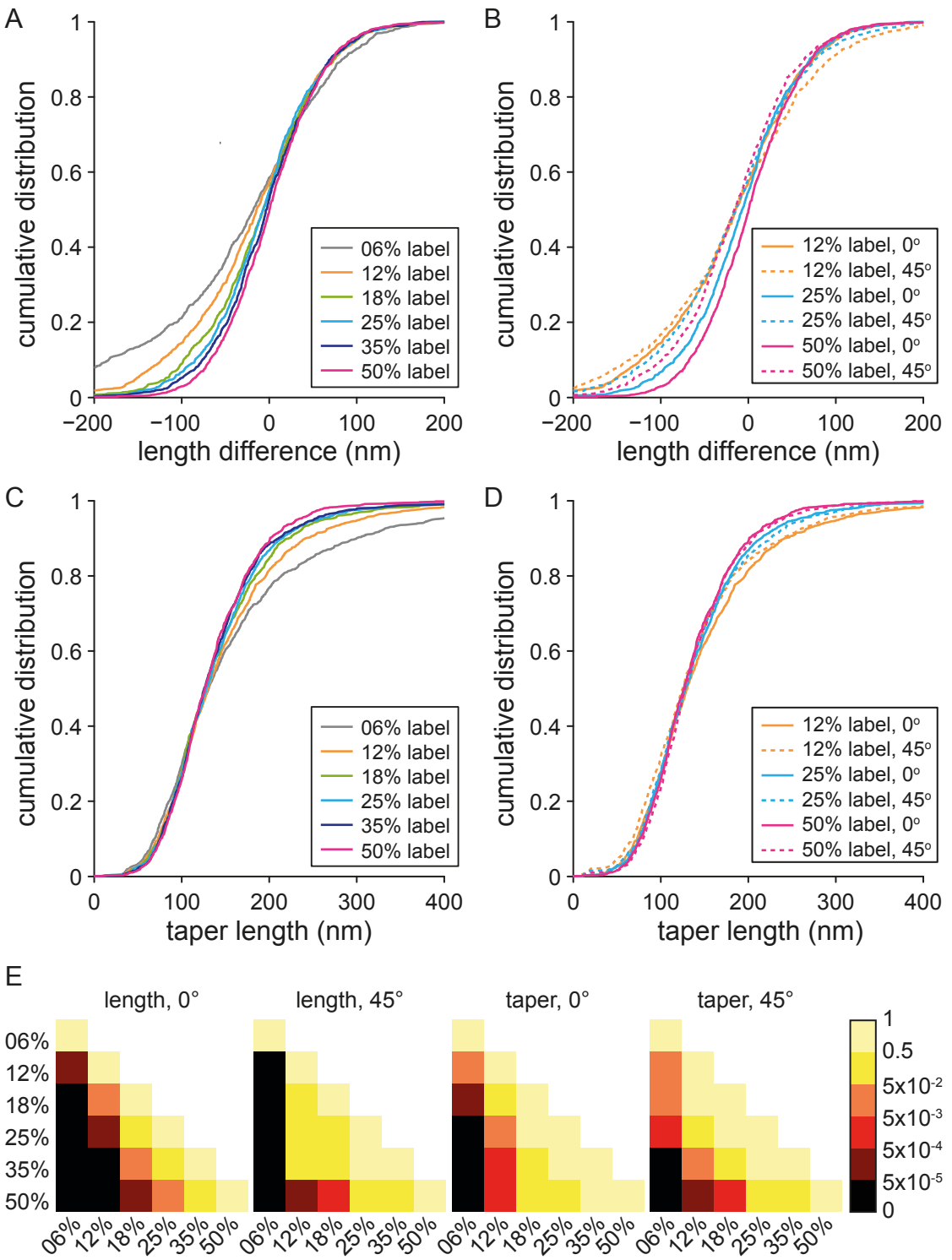

Figure 3.10: **Effect of label percentage on accuracy when fitting the Gaussian error function:** Continued on next page.

Figure 3.10: Effect of label percentage on accuracy when fitting the Gaussian error function: Six different label conditions (label percentage = 6%, 12%, 18%, 25%, 35% and 50%) were used to generate synthetic microtubules (lattice intensity = 12,000; microtubule background = 10,000; and background STD = 2000) for a growing/shrinking microtubule (L= 2000 nm-4000 nm-2000 nm with growth/shrinkage = 50 nm/frame, T=0 nm) end simulated over two angles, (0° and 45°). This results in 810 measurements per condition. (A) Cumulative distributions of microtubule length differences between simulated ($L + T/2$) and measured microtubule length (μ) for all simulations at 0°. (B) Comparison between cumulative distributions of microtubule length differences for microtubules simulated at 0° and 45° for label 12%, 25% and 50%. (C and D) same data as in A and B respectively but displaying measured taper (σ). (E) Significant difference values as calculated by pairwise analysis of each label percentage combination, for each of length differences at 0°, length differences at 45°, taper measurement at 0° and taper measurement at 45°. Statistical test used was the non-parametric Kolmogorov-Smirnov test.

As before the length difference was calculated as the difference between the simulated microtubule length and the measured microtubule length from a dual-ended GEF. The cumulative distributions for all 6 label densities at 0° were plotted for visual comparison, Figure 3.10 A. All of the distributions cross at similar point. However, the spread (or error) of the length differences increases as the label density decreases as expected, Table 3.2 A.

To test whether rotating the simulated microtubule image convolved with a PSF has the same inherent error as observed above, the image was rotated through 45°. The cumulative distributions were plotted pairwise (0° and 45°) for 12%, 25% and 50% label density, Figure 3.10 B. There is a slight shift in the means of the distribution between 0° and 45°. Additionally there is an increase in the variance of the data, Table 3.2 A. Given that the maximum length difference between 0° and 45° is 18 nm the difference whilst less than what was observed above, will be due to pixel binning during rotation issue that was discussed above.

The taper measurements from the dual-ended GEF were analysed the same way. At 0° the distributions of the measured taper values are very similar. For low label density microtubule images there are a greater proportion of large taper values measured (positive skew). These larger values increase the error in the measured taper values for lower label densities. When the comparison between 0° and 45° rotated microtubules for 12%, 25% and 50% is calculated, there is no noticeable difference between the synthetic images at different angles. This is verified by statistical tests, f-tests and t-tests as before, Table 3.2 B.

A - Label Percentage - Length Difference Statistics

perc	Angle = 0°		Angle = 45°		Statistical Tests	
	mean	std	mean	std	-test p value	t-test p value
6	-34.19	109.69	-37.98	130.36	0.0000 ***	N/A
12	-18.98	78.07	-15.90	90.91	0.0000 ***	N/A
18	-9.38	67.03	-19.18	87.26	0.0000 ***	N/A
25	-7.15	62.79	-16.68	78.90	0.0000 ***	N/A
35	-2.53	60.26	-17.08	75.47	0.0000 ***	N/A
50	1.89	55.65	-15.95	66.90	0.0000 ***	N/A

B - Label Percentage - Taper Length Statistics

perc	Angle = 0°		Angle = 45°		Statistical Tests	
	mean	std	mean	std	-test p value	t-test p value
6	163.01	110.77	157.71	117.95	0.0458 *	0.2975
12	148.65	79.54	140.62	76.19	0.1686	0.0201 *
18	141.90	69.44	141.28	73.45	0.0728	0.8467
25	139.81	64.41	139.31	65.79	0.4983	0.8611
35	138.69	65.32	139.65	63.68	0.4161	0.7367
50	135.35	54.53	137.63	54.86	0.8499	0.3456

C - Lattice to Background Std Intensity ratio - Length Difference Stats

S/N ratio	Angle = 0°		Angle = 45°		Statistical Tests	
	mean	std	mean	std	f-test p value	t-test p value
1	49.25	586.69	44.27	627.16	0.1391	0.8976
3	-2.46	145.18	-28.96	180.14	0.0000 ***	N/A
6	-7.10	66.63	-21.97	86.65	0.0000 ***	N/A
9	-10.09	50.73	-17.61	66.27	0.0000 ***	N/A
12	-4.85	43.84	-22.00	57.21	0.0000 ***	N/A
15	-7.98	40.99	-22.60	54.32	0.0000 ***	N/A

D - Lattice to Background Std Intensity ratio - Taper Length Statistics

S/N ratio	Angle = 0°		Angle = 45°		Statistical Tests	
	mean	std	mean	std	f-test p value	t-test p value
1	167.95	199.36	143.67	176.57	0.0072 **	0.0435 *
3	169.26	146.80	163.92	150.77	0.4083	0.4317
6	142.55	70.78	143.29	75.59	0.0356 *	0.8172
9	137.67	49.23	136.85	51.45	0.1583	0.7096
12	135.91	39.81	134.25	42.22	0.0598	0.3589
15	134.54	35.27	135.11	40.31	0.0000 ***	0.7293

Table 3.2: **Microtubule to Background Intensity ratio and Label Percentage Statistics:** Synthetic microtubule time series (also see Figures 3.10 and 3.11) were generated with the same conditions for either 6 different label percentage, or 6 different MT lattice intensity values. All other synthetic values were kept the same, experimented was done at 0° and 45°. Mean and standard deviation of length difference between simulated and measured values, and taper measurements. Statistical tests were carried out between the same simulations at difference angles. The variance of the distributions are tested for significant difference by an f-test and if suitable a t-test to check whether there is significant difference between the means. For the statistical tests * is statistically significant at the 95% level, ** the 99.5% level and *** the 99.95% level.

The main goal of this exercise is to determine if there is a label density below which the data becomes unreliable. To test this the data was tested for significance, pairwise by label density. The tests are calculated for the two measurable parameters, length difference and taper, for both angles 0° and 45°. To test for significance the non-parametric Kolmogorov-Smirnov test that compares for differences in distribution was used, Figure 3.10. Results of test presented as coloured squares, the darker the colour the more significant the difference. Orange is significant at the 95% level. As can be seen the 6% and 12% label density is generally significantly different compared to the other densities. In general (apart from for length difference at 0° between 50% and 25%) there is no statistically significant improvement in using 25%, 35% or 50% label.

From this simulation, microtubule label density doesn't appear to have a large effect on how well the GEF fits so long as a minimum threshold for label is used. The minimum threshold appears to be somewhere between around ∼18% density. Taper measurement are very well conserved above the minimum threshold and don't appear to be largely dependent upon percentage label.

3.6.4 How the signal to noise ratio affects the fitting of the Gaussian Error Function

In order to test what effect the signal to noise ratio (SNR) has on the fitting of the GEF, blunt (taper = 0) microtubules were simulated with length varying from 2000 nm to 4000 nm and back to 2000 nm at a rate of 50 nm per frame as an image stack. Intensity parameters were kept the same as before: microtubule label was set at 18%; microtubule background to 10000; and microtubule background stand deviation to 2000. The simulation was done at two angles, 0° and 45°. The SNR is defined as the lattice intensity divided by the standard deviation of the background noise. To change the SNR the lattice intensity was set at 2000, 6000, 12000, 18000, 24000 and 30000. This gives SNR of 1, 3, 6, 9, 12, and 15 respectively. Each image stack was simulated 10 times.

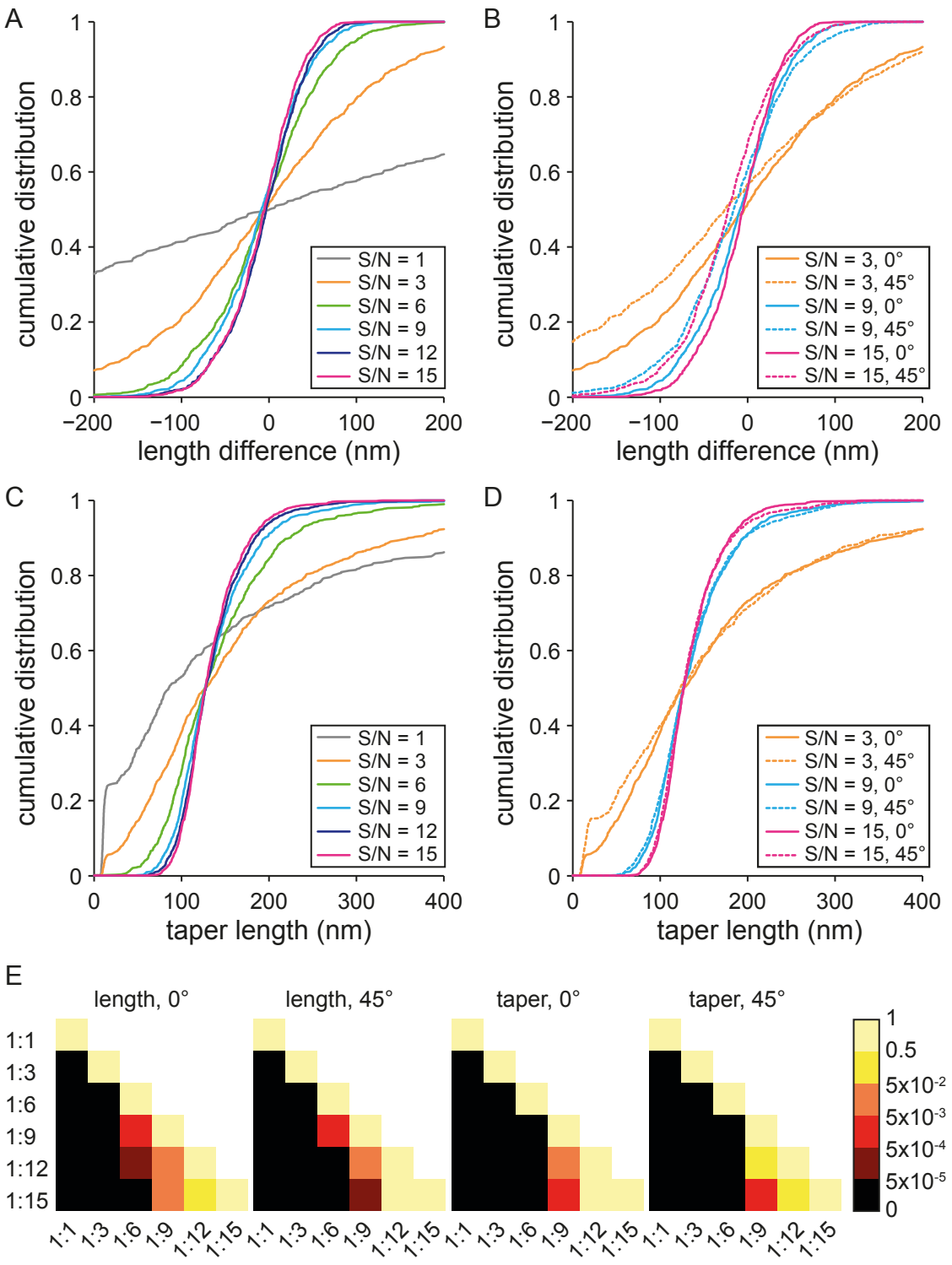

Figure 3.11: **Effect of SNR on accuracy when fitting the Gaussian error function:** Continued on next page.

Figure 3.11: Effect of SNR on accuracy when fitting the Gaussian error function: Six different signal to noise ratios (1, 3, 6, 9, 12, 15) were used to generate synthetic microtubules (label density = 18%, microtubule background = 10,000; and background STD = 2000) for a growing/shrinking microtubule (L= 2000 nm-4000 nm-2000 nm with growth/shrinkage = 50 nm/frame, T=0 nm) end simulated over two angles, (0° and 45°). This results in 810 measurements per condition. To change the signal to noise ratio, the background STD was fixed, and the lattice intensity set at 2,000, 6,000, 12,000, 18,000, 24,000, 30,000. (A) Cumulative distributions of microtubule length differences between simulated ($L + T/2$) and measured microtubule length (μ) for all simulations at 0°. (B) Comparison between cumulative distributions of microtubule length differences for microtubules simulated at 0° and 45° for label 3%, 9% and 15%. (C and D) same data as in A and B respectively but displaying measured taper (σ). (E) Significant difference values as calculated by pairwise analysis of each label percentage combination, for each of length differences at 0°, length differences at 45°, taper measurement at 0° and taper measurement at 45°. Statistical test used was the non-parametric Kolmogorov-Smirnov test.

To test how SNR affects the fitting of a dual-ended GEF, the length difference was calculated as above. The cumulative distributions are plotted for the 6 different SNRs at 0°. All of the distributions have a similar mean, Figure 3.11 A, Table 3.2 C. However there is a large effect on the variance of the distributions with SNR of 1. There is an almost linear relationship when SNR is equal to one, rather than the more normal like distributions of the curves with a SNR of above 1. Only the analysis of simulated microtubule images with a SNR of 9, 12 and 15 appear to be similar to each other.

As before when rotating the simulated microtubule image through 45° has an effect. The cumulative distributions for SNR equal to 3, 9 and 15, were plotted pairwise (0° and 45°), Figure 3.11 A. There is a slight shift in the mean of the distribution, with the measured length of microtubule images rotated by 45° appearing shorter. This will be due to the systematic error discussed before.

The taper measurements from the dual-ended GEF were analysed the same way, Figure 3.11 C. Here as with the length difference there is a large difference between the simulations with SNR of 1 and 3 compared to those with a SNR of 6 or more. When the comparison between angles for 12%, 25% and 50% is drawn, there is no noticeable difference between the angles. This is verified by statistical tests with the exception of two cases, Table 3.2 D. For SNR equal to 1 the distribution is almost linear and an f-test is designed to work on normal distributions. For SNR equal to 15 the distributions become very tight, variance less than half a pixel. Student t-tests and f-tests are sensitive to large sample numbers. In this case with the sample numbers high, and the variance low the

range not to be statistically significant is small. Therefore it is not that surprising that for high SNR the data becomes statistically significant.

To look at below which level the SNR becomes unreliable, the data is tested as before, pairwise by Kolmogorov-Smirnov test, Figure 3.11 E. There is statistical significance between all SNRs apart from between SNR of 12 and 15.

From these results it is clear that the SNR has a large effect on the fitting of the GEF. However to influence the SNR, label density and tubulin concentration would be altered in experimental chambers. Both of these will affect the amount of fluorophores in the lattice, and the amount of free fluorophores in solution. Which in turn affects the lattice intensity, background intensity and background standard deviation. It is not as simple as changing one condition in order to change one of our simulation parameters. Whilst having the same variables as the experimental conditions for the simulation, the complexity for this is great. It would not be worth the time taken either in complexity to code, or the simulation to run. These two investigations, varying label density and signal to noise ratios show how sensitive fitting the GEF is. From the results seen here it is clear that SNR causes a larger variance over the range of ratios used, than varying label density. However the range over which SNR has been varied is more extreme than that varied over by the label percentage. The SNR ratio of 6 in the label percentage experiments will also have a limiting effect on the significance between the difference label percentages observed. Any real experiments should look at maximising both SNR and label density. Unfortunately, changing SNR and label density has positive and negative consequences. Increasing SNR would give a more accurate fit. There are two ways this could be done, either increase the exposure time on the microscope or increase the label density. By increasing the exposure time, the taper is being artificially lengthened as tubulin dimers are allowed to arrive and leave from the microtubule tip. Depending upon the tubulin concentration an increase in exposure time could lead to an increase in error. An increase in exposure time will need to be carefully balanced against the growth speed and resulting increase in SNR. An increase in label density would increase the brightness of the lattice. Although when using more label careful judgment needs to be made when using MAPs. Increasing of the label density may remove a proportion of MAP binding sites as the label may impede binding. Again this should be carefully balanced as required.

3.7 Dynamic Microtubules

The goal for redevelopment of the GEF has been to see if the two-dimensional neighbourhood model presented in Gardner et al. (2011), can explain the paradoxical effect of EB3, where it acts as a promoter of growth and catastrophe. The two-dimensional model of microtubule dynamics attempts to explain the increase in negative excursions seen at higher tubulin growth speeds. In this model higher growth speed increases the possibility of a large taper at the microtubule tip, representative of this underlying change in structure. This change in structure, or neighbourhood, at the microtubule tip increases the number of protofilament capping tubulin dimers most likely to dissociate. This increase in the rate of dissociation led to the estimate of the on and off rates of GTP-tubulin during microtubule growth to be revised to be a magnitude higher. Gardner et al. (2011) developed a model where they proposed that a small stabilisation of lateral or longitudinal bonds would have a drastic effect on microtubule growth rates. It is the stabilisation of these bonds by MAPs that allows cellular based microtubules to have such an inflated growth speed. To see whether this neighbourhood model holds true it was carefully investigated using the re-developed routine used to fit GEF to dynamic microtubule images.

3.7.1 Analysis of Labelled Dynamic Microtubules

In order to investigate the neighbourhood model of microtubule dynamics, labelled tubulin was assembled in total internal reflection fluorescence microscopy chambers. Microtubules are assembled on GMP-CPP stabilised microtubule seeds that were labelled with HiLyte 647™tubulin. Multiple chambers were imaged containing varying concentrations of porcine brain tubulin, all with a final labelling density of 17.5% HiLyte 488™tubulin. Concentrations of 7.7, 9.8, 11.6 and 15.5 μM tubulin (will be referred to as 8, 10, 12, and 16 μM tubulin) were chosen for the assay. The resulting SNRs were 11, 9, 8 and 6 respectively. The SNR was calculated as (backbone intensity – background intensity)/background standard deviation. The SNRs in the live imaging chambers were calculated by drawing a linear ROI along the microtubule lattice to extract the mean

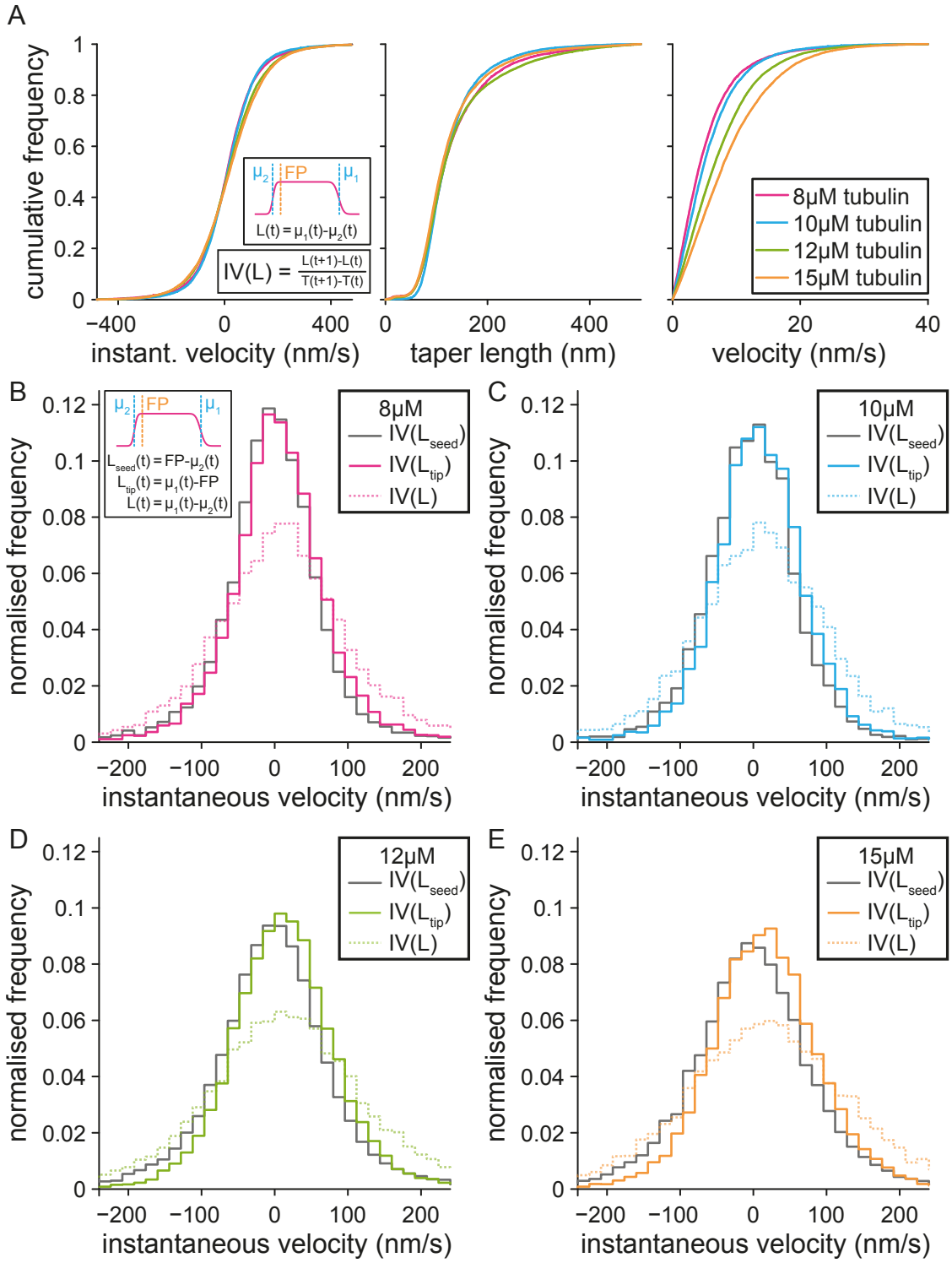

Figure 3.12: **Tubulin concentration has no effect on microtubule tip structure:** Tubulin concentration was varied over 8 μM, 10 μM, 12 μM and 15 μM. (A) cumulative frequency graphs for: Left: instantaneous velocity (IV) - the length difference between two consecutive time points divided by the time difference between those time points. Inset shows cartoons of the equation used and cartoon of GEF fit (FP is the fixed point). Centre: taper length graph - σ_1; and right: velocity - calculated as the gradient through 5 consecutive values for $\mu_1 - FP$. (B-E) Individual graphs for IV for each concentration. Comparison between IV values measured in three separate ways. $IV(L_{\text{seed}})$ (control) is the change between the fixed point and the position of the seed end μ_2. $IV(L_{\text{tip}})$ is the change between the fixed point and the position of the tip end μ_1. $IV(L)$ is the change in difference between μ_1 and μ_2.

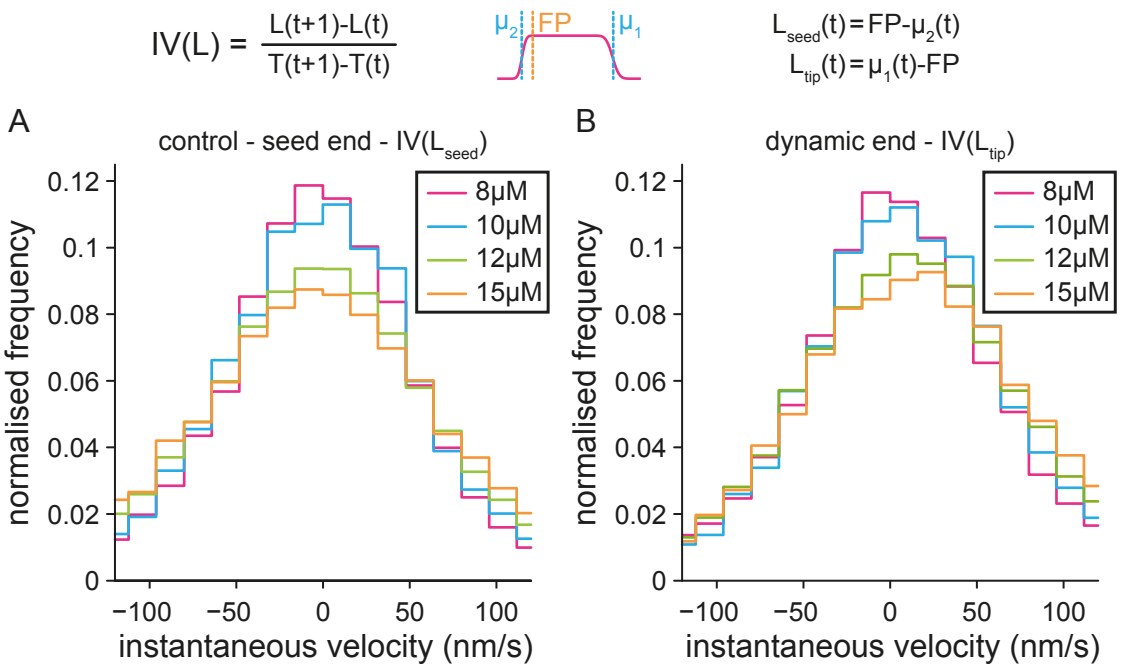

Figure 3.13: **Comparison of the effect of tubulin concentration on microtubule tip structure:** Replot of the instantaneous velocities from Figure 3.12 B-E grouped by microtubule end instead of experimental condition. Top: the equations on the left are used to calculate the instantaneous velocity (IV)). Cartoon shows the locations of the values for the microtubule seed end (μ_2), the fixed point (FP) on the microtubule and the dynamic end (μ_1). The equation on the right shows the how the microtubule length (L) is calculated for each end. (A) shows the comparison for the seed end (B) shows the comparison for the dynamic end.

backbone intensity. A square ROI was drawn in the image background to extract the mean background intensity and standard deviation. The intensity for both ROIs were extracted from the mid way point of the imaging stack. Images were obtained every 500 ms for 720 time points, the exposure time was 300 ms.

Analysis was carried out by fitting a dual-ended GEF to microtubules greater than $\sim$1.5 μm. For each time point the velocity was calculated from the raw microtubule length data extracted from the GEF fit. A linear line of best fit was calculated through five consecutive time points (two before and two after the time point of interest). The gradient of the line was the velocity and was assigned to the central point. The instantaneous differences in microtubule length between time points were also calculated ($dL(t) = L(t) - L(t-1)$). This returned for each time point in each image stack (except the first two time points and the last two time points) comparative values for: the change in microtubule length; taper length; and the microtubule growth speed (average velocity). For analysis these variables

were used to subset the raw data. Individual time points with velocity greater than 0 and less than 40 nm/s, dL between -240 nm and +240 nm and taper between 0 and 500 nm were included. These bounds should restrict the analysis to microtubules in the growth state and remove any extreme outliers from the analysis. The resulting N values for the experiment are 8,948, 6,993, 18,413 and 13,467 time points for tubulin concentrations 8, 10, 12 and 15 μM respectively.

The resulting cumulative distribution functions for these three parameters are plotted, Figure 3.12, with the dL values converted to instantaneous velocities IV by dividing each value by the time step (500 ms). As expected these bounds have no effects on limiting data by instantaneous velocities or taper length with both curves asymptotic at their limits. The velocity curves show a clear increase in growth speed as tubulin concentration increases. The neighbourhood model would predict that an increase in growth speed would result in an increase in taper. However there is no separating the cumulative distributions for the taper lengths for different tubulin concentration between 0 and 200 nm. Above 200 nm a small difference is visible but it does not correlate with concentration and appears to be random. A t-test carried out found that the different concentrations are statistically significant to each other except from when 8 μM was compared to 10 μM, table 3.3 A.

The increase in growth speed isn't strongly represented in the instantaneous velocities cumulative distribution. Whilst there is a slight difference between the curves, there does not appear to be a concentration dependent difference. However, as the SNR ratio decreases as tubulin concentration increases, the variance of instantaneous velocities would naturally be expected to increase. As such it is hard to say whether this increase in variance in instantaneous velocities values is due to uncertainty in the measured values, or because microtubule growth speed increased.

To remove the uncertainty from the data, instantaneous velocities are calculated separately for the microtubule tip (IV_{tip}, and the microtubule seed (IV_{seed}), Table 3.3. The distance is measured for each time point from the fixed point to each end (seed and tip) of the microtubule. Then the change in microtubule length is calculated between each time point and converted to instantaneous velocities as before. The corresponding

A. p-values of 2 sample t-tests for tubulin gradient experiment

	8 μM	10 μM	12 μM
10 μM	0.4513		
12 μM	0.0002	0.0063	
15 μM	0.0001	0.0001	0.0249
significance level	5.00%	0.50%	0.05%

B. Statistics for instantaneous velocities for tubulin gradient experiment

Tubulin Conc	N	MT seed junction Mean	MT seed junction Std	MT dynamic tip Mean	MT dynamic tip Std	Combined Mean	Combined Std
8 μM	8,948	-3.39	76.50	7.52	73.29	10.91	111.33
10 μM	6,993	-2.63	71.58	9.43	67.08	12.06	102.54
12 μM	18,413	-3.31	88.19	13.17	76.89	16.48	119.63
15 μM	13,467	-2.88	90.25	16.67	79.33	19.55	123.01

C. p-values of 2 sample t-tests for EB3 experiment

	control	100 nM	200 nM
100 nM	0.0001		
200 nM	0.0001	0.2249	
2x label	0.3487	0.0001	0.0001
significance level	5.00%	0.50%	0.05%

D. Statistics for instantaneous velocities for EB3 experiment

EB3 conc	N	MT seed junction Mean	MT seed junction Std	MT dynamic tip Mean	MT dynamic tip Std	Combined Mean	Combined Std
control	2,476	-3.19	94.34	13.84	83.73	17.03	132.96
100 nM	3,747	-0.99	81.84	34.08	101.28	35.06	130.80
200 nM	9,457	-0.09	91.12	31.86	95.96	31.95	132.91
2x label	16,482	-1.08	64.34	13.97	62.34	15.06	91.65

Table 3.3: **Instantaneous velocity statistics for dynamic microtubules:** Table to go with Figures 3.12 (A, B) and 3.14 (C, D). (A, C) P values of pairwise t-tests carried on the IV values to test for significant difference. Two-sided t-test carried out, statistical significance is indicated by colour. (B, D) show the values for the mean and standard deviation (STD) for IV, IV_{tip} and IV_{seed} as well as the number of time frames measured (N).

curves (IV, IV_{tip} and IV_{seed}) for each concentration are then plotted as histograms on the same axis, Figure 3.12. Each histogram bin is divided by the corresponding N value for comparison between different tubulin concentrations.

The best control available for this experiment is considered to be the measurements in IV of the seed end. This is because it is internal to the experiment and accurately represents the error associated to fitting to a fixed end in the experimental conditions available. As the concentration of tubulin increases there is a clear reduction in the peak of the histograms. This correlates with our expectations that a decrease in SNR will result in an increase in the variance for the experiment. A t-test carried out between the instantaneous velocity distributions for the seed and the tip end showed that there is a very high statistically significant difference ($p<0.0001$) between the seed and the tip measurements for every experiment. Whilst there is a clear reduction in the peak of the histograms at both ends, the reduction at the seed end is greater than the reduction at the tip end, Figure 3.12 B-E. This can clearly be seen as well in the change in variances between the two distributions, Table 3.3. There is a steady increase in the variance at the seed end as concentration increases, whilst there is little change at the tip end in the variance. This suggests that as tubulin concentration increases there is less variance in the rate of addition of new tubulin-dimers at the growing end.

For each set of curves there is a clear difference between the change in length measured from end to end, and the two curves measured from the fixed point to a single end, Figure 3.12 B-E. The difference measured between the two fitted ends (μ_{seed}, μ_{tip}) contains the error associated with fitting the GEF to both ends. There is also the error associated with the assignment of the fixed point from frame to frame being affected by microscopic drift and microtubule flexing. However, as the same dual-ended GEF fit is used for all of the calculations, the assignment of the fixed point during fitting, determines the length for each of the single ends. As the error associated with the fixed point is included in both IV_{seed} and IV_{tip} measurements. A comparison between IV_{seed} and IV_{tip} is more appropriate than the comparison between IV_{seed} and IV.

When IV_{tip} is compared to the internal control (IV_{seed}) there is a clear positive shift as tubulin concentration increases, Figure 3.12 B-E and Table 3.3 A-B. The entire

distribution is shifted to the right, with a decrease in negative values and an increase in positive values. This is in contradiction to Gardner et al. (2011), who report that there is an increase in negative excursions with an increase in tubulin concentration/growth speed.

Here there is no evidence found that an increase in tubulin concentration has any affect on taper length, or negative excursions. An increase in tubulin concentration does cause an increase in growth velocity. This increase in growth velocity is detectable in a positive shift of microtubule length differences between two consecutive time points.

3.7.2 Analysis of Labelled Dynamic Microtubules in the presence of EB3

To further investigate the lattice neighbourhood model of microtubule dynamics, EB3 is added to the total internal reflection fluorescence microscopy chambers. Microtubules are assembled from GMP-CPP stabilised microtubule seeds as before. The chambers contain a fixed concentration of porcine tubulin (12 μM). Four chambers were imaged in total: control (without EB3); in the presence of 100 nM EB3; and, in the presence of 250 nM EB3. All three chambers contain 12.5% label density. The fourth chamber contains 25% label density. Images were obtained every 500 ms for 600 time points. The exposure time was 300 ms. SNR was measured at 8, 9, 9 and 13 respectively.

Analysis was carried out as before. The same restriction was applied to velocity, instantaneous velocities and taper to reduce data size and remove outliers. Individual time points with velocity greater than 0 and less than 40 nm/s, instantaneous velocities between -480 nm and +480 nm and taper between 0 and 500 nm were included. This restriction lead to the total number of individual time points analysed as 2,476, 3,747, 9,457 and 16,482 for control, 100 nM EB3, 250 nM EB3, and double label respectively.

The resulting cumulative distribution functions for the three parameters (instantaneous velocity, microtubule taper and average velocity) are plotted, Figure 3.14. As expected

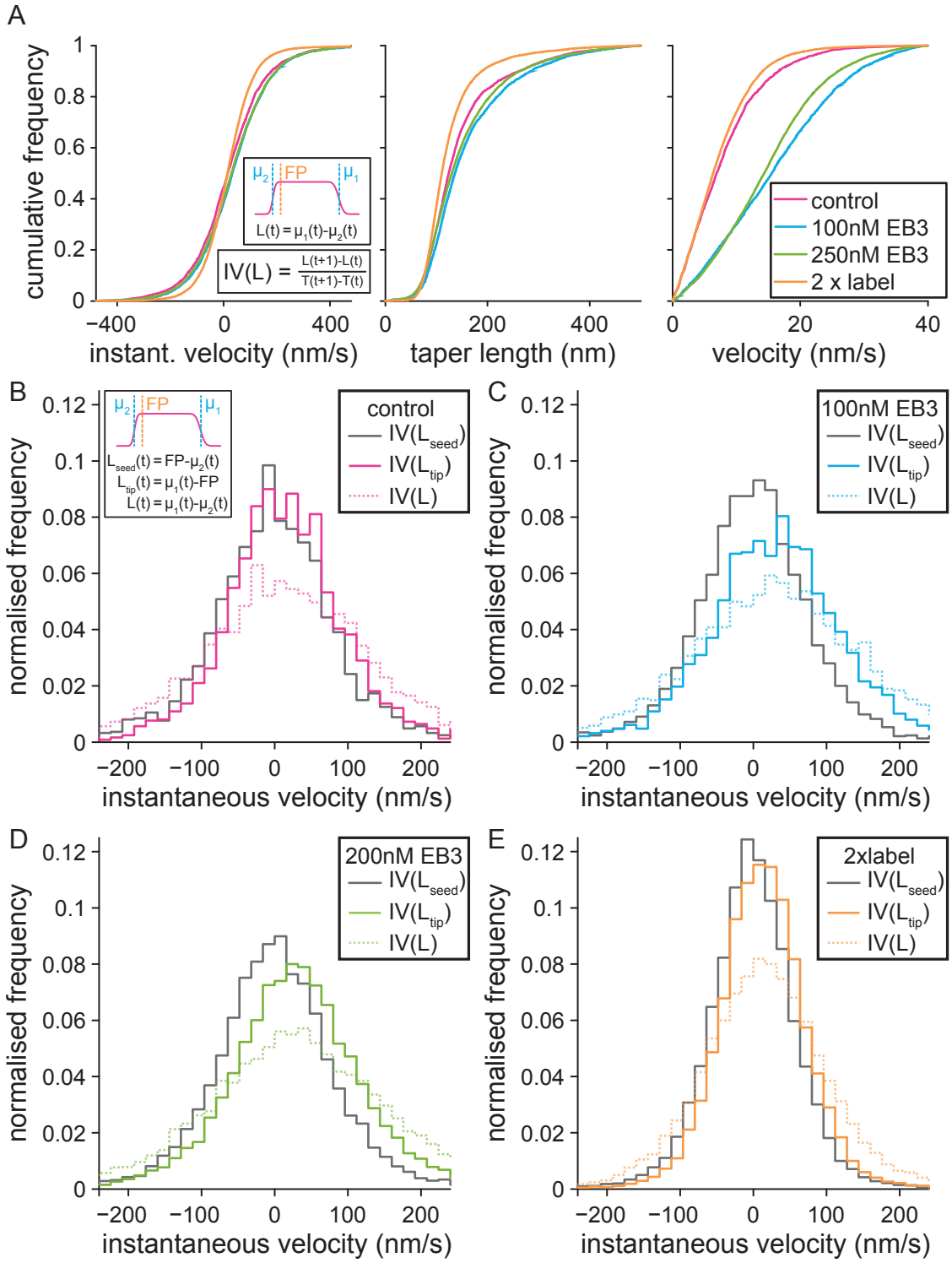

Figure 3.14: **EB3 induces a change in microtubule tip structure:** Tubulin concentration was fixed at 15 μM. Four chambers were imaged, three with 12% label, one with 25% label. The three with 12% label were control, 100 nM EB3 and 250 nM EB3. (A) cumulative frequency graphs for: Left: instantaneous velocity (IV) - the length difference between two consecutive time points divided by the time difference between those time points. Inset shows cartoons of the equation used and cartoon of GEF fit (FP is the fixed point). Centre: taper length graph - σ_1; and right: velocity - calculated as the gradient through 5 consecutive values for $\mu_1 - FP$. (B-E) Individual graphs for IV for each concentration. Comparison between IV values measured in three separate ways. $IV(L_{\text{seed}})$ (control) is the change between the fixed point and the position of the seed end μ_2. $IV(L_{\text{tip}})$ is the change between the fixed point and the position of the tip end μ_1. $IV(L)$ is the change in difference between μ_1 and μ_2.

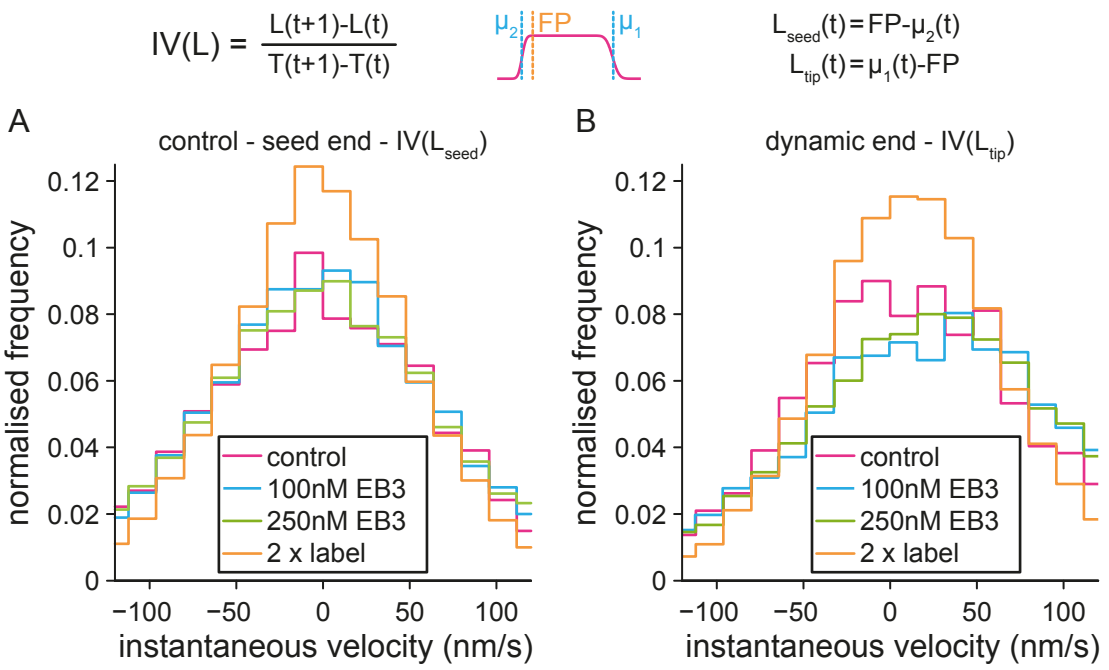

Figure 3.15: **Comparison of the effect of EB3 on microtubule tip structure:** Replot of the instantaneous velocities from Figure 3.14 B-E grouped by microtubule end instead of experimental condition. Top: the equations on the left are used to calculate the instantaneous velocity (IV). Cartoon shows the locations of the values for the microtubule seed end (μ_2), the fixed point (FP) on the microtubule and the dynamic end (μ_1). The equation on the right shows the how the microtubule length (L) is calculated for each end. (A) shows the comparison for the seed end (B) shows the comparison for the dynamic end

these bounds have no effects on limiting data by IV or taper length with both curves asymptotic at their limits. The velocity curves show a clear increase in growth speed between the control curve and the curves with EB protein. There is also a clear increase in taper between control and EB containing curves. As before this difference appears to disappear when looking at the instantaneous velocities. However, this is misleading due to the limits imposed on the axis, the instantaneous velocities are examined in more detail below. A simple t-test between the different distributions shows that there is a statistically significant difference between the experiments containing EB3 and the controls, but not between control and 2xlabel or 100 nM EB3 and 250 nM EB3, Table 3.3 C.

Additionally, as well as comparing to EB3, the control can be compared to the double label curve. As expected the double label curve with its higher SNR has less variance and similar mean for end-to-end length changes. There is a greater difference in the taper length measurements as the distribution has a smaller mean, and a much smaller

variance. Interestingly, the increase in label has a decreased effect on growth speed, but given that this tubulin is from a different purification and source, a small different is not unexpected.

In order to more closely examine the differences in the IV values, IV and IV_{tip} are again plotted as histograms against control IV_{seed} as before, Figure 3.14 B-E and Table 3.3 D. Compared to control, the IV curves for the EB3 experiments show an increase in variance of the data at the microtubule tip, but a decrease at the seed end. For all curves there is a statistical significant difference ($p<0.0001$ in all cases) between the seed end and the microtubule tip end. The EB3 curves both show a strong positive shift. This correlates strongly with the increase in growth speed. Although given the strong shift there is little difference between the seed end and tip end at negative values when EB3 is present. There is a difference observable for control between the two curves at large negative IV values. This suggests that there might an increase in negative growth events for EB3. As predicted, by the lattice neighbourhood model, an increase in growth speed leads to an increase in taper and an increase in shortening events. This appears to be true as for the EB3 experiments there is an increase in growth speed, an increase in taper length, and there is an increase in the number of large negative IV values.

All three seed ends (control, and both EBs) have their peak height between 0.09-0.10. The peak height of the double label histogram is $\sim$ 0.125. The peak height of the corresponding histogram for IV_{tip} is $\sim$0.11 and is clearly shifted to the right, positively. This shows that as expected an increase in label leads to an increase in accuracy/decrease in noise in the measured values.

Here it is observed that there is a clear increase in taper with the addition of EB3 to the assay when compared to control. There is no sign of there being an EB3 concentration effect at the concentrations used. However, both EB3 concentrations are above endogenous EB3 concentrations and this may explain why no concentration effect was seen, as EB3 had reached its maximum potency level. This experiment was repeated but the same effect for EB3 inducing an increase in taper was not seen. As expected an increase in SNR reduces the variance (or error) associated with the experiment.

3.8 Discussion

This chapter began with describing an entirely new methodology for fitting a Gaussian Error Function (GEF) to a microtubule from a total internal reflection fluorescence image. Significant changes were implemented to an existing method for fitting the GEF such that very little similarity remains. The new methodology improves efficiency by allowing multiple microtubules from multiple images to be selected before any fitting of the microtubule is processed. Microtubules are allowed limited flexibility during growth, increasing the number of microtubules available for the code to process. By fitting a dual-ended GEF it was possible to get an accurate seed to tip measurement independent of microscope drift or vibration. Additionally, capability was added for the extraction of intensity along the microtubule in multiple imaging channels. The entire tool was collated into a user-friendlier package.

The method was analysed for sensitivity to various imaging conditions by creating artificial images of microtubules. The artificial images were matched to parameters extracted from measurements made on images from dynamic microtubules imaged using a TIRF microscope. To investigate sensitivity to different parameters, label density and signal to noise ratio was varied over a large range. These two conditions were chosen as they were considered to be most likely to affect the accuracy of the results, but additional as they were the two parameters that could be optimised by changing experimental conditions. It was discovered, that except at very low label percentages, there was no real improvement to increasing the label density. Where as changing SNR had a dramatic effect on accuracy of fitting the GEF to synthetic image of microtubules. These two experiments cannot be directly compared as having a SNR of 6 biased the label density experiment. A fairer comparison would have been to set the SNR to 15 allowing for a greater possible improvement in error with increasing label percentage. In reality it is impossible to separate these two variables as they are linked. For the same exposure time, an increase in label density will also increase the SNR, and therefore accuracy of fitting to the microtubule tip.

	Measured using	Associated Protein	Fluorophore	Temperature (°C)	Nucleotide	Tubulin Conc (μM)	Growth Speed (nm/s)	Taper Change	Negative Excursions
This Study	GEF	N/A	HyLyte 488	25	GTP	8-15	8-17	No	No
		EB3				12	13-35	Yes	No
Gardner et al. (2011)	GEF	N/A	Alexa 488	27	GMP-CPP	0.8-1.5	1.9-1.8	Yes	Yes
					GTP	7-12	5.7-10.7	Yes	Not mentoned
Maurer et al. (2014)	GEF	EB1	Cy5	30	GTP	11-38	49-95	No	Not examined
		XMAP215					55-105	No	Not examined
Schek et al. (2007)	Laser Tweezers	N/A	N/A	36	GMP-CPP	5		N/A	Yes
					GTP	5	6-10	N/A	Yes
Kerssemakers et al. (2006)	Laser Tweezers	N/A	N/A	25	GTP	20	18.3	N/A	Not Mentioned/ Observable

Table 3.4: **Summary of published results:** Comparison of this study with other published results looking at shortening excursion and microtubule taper. Experiments form two types. The first experiment types are those that have used a Gaussian Error Function (GEF) in order to measure microtubule end position and microtubule taper. The second experiment type have used laser tweezers in order to accurately measure the end of the microtubule.

The algorithm was then used to measure changes to dynamic microtubules as tubulin concentration is increased. Whilst an increase in tubulin concentration led to an increase in growth speed, there was no change to taper length nor was there an increase in negative excursions as shown in Gardner et al. (2011). Taper length has been shown to be correlated to tubulin concentration, and hence growth rate (Gardner et al., 2011). Our inability to observe changes in microtubule tip structure when changing tubulin concentration may be down to not using a range of tubulin large enough to promote growth speed differences. As our experiments are at a relatively low tubulin concentration, the microtubule growth speed and hence any resultant microtubule structure change might be below the detectable taper limit of $\sim$200 nm. Indeed when EB3 was added a larger change in growth speed occurred and an increase in microtubule taper was observed.

Our experiments failed to confirm the existence of negative excursions (Gardner et al., 2011; Schek et al., 2007). Whilst there is no clear answer to explain this, the difference in microtubule dynamics and imaging temperatures might play a part, Table 3.4. We believe that using the dark GMP-CPP seed, dynamic microtubule boundary provides a more accurate control for changes in microtubule length. Gardner et al. (2011) used fixed microtubules as their control. Additionally we believe that the act of creating fixed microtubules has the potential to dilute the free tubulin concentration in solution, thereby increasing SNR. As seen in the results here, where the control exhibits a decrease in peak height and an increase in standard deviation as the amount of free fluorophores (tubulin concentration) increases. Removing any of the free fluorophores to create a control removes some of the experimental error, creating an unrealistic control.

Two different concentrations of EB3 were also examined at a fixed tubulin concentration. EB3 was found to increase the taper length at the microtubule tip. Unfortunately a repeat experiment failed to confirm previously observed results. The ability of EB3 to promote microtubule taper length is in agreement with literature, where the addition of EB1 at a fixed free tubulin concentration saw an increase in the size of the end structure at the microtubule plus end (Vitre et al., 2008). Vitre et al. (2008) also reported a reduction in microtubule tip structure size for similar MT growth speeds. To obtain similar growth speed the tubulin concentration was reduced for the EB1 containing experiments.

This is in agreement with Maurer et al. (2014) where at similar microtubule growth speeds, an increase in EB1 concentration promotes maturation of the microtubule tip structure. Maurer et al. (2014) did not detect any change in taper, but a reduction in the distance between the microtubule tip and the peak EB signal was observed at higher EB concentrations, Table 3.4. Gardner et al. (2011) predict that an increase in microtubule growth speed would present an increase in microtubule taper, and an increase in the dissociation rate.

The addition of EB3 changes the microtubule growth speed by a significant amount for taper changes to be detected. As EB1 reduces taper length at fixed speeds it is likely that the change in tip structure is a direct effect of an increase in growth speed and not EB ability. Strangely the ability of EB1 to reduce microtubule taper at a fixed growth speed, provides an explanation for it to increase growth speed. One would presume that in order to reduce taper, EB1 is able to prohibit dissociation of tubulin dimers from shorter protofilaments. By prohibiting dissociation this would naturally reduce microtubule taper length. However, at a fixed tubulin concentration this small inhibition of dissociation will have a small but significant effect on the microtubule growth rate thereby increasing microtubule growth speed (Gardner et al., 2011).

Additionally, the 2D model of microtubule dynamics predicts an increase in dissociation rate with an increase in growth speed. As we think that EB1/3 stabilise shorter protofilaments, decreasing the dissociation rate it will need to be carefully validated at fixed microtubule growth speeds. This stabilisation does not help in providing an answer to how EB3 was able to promote catastrophe as well as microtubule growth. A possible explanation could be provided for by the observation that EB1 promotes a maturation step within the microtubule lattice (Maurer et al., 2014; Zhang et al., 2015). By increasing the maturation rate, the size of the stabilising GTP cap at the tip of the microtubule was likely decreased. This decreased cap reduces the tolerance for shortening events, or pause events, during microtubule growth, leaving the microtubule more susceptible to catastrophe.

Chapter 4

Mammalian EB's bind to distinct sites on the microtubule lattice in vitro

4.1 Introduction

Mammalian cells express three members of the End Binding (EB) microtubule associated protein (MAP) family of proteins. EB1 has had homologues identified in all other Eukaryotes, with most Eukaryotes only expressing the EB1 variant (des Georges et al., 2008; Juwana et al., 1999; Tirnauer et al., 1999; Rehberg and Gräf, 2002; Beinhauer et al., 1997). This raises the question as to why mammalian cells express three EB proteins?

Cellular based studies have shown that whilst EB1 is ubiquitously expressed, EB2 and EB3 are differentially regulated (Straube and Merdes, 2007; Nakagawa et al., 2000; Goldspink et al., 2013). EB1 and EB3 have been indicated in specific roles within the cellular environment, (Komarova et al., 2005; Ferreira et al., 2013). Komarova et al. (2009) showed that EB2 binds further from the microtubule tip in a diffuse pattern. Unpublished results from the Straube Lab show the same result for EB2, Section A.2.

However, EB1 and EB3 also have differential binding locations, Section A.2. EB1 is found binding closest to the microtubule tip and EB2 furthest from the tip, sandwiching EB3 in the middle. EB2 has a distinctly different profile to EB1 and EB3, as EB2 is more dispersed along the lattice without the standard EB comet shape seen with EB1 and EB3. Here we aim to determine whether this differentiable binding is due to inherent binding properties of the EB proteins.

To investigate this, EB1, EB2 and EB3 were re-combinantly expressed as GFP-6xHis fusions and purified. The proteins were then added to imaging chambers containing dynamic microtubules for imaging on a total internal reflection fluorescence (TIRF) microscope. Experiments were carried out to carefully investigate differences in shape of the comet and localisation relative to the microtubule tip between the members of the mammalian EB family. To enable careful investigation sub-pixel image analysis methods were developed for custom analysis in each case. For experiments involving a labelled microtubule the analysis algorithm developed in the previous chapter was used as a base for custom analysis scripts to be developed from.

4.2 Purification of EB1, EB2 and EB3

In order to examine in detail intrinsic differences between different members of the EB family, recombinant EB1, EB2 and EB3, with either a GFP or mCherry fluorophore fused to the C-terminal were purified. The Straube labs standard protocol for EB purification for use in in-vitro TIRF microscopy reconstitution assays, involved affinity chromatography using a HIS-tag followed by size exclusion chromatography. To maximise the distance between the HIS affinity tag and the EB microtubule-binding domain, the tag was located on the C-terminal of the fluorophore. Size exclusion chromatography resulted in relatively pure EB1, however following a lab move and change in equipment there were impurities noticed in the purification for EB2 and EB3. From gels of the purified protein, there is a protein band visible just above the purified versions of EB1 and EB3 at around 70 kDa, Figure 4.1 B. This band is not visible for EB2, as EB2 has a very similar molecular weight to the observed impurity. Due to the differences in expression levels between EB1, EB2

and EB3, where EB2 was the lowest, this unknown impurity began to dominate the EB2 peak. A western blot showed that the proportion of GFP positive protein was significantly less than the amount of protein present.

In an attempt to remove this impurity the purification of the EB proteins was extended to include an anion-exchange chromatography followed by a cation-exchange chromatography. These additional columns were added to separate out impurities based on there charge. By using both columns and eluting using a salt gradient, impurities with a more positive or negative charge are removed. SP and Q columns were used based on the protocol present by the Goodson lab, (Skube et al., 2010). These additional purification steps removed the majority of the impurities from the protein purification for the GFP proteins, Figure 4.1 D-G, Figure 4.2 A-D. A further benefit from adding the ion exchange chromatography was the elution was obtained in a smaller volume. This removed the need to spin concentrate the protein sample following size exclusion chromatography and reduced the loss of protein associated with protein attaching/precipitating against the membrane of the spin column.

Following purification, all 3 EB-GFP proteins were tested for autonomous plus-end tracking ability and functionality. This was tested using a dynamic microtubule chamber on a TIRF microscope. Preformed HiLyte 647™-labelled GMP-CPP microtubule seeds were attached to a PLL-PEG-50% biotin-passivated glass coverslip via a streptavidin-biotin linker created chambers. To create a dynamic microtubule chamber a tubulin reaction mix supplemented with EB proteins was added to the chamber and the chamber sealed. These chambers showed that all three EB-mCherry and all three EB-GFP proteins showed autonomous plus-end tracking with comet-like distributions at the microtubule tip, Figure 4.3.A-F. All three EB proteins track the microtubule end during microtubule growth and unbind during catastrophe.

4.3 EB1, EB2 and EB3 have the same comet shape

In the cellular environment, EB proteins have different binding locations to each other, but also different binding profiles. This is most noticeable for EB2, whose binding is

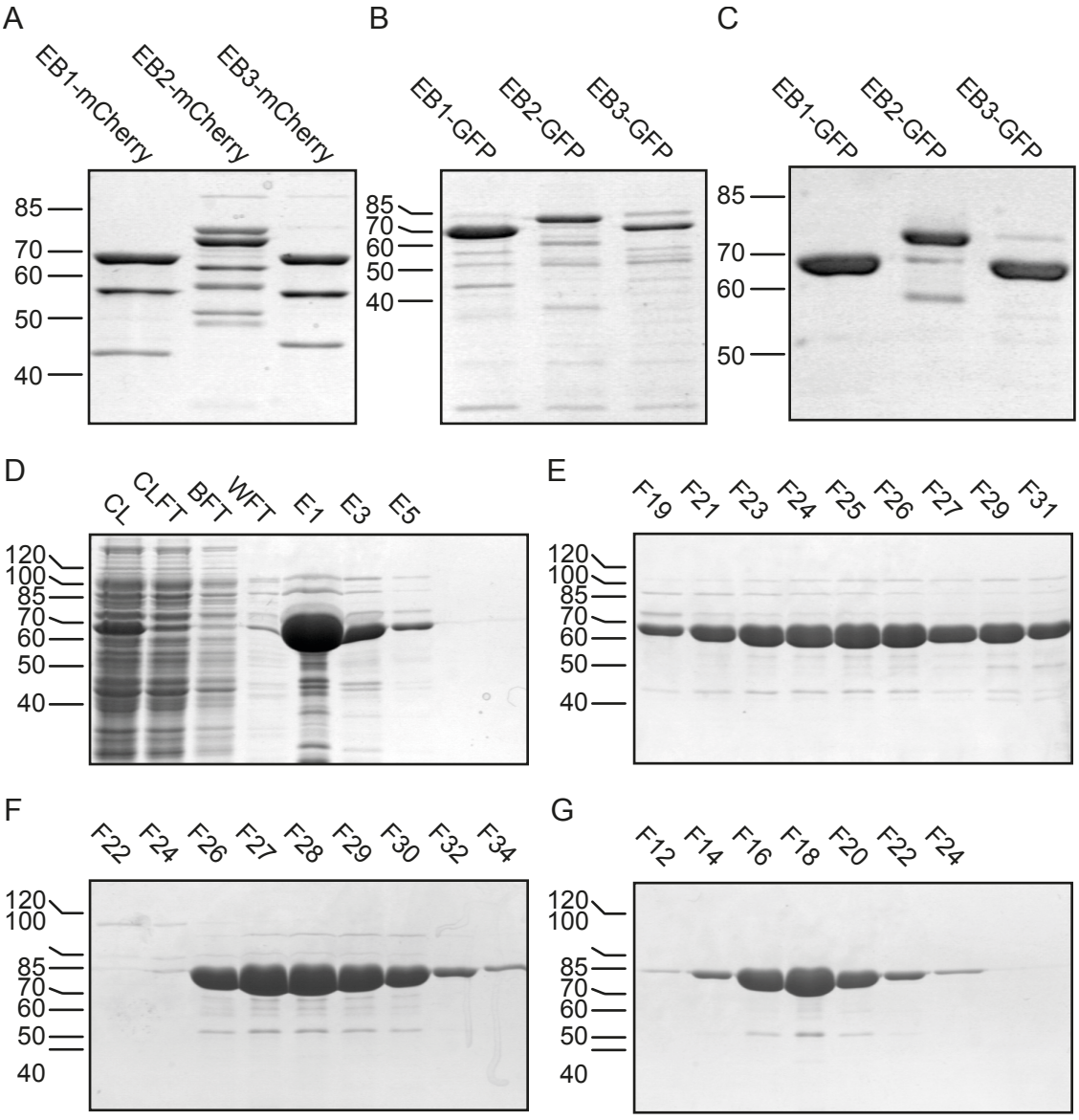

Figure 4.1: **Image of a gel run using Sodium Dodecyl Sulphate Polyacrylamide Gel Electrophoresis showing the Purification Process for EB1:** All gels were stained with SimplyBlue™ Safe Stain (Life Technologies). (A) SDS PAGE gel for EB1, EB2, and EB3-mCherry purified via HIS trap and size exclusion chromatography. (B) SDS PAGE gel of EB1, EB2, and EB3-GFP purified via HIS trap and size exclusion chromatography. (C) SDS PAGE gel of EB1, EB2, and EB3-GFP purified via HIS trap, size exclusion chromatography and affinity chromatography. (D) SDS PAGE Gel showing various stages of the clear lysate and HIS trap purification step for EB1-GFP. CL - clear lysate, CLFT - clear lysate flow through during binding to the HIS column, BFT - binding buffer flow through during wash step of HIS column, WFT - wash buffer flow through during wash step of HIS column, E1,E3 and E5 are elution's one, three and five during elution of HIS column. (E) Size exclusion chromatography elution's, F# - Fraction #. Corresponds to the fraction from Figure 4.2 B. (F) Q affinity column elution's, F# - Fraction #. Corresponds to the fraction from Figure 4.2 C. (G) SP affinity column elution's, F# - Fraction #. Corresponds to the fraction from Figure 4.2 D. Size markers are all in kDa. The omnipresent band at $\sim$50 kDa is believed to be a protein degradation product.

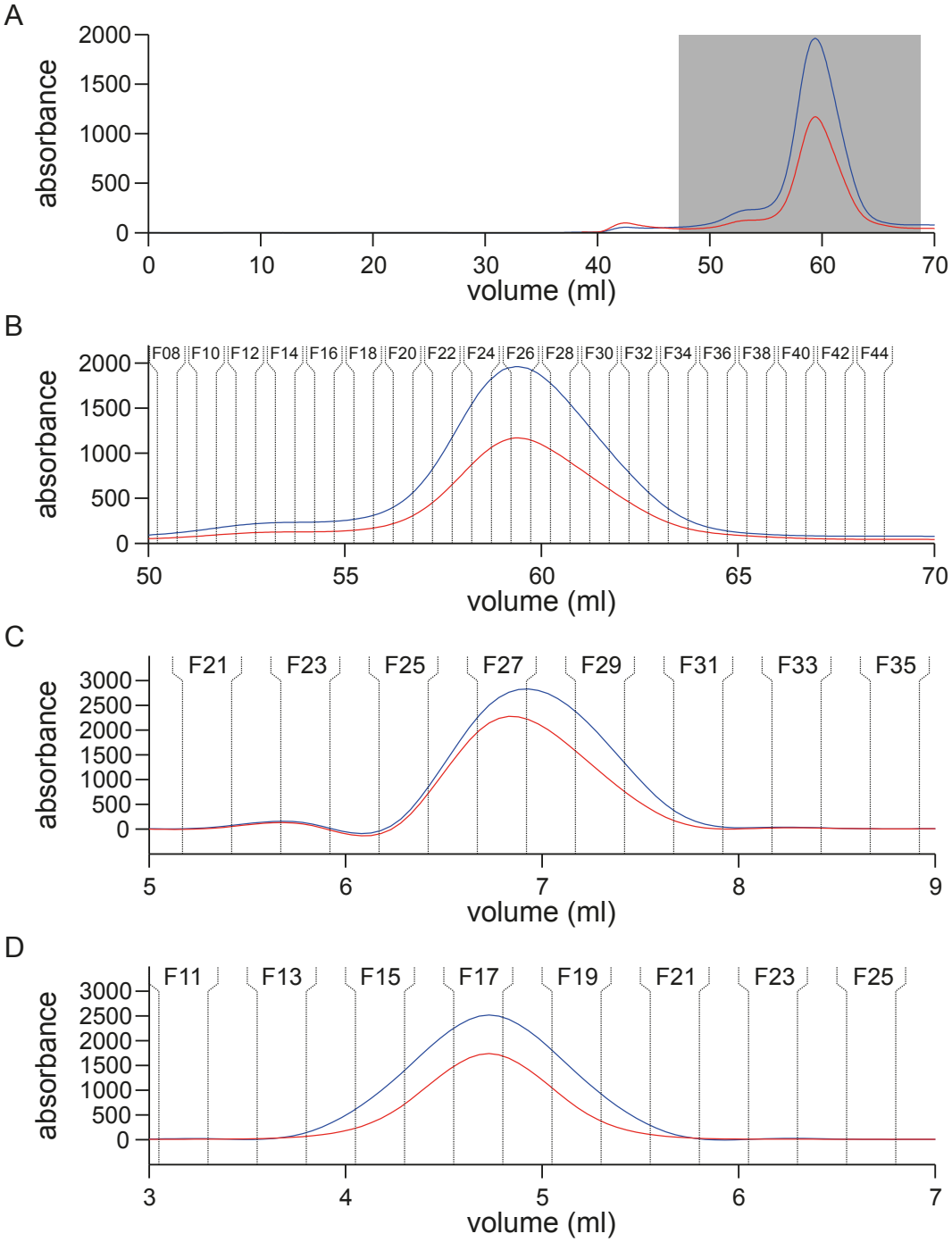

Figure 4.2: **AKTA chromatography profiles for size exclusion and affinity chromatography:** All graphs are off EB1-GFP, corresponds with Figure 4.1 E-G. Blue lines are absorbance at 280 nm, red lines are absorbance at 260 nm. (A) Full elution profile of size exclusion chromatography using a Superdex 200 600/16 column. Grey squared represents the profile shown in (B). (B) Zoomed profile of size exclusion chromatography, F# - Fraction #, Fractions are 0.5 ml each. (C) Profile of SP affinity chromatography F# - Fraction #, Fractions are 0.25 ml each. (D) Profile of Q affinity chromatography F# - Fraction #, Fractions are 0.25 ml each.

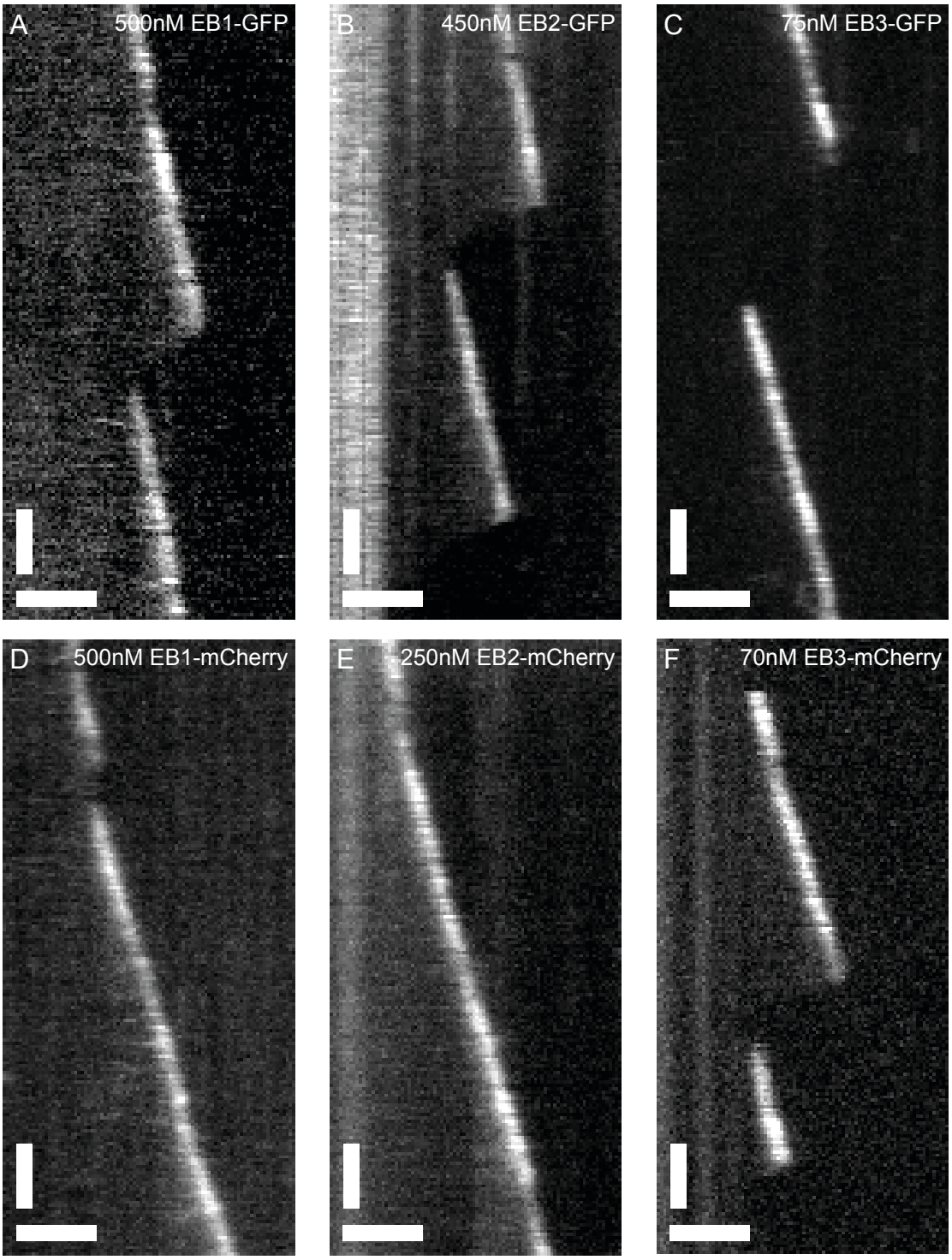

Figure 4.3: **Kymographs showing EB1, EB2 and EB3 -mCherry and GFP fusion proteins tip tracking ability on dynamic microtubules:** Kymographs showing the tip tracking ability of EB1, EB2 and EB3 fusion proteins at various concentration, binding during growth and not present during catastrophe. (A) 500 nM EB1-GFP. (B) 450 nM EB2-GFP. (C) 70 nM EB3-GFP. (D) 500 nM EB1-mCherry. (E) 250 nM EB2-mCherry. (F) 70 nM EB3-mCherry. Time on the y-axis, scale bar 20 s, images obtained every 1 s. Distance on the x-axis, scale bar 2 μm.

distributed over a large region and offset from the microtubule tip, compared to EB1 and EB3. It is interesting to know whether the observed differences in comet shape seen in cells are an inherent property of the EB proteins or due to the large number of accessory proteins found in cells. The large number of accessory proteins could have an effect for two reasons. Firstly, there could be greater competition between the EBs and other +TIP proteins for binding sites. Secondly, the accessory proteins might bind to the different EBs changing their binding kinetics and therefore microtubule tip localisation and binding profile.

To test for the inherent shape of EB comets a range of concentrations for EB1-GFP (100, 200, 400, 600, 800 nM), EB2-GFP (50, 100, 200, 400, 600 nM), and EB3-GFP (20, 50, 100, 200, 400 nM), were added to the dynamic microtubule assay and imaged by TIRF microscopy. Images were obtained every 1 s for 100 s. From the raw image files kymographs were obtained, which were cropped to areas of constant microtubule growth velocity, Figure 4.5.A. In order to analyse these images for comet shape a custom made script/routine was designed in MATLAB.

4.3.1 Comet Shape Analysis

In brief the script averaged the intensity profile of the EB comet over the linear growth region, correcting for growth speed. This created a curve that is referred to as the average 'comet profile'. From this average comet profile the comet area, decay rate, and velocity are extracted.

Kymographs were orientated manually such that time was on the y-axis and that the microtubules grew away from x=0, Figure 4.4.A. As the goal was to align EB comets over linear growth regions, spatial resolution was increased 10-fold to 8.1 nm/pixel by cubic interpolation for each time point, to allow more precise alignment, Figure 4.4.B. The EB comet is initially detected by looking for the last pixel in each row (time point) that is greater than 90% of the maximal value in that row, Figure 4.4 C. The 90% point was used as noise can confuse the exact location of the tip. By picking the 90% point the peak, which was flat and imprecise, was avoided and the top of the comet in front

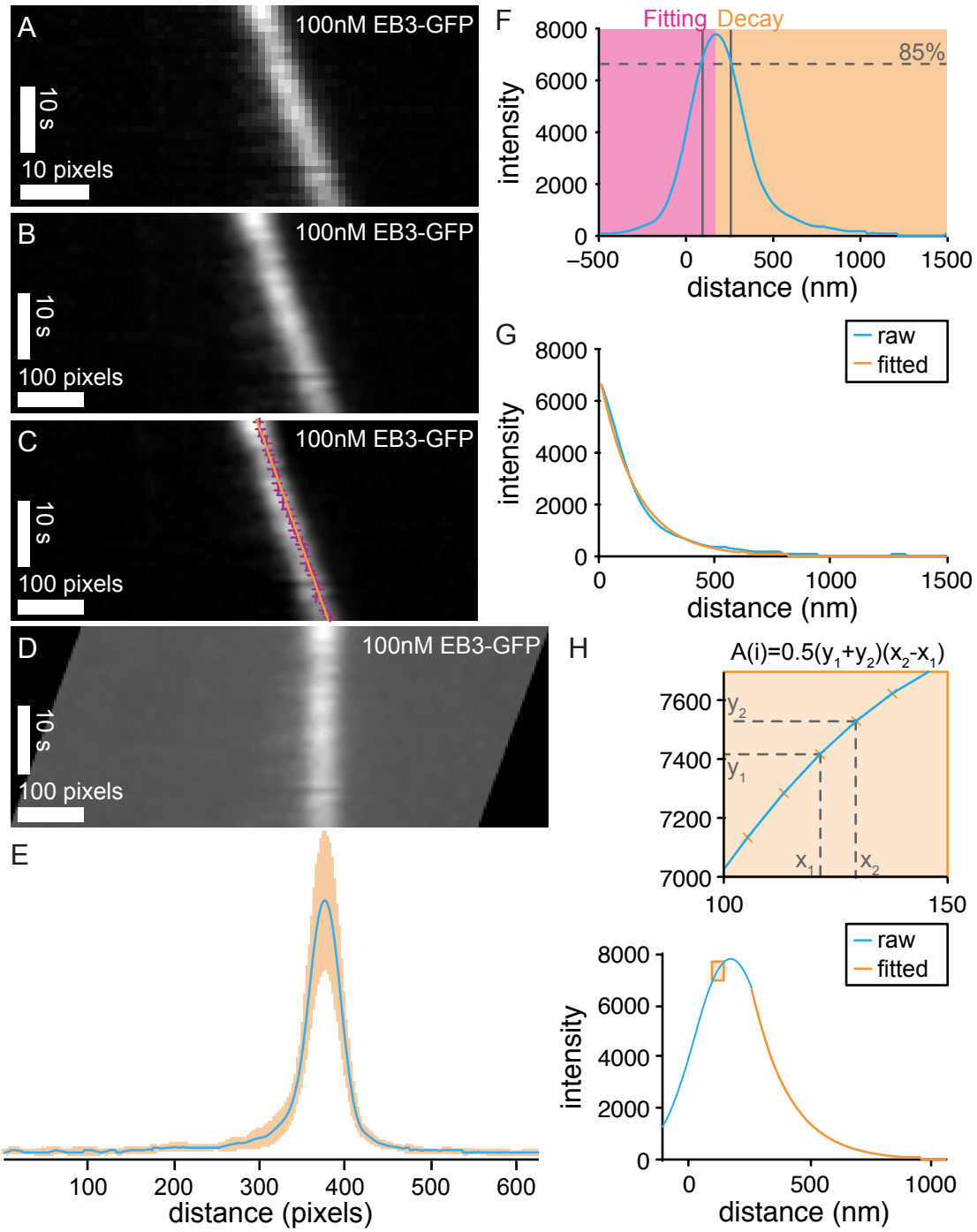

Figure 4.4: **Comet Shape Analysis - Fitting and Averaging:** (A) Kymograph showing a linear growth segment, 100 nM EB3-GFP. (B) Kymograph in (A) cubically interpolated x10 for each row of the image matrix. (C) Kymograph in (B) with magenta crosses as the identification of 90% maximum point, and in orange the fitted linear line. (D) Straightened kymograph from (C) based on the linear fitted line in (C). (E) In blue the time-averaged curve of the intensity from the kymograph shown in (D), the orange shadow is the standard deviation. (F) Same curve, blue, as in E, reflected in the y-axis so that distance increases positively along the microtubule away from the tip, zeroed at the 50% point. Magenta box shows the identification region and orange box the decay region. Solid charcoal lines indicates the 85% intensity, dashed charcoal line indicates the 85% intensity point. (G) Fitting of exponential decay function to time averaged intensity profile, blue is raw data, and orange is the fitted curve. (H) Area under the curve calculations, graph shows raw data in blue and the decaying exponential from the posterior 85% point in orange. Subset orange box shows zoomed curve and calculation by trapezium rule for each section.

of the microtubule tip was selected, where the curve was relatively steep and therefore more precise. Using the 90% maximal points, a linear line was fitted using least squares linear regression. To exclude erroneous high intensity spots in the image field, the fitted line was used as a guide to created a ± 5 pixel (40 nm) confidence interval around the fitted line. The EB comet identification step was repeated, restricting the location of the 90% maximal point to the confidence interval. Again a linear line is fitted to the identified points. The resulting line of best fit was rejected if the residual error was greater than 1 pixel (81 nm). If accepted this line was used as the reference to align EB comet data in time, and the gradient was used for the velocity measurement. The intensity profiles for each time point were shifted such that the nearest pixel (8.1 nm) to the reference line was aligned into a vertical column, Figure 4.4 D. The kymograph was then averaged over time to create an average 'comet profile' over the linear growth period, Figure 4.4 E. The resulting comet profile had its first 50% maximal point set at zero, with distance calculated positively along the microtubule lattice from this point, Figure 4.4 F. This effectively flipped the comet profile, as the background in front of the tip was now closest to the y-axis. The average background before the microtubule tip (negative distance values) was subtracted from the whole comet profile to remove background noise.

From the comet profile three values were calculated. Firstly, the peak width; secondly, the area under the curve, both of the raw and the normalised (maximum intensity equal to one) comet profiles; and thirdly, the value of the half-length of the decay. The area under the curve was representative of the amount of protein bound if non-normalised, or when normalised it was representative of the number of binding sites. The half-length was indicative of the length of the EB binding region.

The peak width was the distance between the first (before the maximal point, background side) and last (after the maximal point, microtubule lattice) data point greater than 85% of the maximum, Figure 4.4 F.

The half-length was calculated by fitting an exponential decay function, $f(x)$ to the data from the posterior 85% point:

$$f(x) = Ae^{mx} + B,$$

where A is the amplitude of the data, B is the background intensity level and m is the decay, Figure 4.4 G. The half-length of the decay, λ, can be calculated as $\lambda = -\ln(2)/m$.

The area under the comet profile was calculated using the trapezoidal rule over two different ranges. Firstly, from the background side of the peak 10% maximal point to the lattice side of the peak 85% maximal point in the decay region of the curve, the averaged intensity values are used. Secondly, from the 85% maximal point onwards the area was calculated based on the theoretical decay as provided by the half-length to avoid inclusion of lattice-bound EB signal. The area was calculated by summing over the theoretical decay for 400 points at 8.1 nm/pixel resolution.

The results were outputted in a comma-delimited file containing protein name, protein concentration, microtubule growth velocity, and the above values. In addition a MATLAB structure is also exported containing the same information as well as the averaged comet profiles.

4.3.2 Comet Shape Results

After analysing the kymographs using the above script, the data from different EB proteins and different concentrations were analysed to test for any comet shape differences associated with these. To normalise, for any effect from differences in growth speed, microtubules were selected with a growth speed of between 15 and 35 nm/s, Figure 4.5 B. This speed range captured the majority of data for each protein concentration. As can be seen from the box and whisker plots there is an effect on growth speed distribution depending upon the EB protein and its concentration. While this graph suggests a direct effect of protein and protein concentration on microtubule growth velocity, it cannot be taken as direct evidence for the size of the effect as data were manually selected and any non-linear growth regions excluded. Plotting each averaged profile, grouped by EB protein, shows an identical profile for the range of concentrations used for each EB, Figure 4.5 C. Any concentration dependence was tested further by looking at how the half-length of comet profiles, and the normalised area under the curve, varied with EB concentration.

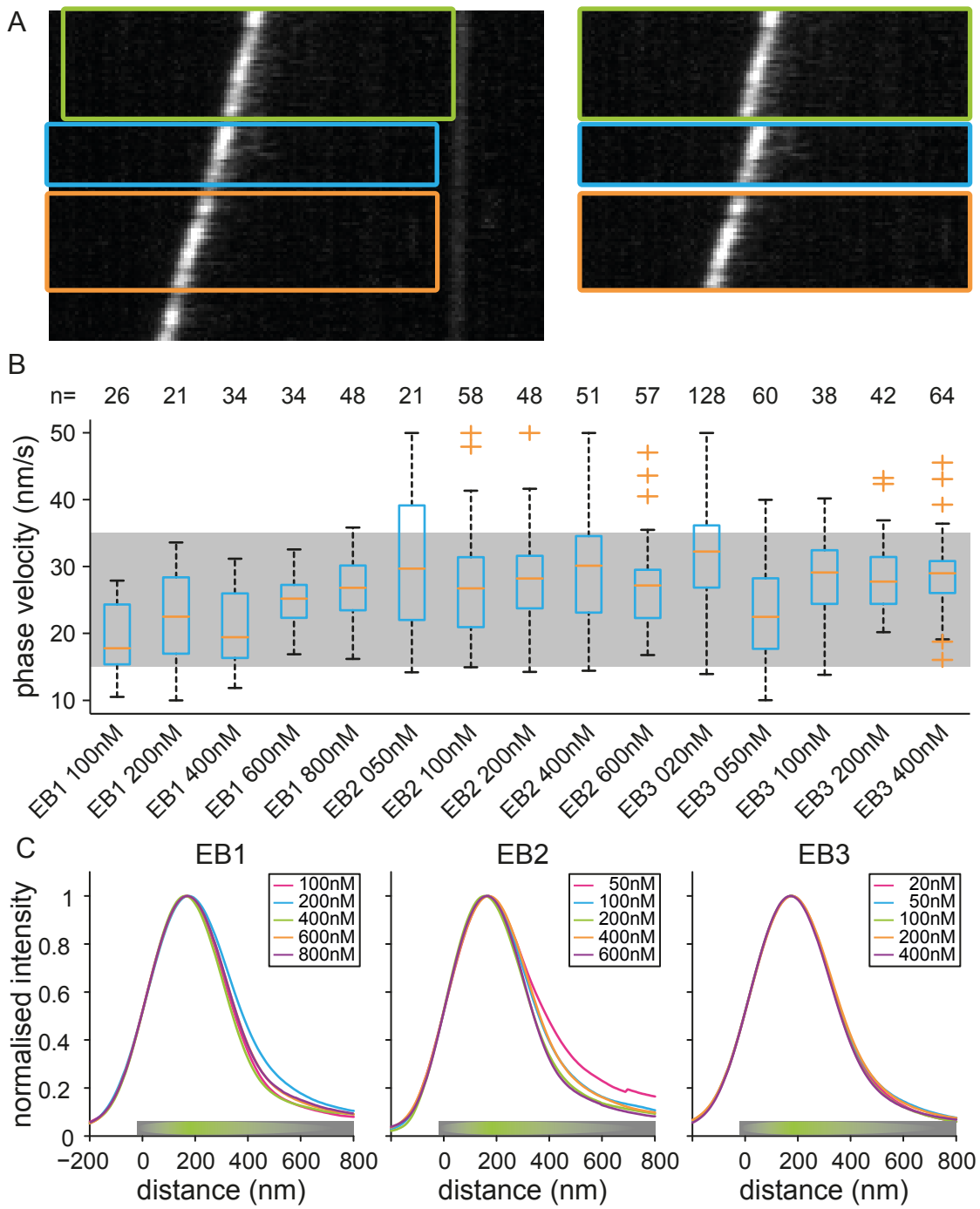

Figure 4.5: **Parameters and Individual EB Shape analysis:** (A) Example EB3-GFP kymograph. Coloured boxes show the cropped regions of interested of linear growth phases. (B) Box plots of velocity distributions of selected cropped linear growth phases, together with n values. Grey rectangles show the range of values used to select EB profile curves for averaging. (C) Averaged EB profiles for EB1, EB2 and EB3 aligned at the 50% anterior maximal point. Each graph shows a range of concentrations, each graph has been normalised for comparison between different concentrations. Cartoon along x-axis shows the direction of the microtubule in grey, with the rough EB position in green.

For each concentration of each EB, the mean and standard deviation is calculated and plotted with error bars, Figure 4.6 E-F. For each protein a mean half-length of $\sim$120 nm and a mean normalised area of $\sim$400 nm was recorded. In each case there was no observable trend for concentration dependence for EB1, EB2 or EB3. Over the range of concentrations tested, it was concluded that EB comet profiles are independent of EB1, EB2 and EB3's concentration.

As the graphs of the half-lengths and normalised areas show no concentration dependence, the different concentrations were pooled together to create an average comet profile for each EB, Figure 4.6 A-C. To test whether there was any difference between the three EBs the average comet profiles were plotted on the same axes, Figure 4.6 D. Again there was no observable difference between the profiles of EB1, EB2 and EB3.

The experiment shows that over the range of concentrations tested, that EB1, EB2 and EB3 concentration is independent of comet shape and size. In addition there is no difference in comet shape between EB1, EB2 and EB3.

4.4 EB Position at the MT tip in relation to each other

Following the discovery that EB proteins have no inherent difference in their comet shape, the question remained as to whether there was any difference in their localisation relative to the tip of the microtubule. To test this, two approaches were taken. Firstly, the distance between the comets of differently fluorescently labelled EB proteins was measured. Secondly, the offset of the EB signal from the tip of the microtubule was measured.

To study the difference between comet positions of EBs, two differently fluorescently labelled EB protein samples were added simultaneously to the dynamic microtubule assay and imaged by TIRF microscopy. The EB1, EB2 and EB3 proteins were used at physiological concentrations. To determine these, whole cell extracts were compared to serial dilutions of purified EB proteins on immunoblots. The endogenous levels in C2C12 myoblasts were estimated at 500nM, 250nM and 70nM respectively for EB1,

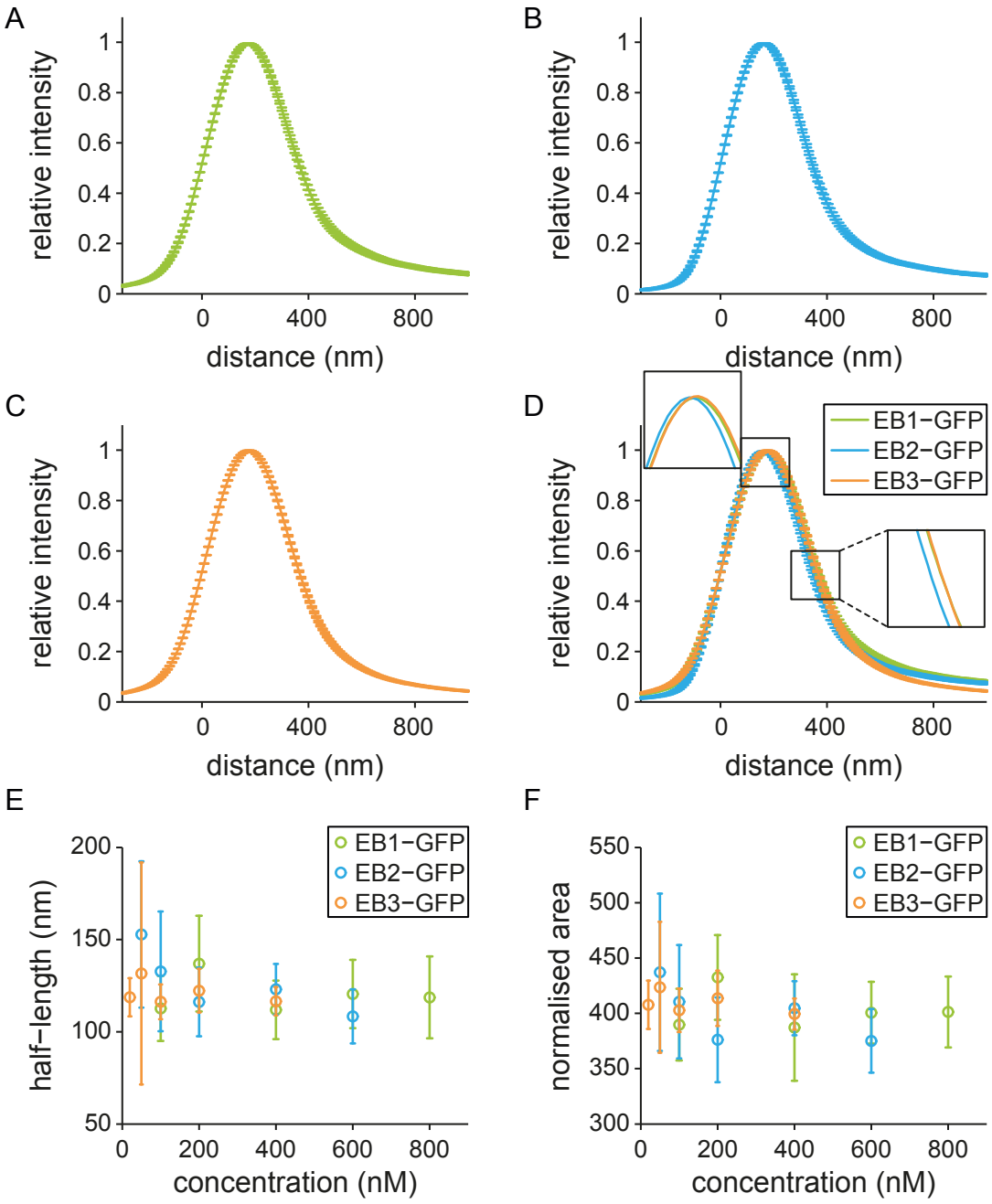

Figure 4.6: **EB Comet Shape Profiles:** (A-C) Averaged profiles across all concentrations for EB123, (A) EB1, (B) EB2, (C) EB3, aligned at the anterior 50% maximal point. (D) Graphs A-C plotted on the same axis for comparison. Insets show a zoomed in look at the difference between the average curve lines (minus the error bars). As can be seen there is very little difference between the averaged curves. (E) Half-length of comet decay plotted for each of the concentrations for EB123-GFP. (F) Area under the normalised peak of the profile curves for different EB123-GFP concentrations. Error bars (A-D) are standard error of the mean, (E-F) are standard deviation.

EB2 and EB3. Due to known negative effect on EB2 binding by competition with EB1 and EB3, 250 nM EB2-GFP had low signal to noise so it was necessary to increase EB2s concentration to 450 nM (Unpublished Straube Lab results). The experiment was conducted by mixing GFP fusion proteins of one EB with mCherry fusion proteins of another EB. In total six different combinations, EB1-mCherry with all 3 EB-GFP variants, and EB3-mCherry with all 3 EB-GFP variants were analysed. Tubulin was held constant at 15 μM, and the temperature at 25°C.

Images were obtained by TIRF microscopy every 500 ms alternating excitation between 561 nm and 488 nm lasers with 300 ms exposure per laser. To remove any possible effect from the imaging order, half of the time series were captured with the 488 nm channel being imaged first, and the other half with the 561 nm channel imaged first. As with the comet shape analysis, kymographs were generated from dynamic microtubules and cropped to linear growth segments. These were analysed by custom designed code in MATLAB as described below.

4.4.1 Dual Comet Analysis

In brief, the script averages the fluorescence intensities from the reference channel over the linear growth regions to generate an average comet profile as before. The transformations from this were passed to the secondary channel. The average comet profiles could then have the distance between the peaks calculated, or be aligned and then super-averaged. For this as each EB-GFP protein was measured against an EB-mCherry protein, the channel excited by the 561 nm laser (i.e. the one that contained the mCherry fluorophores) was set as the reference channel. The channel excited by the 488 nm channel (EB-GFP) was set as the secondary channel.

The code assumes that images are obtained sequentially alternating between the two channels at equal time intervals, Figure 4.7 A. A line ROI was drawn in the reference channel of the raw TIRF image and a kymograph constructed. The ROI was then copied to the secondary channel and a kymograph constructed. The resulting kymographs were cropped to linear growth segment by drawing a rectangular ROI on a composite

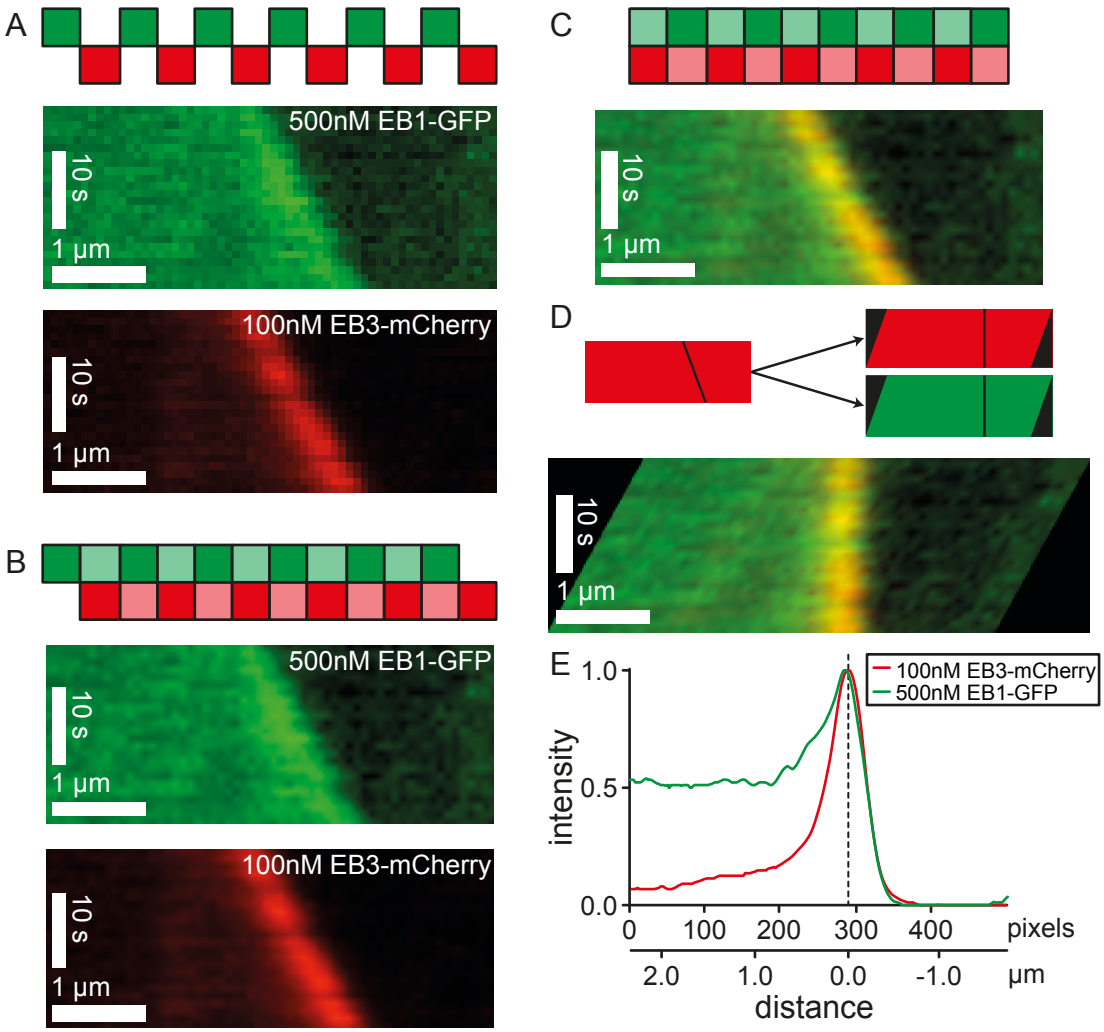

Figure 4.7: **Dual Comet Analysis - Expansion and Averaging:** Green represents the 488 nm excitation and red 561 nm excitation. Example work through of dual comet alignment using 500nM EB1-GFP and 100nM EB3-mCherry viewed using the 488 nm and 561 nm channels respectively. (A) Images are obtained alternatively every 500 ms, kymographs are drawn and cropped to linear growth segments. (B) Kymographs from (A) are interpolated first 10 fold in space, and secondly 2 fold in time, cartoon shaded region represents the interpolated time points. (C) the kymographs from B can now be cropped by removing the first time point from the channel imaged first and the last time point from the channel imaged second. Following cropping the kymographs now represent the same spatial temporal points and can be combined. (D) the comet is detected as in Figure 4.4 in the 561 nm channel. The shift used to straighten the linear growth segment was then applied to both the 488 nm and 561 nm channel. (E) The aligned growth phases are now averaged over time, and for easy comparison normalised so that the max = 1.

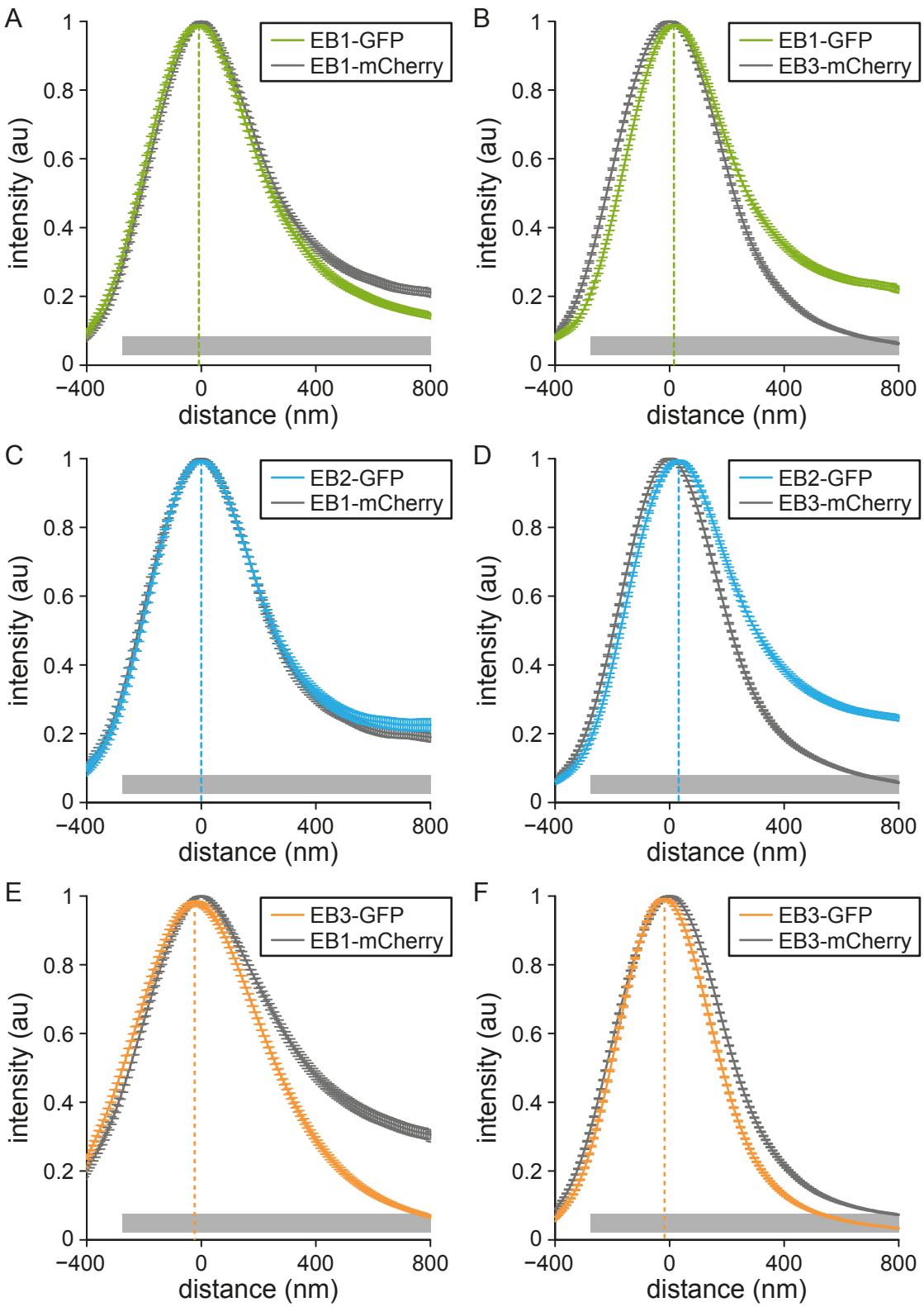

Figure 4.8: **Super-Averaged Intensity profiles of pairwise EB competition experiments:** Caption is on the following page.

Figure 4.8: **Super-Averaged Intensity profiles of pairwise EB competition experiments:** Example comet profiles of a representative experiment were aligned using the peak of the 561 nm channel as the reference point. Each experiment contains two labelled EB proteins. Each of EB1-GFP (A,B), EB2-GFP (C,D) and EB3-GFP (E,F) was mixed with EB1-mCherry (A,C,E) and EB3-mCherry (B,D,F). The intensity profile of the EB-mCherry protein used as a reference for fitting is coloured charcoal. The intensity of the EB-GFP protein is shown in a bright colour. Vertical lines show the peak position of each curve of each of the EB-GFP proteins relative to the EB-mCherry protein which has been aligned with the peak = 0nm. (All) Bar on x-axis shows the direction of the microtubule.

image of the kymographs where both channels showed consistent tip signal. This ROI was copied to the non-composite kymographs and cropped individually. To correct for temporal shift associated with the alternating exposure of the different channels, the cropped kymographs were interpolated 2-fold in time, Figure 4.7 B. The first pixel row was deleted from the channel imaged first, and the last pixel row deleted from the channel imaged second, Figure 4.7 C. The cropped kymograph from the reference channel was passed through the algorithm for single colour kymographs described above, Section 4.3. The transformations applied to the reference channel were stored and then applied to the secondary channel, Figure 4.7 D.

This resulted in two averaged intensity profiles for each linear growth segment, Figure 4.7 E. For each linear growth segment the positional difference between the two EB comet profiles was calculated as the difference between the two peak positions. To obtain an average comet profile for each pairwise combination, all profiles were aligned at the first (i.e. closest to the microtubule tip) half maximal point, in the reference channel. The intensities were then averaged into a super-averaged comet profile.

4.4.2 Dual Comet Results

To study the shifts between the different EB comets, two methods were employed. The first method measured the peak-to-peak distance between the super-averaged profiles, Figure 4.8. The second method measured the peak distances between the profiles from each growth phase. These distances were then plotted as histograms normalised by total count, Figure 4.9. In addition, a Gaussian distribution function was fitted to the histograms and used to determine statistically significant differences between the different experiments.

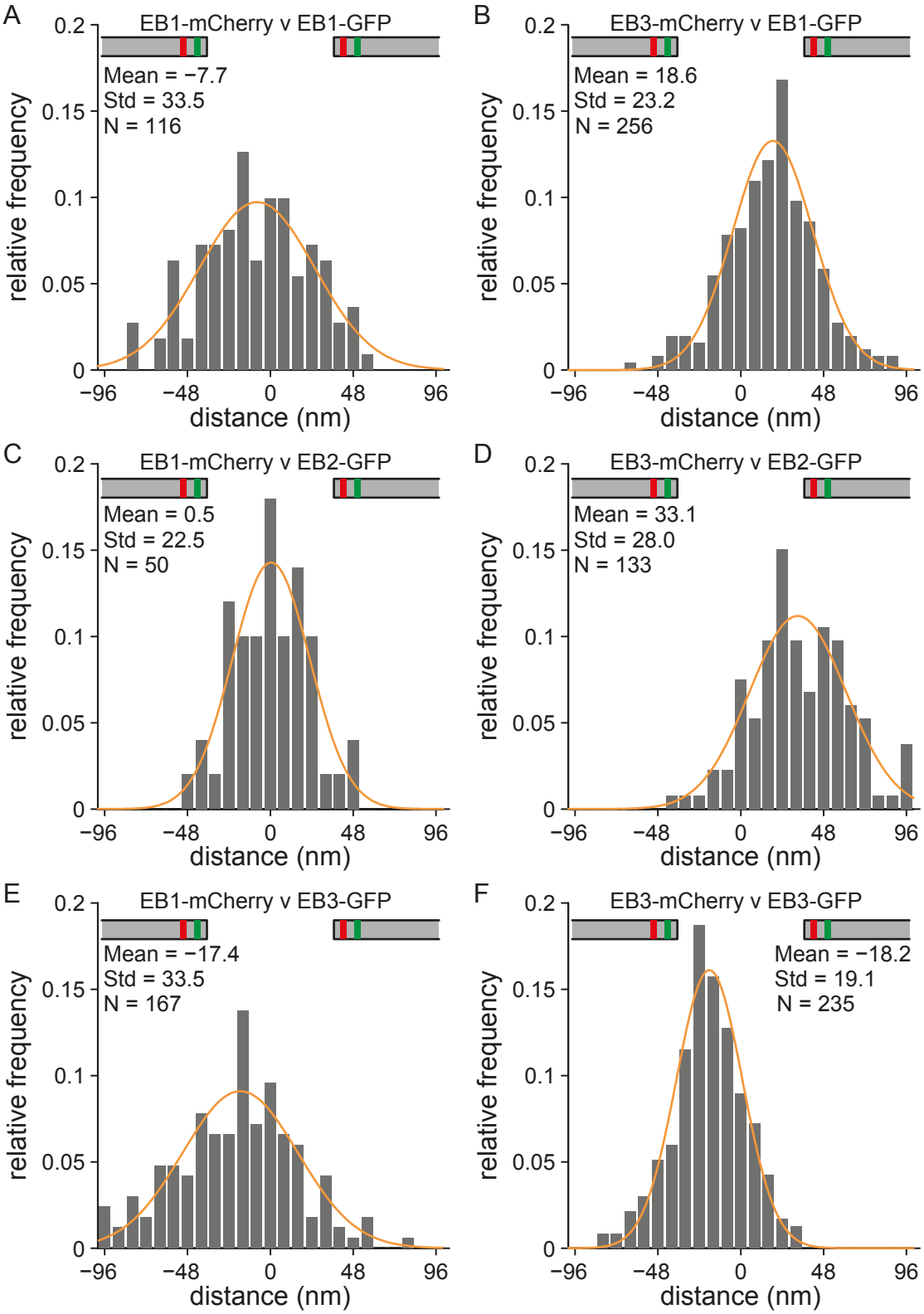

Figure 4.9: **Histograms of the pairwise differences between EB profiles:** Caption is on the following page.

Figure 4.9: **Histograms of the pairwise differences between EB profiles:** Each experiment contains two labelled EB proteins. Each of EB1-GFP (A,B), EB2-GFP (C,D) and EB3-GFP (E,F) was mixed with EB1-mCherry (A,C,E) and EB3-mCherry (B,D,F). Histograms show the differences between the peaks of the average comet profile for each linear growth phase. Histograms have been normalised (total = 1) for easy comparison. Orange line shows a fitted Gaussian to the histograms. Mean and STD are of the fitted Gaussian. (All) Cartoon shows in which order the fluorophores appear based on whether the difference between them is positive of negative, i.e. positive values have the m-Cherry tagged protein at the tip of the microtubule whilst negative values have GFP tagged protein at the tip of the microtubule.

Each protein (EB1, EB2 and EB3 fused to GFP) was compared to EB1-mCherry. For the first method, the distance between the super-averaged comet peaks was 8, 0 and 24 nm respectively, Figure 4.8 A, C, E and Table 4.1 A. When corrected for the internal control (i.e. EB1-GFP) this resulted in EB3 being 16 nm in front of EB1, and EB2 8 nm behind EB1, Table 4.1 B. The second method gave shifts of 8, -1 and 17 nm respectively for EB1, EB2 and EB3, Figure 4.9 A, C, E and Table 4.1 A. Which when corrected gave EB3 as 9 nm in front of EB1, and EB2 as 9 nm behind, Table 4.1 B. Both methods gave a similar distance between the different EBs and the same order of protein being EB3-EB1-EB2. A t-test shows the EB3 peak position to be statistical significantly different from EB1's position ($p = 0.016$), but the distribution of EB2 was not significantly different from EB1's.

Each GFP fusion protein was also compared to EB3-mCherry. For the first method, the distance between the super-averaged comet peaks was 16, 32 and -16 respectively for EB1, EB2 and EB3, Figure 4.8 B, D, F and Table 4.1 A. When corrected for the internal control (i.e. EB3-GFP) this resulted in EB1 being 36 nm behind EB3, and EB2 a further 15 nm behind that 4.1 B. The second method gave shifts of 18, 33 and -18 respectively Figure 4.9 B, D, F and Table 4.1 A. Which when corrected gave EB1 as 36 nm behind EB3, and EB2 as 15 nm behind EB1, Table 4.1 A. EB1 was very statistically significantly different to EB3 and EB2 ($p<0.0001$ in both cases). This gave the same order as before EB3-EB1-EB2 when EB1 was used as the reference channel.

A summary of the difference between using EB1-mCherry as a control and EB3-mCherry as a control can be seen in Table 4.1 C. The values have been converted to represent the number of dimer layers between the peak positions of the relative proteins. In both cases the order observed was EB3 at the tip of the microtubule, EB1 in the middle and

A. Raw Data

	EB1-mCherry as the control		EB3-mCherry as the control	
	Peak to Peak Distance (nm)	Mean of Fitted Gaussians (nm)	Peak to Peak Distance (nm)	Mean of Fitted Gaussians (nm)
EB1-GFP	8	8	16	18
EB2-GFP	0	-1	32	33
EB3-GFP	24	17	-16	-18

B. Adjusted for the control

	EB1-mCherry as the control		EB3-mCherry as the control	
	Peak to Peak Distance (nm)	Mean of Fitted Gaussians (nm)	Peak to Peak Distance (nm)	Mean of Fitted Gaussians (nm)
EB1-GFP	0	0	32	36
EB2-GFP	-8	-9	48	51
EB3-GFP	16	9	0	0

C. Summary

EB1-mCherry	MT tip	EB3-mCherry
	EB3-GFP	
~2 dimers	⬇	4-5 dimers
	EB1-GFP	
~1 dimer	⬇	~2 dimers
	EB2-GFP	

Table 4.1: **Summary of the pairwise EB competition experiments:** Summarises the data from the super-averaged curves and the means of the fitted Gaussians to the individual distances between peaks. Data is summary of that included in Figures 4.8 and 4.9. (A) shows the raw data. (B) is adjusted for the control, the EB-mCherry channel. (C) shows the summary converted into dimers and adjusted to reflect the individual measurements and the super averaged curve.

EB2 furthest along the lattice from the microtubule tip. In all cases the difference between the peaks are statistically significant except for between EB1-GFP and EB2-GFP using EB1-mCherry as a control. When using EB1-mCherry or EB3-mCherry as a control, it is the same protein fused to GFP that acts as the internal control for accuracy of the experiment. For EB1-mCherry v EB1-GFP the difference was 8 nm with a standard deviation of 33 nm, Figure 4.9 A. For EB3-mCherry v EB3-GFP the peak-to-peak distance was greater at 18 nm with a standard deviation of 19 nm, Figure 4.9 F. The reason for the difference between the two controls is unknown. In a separate, stand-alone, EB3-mCherry v EB3-GFP control experiment (not shown as was a one off experiment) the peak to peak difference was found to be 8 nm. As EB3 binds to the microtubule with higher affinity, it is our belief that this, twinned with the smaller standard deviation, makes it a better control for this experiment. It is clear and statistically significant in both

cases that EB3 binds in front of EB1. Whether EB1 binds in front of EB2 or alongside is dependent upon which of the controls is believed. In either case the distance between EB1 and EB2 is at most 16 nm.

4.5 EB localisation relative to the microtubule tip

The differences observed in the EB pairwise mixing experiments could be due to intrinsic properties of the EB, or due to competition between the EBs. To test whether the differences are an intrinsic property of the EB proteins, the EB comet peak location was measured relative to the tip of the microtubule for each protein individually. The experiment involved EB1, EB2 and EB3-mCherry fusion proteins being added to TIRF microscopy chambers containing dynamic HiLyte 488™microtubules, Figure 4.10 A. Three different experimental combinations were analysed. Firstly, EB1, EB2 and EB3-mCherry proteins were used at physiological conditions, 500 nM, 250 nM and 70 nM respectively, at 15% labelled tubulin, 15 μM total tubulin (physiological data set). Secondly, all three EBs were fixed at 100 nM at 15% label, 15 μM tubulin (lower tubulin concentration data set). Thirdly, all three EBs were fixed at 100 nM and to increase any observed shifts, the tubulin concentration was increased to 24 μM tubulin with 9% label (higher tubulin concentration data set). All experiments were repeated three times.

Chambers were imaged every 500 ms, alternating with excitation by 488 nm and 561 nm wavelengths, for 200 seconds. The resulting images were passed through the code described in Section 3.3.3 and Section 3.4. Briefly, user-selected microtubules were extracted from the 488 nm channel and by fitting Gaussians across the microtubule lattice the microtubule was found to a high degree of accuracy in each image frame. The intensities were extracted along the curve fitted to the microtubule lattice in the 488 nm and 561 nm channels. To further analyse the resulting data, custom code was written in MATLAB as below.

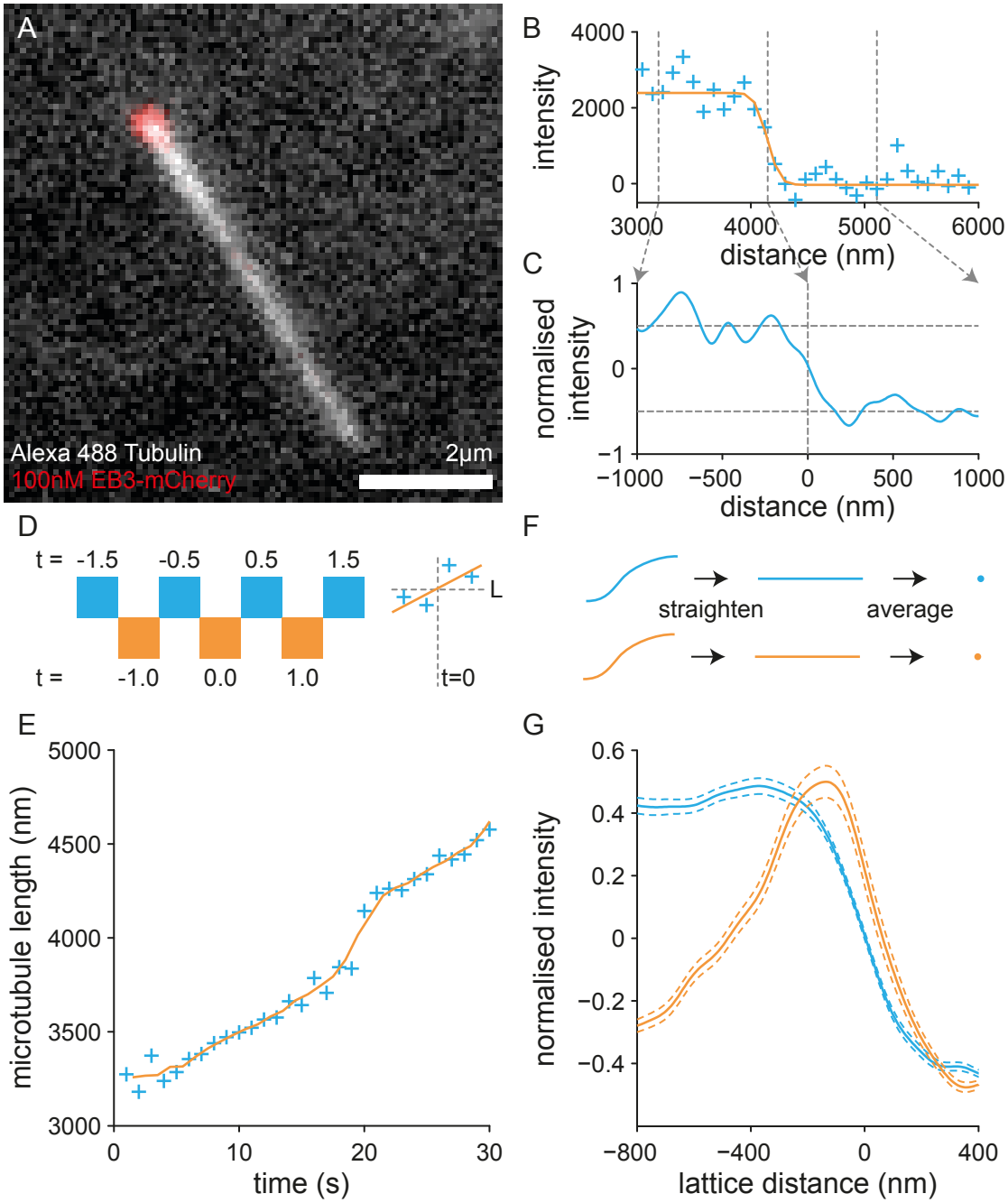

Figure 4.10: **EB peak to MT tip distance calculation:** (A) Instance in time of a Alexa 488 labelled microtubule together with 100 nM EB3-mCherry. (B) Raw microtubule intensity data, (blue crosses) fitted to the decay function (orange). (C) Same raw data (blue) as in (B) normalised using the fitted decay function from (B) to have background at -0.5, and lattice intensity at 0.5. The MT tip is moved to distance = 0. (D) Cartoon showing how the microtubule length is calculated for each image in the EB channel. As the EB/MT channels were imaged sequentially, 0.5 s apart, the end position for the EB channel needs to be calculated by using the microtubule length values (the mean associated to the GEF fit from (B)) from two time points either side. A straight line is fitted through these lengths using t values of (-1.5, -0.5, 0.5, 1.5). The y-intercept of the fitted linear line is taken as the length of the microtubule for that time point in the EB channel. (E) Means (blue) of the fitted GEF function from (B) showing the microtubule length. y-intercepts (orange) of fitted line through four consecutive intensity points as described in (D) . Shown for the first 30 time points out of a 100 second trace. *Caption continued on next page.*

Figure 4.10: **Caption continued:** (F) Cartoon showing how the y-intercepts and microtubule lengths are used to align the microtubule tip to the same value in both channels. In this case x=0 and normalised as shown in (C). The intensities are then averaged over time to create an average comet profile for that time trace. (G) Average profile after summing for a 100 second trace aligned at the mean of the fitted decay function (B,E) for the microtubule intensity (blue) and to the fitted y-intercepts (D,E) for the EB intensity values (orange).

4.5.1 EB localisation Analysis

To the intensities in the 488 nm channel a single ended Gaussian Error Function (GEF) was fitted to extract end positions and taper measurements for each time point, Equation 3.3, Section 3.4.1, Figure 4.10 B. This fit was used for several purposes:

Firstly, the fit from the GEF was used to calculate the instantaneous microtubule growth rates. The growth velocities were calculated for each time point from the 561 nm channel. To calculate the growth velocity four consecutive microtubule length measurements centred on the current time point were used. To these time points a linear line was fitted, the gradient of which was classified as the velocity. The line was fitted using the x-values (-1.5, -0.5, 0.5 1.5) the y-intercept gave the position of the microtubule tip for that time point, Figure 4.10 D and E.

Secondly, the fit from the GEF was used to average the intensity profiles for both the 488 nm and 561 nm channel. Using a fixed 8 nm distance grid (-1000, -992, -984, ..., 1000), the microtubule lattice intensity was interpolated, fixing the microtubule tip at zero for every time point in the 488 nm and 561 nm channel, Figure 4.10 C. For the 488 nm channel the means from the fitted GEF was used as the zero point. For the 561 nm channel the zero point was the y-intercept from the fitted line above. For the 488 nm channel each intensity profile was normalised by subtracting the background (B, Equation 3.3) and dividing by the microtubule intensity (A, Equation 3.3), Figure 4.10 G. This scales the lattices intensity to a mean of 0.5, and the background intensity to a mean of -0.5. The intensity profile was saved for each time point so that there was correlative data for velocity, taper, microtubule intensity profile, EB intensity profile, EB signal to noise, and the difference between EB position and microtubule end. The difference between the microtubule end and the EB position was the location of the peak position on the

interpolated 8 nm pixel grid. EB signal to noise was calculated as the intensity of the EB peak position divided by the standard deviation of the EB intensity trace. The time point from the 488 nm channel was linked with the time point from the 561 nm channel half a second later. For obtaining averaged profiles for each condition, all the images from the 488 nm channel were averaged Figure 4.10 F. For the 561 nm channel the profiles were summed together, divided by the max, before subtracting 0.5, Figure 4.10 G.

4.5.2 EB localisation Results

To ensure that no erroneous fits were included in the analysis the raw individual time point data was restricted by the four calculated quantities described above: EB signal to noise; velocity; taper length; and the difference between MT tip and peak EB signal. For the three different datasets (physiological, lower and higher tubulin) the EB signal to noise ratio needed to have a value greater than 3 to ensure that only EB comets with a good signal were included. The difference between MT tip and EB peak was selected to be between -100 nm and 500 nm for the physiological and lower tubulin concentration datasets and -250 nm and 500 nm for the higher tubulin concentration datasets. The taper length was restricted to be between 20 nm and 250 nm for the physiological and lower tubulin datasets, and 20 nm and 400 nm for the higher tubulin dataset. Velocity was restricted to 10-80 nm/s for the physiological and lower tubulin datasets, and 30-150 nm/s for the higher tubulin datasets. The cumulative distributions for velocity, taper length and difference for the above parameter restrictions are shown in Figure 4.11 A-C.

The datasets were reduced in size so that the three EB proteins could be compared over a similar range of values between experiments. Whilst it would be good for this restriction to remove any differences between the proteins in terms of growth speed and taper, this does not happen. As EB3 has been shown to have a positive effect on growth speed, this should skew the cumulative distributions positively towards larger values. This effect can clearly be seen in the higher tubulin concentration dataset, Figure 4.11 C. However it is barely noticeable in the physiological data set, Figure 4.11 B, and is only present in one of the repeats for the lower tubulin concentration data set, Figure 4.11 A. For all three conditions there is no noticeable trend in the taper length measurements. In the lower

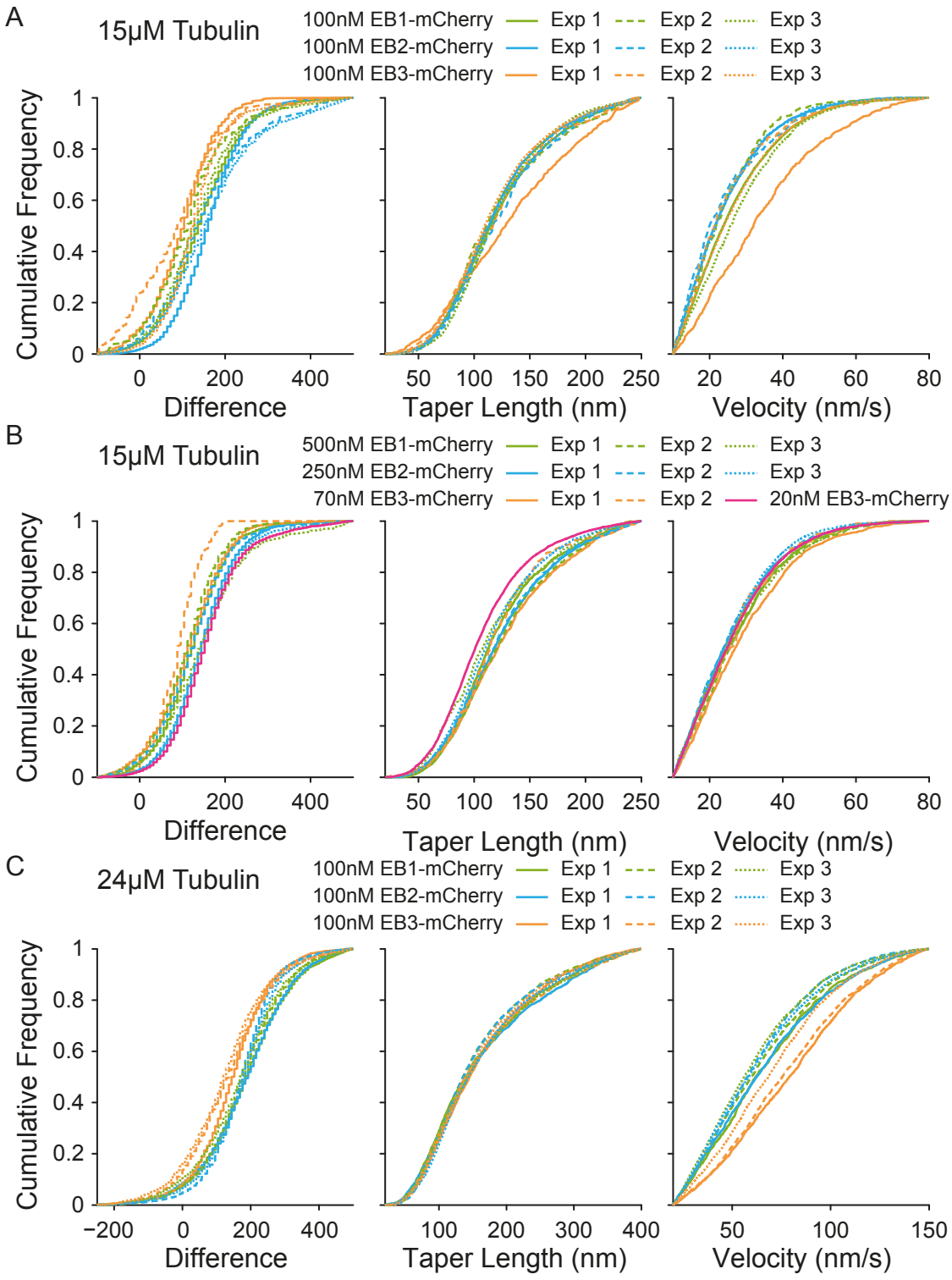

Figure 4.11: **EB peak to MT tip distance calculation measured parameters:** Cumulative distribution plots of individual time points for: (1) the difference between the microtubule tip and the peak of the EB signal; (2) the measured taper length; (3) the velocity of growth of the microtubule calculated as the gradient during EB end position fitting, Figure 4.10 (D). Three experiments are shown: (A) 15 μM tubulin all three EB-mCherry's at 100 nM; (B) 15 μM tubulin EB-mCherry's at endogenously measured concentrations; (C) 24 μM tubulin all three EB-mCherry's at 100 nM. Each experiment has three repeats.

tubulin concentration data set the same repeat of EB3 that was an anomaly for growth speed is distinguishable, giving a larger taper. Why only one of the three chambers shows an increase a noticeable change in growth speed for EB3 is unknown. However it closely aligns with published results in that it shows that an increase in microtubule growth speed leads to an increased taper length (Gardner et al., 2011).

From the cumulative distributions of the difference between microtubule tip and the peak location of the EB signal it appears that EB3 is negatively skewed compared to EB2 and EB1, Figure 4.11. This implies that EB3 is closer to the microtubule tip than EB1 and EB2, though the effect is less clear for the physiological dataset. On average it also appears that EB1 is closer to the microtubule tip than EB2 in the physiological and lower tubulin datasets, although this is lost for the higher tubulin dataset where EB1 and EB2 cannot be separated. To clarify the situation two different methods were employed.

Firstly, the EB intensity profiles were averaged over all time points within the above constraints, with additional restriction on the velocity measurements. The velocity was further constrained to be within 15-35 nm/s for both the physiological and the lower tubulin datasets. For the higher tubulin dataset the velocity range was narrowed to 45-85 nm/s. This selects a linear range in speed for each of the different EB proteins from the cumulative distribution plots of velocity. The averaged EB profiles were then divided by the maximum intensity value, and subtracted by 0.5 to normalise the intensity between -0.5 and 0.5. The resulting curves along with the corresponding averaged microtubule intensity profiles were plotted, Figure 4.12 A,C,E.

Secondly, the data was partitioned based on velocity into 10 nm/s bins based at (10,20,30,40) nm/s for the physiological and lower tubulin datasets, and at (30,40,...,120) nm/s for the higher tubulin dataset. For each bin, the difference between the tip and the EB signal was averaged. Then the mean and standard deviation between the different repeats for each experiment was calculated and plotted, Figure 4.12 B,D,F.

For the lower tubulin dataset there was a clear consensus across both methods of analysis that EB3 was located closest to the microtubule tip, followed by EB1 and then

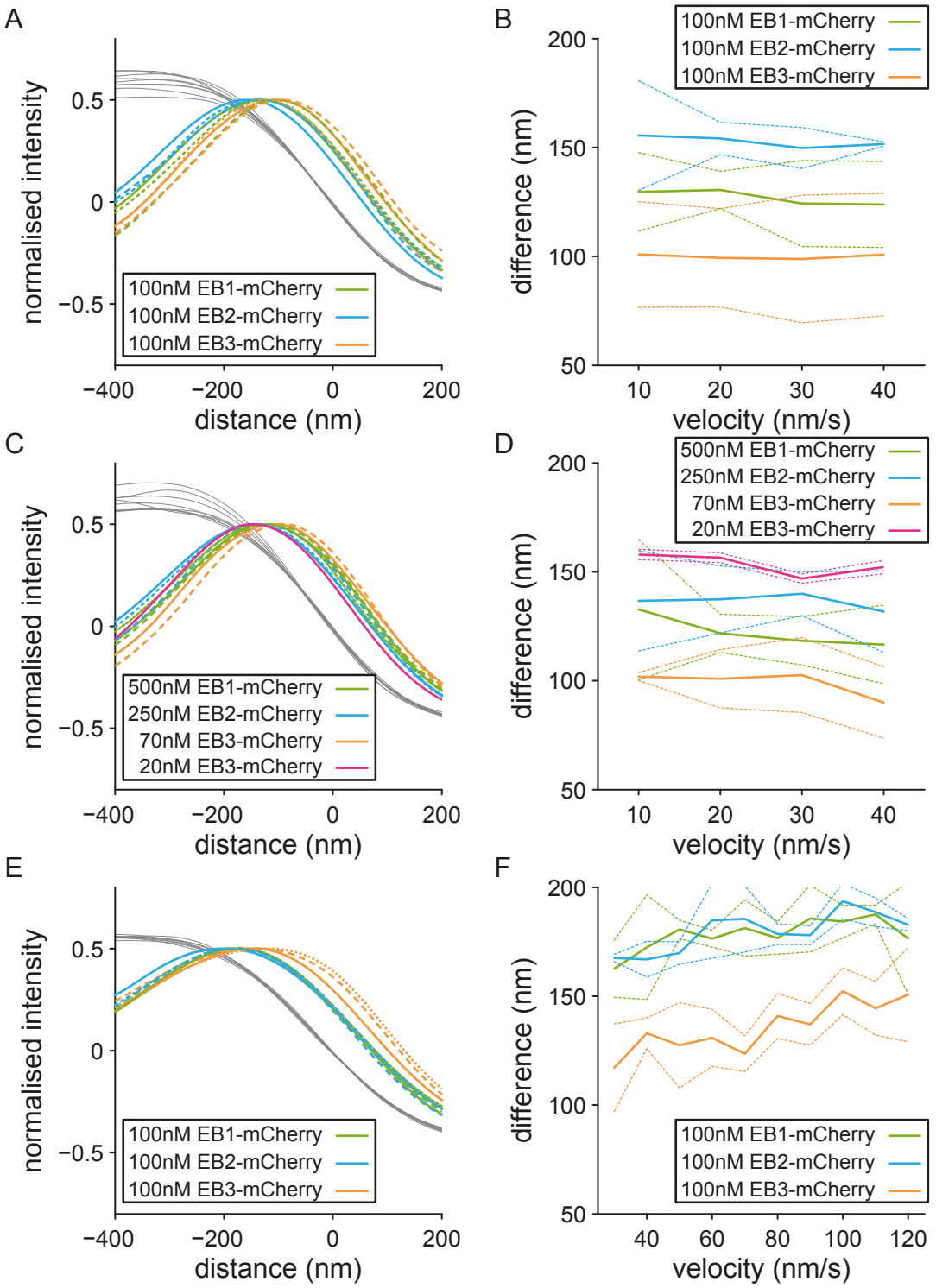

Figure 4.12: **EB peak to MT tip distance calculation results:** Results of the data shown in Figure 4.11. (A,C,E) The averaged EB curves (coloured) and the corresponding microtubule intensity profiles (charcoal). (B, D, F) Distance from the microtubule tip as a function of velocity, data is grouped into 10 nm bins and the shift calculated as the mean of the differences for each time point, error bars are standard deviation except (D) 20 nm EB3-mCherry which is standard error of the mean within that experiment. Three experiments are shown: (A,B) 15 μM tubulin all three EB-mCherry's at 100 nM; (C,D) 15 μM tubulin EB-mCherry's at endogenously measured concentrations; (E,F) 24 μM tubulin all three EB-mCherry's at 100 nM. Each experiment has three repeats (solid - experiment 1, dashed - experiment 2, and dotted - experiment 3).

EB2. This closely follows the trend observed in the velocity binning graphs where EB3 has a mean around ∼100 nm, EB1 at ∼130 nm and EB2 at just over 150 nm. Neither of EB1, EB2 or EB3 showed any speed dependent relationship with the measured difference from the microtubule tip.

For the physiological EB concentration dataset a similar consensus was found as for the lower tubulin concentration dataset, EB3 comes before EB1 with EB2 last. For velocity binning, EB3 was roughly a similar distance away from the microtubule tip as before, ∼100 nm, whilst EB2 and EB1 came closer to the tip 140 nm and 120 nm respectively. Due to a pipetting error one of the chambers only had ∼20 nm EB3-mCherry present. The 20 nm EB3-mCherry location was found more distal from the microtubule tip under both methods of analysis at around 160 nm. EB2 shows no velocity dependent difference. However EB1, and both concentrations of EB3 have a very slight negative correlation.

For the higher tubulin dataset there is a much larger variation in microtubule growth speed. The average microtubule growth speed increases from 20-25 nm/s to being 60-80 nm/s depending upon EB protein. As before EB3 was the least distant from the microtubule tip of the three EB proteins. This time though there was no measurable difference between EB1 and EB2 in either the averaged EB comet profiles or when binned by velocity. However, unlike the lower tubulin concentration and physiological EB concentration datasets, there was a definite trend of the distance from the tip increasing with increased microtubule growth speed for all three EB proteins.

This set of experiments and the EB competition experiments gave the same result, EB3 binds closest to the microtubule tip, and EB1 and EB2 further away. Depending upon the experiment either EB1 was between EB3 and EB2, or it localises in a very similar location to EB2. This reinforces the differences observed in experiments reported in the competition experiment and rules out the possibility of competition between the EB proteins being responsible.

EB Peak to Peak Experiment			EB from MT tip experiment		
EB1-mCherry	EB3-mCherry	MT tip	15μM Tub 100nM EB	15μM Tub physio. EB	24μM Tub 100nM EB
~2 dimers	4-5 dimers	EB3-GFP ⬇ EB1-GFP	~3 dimers	~3 dimers	~6 dimers
~1 dimer	~2 dimers	⬇ EB2-GFP	~3-4 dimers	~2 dimers	~0-1 dimers

Table 4.2: **Summary of the two experiments looking at the distance between binding sites for EB1, EB2 and EB3:** Comparison of the two experiments conducted in this chapter looking at the distance between the different binding sites of the EB proteins. Data is taken from Table 4.1 and Figure 4.12. The data from Figure 4.12 has been taken from the 40 nm/s bins from panels (B), (D), (E). This is to allow comparison between the experiments.

4.6 Discussion

We have shown that the three mammalian members of the end binding family localise to spatially distinct sites at the microtubule tip in vitro, Table 4.2. This suggests the spatially distinct binding sites observed in cells may be due to intrinsic differences in the preferred microtubule-binding site of EB1, EB2 and EB3. Within cells, however, EB1 is located closest to the microtubule tip, closely followed by EB3, with EB2 localising furthest from the tip. In our TIRFM experiments on dynamic microtubules in vitro, EB3 and EB1 seem to swap positions with EB3 being located closest to the microtubule tip and EB1 binding further behind. It needs to be noted, that the localisation of EB1 is very variable between experiments compared to the relative positions of EB3 and EB2. It is difficult to ascertain why that is the case, but could relate to the low level of occupancy of binding sites by EB1 achieved in our experiments. Whilst we observed a difference in the binding locations of the three EB proteins there was no difference observed in the shape of the comets. The lack of difference in EB comet shape suggests that the binding sites have an extremely similar distribution. However, the lack of difference in shape, given different binding locations is surprising. This could imply that the binding site is the same but that it is shifting along the microtubule. A possible solution could be linked to residency time of the EB proteins on the microtubule lattice. EB1 has been shown to have an average dwell time of $\sim$0.3 s on pure GTPγS-tubulin lattices (Maurer et al., 2011). In our experiments when the microtubule is growing at 40 nm/s the gap between EB3 and EB1 is $\sim$3 dimers or 24 nm, therefore it seems highly unlikely that different binding kinetics are responsible

for this difference, Table 4.2. This idea that the EB binding site is the same and simply shifts along the lattice is undermined by the EB competition experiment as this shows a difference between EB3 and EB1 on the same microtubule. If EB1 and EB3 were binding to the same binding site then there would be no difference between their peaks measurable in the competition experiment.

It is possibly that the EB proteins have different comet shapes but at the microtubule growth speeds in our experiment (15-30 nm/s), the microtubule does not grow fast enough for us to distinguish the difference in comet shape. In cells, where microtubules have a ten-fold greater growth speed, EB1 and EB3 have a roughly similar comet shape, yet it is EB2 that is distinct and spread along the lattice. In combination with this possibility and the evidence of three distinct sites within cells, the EB proteins could be recognising distinct binding sites on the microtubule lattice. The likely solution is that the EB proteins are recognising changes in the tubulin configuration as GTP-tubulin is hydrolysed, and undergoes phosphate release to form a GDP-lattice. This possibility is investigated in detail in the next chapter and the results discussed in more detail at the end of that chapter.

Chapter 5

EB2 is a non-canonical mammalian EB Protein

5.1 Introduction

In the previous chapter (Chapter 4) it was shown that EB proteins bind to distinct sites on the microtubule lattice in agreement with unpublished results from cells, Section A.2. However the order of displacement from the microtubule tip is not consistent. In Chapter 4 EB3 binds closest to the microtubule tip with EB2 furthest away. The exact binding location of EB1 is still unclear with evidence for it binding alongside EB2, as well as it having its own distinct binding site.

EB proteins are thought to track the growing microtubule tip by recognising the nucleotide state of tubulin. This is due to EB proteins only being able to track growing microtubules (Bieling et al., 2007). EB1 has been shown to bind preferentially to the GTP analogues, GTPγS and GMP-CPP, over the microtubule GDP lattice (Maurer et al., 2012; Zanic et al., 2009; Maurer et al., 2011). Unpublished results from the Straube Lab compared all three EBs to four different tubulin nucleotide substrates (GDP, GTP, GMP-CPP and GTPγS) within the same image, Section A.3. The experiment showed that for each of the different nucleotide substrates there was a clear order in binding affinity of EB3 having the highest

affinity, and EB1 the weakest affinity. This was true for all analogues tested except for GMP-CPP where EB2 showed the greatest affinity.

So whilst there is uncertainty over whether EB1 binds to a distally different site to EB2, there is a clear nucleotide preference difference between the two proteins. Therefore there are clearly three distinct binding sites at the microtubule tip for the three different EB proteins to bind to.

In order to test the assumption that EB proteins recognise the nucleotide state of tubulin at the microtubule tip, nucleotide hydrolysis is modelled. As simply nucleotide hydrolysis only shows two distinct binding sites a dual recognition model was developed. To verify that the model was correct a mixed nucleotide lattice experiment was conceived and conducted. These experiments agreed with the model. To try to understand the molecular determinants for the different microtubule binding of EB2 and EB3, chimeric constructs of EB2 and EB3 were cloned and proteins purified.

5.2 Mixed nucleotide lattice binding for EB1, EB2, EB3

To test the feasibility of the assumption that EB proteins recognise different nucleotide states of tubulin within the lattice, nucleotide hydrolysis was modelled as a multi-protofilament coupled-random hydrolysis (Bowne Anderson et al., 2013). A multi-protofilament coupled-random hydrolysis means that every tubulin dimer is independent of all the other tubulin dimers. So upon arrival at the microtubule tip, a GTP bound tubulin dimer was incorporated into the microtubule lattice. GTP-tubulin undergoes nucleotide hydrolysis into GDP+Pi-tubulin. The phosphate is then released, leaving a lattice containing only GDP-tubulin dimers. For simplicity a blunt ended microtubule was assumed for the model and dimer association/disassociation was ignored. The process of nucleotide decay and phosphate release was modelled as first order kinetics. The system undergoes nucleotide hydrolysis with a rate constant of k_1 nm^{-1}. Upon hydrolysis the phosphate is released with rate constant of k_2 nm^{-1}. The system is described by the

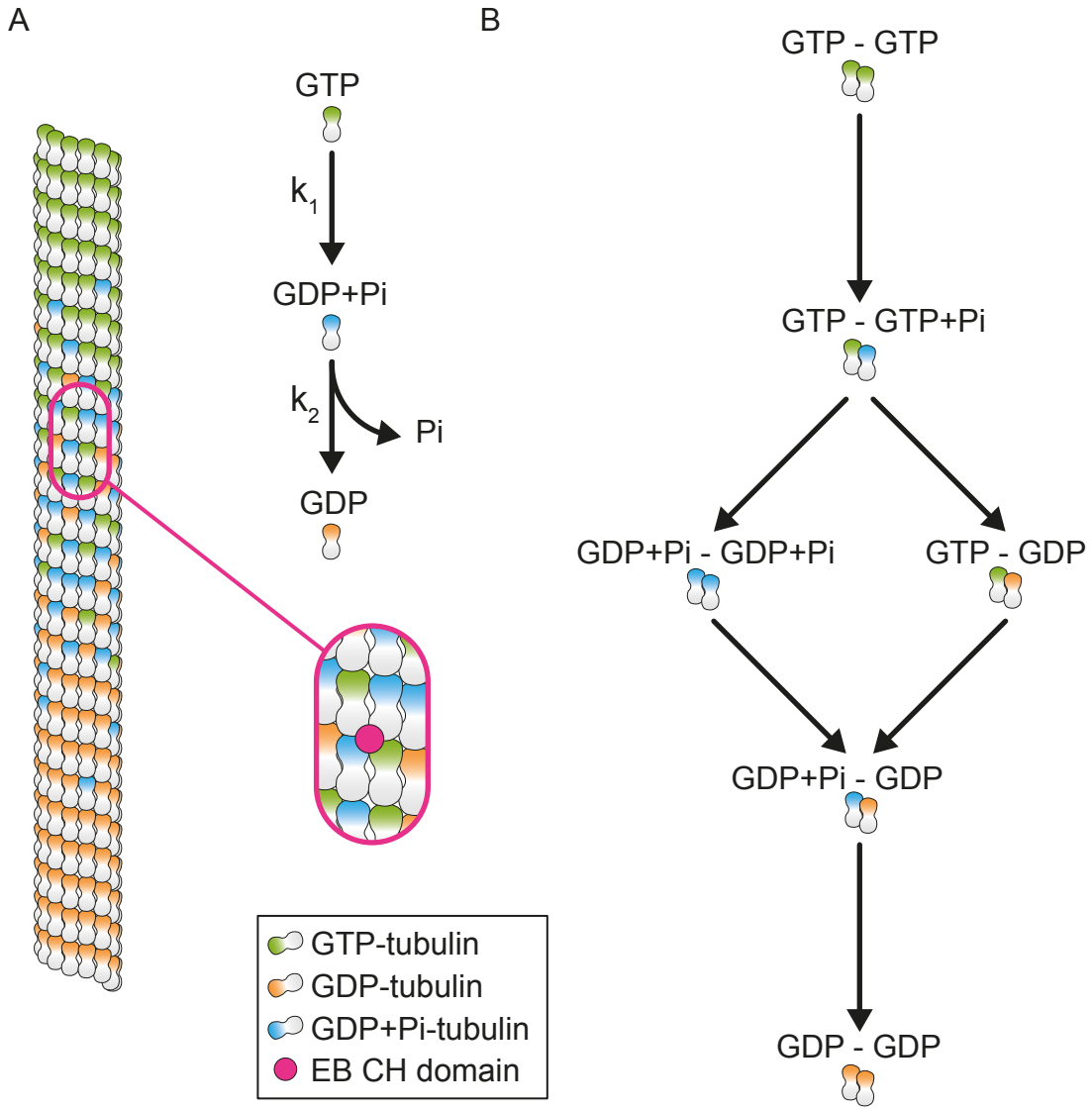

Figure 5.1: **Nucleotide Decay Model and Dual Recognition Model:** (A) shows a dynamic microtubule with GTP-tubulin dimers being added to a growing plus end. The GTP-tubulin dimers hydrolysis into GDP+Pi-tubulin dimers at rate k_1. The GDP+Pi-tubulin dimers undergo phosphate release into GDP-tubulin dimer at rate k_2. The binding position of EB proteins is shown in the inset between two laterally associating β-tubulins. (B) Schematic of nucleotide decay applied to pairwise tubulin dimers to show the six possible options that are present in a microtubule lattice. At the microtubule tip there are only GTP-GTP subunits. One of the GTP-tubulin dimers can undergo hydrolysis into a GDP+Pi-tubulin dimer. At this point either the GTP-Pi-tubulin dimer can undergo phosphate release, or the GTP-tubulin dimer can undergo hydrolysis to give GDP-GTP pair or GDP+Pi-GDP+Pi pair respectively. From each of these pairs there is only one option, either phosphate release from the GDP+Pi-GDP+Pi pair, or hydrolysis from the GDP-GTP pair. In either case the result is the same generate a GDP+Pi-GDP pair. The GDP-GDP+Pi pair only has one option, which is to undergo phosphate release into a GDP-GDP pair.

following equations:

$$\frac{dT}{dL} = -k_1 T$$
$$\frac{dP}{dL} = -k_2 P + k_1 T$$
$$\frac{dD}{dL} = k_2 P$$

where T, P, D are the number of GTP, GDP+Pi and GDP tubulin subunits in each lateral ring, L was the length from the microtubule tip, Figure 5.1 A.

The system was solved numerically using an explicit Runge-Kutta (4,5) formula, with initial conditions $T = 13, L = 0$. As there were no known rates for k_1, k_2, and no definitive answer to the size of the GTP cap, three different possibilities were considered. Firstly when there was no difference between decay and release, $k_1 = k_2$. Secondly when release was much quicker than decay $k_1 = 4 \times k_2$. Lastly the opposite scenario, decay was much quicker than release $4 \times k_1 = k_2$. There was no basis by which to assign values to k_1 and k_2 given they represent a complicated combination of temperature, growth speed, salt concentration etc. The rates were chosen by trial and error till sensible looking results were produced. From the earlier experiments for comet shape, Figure 4.6, we had obtained half height peak width to be about 300 nm once convolved. For this the rates were set at $k_1 = k_2 = 0.1\,\text{nm}^{-1}$, $4k_1 = k_2 = 0.1\,\text{nm}^{-1}$ and $k_1 = 4k_2 = 0.1\,\text{nm}^{-1}$. These combinations of k_1 and k_2 were solved and the solutions plotted, Figure 5.2 A,C,E. As these curves did not represent the observed profiles from the experimental setup, they were convolved with a representative point spread function of the TIRF microscope. To allow easy comparison between the different curves they were normalised, Figure 5.2 B,D,F. The point-spread function was generated as a Gaussian distribution function with a standard deviation of 125 nm as previously mentioned and determined, Section 3.5.

Visual comparison of these curves clearly demonstrates that there are only two possible binding sites. The analysis so far has shown three possible binding sites for EB1, EB2 and EB3. Whilst the evidence from Chapter 4 only give evidence for EB3 binding in a

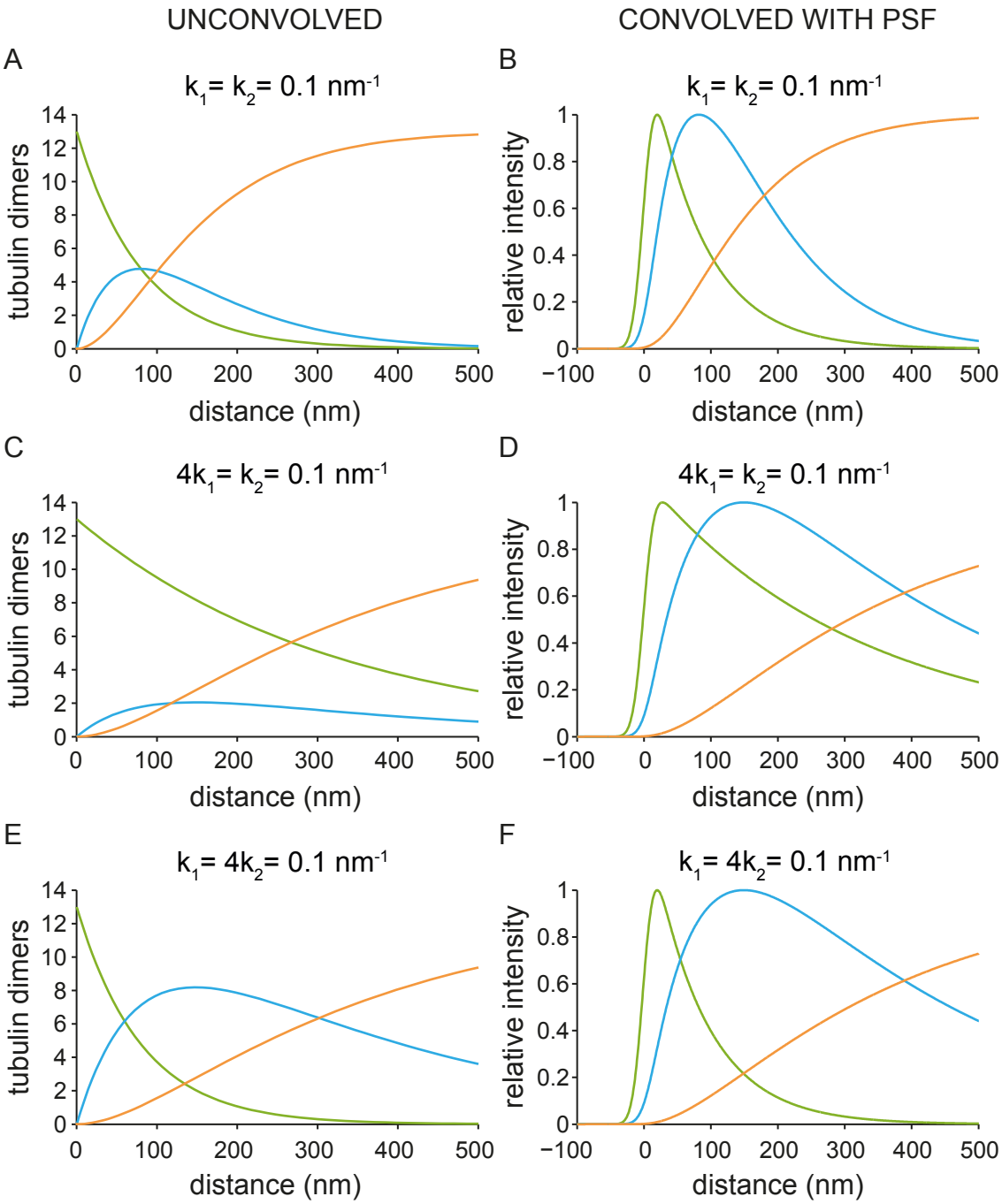

Figure 5.2: **First order GTP hydrolysis simulation:** (A,C,E) Distribution of GTP-tubulin, GTP+Pi- tubulin and GDP-tubulin relative to the microtubule end, assuming uncoupled, first order kinetics of GTP hydrolysis and phosphate release. (B,D,F) Distributions from (A,C,E) respectively convolved with a theoretical PSF for GFP. and normalised (maximum peak intensity equal to one).

spatial distinct location to EB1 and EB2, nucleotide preference data shows that EB2 has differing preferences to EB1 and EB3, Section A.3. As this modelling solution only gives two possible binding sites it seems unlikely that it is correct.

Electron microscopy studies show the calponin-homology domain of the EB1 ortholog, Mal3, binds between the E-site of two laterally associated tubulin dimers in a GTPγS microtubule (Maurer et al., 2012). Additionally EB3 is found in a similar binding location on GMP-CPP and GTPγS microtubule (Zhang et al., 2015). This gave the possibility that EB proteins might be sensitive to the nucleotide state of two laterally associated tubulin dimers. To test this dual nucleotide model, the simulation was extended. The statistical probability of finding different pairwise combinations of nucleotide within the E-site of two lateral associating tubulin dimers was calculated for the longitudinal distance from the microtubule tip. The probability of finding a GTP, GDP+Pi or GDP tubulin dimer was taken from the above simulation. It was calculated that there were six possible combinations of pairwise laterally associating tubulin dimers, Figure 5.1 B. At the tip of the microtubule, arriving dimers were assumed to be GTP, so the only pairwise combination could be GTP-GTP. One of these tubulin dimers would undergo nucleotide hydrolysis to create a GTP-GDP+Pi pairwise combination. Next there were two options, either the GTP would undergo hydrolysis to create a GDP+Pi-GDP+Pi pairwise combination; or the GDP+Pi would undergo phosphate release to create a GTP-GDP pairwise combination. In either case the next step creates a GDP+Pi-GDP pairwise combination. The GTP in the GTP-GDP pairwise combination would undergo nucleotide hydrolysis, or one of the GDP+Pi's would undergo phosphate release, to create the GDP+Pi-GDP pairwise combination. The only thing left was for the remaining GDP+Pi to undergo phosphate release into GDP creating the GDP-GDP pairwise combination that was expected in the microtubule lattice. This gave the six pairwise combinations of, GTP-GTP; GTP-GDP+Pi; GTP-GDP; GDP+Pi-GDP+Pi; GDP+Pi-GDP; and GDP-GDP. The statistical probabilities were calculated by multiplying the respective probabilities of finding each of the tubulin dimers in the pair together (i.e. P(GTP-GDP) = P(GTP)$\times$P(GDP)). For pairwise combinations involving different nucleotide states the probability was doubled. This took account of the fact that the assumption does not assign which nucleotide was in the right or left tubulin dimer, so there were two different probabilities. For pairwise combinations

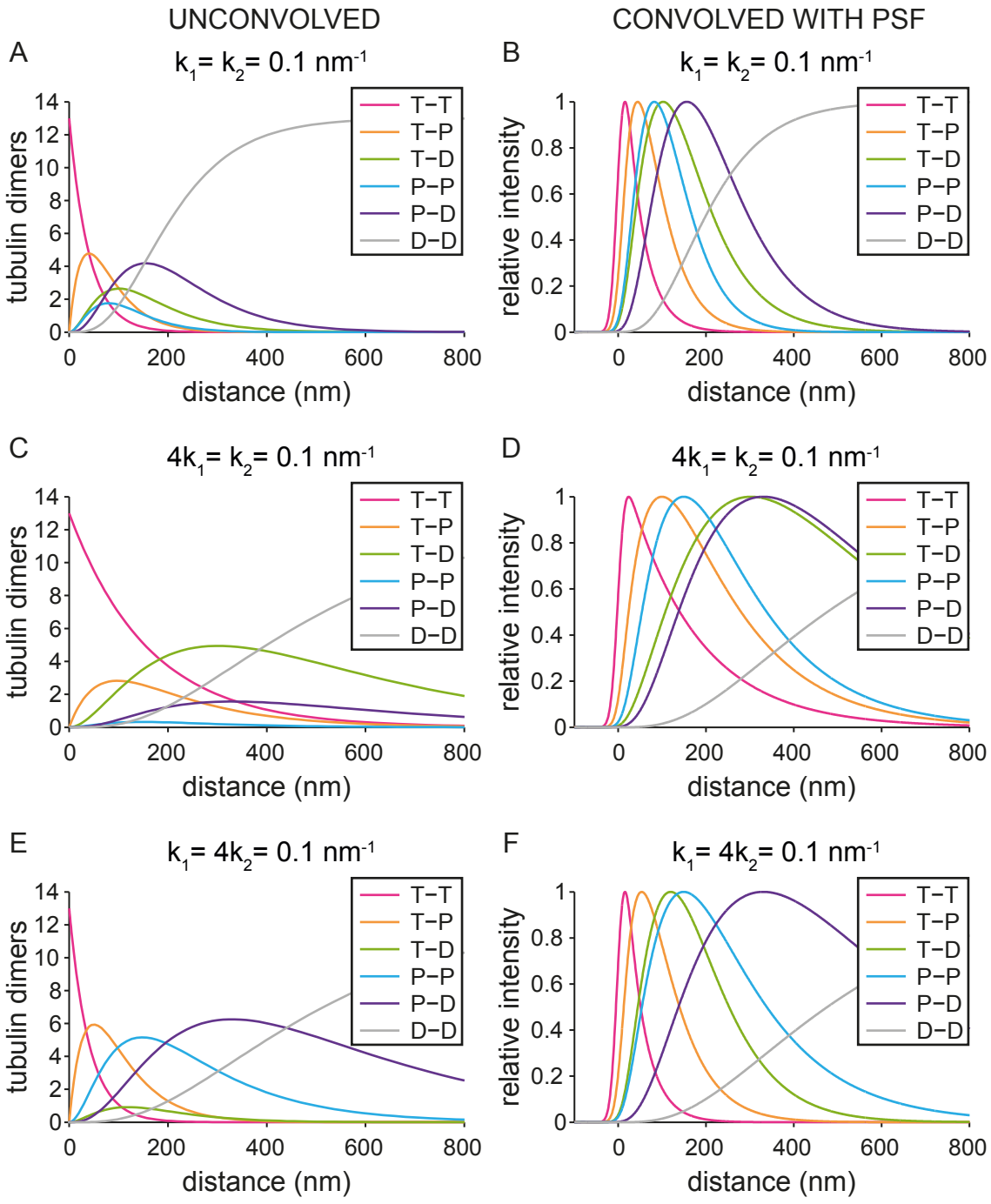

Figure 5.3: **Distributions of paired nucleotides:** (A,C,E) Probabilistic distribution of nucleotide present in laterally adjoining tubulin dimers. Six combinations considered: (1) GTP-GTP (T-T); (2) GTP-GDP+Pi (T-P); (3) GTP-GDP (T-D); (4) GDP+Pi-GDP+Pi (P-P); (5) GDP+Pi-GDP (P-D); (6) GDP-GDP (D-D). Probabilities calculated from the solved first order hydrolysis distributions in Figure 5.2. (B,D,F) Distributions from (A,C,E) respectively convolved with a theoretical PSF for GFP and normalised (maximum peak intensity equal to one).

that contain the same nucleotides this did not need to be taken into account, as they were symmetric. To get a realistic idea of the numbers of each pairwise combination the resulting probabilities were multiplied by thirteen, Figure 5.3 A,C,E. These curves were then convolved with the PSF of the microscope and normalised for easy comparison, Figure 5.3 B, D, F.

The same three combinations as before for k_1 and k_2 were used to generate results. Visual comparison of the normalised curves shows a complicated picture. All of the curves, apart from GDP-GDP curve, have very similar comet like profiles. Additionally, when the rates, k_1 and k_2, change the order of the curves change. For $k_1 = 4k_2$ the GTP-GDP and GDP+Pi-GDP+Pi curves have changed order compared to the other two simulated combinations. This could help to explain the observed discrepancy in where EB1 appears to bind. If EB1 preferred the structural representation of one of these binding sites then it could explain how its binding location can move with a change in conditions.

5.3 Binding of EB1, EB2, EB3 to Mixed Nucleotide Lattices

For the hypothesis that EB proteins are able to sense the nucleotide state of two laterally associated tubulin dimers to be true, at least one of the EB*s must be able to bind to a mixed nucleotide lattice microtubule. To test this assumption, microtubules with mixed nucleotide lattices were assembled, Figure 5.4 A. To show that the microtubules created, contained a mixed nucleotide lattice, each nucleotide was incubated on ice with tubulin containing different fluorophores. Three different mixed nucleotide lattice combinations of nucleotide were considered. The first was GMP-CPP and GTPγS; the second was GMP-CPP and GDP; and, the third was GTPγS and GDP. For GDP, GTP was incubated with labelled tubulin on ice, but it was assumed that as the microtubules form all of the GTP would be hydrolysed into GDP. Each chamber contained GMP-CPP seeds and GTPγS seeds as well as a mixed nucleotide lattice seed. Each type of seed was composed of tubulin labelled with a different fluorophore. For example the

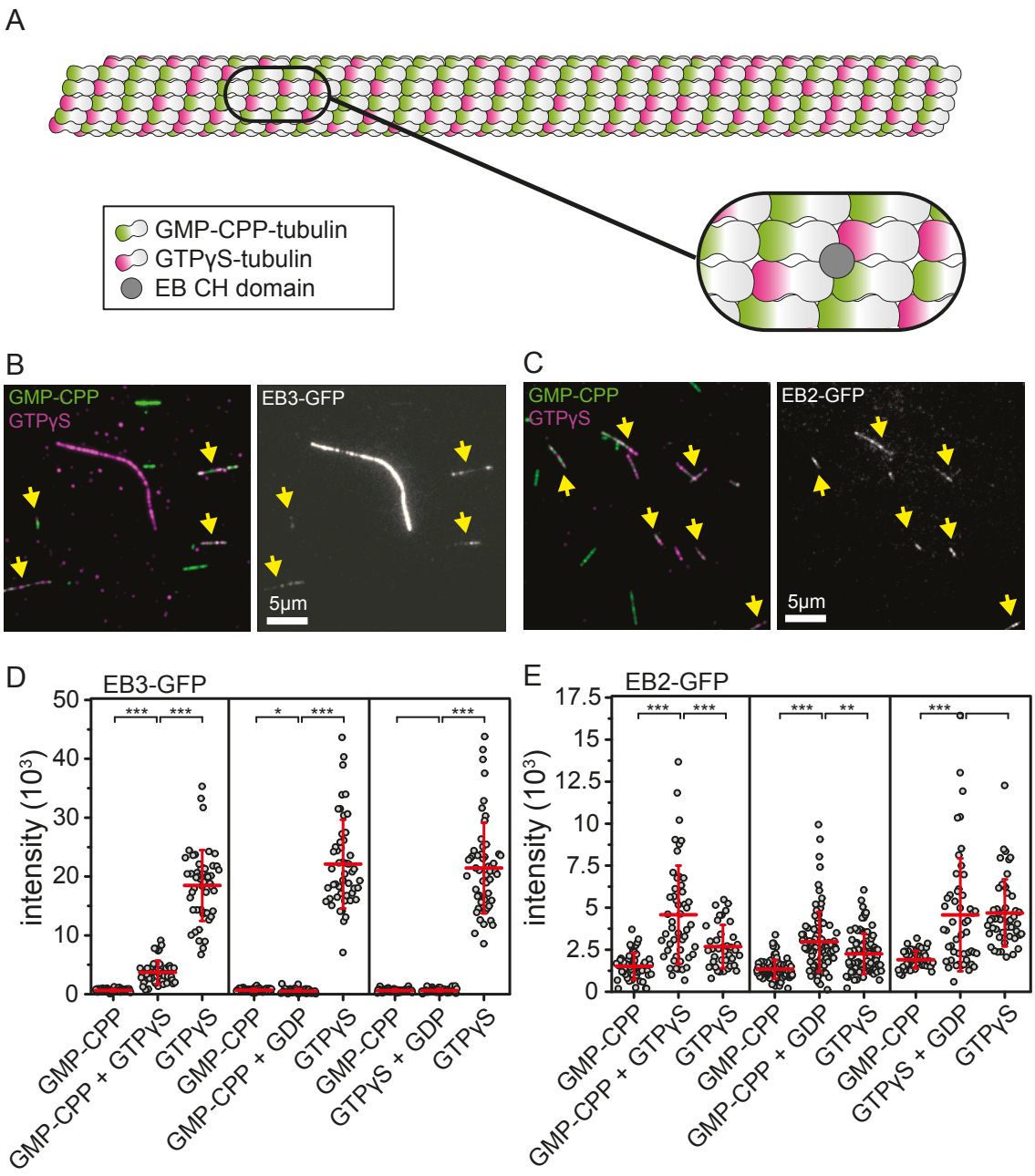

Figure 5.4: **EB2 prefers a mixed nucleotide lattice:** A) Cartoon representation of a microtubule composed of a mixed lattice of GMP-CPP tubulin and GTPγS tubulin. Inset shows the binding location of the EB microtubule-binding domain. (B-C) Microtubules polymerised from tubulin equilibrated with different non-hydrolysable GTP analogues. Examples of differential binding of EB3-GFP (B) and EB2-GFP (C) to pure GMP-CPP (green) tubulin and GTP*S (magenta) tubulin as well as mixed GMP-CPP+GTPγS tubulin lattices (yellow arrows). (D-E) Quantification of EB3-GFP (D) and EB2-GFP (E) intensity on mixed and pure substrates of GMP-CPP, GTP*S and GDP. Data are overlaid by mean * standard deviation in red. Different scale used as EB3 has a much higher affinity for the microtubule lattice that EB2 does. Statistical different means are indicated by * for $p<0.05$, ** for $p<0.005$, *** for $p<0.0005$ (t-test)

GMP-CPP seed would be identifiable because it contained X-rhodamine-labelled-tubulin. The GTPγS seed would be identifiable because it contained tubulin labelled with HiLyte 647™-labelled-tubulin. The seed with the mixed nucleotide lattice would be identifiable because it contained a lattice with both X-rhodamine-labelled-tubulin and HiLyte 647™-labelled-tubulin. To each chamber an EB-GFP protein was added, giving nine combinations in total.

Initial visual inspections of the static images from the chambers containing the GMP-CPP+GTPγS mixed nucleotide lattice combination showed that mixed nucleotide lattice seeds were created, Figure 5.4 B-C. In each chamber there were microtubule seeds fluorescing in single colours showing the presence of GMP-CPP and GTPγS microtubule seeds. There were also seeds fluorescing in both the 561 nm and 640 nm channels, showing that mixed nucleotide lattice seeds were successfully created.

As expected from the experiment on nucleotide binding, Section A.3, EB3-GFP showed very strong binding to the GTPγS seeds. It showed much weaker binding to GMP-CPP seeds. On the mixed nucleotide lattice seeds EB3-GFP is visible, Figure 5.4 B. The brightness of EB3-GFP on the mixed seeds is not as high as on GTPγS seeds.

For EB2-GFP, interestingly, the seeds with the highest level of binding were the mixed seeds. For both proteins, EB2 and EB3, the raw intensities from many different areas of each chamber for each combination of mixed nucleotide lattice were imaged and plotted. In each case the statistical significance between each of the GMP-CPP and GTPγS seeds, and the mixed nucleotide lattice seed was calculated. Figure 5.4 D-E.

For EB3 the only mixed nucleotide lattice to show a large ($p<0.005$) statistically significant difference from both GMP-CPP and GTPγS was the mixed GMP-CPP+GTPγS combination. As seen from the static images the brightness of the mixed seed was in-between that of the two pure seeds. However, for the other two cases there was very little discernible differences between the two mixed nucleotide lattices GMP-CPP+GDP and GTPγS+GDP.

For EB2-GFP the difference in intensity was not as extreme as it had a lower preference for GTPγS seeds and a higher preference to GMP-CPP seeds compared to EB3-GFP.

Despite this switch, EB2-GFP still had a preference for GTPγS over GMP-CPP seeds. For two of the three mixed seed combinations, the mixed seed was brighter than either of the two pure seeds. For GTPγS+GDP combination there was no statistically significant difference between it and the pure GTPγS seed. The only explanation for EB2-GFP preferably binding to the mixed nucleotide lattice seeds was that it prefers a different nucleotide to be present in the E-site of each of the tubulin dimers that it is bound to.

Whilst the evidence shows that EB2-GFP recognises a mixed nucleotide lattice proving the dual nucleotide model to be true for EB2 but not for EB1 or EB3. EB3-GFP only shows a preference for the mixed nucleotide lattice over pure GMP-CPP in one case, the GMP-CPP+GTPγS mixed nucleotide lattice. If EB3-GFP were to only care about the nucleotide state of one of the tubulin dimers it was bound to then it would show similar preference to the mixed nucleotide lattice in both cases when GTPγS was involved. However, this is not true. It only shows preference when the combination involves both GMP-CPP and GTPγS. If anything when GDP is involved it has a negative effect on the binding of EB3-GFP to the mixed nucleotide lattice. To check whether EB3 was truly able to sense the nucleotide present in two laterally associated tubulin dimers, the distribution of binding sites was modelled as a percentage of GTPγS present. Two options were considered. The first was that EB3 only cares about what is present in one of the two binding sites it is bound to. So as the percentage (or fraction) of GTPγS present in the microtubule lattice increases, the amount of EB3 bound will increase. This gives a linear relationship between the number of preferential binding sites and fraction of GTPγS in the microtubule lattice, Figure 5.5 A. The second model was that EB3 cares about it's 2D lattice environment and preferentially binds only when two laterally associating tubulin dimers contain GTPγS in their E-sites. To do this the probability of finding two GTPγS bound tubulin dimers associating laterally was calculated. This was simply the number of GTPγS tubulin dimers in the lattice squared. The percentage of binding sites for each of these situations was plotted against the fraction of GTPγS bound tubulin in the lattice, Figure 5.5 B.

To look at which of these situations EB3 preferred, the raw binding data was normalised using the intensity of EB3 binding to both of the pure nucleotide lattices. For each image the intensity of EB3 bound to each GMP-CPP lattice, each GTPγS lattice and each mixed

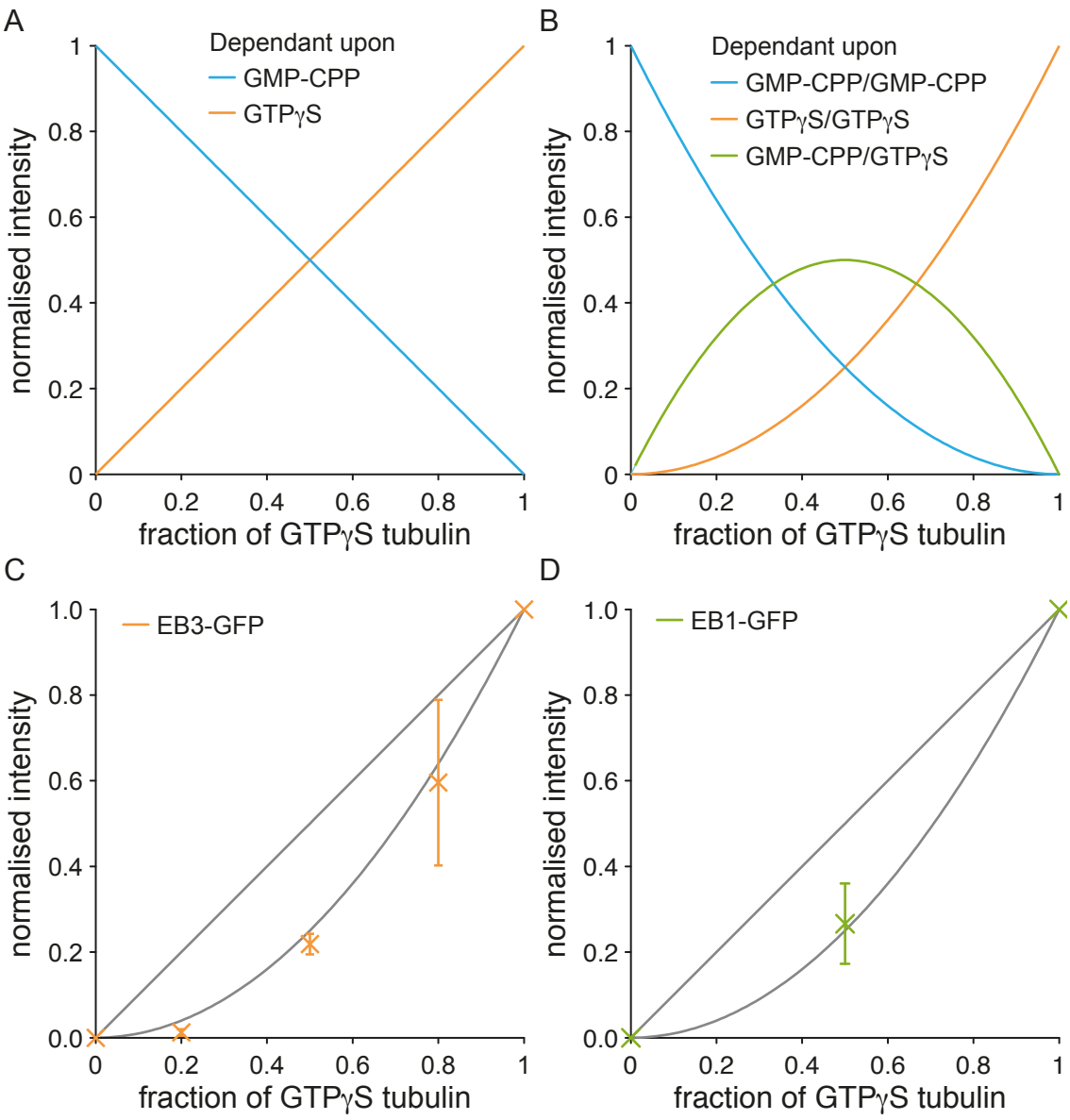

Figure 5.5: **Model of EB binding profiles when binding to different mixed lattice fractions:** ((A-B) Shows the difference in expected binding between an EB sensitive to the state of the nucleotide in the exchange site in one of the two tubulin dimers it is bound to (A), as apposed to if it was sensitive to both (B), in a dual recognition model. Plotted as a fraction of the total binding sites available against the fraction of GTPγS in the microtubule lattice. (C-D) Experiment for EB3 (C) and EB1 (D) showing how the binding profile changes as the fraction of GTPγS tubulin changes in a mixed GMP-CPP+GTPγS lattice.

nucleotide lattice was calculated. The average intensity of EB3 bound to GMP-CPP lattices was calculated and subtracted from the intensity of each individual seed. The average intensity of EB3 bound to GTPγS lattices was calculated and used to additionally normalise the intensity of EB3 bound to each individual seeds in the image. Every seed had its EB3 bound intensity divided by the mean intensity of EB3 bound to GTP-$gamma$ lattices.

This normalisation effectively gave pure GMP-CPP lattices a brightness of 0, and pure GTPγS lattices a brightness of 1. This matched up with the previously theoretically modelled situations, Figure 5.5 A-B.

The experiment was carried out for three mixed nucleotide lattice ratios, 20-80, 50-50 and 80-20. When the intensities from these three experiments were normalised and plotted on the same axis as the two simulated models the intensities clearly followed the quadratic curve, Figure 5.5 C. This showed that EB3 as well as EB2 is sensitive to a dual-nucleotide binding site. To see whether EB1 was more EB2 or EB3 like, a single experiment with 50/50 ratio was used. EB1, as expected, continues to show similar properties in binding affinities as EB3, Figure 5.5 D.

5.4 Investigation of Shortened and Chimeric Proteins of EB2 and EB3

There are a number of key differences in binding properties between EB1/EB3 and EB2. EB2 has been found to bind more distant from the microtubule tip than EB3, but has a similar comet shape. EB2 has a distinctly different binding preference when binding to pure nucleotide lattices compared to EB1 and EB3. EB2 showed the greatest preference for pure GMP-CPP lattices, whereas EB3 had the greatest preference for the other pure nucleotide lattices tested. When binding to mixed nucleotide lattice microtubules, EB2 showed a higher preference to a mixed nucleotide lattice microtubule than to a pure lattice microtubule. To investigate the cause of these differences between EB2 and EB3 a number of shortened and chimeric EB2/EB3 hybrids were designed. EB2 has

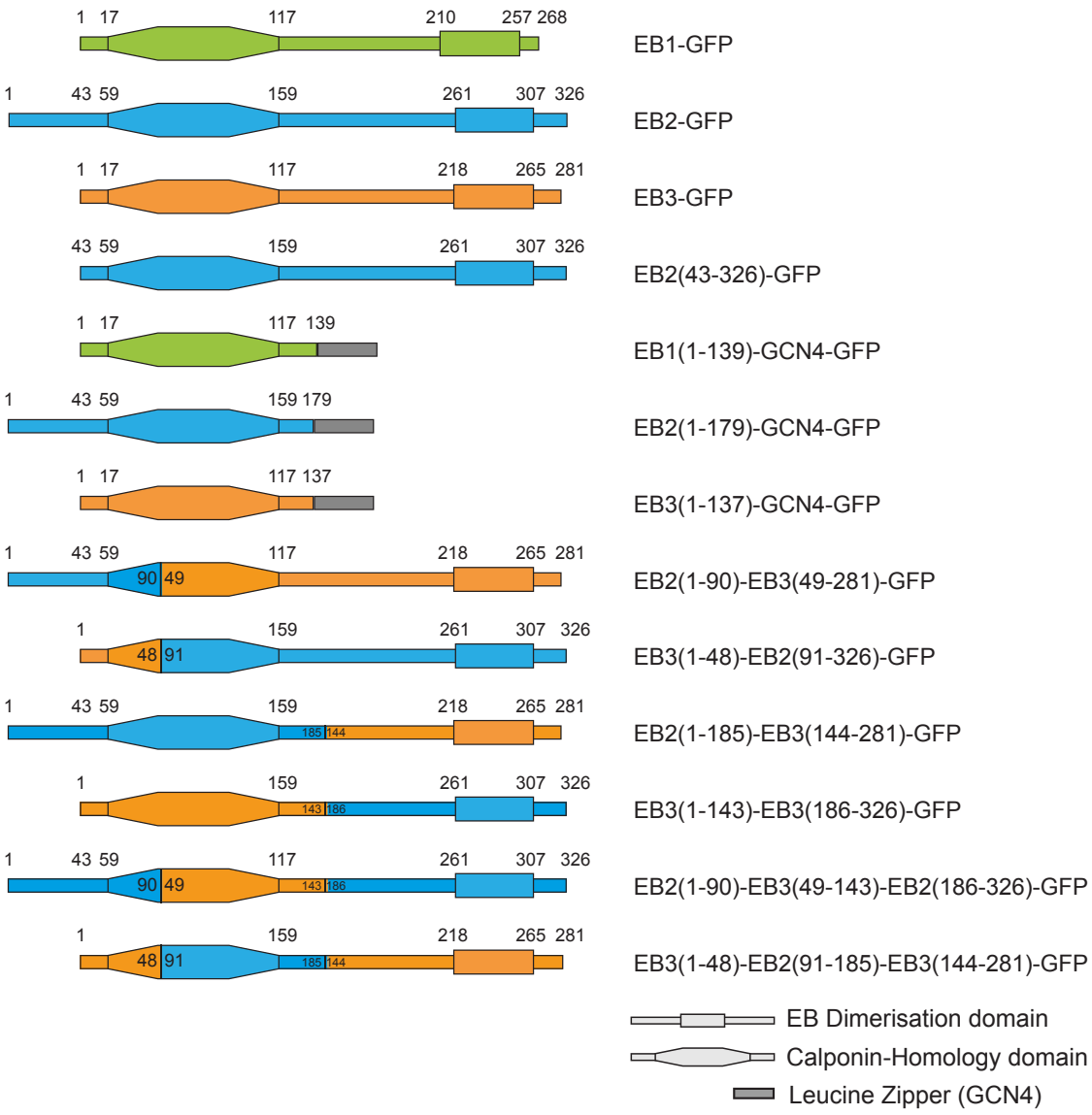

Figure 5.6: **Schematic showing all the GFP variants of the EB proteins; full-length, shortened and chimeric forms:** The three full length EB proteins are showed first, coloured by protein, EB1-green, EB2-blue, EB3-orange. Following this there is EB2 minus its N terminus (EB2ΔN). Then the three EB proteins cut just after the calponin-homology domain and bound together using a Leucine Zipper in place of the EB dimerisation-domain. These are refer to as EB#ΔT. Next come the six different chimeras created from splicing different parts of EB2 and EB3 together. Two equivalent cutting points were located in conserved regions of the protein. One of these was located in the middle of the calponin-homology domain. The other was located in the unstructured linker region between the calponin-homology domain and the EB Dimerisation domain. For ease a naming convention was created based upon which part of EB2 or EB3 was placed where. For example EB3, which was composed of three segments of EB3, would be EB333 under this convention as it has the EB3 part from each of the zones used for splicing. When the EB3 is cut in the middle of the calponin-homology domain and the N terminus replaced with EB2's N terminus the chimera is known as EB233.

an N-terminal extension that is not present on either EB1 or EB3 (Hayashi and Ikura, 2003). Other than the N terminal extension there is a high degree of similarity between all three EB proteins. This N-terminal was identified as a prime candidate for the cause of the difference between EB2 and EB3. The first shortened construct was EB2 minus its N terminal extension, EB2(43-326)-GFP-His (EB2ΔN), Figure 5.6.

As the tail region of EB1 and EB3 had been indicated in prohibiting EB binding by long-range electrostatic interactions (Buey et al., 2011). This was reinvestigated here. Each of the three EB proteins had their tails removed and replaced with a GCN4 linker to ensure that a dimer was still created. The three proteins created were; EB1(1-139)-GCN4-GFP-His (EB1ΔT), EB2(1-179)-GCN4-GFP-His (EB2ΔT), and EB3(1-137)-GCN4-GFP-His (EB3ΔT), Figure 5.6.

Chimeric proteins of EB2 and EB3 were created by considering differences in the tail region and in the CH microtubule-binding domain. To test the effect of the EB2 and EB3 tail on the alternative protein, a conserved region was identified in the unstructured region between the CH domain and the DD as a ligation sites. To test for differences within the CH domain a highly conserved region was identified within the CH to use a ligation sites. Using the ligation points cDNA fragments were created and ligated together to create six chimeric EB2/EB3 proteins. All chimeric proteins had a GFP tag at the C terminus, with a histadine tag attached to the GFP tag similar to the full-length EB-GFP variants.

The six chimeric constructs are fusions of EB2 and EB3. Two ligation sites were identified in different conserved regions for both EB2 and EB3. For EB2 the ligation sites were between the 90th and 91st amino acid residues, and between the 185th and 186th amino acid residues. For EB3 these sites were between 48th and 49th, and the 143rd and 144th amino acid residues respectively. Each possible chimera was created, four with a single ligation:

1. EB2(1-90)-EB3(49-281)-GFP-6xHis (EB233)
2. EB2(1-185)-EB3(144-281)-GFP-6xHis (EB223)
3. EB3(1-48)-EB2(91-326)-GFP-6xHis (EB322)
4. EB3(1-143)-EB2(186-326)-GFP-6xHis (EB332)

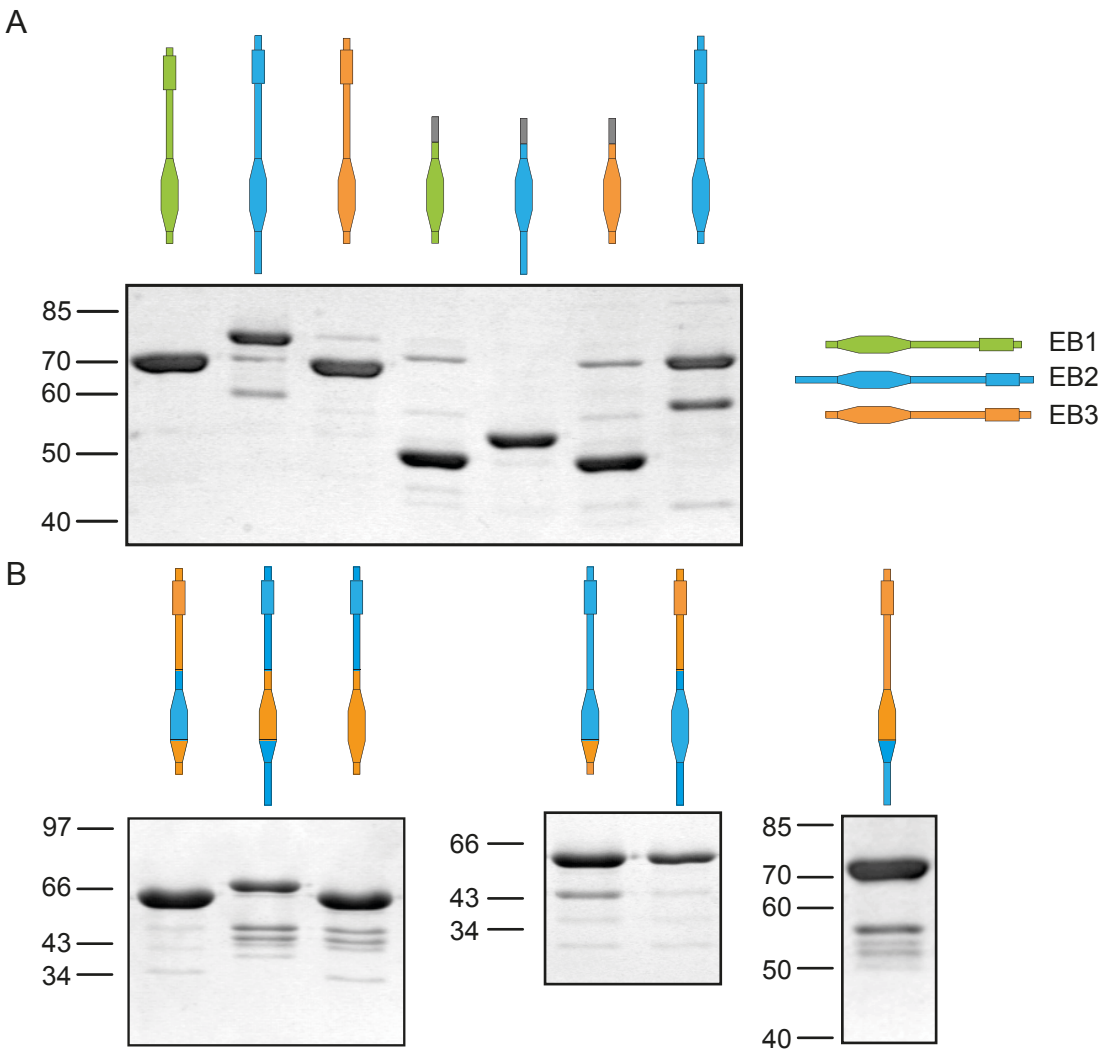

Figure 5.7: **Gels of the purified shortened and chimeric forms of the EB proteins:** Gels show the final purified protein of the EB chimera. All proteins were purified by affinity chromatography followed by anion and cation chromatography, except the three full-length proteins, which underwent an extra size exclusion step following affinity purification. (A) shows the full-length proteins alongside the four shortened constructs. (B) shows the six chimera. Proteins are indicated by their cartoon representations from Figure 5.6.

In addition two chimera were created with a dual ligation, i.e. EB2 with an EB3 centre, or EB3 with an EB2 centre:

5. EB2(1-90)-EB3(49-143)-EB2(186-326)-GFP-6xHis (EB232)
6. EB3(1-48)-EB2(91-185)-EB3(144-281)-GFP-6xHis (EB323)

Each protein was purified as previously described with one modification, Section 4.2. Due to the large numbers of proteins requiring purification the size exclusion chromatography step was skipped. This was because the size exclusion chromatography column was the rate limiting process in the purification procedure. By removing this step, it was possible to parallelise the purification and purify three/four proteins simultaneously. Each protein was still subject to three rounds of purification and for initial exploratory experiments the three remaining columns were sufficient, Figure 5.7. Whilst some of the proteins show a number of contaminating bands, it is my belief that these are degradation products. This is due to the fact that the bands are not of a consistent weight but vary according to the weight of the purified protein. As such for investigatory experiments the purity of the protein was considered sufficient. If any of the proteins show promise in assisting explanation of the differences between EB2 and EB3 the protein will be re-purified with the inclusion of the size exclusion step.

Following purification each protein was tested for functionality in a standard dynamic microtubule TIRF microscopy chamber. All of the new proteins showed autonomous plus end tracking behaviour, Figure 5.8. For the majority of the chambers the EB chimera were at 200 nM, however for some chambers the concentration had to be increased to 400 nM in order to obtain an observable signal.

From the functionality test images, initial analysis of the proteins was conducted. Kymographs were created to obtain averages for EB peak intensity, EB lattice intensity, and EB seed intensity. These were used to create two ratios, tip/seed ratios, and lattice/seed ratios. The shortened constructs were tested against the full-length constructs, Figure 5.9 A-B. The chimeric constructs were compared against each of the full length EB2 and EB3 constructs, Figure 5.9 C-D. In each case the tip/seed and lattice/seed ratios were plotted. These two ratios were selected, as the main difference between EB2 and EB3 is a switch in preference from GMP-CPP for EB2 to GTP at the tip

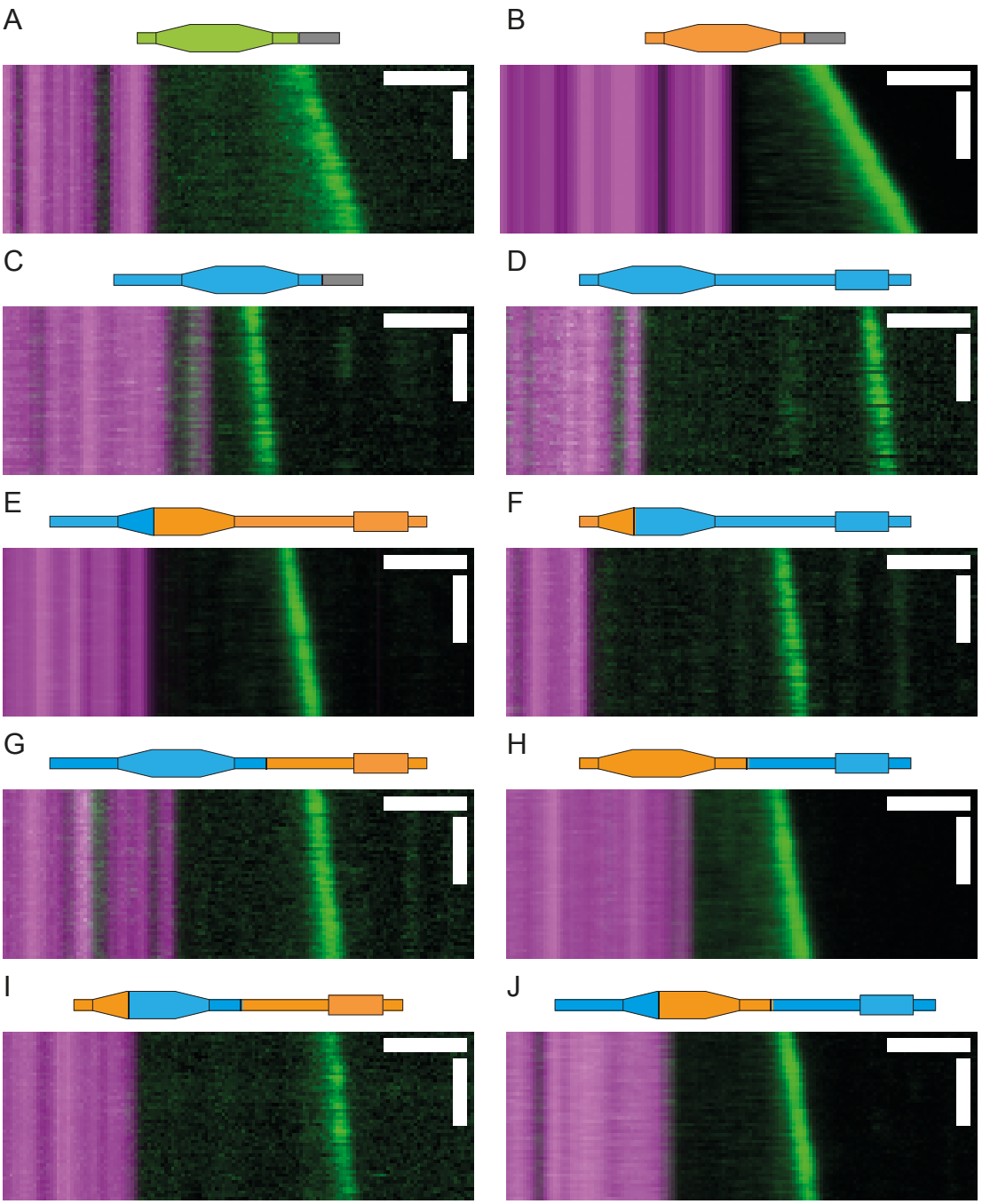

Figure 5.8: **Kymographs of the purified shortened and chimeric forms of the EB proteins:** Demonstrates proof of concept of EB plus tip tracking ability for each of the modified EB proteins. Distinct protein is indicated by the cartoon representation from Figure 5.7. Time is on the y-axis, distance on the x-axis, scale bars are 10 s and 2 μm respectively.

for EB3. So as the chimera change in preference from EB2 to EB3 these ratios should give a large range and two measures by which to observe the shift in characteristics in binding from EB2 to EB3.

The removal of the N terminus for EB2, EB2ΔN had a small positive effect on the tip/seed ratio compared to EB2, Figure 5.9 A. However, there was no data available for lattice/seed ratio due to weak binding to the microtubule. A more detailed investigation of the binding intensities shows that removal of the N terminus for EB2 has reduces the binding ability of EB2ΔN to the microtubule for all three lattices (GTP-tip, GDP-lattice and GMP-CPP-seed), Table 5.1 A.

Similar analysis carried out between each of the EBΔT-GFP constructs and its corresponding EB-GFP construct showed a significant difference in each case. Whilst both ratios decreased for the EB1ΔT, they increased for EB2 and EB3, Figure 5.9 A-B. The raw intensities however actually show a drop in intensity for the EB1ΔT and EB2ΔT, Table 5.1 A. EB3δT shows a much stronger intensity at the tip and the lattice compared to EB3, but very similar seed intensity.

Following testing on the shortened constructs, the same rough quantitative analysis was applied to the EB3 chimera data. The aim was to say which chimeras were more similar to EB3 and which were more similar to EB2. As stated above there is a large variety between the binding affinity of the different chimeric EB proteins. The tip intensity varies from 3,000-16,000, a five-fold difference, and the seed varies from 400-4,000, a ten-fold difference, Table 5.1. For this reason the ratios were chosen as the best way to neutralise the variance in affinity. The ratios show that all of the six constructs have ratios between the ratios for EB2 and EB3, Figure 5.9 and Table 5.1. A closer examination shows that no conclusive conclusion can be drawn from this analysis except that in nearly every case examined one of the three possibilities disproves the point.

The one contradiction is the three constructs that contain EB3(49-143) region of the protein. Proteins containing EB3(49-143) have the highest affinity to the microtubule, Table 5.1. Other than this result, these experiments have provided no meaningful analysis as to the source of difference between EB2 and EB3. From these limited results it is

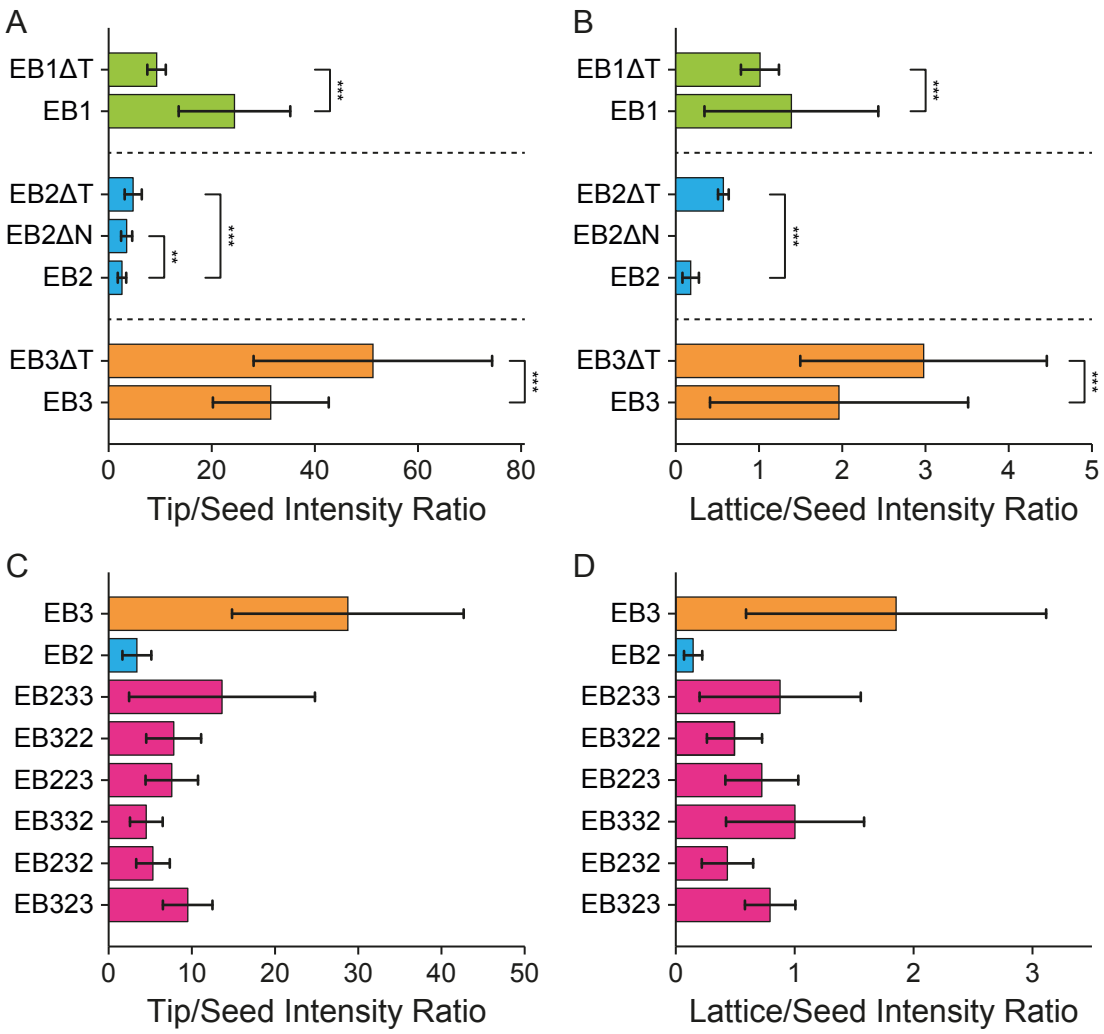

Figure 5.9: **Results of the purified shortened and chimeric forms of the EB proteins:** Quick look at the ratios obtained from the same experiment used to test functionality of the modified EB constructs, Figure 5.8. Bars show the mean, and the error bars the standard deviation of each of the experiments. (A,B) compares each of the shortened constructs to its parent construct. T-tests were carried out between each of the shortened constructs and its parent, significance is as follows; * - $p<0.05$, ** - $p<0.005$, *** - $p< 0.0005$. (C,D) compares each of the chimeras to EB2 and EB3. (A,C) show the tip/seed ratio. (B,D) show the lattice/seed ratio. Full stats including tip, lattice and seed intensities are shown in Table 5.1.

A. EB Constructs

	TIP	LATTICE	SEED	TIP/SEED	LATTICE/ SEED
EB1ΔT	2,291 ± 494	254 ± 43	251 ± 44	9.2 ± 1.8	1.0 ± 0.2
EB1	7,121 ± 2,204	417 ± 259	308 ± 58	24.2 ± 10.7	1.4 ± 1.0
EB2ΔT	2,361 ± 575	357 ± 32	534 ± 149	4.7 ± 1.6	0.6 ± 0.1
EB2ΔN	1,530 ± 292		475 ± 132	3.4 ± 1.1	
EB2	8,258 ± 2,795	391 ± 193	2,730 ± 1,028	3.4 ± 1.7	0.1 ± 0.1
EB3ΔT	26,614 ± 6,023	1,579 ± 629	612 ± 261	50.8 ± 22.9	3.0 ± 1.5
EB3	16,179 ± 4,044	1,063 ± 545	646 ± 242	28.7 ± 13.9	1.9 ± 1.3

B. EB Chimera

	TIP	LATTICE	SEED	TIP/SEED	LATTICE/ SEED
EB3	16,179 ± 4,044	1,063 ± 545	646 ± 242	28.7 ± 13.9	1.9 ± 1.3
EB2	8,258 ± 2,795	391 ± 193	2,730 ± 1,028	3.4 ± 1.7	0.1 ± 0.1
EB233	14,804 ± 5,933	1,036 ± 665	1,384 ± 723	13.6 ± 11.2	0.9 ± 0.7
EB322	4,317 ± 1,406	323 ± 115	594 ± 169	7.8 ± 3.3	0.5 ± 0.2
EB223	3,454 ± 1,284	296 ± 75	495 ± 190	7.6 ± 3.2	0.7 ± 0.3
EB332	16,329 ± 4,357	3,635 ± 1,483	4,558 ± 2,566	4.5 ± 2.0	1.0 ± 0.6
EB232	9,350 ± 2,063	789 ± 424	1,841 ± 350	5.3 ± 2.0	0.4 ± 0.2
EB323	3,165 ± 913	336 ± 103	350 ± 87	9.5 ± 3.0	0.8 ± 0.2

Table 5.1: **Full statistics of the purified shortened and chimeric forms of the EB proteins experiment:** Full statistics obtained from the same experiment used to test functionality of the modified EB constructs, Figure 5.8. Shows the raw intensity values obtained from analysis of kymographs during constant growth phases for the microtubule seed, lattice and tip. Additionally shows the ratio of the tip intensity to seed intensity and the lattice intensity to the seed intensity. Errors are standard deviation. (A) compares each of the shortened constructs to its parent construct. (B) compares each of the chimera to EB2 and EB3.

very hard to draw any firm conclusions from these experiments. Any future experiments will need to be carefully planned to take account of the vast difference in affinity to the microtubule between the various chimeric proteins.

5.5 Discussion

To support the discovery of three spatially distinct binding sites, a dual nucleotide model was developed, based on structural evidence that the calponin-homology domains of the yeast ortholog Mal3 and human EB3 bind close to the E-site of two protofilaments (Maurer et al., 2012; Zhang et al., 2015). This binding site might allow EB proteins to sense the nucleotide state of two laterally associating tubulin dimers. Our modelling of the pairwise combinations during GTP decay in the microtubule lattice results in EB

comet-like distributions that are indistinguishable by shape, but shifted in position relative to the microtubule end. In mixed nucleotide lattice experiments we show that EB2 prefers to bind to a mixed GMP-CPP/GTPγS lattice over a pure GMP-CPP, or GTPγS lattice. Whereas EB3 and EB1 show sensitivity to a mixed nucleotide lattice consistent with a requirement of both nucleotides at the binding site to be the same.

A study of the nucleotide preferences for EB1, EB2 and EB3, Appendix A.3, show that EB2 has a different preference with higher relative affinity to GMP-CPP than EB1 and EB3. In agreement with the literature (Maurer et al., 2011), EBs prefer GTPγS over all other substrates tested. It has been suggested that GMP-CPP is a mimic for GTP, while GTPγS is a mimic for GDP+Pi based on their ability to nucleate microtubules (Maurer et al., 2014; Zhang et al., 2015). Further, the yeast EB1 ortholog, Mal3 has been shown to bind to GDP-BeF_3 lattices with a three-fold higher affinity than GDP-microtubules (Maurer et al., 2011). BeF_3^- is thought to mimic the γPhosphate and thus GDP-BeF_3^- imitates the GDP+Pi state of tubulin. However, these and our experiment do still not ascertain whether EBs have a preference for GTP-tubulin or GDP+Pi-tubulin unless we can test such lattices directly. The largely different affinities of EBs, for lattices containing different non-hydrolysable GTP analogues, suggest that they are very sensitive to small conformational changes in tubulin resulting from the molecules bound in the E-site. This indeed has been confirmed by a recent high-resolution cryo-EM structure showing intimate contacts of EB3 with four tubulin subunits adjoining its binding site and conformational changes in tubulin at the contact sites in the presence of different nucleotides (Zhang et al., 2015). However, we cannot exclude that EB2 binds to a completely different site than EB1/EB3. There is precedence for EB2 binding to a completely different site, as the kinetochore protein Ndc80, which also contains a microtubule-binding calponin-homology domain and binds MTs at a non-overlapping site with a different surface (Alushin et al., 2010).

Our in vitro experiments failed to determine whether there was or was not a definitive difference in binding location between EB2 and EB1. However our binding preference experiments clearly show that there is a distinct difference between EB1/EB3 and EB2. In fact our experiments probing the binding preferences to pure and mixed nucleotide lattices suggest that EB1 has a similar preference as EB3, with EB3 having a greater

affinity to the microtubule than EB1 for all of the substrates tested. This is in contradiction to the in vitro spatial distribution experiments that clearly show that EB3 binds in front of EB1, which is in contradiction to cellular data where EB1 binds in front of EB3. Within cells it is possible that the large number of EB binding partners could further modify the position of EBs away from their intrinsically preferred binding site. The discovery of specific peptide aptamers that interact uniquely with EB1 over EB3 show the possibility of specific EB1/EB3 interaction partners (Leśniewska et al., 2014). Such interactions could have two possible effects: The binding partner could affect the binding kinetics of EBs for example by reducing the off rate, which would shift the distribution away from the tip of the microtubule. Alternatively, EBs could interact with proteins that also directly bind to the microtubule. Amongst EB interaction partners is a long list of MAPs, some of which can also track the microtubule end by an EB-independent mechanism (Buey et al., 2012; Jiang et al., 2012; Dixit et al., 2009; van der Vaart et al., 2011). Such an interaction could recruit EBs either closer to the microtubule tip or increase their affinity for the lattice and thus shift the profile further away from the microtubule tip. Differences in the affinity of the different EB family members for interaction partners can thus modulate their binding profile in cells in addition to the accumulation at their intrinsically preferred binding sites. EB binding can also be affected by non-binding partners altering the microtubule lattice. Microtubule grown in the presence of CLASP have been shown to increase the EB1 tip to lattice intensity ratio when compared to microtubules grown in the absence of CLASP, Appendix B, (Grimaldi et al., 2014). A reduction/increase in lattice binding for one of the EBs would result in the EB comet appearing to move forward/backwards on the microtubule relative to the microtubule tip.

These results bring into question the de facto assumption that EB proteins are a marker for GTP-tubulin within the microtubule, (Seetapun et al., 2012). It is entirely possible that none of the EB proteins binds to GTP-tubulin. The closest that EB3 binds to the microtubule tip in our EB localisation experiments is $\sim$100 nm. Likewise, experiments in cells reported a distance of 100 nm between EB1 and XMAP215, the latter being thought to bind to the very tip of the microtubule by recognising the protruding beta-tubulin (Nakamura et al., 2012). This finding is in agreement to in vitro experiments also showing a positional difference between EB1 and XMAP215 (Maurer et al., 2014). Based on the

distribution of GTP following a coupled-random hydrolysis model (Bowne Anderson et al., 2013), which is comparable to our model used here, it is unlikely that GTP-tubulin would be distributed in the lattice as binding sites for EB proteins. Having said this, one cannot exclude that structural determinants other than nucleotide status influence the EB binding site and that EB1/EB3 recognise a subset of GTP-tubulin dimers further away from the tip.

An alternative explanation for the difference in EB binding position on the microtubule is based on the observation that EB1 accelerates both the generation and the removal of its binding site (Maurer et al., 2014). If there are differences in EB1 and EB3 with regards to their ability to modify the conformation of the microtubule lattice, a spatial shift in their binding site could be explained without the requirement for a different conformation of the binding site itself. Maurer et al. (2014) show that the EB1 comet moves closer to the microtubule tip with increasing concentration of EB1. We did not find this in our experiments, but there is a notable difference in the range of concentrations used. Maurer et al. (2014) used 1 nM to 50 nM of EB1, while we used concentrations in the physiologically more relevant range of 100 nM to 500 nM. Both results would be consistent if the activity resulting in the acceleration of the EB binding site formation at the microtubule tip was saturated at concentrations above 100 nM. Additional differences in the constructs used (chemically labelled versus GFP fusion, tag position and buffer differences) could also underlie the differences. In fact, EB1 has a much lower binding affinity to microtubules in our hands – in line with its behaviour in cells, than the N-terminally His-tagged construct used in other laboratories (Maurer et al., 2011; Skube et al., 2010; Vitre et al., 2008). Thus additional experiments are required to understand the concentration-dependence of the EB binding position.

It has been proposed that the mechanism underlying the maturation of the EB binding site is coupled to GTP hydrolysis and that EBs stimulate GTP hydrolysis at the E-site (Zhang et al., 2015). Direct evidence for that is provided by the fact that GMP-CPP-microtubules assembled in the presence of EB3 lack the Mg_2^+ ion and the γ-Phosphate in the cryo-EM structure (Zhang et al., 2015). Whether EB3 directly binds to GTP-tubulin or an intermediary state is not fully understood, but the binding of EB3 causes a lattice compaction that promotes a twist in the lattice. The lattice compaction could influence

events away from the EB binding site by causing a local re-arrangement in residues from α and β-tubulin around the E-site catalysing hydrolysis. As EB proteins preferentially bind to this intermediary state it has been proposed that they preferentially bind to GDP-Pi state of tubulin Zhang et al. (2015).

If the EB binding site is coupled to nucleotide hydrolysis, then the binding site should move away from the tip with a greater microtubule assemble rate. We found only a weak correlation between microtubule growth speed and EB peak position in our experiments. Maurer et al. (2014) show a doubling of the tip-EB distance with roughly a doubling of the microtubule growth rate. The main difference between our experiments, and Maurer et al. (2014) experiments, is that we compared different growth speeds at the same tubulin concentration, rather than using increasing concentrations of tubulin to increase growth speed. Our limited knowledge about the rates of GTP hydrolysis and to which extent they are coupled to the distance from the microtubule tip, the lateral interactions of a given tubulin subunit and thus the structure of the microtubule end or the nucleotide state of neighbouring tubulin subunits is not sufficient to actually understand the consequences in experimental setup. However, this work suggests routes to carefully explore this area in the future.

EB3s prominence as the EB protein with the highest affinity, together with its ability to induce both an increase in growth speed and catastrophe is highly useful in a cellular context. EB3 has been shown to be up-regulated in differentiated highly polarised cells such as neurons and muscle (Straube and Merdes, 2007; Nakagawa et al., 2000). It is important that microtubules grow longer to reach the cell cortex, while maintaining the ability to undergo dynamic instability once they reach the cell boundary (Komarova et al., 2002). Depletion of EB3 in these cells causes defects in persistent microtubule growth in the cell interior as well as defects in undergoing fast transitions between microtubule growth and shrinkage at the cell cortex (Komarova et al., 2009; Straube and Merdes, 2007). This in turn results in problems with cell polarisation (Straube and Merdes, 2007).

Our results raise a number of new questions: Which structural determinants result in the different binding preferences of EB1/EB3 and EB2? How are EB1 and EB3 binding

modulated by interaction partners? Do EBs cooperate/compete in the generation/removal of their binding sites?

In conclusion we identify that the three EB proteins appear to bind to three distinct binding sites at the microtubule tip. It is unclear as to whether there is any real difference in the binding localisation between EB1 and EB2 as there are contradicting experiments, however nucleotide affinity experiments show that EB2 is a non-canonical EB protein. To explain these results a dual nucleotide model of laterally associating tubulin dimers was developed and tested, which showed that EB2 preferred a mixed binding site. Whilst we observed a positional difference between EB1 and EB3, we cannot identify any difference between them in binding preference to a range of different tubulin nucleotide combinations, other than affinity. This brings us to conclude that EB1 and EB3 likely bind to the same site and that any positional difference is due to differing effects on the maturation of their own binding site at the microtubule tip.

References

M R Adelman, G G Borisy, M L Shelanski, R C Weisenberg, and E W Taylor. Cytoplasmic filaments and tubules. *Federation proceedings*, 27(5):1186–1193, September 1968.

Anna Akhmanova and Michel O Steinmetz. Control of microtubule organization and dynamics: two ends in the limelight. *Nature reviews. Molecular cell biology*, 16(12): 711–726, December 2015.

Gregory M Alushin, Vincent H Ramey, Sebastiano Pasqualato, David A Ball, Nikolaus Grigorieff, Andrea Musacchio, and Eva Nogales. The Ndc80 kinetochore complex forms oligomeric arrays along microtubules. *Nature*, 467(7317):805–810, October 2010.

Gregory M Alushin, Gabriel C Lander, Elizabeth H Kellogg, Rui Zhang, David Baker, and Eva Nogales. High-resolution microtubule structures reveal the structural transitions in $\alpha\beta$-tubulin upon GTP hydrolysis. *Cell*, 157(5):1117–1129, May 2014.

L Amos and A Klug. Arrangement of subunits in flagellar microtubules. *Journal of cell science*, 14(3):523–549, May 1974.

Pelin Ayaz, Sarah Munyoki, Elisabeth A Geyer, Felipe-Andrés Piedra, Emily S Vu, Raquel Bromberg, Zbyszek Otwinowski, Nick V Grishin, Chad A Brautigam, and Luke M Rice. A tethered delivery mechanism explains the catalytic action of a microtubule polymerase. *eLife*, 3:e03069, 2014.

Alice Bachmann and Anne Straube. Kinesins in cell migration. *Biochemical Society transactions*, 43(1):79–83, February 2015.

James Bancroft, Philip Auckland, Catarina P Samora, and Andrew D McAinsh. Chromosome congression is promoted by CENP-Q- and CENP-E-dependent pathways. *Journal of cell science*, 128(1):171–184, January 2015.

Susanne Bechstedt and Gary J Brouhard. Doublecortin recognizes the 13-protofilament microtubule cooperatively and tracks microtubule ends. *Developmental cell*, 23(1): 181–192, July 2012.

J D Beinhauer, I M Hagan, J H Hegemann, and U Fleig. Mal3, the fission yeast homologue of the human APC-interacting protein EB-1 is required for microtubule integrity and the maintenance of cell form. *The Journal of Cell Biology*, 139(3):717–728, November 1997.

Peter Bieling, Liedewij Laan, Henry Schek, E Laura Munteanu, Linda Sandblad, Marileen Dogterom, Damian Brunner, and Thomas Surrey. Reconstitution of a microtubule plus-end tracking system in vitro. *Nature*, 450(7172):1100–1105, December 2007.

Saša Bjelić, Christian O De Groot, Martin A Schärer, Rolf Jaussi, Katja Bargsten, Mara Salzmann, Daniel Frey, Guido Capitani, Richard A Kammerer, and Michel O Steinmetz. Interaction of mammalian end binding proteins with CAP-Gly domains of CLIP-170 and p150glued. *Journal of Structural Biology*, 177(1):160–167, January 2012.

G G Borisy and E W Taylor. The mechanism of action of colchicine. Colchicine binding to sea urchin eggs and the mitotic apparatus. *The Journal of Cell Biology*, 34(2):535–548, August 1967a.

G G Borisy and E W Taylor. The mechanism of action of colchicine. Binding of colchincine-3H to cellular protein. *The Journal of Cell Biology*, 34(2):525–533, August 1967b.

Hugo Bowne Anderson, Marija Zanic, Monika Kauer, and Jonathon Howard. Microtubule dynamic instability: A new model with coupled GTP hydrolysis and multistep catastrophe. *Bioessays*, 35(5):452–461, May 2013.

J Bryan and L Wilson. Are cytoplasmic microtubules heteropolymers? *Proceedings of the National Academy of Sciences*, 68(8):1762–1766, August 1971.

Rubén M Buey, Renu Mohan, Kris Leslie, Thomas Walzthoeni, John H Missimer, Andreas Menzel, Saša Bjelić, Katja Bargsten, Ilya Grigoriev, Ihor Smal, Erik Meijering, Ruedi Aebersold, Anna Akhmanova, and Michel O Steinmetz. Insights into EB1 structure and the role of its C-terminal domain for discriminating microtubule tips from the lattice. *Molecular Biology of the Cell*, 22(16):2912–2923, August 2011.

Rubén M Buey, Indrani Sen, Oliver Kortt, Renu Mohan, David Gfeller, Dmitry Veprintsev, Ines Kretzschmar, Jörg Scheuermann, Dario Neri, Vincent Zoete, Olivier Michielin, José María de Pereda, Anna Akhmanova, Rudolf Volkmer, and Michel O Steinmetz. Sequence determinants of a microtubule tip localization signal (MtLS). *Journal of Biological Chemistry*, 287(34):28227–28242, August 2012.

M Caplow and J Shanks. Evidence that a single monolayer tubulin-GTP cap is both necessary and sufficient to stabilize microtubules. *Molecular Biology of the Cell*, 7(4): 663–675, April 1996.

M Caplow and J Shanks. Microtubule dynamic instability does not result from stabilization of microtubules by tubulin-GDP-Pi subunits. *Biochemistry*, 37(37):12994–13002, September 1998.

M F Carlier and D Pantaloni. Kinetic analysis of guanosine 5'-triphosphate hydrolysis associated with tubulin polymerization. *Biochemistry*, 20(7):1918–1924, March 1981.

Marie France Carlier, Dominique Didry, Colette Simon, and Dominique Pantaloni. Mechanism of GTP hydrolysis in tubulin polymerization: characterization of the kinetic intermediate microtubule-GDP-Pi using phosphate analogs. *Biochemistry*, 28(4): 1783–1791, February 1989.

Andrew P Carter, Aristides G Diamant, and Linas Urnavicius. How dynein and dynactin transport cargos: a structural perspective. *Current opinion in structural biology*, 37: 62–70, January 2016.

D Chasey. Subunit arrangement in ciliary microtubules from Tetrahymena pyriformis. *Experimental Cell Research*, 74(1):140–146, September 1972.

D Chrétien, F Metoz, F Verde, E Karsenti, and R H Wade. Lattice defects in microtubules: protofilament numbers vary within individual microtubules. *The Journal of Cell Biology*, 117(5):1031–1040, June 1992.

D Chrétien, S D Fuller, and E Karsenti. Structure of growing microtubule ends: two-dimensional sheets close into tubes at variable rates. *The Journal of Cell Biology*, 129(5):1311–1328, June 1995.

Christian O De Groot, Ilian Jelesarov, Fred F Damberger, Saša Bjelić, Martin A Schärer, Neel S Bhavesh, Ilia Grigoriev, Rubén M Buey, Kurt Wüthrich, Guido Capitani, Anna Akhmanova, and Michel O Steinmetz. Molecular insights into mammalian end-binding protein heterodimerization. *Journal of Biological Chemistry*, 285(8): 5802–5814, February 2010.

Alexei O Demchouk, Melissa K Gardner, and David J Odde. Microtubule tip tracking and tip structures at the nanometer scale using digital fluorescence microscopy. *Cellular and molecular bioengineering*, 4(2):192–204, June 2011.

Amédée des Georges, Miho Katsuki, Douglas R Drummond, Michael Osei, Robert A Cross, and Linda A Amos. Mal3, the Schizosaccharomyces pombe homolog of EB1, changes the microtubule lattice. *Nature structural & molecular biology*, 15(10): 1102–1108, October 2008.

A Desai and T J Mitchison. Microtubule polymerization dynamics. *Annual review of cell and developmental biology*, 13:83–117, 1997.

Ram Dixit, Brian Barnett, Jacob E Lazarus, Mariko Tokito, Yale E Goldman, and Erika L F Holzbaur. Microtubule plus-end tracking by CLIP-170 requires EB1. *Proceedings of the National Academy of Sciences of the United States of America*, 106(2):492–497, January 2009.

H P Erickson. Microtubule surface lattice and subunit structure and observations on reassembly. *The Journal of Cell Biology*, 60(1):153–167, January 1974.

Don W Fawcett and Keith R Porter. A study of the fine structure of ciliated epithelia. *Journal of Morphology*, 94(2):221–281, March 1954.

Jorge G Ferreira, António J Pereira, Anna Akhmanova, and Helder Maiato. Aurora B spatially regulates EB3 phosphorylation to coordinate daughter cell adhesion with cytokinesis. *The Journal of Cell Biology*, 201(5):709–724, May 2013.

Melissa K Gardner, Blake D Charlebois, Imre M Jánosi, Jonathon Howard, Alan J Hunt, and David J Odde. Rapid microtubule self-assembly kinetics. *Cell*, 146(4):582–592, August 2011.

Melissa K Gardner, Marija Zanic, and Jonathon Howard. Microtubule catastrophe and rescue. *Current opinion in cell biology*, 25(1):14–22, February 2013.

Deborah A Goldspink, Jonathan R Gadsby, Gemma Bellett, Jennifer Keynton, Benjamin J Tyrrell, Elizabeth K Lund, Penny P Powell, Paul Thomas, and Mette M Mogensen. The microtubule end-binding protein EB2 is a central regulator of microtubule reorganisation in apico-basal epithelial differentiation. *Journal of cell science*, 126(Pt 17):4000–4014, September 2013.

Holly V Goodson, Susan B Skube, Romaine Stalder, Caterina Valetti, Thomas E Kreis, Ewan E Morrison, and Trina A Schroer. CLIP-170 interacts with dynactin complex and the APC-binding protein EB1 by different mechanisms. *Cell Motility and the Cytoskeleton*, 55(3):156–173, July 2003.

Ashley D Grimaldi, Takahisa Maki, Benjamin P Fitton, Daniel Roth, Dmitry Yampolsky, Michael W Davidson, Tatyana Svitkina, Anne Straube, Ikuko Hayashi, and Irina Kaverina. CLASPs are required for proper microtubule localization of end-binding proteins. *Developmental cell*, 30(3):343–352, August 2014.

Ikuko Hayashi and Mitsuhiko Ikura. Crystal structure of the amino-terminal microtubule-binding domain of end-binding protein 1 (EB1). *Journal of Biological Chemistry*, 278 (38):36430–36434, September 2003.

Melissa C Hendershott and Ronald D Vale. Regulation of microtubule minus-end dynamics by CAMSAPs and Patronin. *Proceedings of the National Academy of Sciences of the United States of America*, 111(16):5860–5865, April 2014.

Srinivas Honnappa, Corinne M John, Dirk Kostrewa, Fritz K Winkler, and Michel O Steinmetz. Structural insights into the EB1-APC interaction. *The EMBO journal*, 24 (2):261–269, January 2005.

Srinivas Honnappa, Oksana Okhrimenko, Rolf Jaussi, Hatim Jawhari, Ilian Jelesarov, Fritz K Winkler, and Michel O Steinmetz. Key interaction modes of dynamic +TIP networks. *Molecular cell*, 23(5):663–671, September 2006.

T Horio and H Hotani. Visualization of the dynamic instability of individual microtubules by dark-field microscopy. *Nature*, 321(6070):605–607, June 1986.

Florian Huber, Adeline Boire, Magdalena Preciado López, and Gijsje H Koenderink. Cytoskeletal crosstalk: when three different personalities team up. *Current opinion in cell biology*, 32:39–47, February 2015.

A A Hyman, S Salser, D N Drechsel, N Unwin, and T J Mitchison. Role of GTP hydrolysis in microtubule dynamics: information from a slowly hydrolyzable analogue, GMPCPP. *Molecular Biology of the Cell*, 3(10):1155–1167, October 1992.

Kai Jiang, Grischa Toedt, Susana Montenegro Gouveia, Norman E Davey, Shasha Hua, Babet van der Vaart, Ilya Grigoriev, Jesper Larsen, Lotte B Pedersen, Karel Bezstarosti, Mariana Lince-Faria, Jeroen Demmers, Michel O Steinmetz, Toby J Gibson, and Anna Akhmanova. A proteome-wide screen for mammalian SxIP motif-containing microtubule plus-end tracking proteins. 22(19):1800–1807, October 2012.

J P Juwana, P Henderikx, A Mischo, A Wadle, N Fadle, K Gerlach, J W Arends, H Hoogenboom, M Pfreundschuh, and C Renner. EB/RP gene family encodes tubulin binding proteins. *International journal of cancer. Journal international du cancer*, 81(2): 275–284, April 1999.

Santwana Kar, Juan Fan, Michael J Smith, Michel Goedert, and Linda A Amos. Repeat motifs of tau bind to the insides of microtubules in the absence of taxol. *The EMBO journal*, 22(1):70–77, January 2003.

Miho Katsuki, Douglas R Drummond, and Robert A Cross. Ectopic A-lattice seams destabilize microtubules. *Nature communications*, 5:3094, 2014.

Irina Kaverina and Anne Straube. Regulation of cell migration by dynamic microtubules. *Seminars in cell & developmental biology*, 22(9):968–974, December 2011.

Jacob W J Kerssemakers, E Laura Munteanu, Liedewij Laan, Tim L Noetzel, Marcel E Janson, and Marileen Dogterom. Assembly dynamics of microtubules at molecular resolution. *Nature*, 442(7103):709–712, August 2006.

Yulia Komarova, Gideon Lansbergen, Niels Galjart, Frank Grosveld, Gary G Borisy, and Anna Akhmanova. EB1 and EB3 control CLIP dissociation from the ends of growing microtubules. *Molecular Biology of the Cell*, 16(11):5334–5345, November 2005.

Yulia Komarova, Christian O De Groot, Ilya Grigoriev, Susana Montenegro Gouveia, E Laura Munteanu, Joseph M Schober, Srinivas Honnappa, Rubén M Buey, Casper C

Hoogenraad, Marileen Dogterom, Gary G Borisy, Michel O Steinmetz, and Anna Akhmanova. Mammalian end binding proteins control persistent microtubule growth. *The Journal of Cell Biology*, 184(5):691–706, March 2009.

Yulia A Komarova, Ivan A Vorobjev, and Gary G Borisy. Life cycle of MTs: persistent growth in the cell interior, asymmetric transition frequencies and effects of the cell boundary. *Journal of cell science*, 115(Pt 17):3527–3539, September 2002.

Praveen Kumar and Torsten Wittmann. +TIPs: SxIPping along microtubule ends. *Trends in Cell Biology*, 22(8):418–428, August 2012.

Stefan Lakämper and Edgar Meyhöfer. Back on track - on the role of the microtubule for kinesin motility and cellular function. *Journal of muscle research and cell motility*, 27 (2):161–171, 2006.

M C Ledbetter and K R Porter. A "Microtubule" in Plant Cell Fine Structure. *The Journal of Cell Biology*, 19(1):239–250, October 1963.

Myron C Ledbetter and Keith R Porter. Morphology of Microtubules of Plant Cell. *Science*, 144(3620):872–874, May 1964.

Karolina Leśniewska, Emma Warbrick, and Hiroyuki Ohkura. Peptide aptamers define distinct EB1- and EB3-binding motifs and interfere with microtubule dynamics. *Molecular Biology of the Cell*, 25(7):1025–1036, April 2014.

E M Mandelkow, E Mandelkow, and R A Milligan. Microtubule dynamics and microtubule caps: a time-resolved cryo-electron microscopy study. *The Journal of Cell Biology*, 114 (5):977–991, September 1991.

I Manton and B Clarke. An Electron Microscope Study of the Spermatozoid of Sphagnum on JSTOR. *Journal of Experimental Botany*, 1952.

Sebastian P Maurer, Peter Bieling, Julia Cope, Andreas Hoenger, and Thomas Surrey. GTPγS microtubules mimic the growing microtubule end structure recognized by end-binding proteins (EBs). *Proceedings of the National Academy of Sciences*, 108 (10):3988–3993, March 2011.

Sebastian P Maurer, Franck J Fourniol, Gergő Bohner, Carolyn A Moores, and Thomas Surrey. EBs recognize a nucleotide-dependent structural cap at growing microtubule ends. *Cell*, 149(2):371–382, April 2012.

Sebastian P Maurer, Nicholas I Cade, Gergő Bohner, Nils Gustafsson, Emmanuel Boutant, and Thomas Surrey. EB1 accelerates two conformational transitions important for microtubule maturation and dynamics. *Current biology : CB*, 24(4):372–384, February 2014.

R Melki, M F Carlier, D Pantaloni, and S N Timasheff. Cold depolymerization of microtubules to double rings: geometric stabilization of assemblies. *Biochemistry*, 28 (23):9143–9152, November 1989.

Ronald Melki, Marie France Carlier, and Dominique Pantaloni. Direct evidence for GTP and GDP-inorganic phosphate intermediates in microtubule assembly. *Biochemistry*, 29(38):8921–8932, September 1990.

Yuko Mimori-Kiyosue, Ilya Grigoriev, Gideon Lansbergen, Hiroyuki Sasaki, Chiyuki Matsui, Fedor Severin, Niels Galjart, Frank Grosveld, Ivan Vorobjev, Shoichiro Tsukita, and Anna Akhmanova. CLASP1 and CLASP2 bind to EB1 and regulate microtubule

plus-end dynamics at the cell cortex. *The Journal of Cell Biology*, 168(1):141–153, January 2005.

T Mitchison and M Kirschner. Dynamic instability of microtubule growth. *Nature*, 312 (5991):237–242, November 1984.

H Mohri. Amino-acid composition of "Tubulin" constituting microtubules of sperm flagella. *Nature*, 217(5133):1053–1054, March 1968.

Susana Montenegro Gouveia, Kris Leslie, Lukas C Kapitein, Rubén M Buey, Ilya Grigoriev, Michael Wagenbach, Ihor Smal, Erik Meijering, Casper C Hoogenraad, Linda Wordeman, Michel O Steinmetz, and Anna Akhmanova. In vitro reconstitution of the functional interplay between MCAK and EB3 at microtubule plus ends. *Current biology : CB*, 20(19):1717–1722, October 2010.

H Nakagawa, K Koyama, Y Murata, M Morito, T Akiyama, and Y Nakamura. EB3, a novel member of the EB1 family preferentially expressed in the central nervous system, binds to a CNS-specific APC homologue. *Oncogene*, 19(2):210–216, January 2000.

Satoko Nakamura, Ilya Grigoriev, Taisaku Nogi, Tomoko Hamaji, Lynne Cassimeris, and Yuko Mimori-Kiyosue. Dissecting the nanoscale distributions and functions of microtubule-end-binding proteins EB1 and ch-TOG in interphase HeLa cells. *PloS one*, 7(12):e51442, 2012.

Agata Nawrotek, Marcel Knossow, and Benoît Gigant. The determinants that govern microtubule assembly from the atomic structure of GTP-tubulin. *Journal of Molecular Biology*, 412(1):35–42, September 2011.

Tim L Noetzel, David N Drechsel, Anthony A Hyman, and Kazuhisa Kinoshita. A comparison of the ability of XMAP215 and tau to inhibit the microtubule destabilizing activity of XKCM1. *Philosophical transactions of the Royal Society of London. Series B, Biological sciences*, 360(1455):591–594, March 2005.

E Nogales, S G Wolf, and K H Downing. Structure of the alpha beta tubulin dimer by electron crystallography. *Nature*, 391(6663):199–203, January 1998.

Meritxell Orpinell, Marjorie Fournier, Anne Riss, Zita Nagy, Arnaud R Krebs, Mattia Frontini, and Làszlò Tora. The ATAC acetyl transferase complex controls mitotic progression by targeting non-histone substrates. *The EMBO journal*, 29(14):2381–2394, July 2010.

D M Phillips. Substructure of flagellar tubules. *The Journal of Cell Biology*, 1966.

Liang Qiang, Wenqian Yu, Athena Andreadis, Minhua Luo, and Peter W Baas. Tau protects microtubules in the axon from severing by katanin. *The Journal of neuroscience : the official journal of the Society for Neuroscience*, 26(12):3120–3129, March 2006.

Markus Rehberg and Ralph Gräf. Dictyostelium EB1 is a genuine centrosomal component required for proper spindle formation. *Molecular Biology of the Cell*, 13 (7):2301–2310, July 2002.

F L Renaud, A J Rowe, and I R Gibbons. Some properties of the protein forming the outer fibers of cilia. *The Journal of Cell Biology*, 36(1):79–90, January 1968.

Luke M Rice, Elizabeth A Montabana, and David A Agard. The lattice as allosteric effector: structural studies of alphabeta- and gamma-tubulin clarify the role of GTP

in microtubule assembly. *Proceedings of the National Academy of Sciences of the United States of America*, 105(14):5378–5383, April 2008.

D D Sabatini, K Bensch, and R J Barrnett. Cytochemistry and electron microscopy. The preservation of cellular ultrastructure and enzymatic activity by aldehyde fixation. *The Journal of Cell Biology*, 17(1):19–58, April 1963.

Linda Sandblad, Karl Emanuel Busch, Peter Tittmann, Heinz Gross, Damian Brunner, and Andreas Hoenger. The Schizosaccharomyces pombe EB1 Homolog Mal3p Binds and Stabilizes the Microtubule Lattice Seam. *Cell*, 127(7):1415–1424, December 2006.

Henry T Schek, Melissa K Gardner, Jun Cheng, David J Odde, and Alan J Hunt. Microtubule assembly dynamics at the nanoscale. 17(17):1445–1455, September 2007.

R Schultheiss and E Mandelkow. Three-dimensional reconstruction of tubulin sheets and re-investigation of microtubule surface lattice. *Journal of Molecular Biology*, 170(2): 471–496, October 1983.

Dominique Seetapun, Brian T Castle, Alistair J McIntyre, Phong T Tran, and David J Odde. Estimating the microtubule GTP cap size in vivo. *Current biology : CB*, 22(18): 1681–1687, September 2012.

A Seitz. Kymograph plugin for ImageJ. URL `\url{http://biop.epfl.ch/TOOL_KYMOGRAPH.html}`.

Indrani Sen, Dmitry Veprintsev, Anna Akhmanova, and Michel O Steinmetz. End binding proteins are obligatory dimers. *PloS one*, 8(9):e74448, 2013.

M L Shelanski and E W Taylor. Isolation of a protein subunit from microtubules. *The Journal of Cell Biology*, 34(2):549–554, August 1967.

Susan B Skube, José M Chaverri, and Holly V Goodson. Effect of GFP tags on the localization of EB1 and EB1 fragments in vivo. *Cytoskeleton*, 67(1):1–12, January 2010.

Kevin C Slep and Ronald D Vale. Structural basis of microtubule plus end tracking by XMAP215, CLIP-170, and EB1. *Molecular cell*, 27(6):976–991, September 2007.

Kevin C Slep, Stephen L Rogers, Sarah L Elliott, Hiroyuki Ohkura, Peter A Kolodziej, and Ronald D Vale. Structural determinants for EB1-mediated recruitment of APC and spectraplakins to the microtubule plus end. *The Journal of Cell Biology*, 168(4): 587–598, February 2005.

Ihor Smal, Ilya Grigoriev, Anna Akhmanova, Wiro J Niessen, and Erik Meijering. Microtubule dynamics analysis using kymographs and variable-rate particle filters. *IEEE transactions on image processing : a publication of the IEEE Signal Processing Society*, 19(7):1861–1876, July 2010.

Virupakshi Soppina, Jeffrey F Herbstman, Georgios Skiniotis, and Kristen J Verhey. Luminal localization of α-tubulin K40 acetylation by cryo-EM analysis of fab-labeled microtubules. *PloS one*, 7(10):e48204, 2012.

Martin Srayko, Eileen T O'toole, Anthony A Hyman, and Thomas Müller-Reichert. Katanin disrupts the microtubule lattice and increases polymer number in C. elegans meiosis. *Current biology : CB*, 16(19):1944–1949, October 2006.

Tatiana Stepanova, Jenny Slemmer, Casper C Hoogenraad, Gideon Lansbergen, Bjorn Dortland, Chris I De Zeeuw, Frank Grosveld, Gert van Cappellen, Anna Akhmanova,

and Niels Galjart. Visualization of microtubule growth in cultured neurons via the use of EB3-GFP (end-binding protein 3-green fluorescent protein). *The Journal of neuroscience : the official journal of the Society for Neuroscience*, 23(7):2655–2664, April 2003.

Anne Straube and Andreas Merdes. EB3 regulates microtubule dynamics at the cell cortex and is required for myoblast elongation and fusion. 17(15):1318–1325, August 2007.

Anne Straube, Marianne Brill, Berl R Oakley, Tetsuya Horio, and Gero Steinberg. Microtubule organization requires cell cycle-dependent nucleation at dispersed cytoplasmic sites: polar and perinuclear microtubule organizing centers in the plant pathogen Ustilago maydis. *Molecular Biology of the Cell*, 14(2):642–657, February 2003.

Anne Straube, Gerd Hause, Gero Fink, and Gero Steinberg. Conventional kinesin mediates microtubule-microtubule interactions in vivo. *Molecular Biology of the Cell*, 17(2):907–916, February 2006.

L K Su and Y Qi. Characterization of human MAPRE genes and their proteins. *Genomics*, 71(2):142–149, January 2001.

Ulrike Theisen, Ekkehard Straube, and Anne Straube. Directional persistence of migrating cells requires Kif1C-mediated stabilization of trailing adhesions. *Developmental cell*, 23(6):1153–1166, December 2012.

L G Tilney, J Bryan, D J Bush, K Fujiwara, M S Mooseker, D B Murphy, and D H Snyder. Microtubules: evidence for 13 protofilaments. *The Journal of Cell Biology*, 59(2 Pt 1): 267–275, November 1973.

J S Tirnauer, E O'Toole, L Berrueta, B E Bierer, and D Pellman. Yeast Bim1p promotes the G1-specific dynamics of microtubules. *The Journal of Cell Biology*, 145(5):993–1007, May 1999.

P T Tran, R A Walker, and E D Salmon. A metastable intermediate state of microtubule dynamic instability that differs significantly between plus and minus ends. *The Journal of Cell Biology*, 138(1):105–117, July 1997.

Babet van der Vaart, Cristina Manatschal, Ilya Grigoriev, Vincent Olieric, Susana Montenegro Gouveia, Saša Bjelić, Jeroen Demmers, Ivan Vorobjev, Casper C Hoogenraad, Michel O Steinmetz, and Anna Akhmanova. SLAIN2 links microtubule plus end-tracking proteins and controls microtubule growth in interphase. *The Journal of Cell Biology*, 193(6):1083–1099, June 2011.

Babet van der Vaart, Mariella A M Franker, Marijn Kuijpers, Shasha Hua, Benjamin P Bouchet, Kai Jiang, Ilya Grigoriev, Casper C Hoogenraad, and Anna Akhmanova. Microtubule plus-end tracking proteins SLAIN1/2 and ch-TOG promote axonal development. *The Journal of neuroscience : the official journal of the Society for Neuroscience*, 32(42):14722–14728, October 2012.

Vincent VanBuren, David J Odde, and Lynne Cassimeris. Estimates of lateral and longitudinal bond energies within the microtubule lattice. *Proceedings of the National Academy of Sciences*, 99(9):6035–6040, April 2002.

P Venier, A C Maggs, M F Carlier, and D Pantaloni. Analysis of microtubule rigidity using hydrodynamic flow and thermal fluctuations. *Journal of Biological Chemistry*, 269(18): 13353–13360, May 1994.

Juan Jesus Vicente and Linda Wordeman. Mitosis, microtubule dynamics and the evolution of kinesins. *Experimental Cell Research*, 334(1):61–69, May 2015.

Benjamin Vitre, Frédéric M Coquelle, Claire Heichette, Cyrille Garnier, Denis Chrétien, and Isabelle Arnal. EB1 regulates microtubule dynamics and tubulin sheet closure in vitro. *Nature cell biology*, 10(4):415–421, April 2008.

R A Walker, E T O'Brien, N K Pryer, M F Soboeiro, W A Voter, H P Erickson, and E D Salmon. Dynamic instability of individual microtubules analyzed by video light microscopy: rate constants and transition frequencies. *The Journal of Cell Biology*, 107(4):1437–1448, October 1988.

R A Walker, N K Pryer, and E D Salmon. Dilution of individual microtubules observed in real time in vitro: evidence that cap size is small and independent of elongation rate. *The Journal of Cell Biology*, 114(1):73–81, July 1991.

Geoffrey O Wasteneys. Microtubule organization in the green kingdom: chaos or self-order? *Journal of cell science*, 115(Pt 7):1345–1354, April 2002.

Anke Weisbrich, Srinivas Honnappa, Rolf Jaussi, Oksana Okhrimenko, Daniel Frey, Ilian Jelesarov, Anna Akhmanova, and Michel O Steinmetz. Structure-function relationship of CAP-Gly domains. *Nature structural & molecular biology*, 14(10):959–967, October 2007.

R C Weisenberg. Microtubule formation in vitro in solutions containing low calcium concentrations. *Science*, 177(4054):1104–1105, September 1972.

R C Weisenberg, W J Deery, and P J Dickinson. Tubulin-nucleotide interactions during the polymerization and depolymerization of microtubules. *Biochemistry*, 15(19): 4248–4254, September 1976.

Hiroaki Yajima, Toshihiko Ogura, Ryo Nitta, Yasushi Okada, Chikara Sato, and Nobutaka Hirokawa. Conformational changes in tubulin in GMPCPP and GDP-taxol microtubules observed by cryoelectron microscopy. *The Journal of Cell Biology*, 198(3):315–322, August 2012.

Marija Zanic, Jeffrey H Stear, Anthony A Hyman, and Jonathon Howard. EB1 recognizes the nucleotide state of tubulin in the microtubule lattice. *PloS one*, 4(10):e7585, 2009.

Marija Zanic, Per O Widlund, Anthony A Hyman, and Jonathon Howard. Synergy between XMAP215 and EB1 increases microtubule growth rates to physiological levels. *Nature cell biology*, 15(6):688–693, June 2013.

Rui Zhang, Gregory M Alushin, Alan Brown, and Eva Nogales. Mechanistic origin of microtubule dynamic instability and its modulation by EB proteins. *Cell*, 162(4): 849–859, August 2015.

Chapter A

Straube Lab Unpublished Results

This appendix presents unpublished results essential for the either background information or informed key decisions throughout the thesis. Three results are presented here with little discussion.

Firstly, microtubule growth parameters in the presence of the three EB proteins all at 100 nM. Essential for acknowledging the paradoxical effect of EB3 that led to the first research question that was looked at in Chapter 3.

Secondly, the shape and offset of the three EB protein profiles imaged in C2C12 and RPE1 cells, which informed the second research question, Chapter 4.

Thirdly, the affinity of EB proteins to different nucleotide substrates. This helped to inform differences between the EB proteins and help develop thought towards the dual recognition model.

All the results in this section are unpublished results produced by the Straube lab either prior to my joining of the lab or within the first year. They have strongly informed some the decision made throughout this thesis and underpin the basic research questions which I have sought to answer. The results presented here was due to the work done by Daniel Roth and Anne Straube.

	Control	100 nM EB1	100 nM EB2	100 nM EB3
GFP tip intensity (x10^3)	N/A	4.9±1.9	14.8±4.5	47.3±4.7
growth rate (nm/s)	9.3±7.4	9.5±8.1	13.0±8.8	16.4±8.9
shrinkage rate (nm/s)	24±35	20±36	27±49	67±54
catastrophe freq (min^{-1})	0.002	0.002	0.006	0.107
rescue freq (min^{-1})	1.8	4.8	1.9	4.2
percent time spent in				
pause	21.6	17.1	12.5	10.4
growth	78.3	82.8	87.2	87.3
shrinkage	0.12	0.04	0.28	2.3
dynamicity (dimers/s)	11.9	12.9	18.6	25.8
number of microtubules	181	116	162	126

Table A.1: **Microtubule dynamics parameters in the presence of different EB proteins.** Pause is defined as phases with rate of length change $<$1nm/s. Catastrophe is defined as shrinkage eventsfollowing growth or pause. Rescue is defined as growth event following shrinkage. The transition frequencies are given as (number of events)/(total time in pre-transition phase(s)). Data shown are pooled from 116-187 microtubules, each observed for 10 minutes at 1 fps (600 data points) from two independent experiments. Frame-to-frame growth and shrinkage rates are given as mean values ± SD. Values with an orange background are significantly different from control at level 0.05 or below (two-sample Kolmogorov-Smirnov test). Values with a blue background are more than 10-fold different from control.

A.1 Affect of EB proteins on microtubule growth parameters

To test the effect of EB proteins on microtubule dynamics, a fixed concentration of 100 nM EB1-GFP, EB2-GFP and EB3-GFP was added to labelled dynamic microtubules and imaged via TIRF microscopy. The different EBs were compared to control, using the same conditions with EB storage buffer replacing the EB protein. Dual colour kymographs were created from the raw image files. Segmented lines were drawn following the microtubule tip location in each kymograph. The co-ordinates of the segments were saved and passed to a routine in MATLAB which automatically extracted microtubule growth parameters. A summary of the effects on microtubules by the three different EB proteins, and the control is shown in Table A.1.

Each protein shows a differing affinity to the microtubule tip as shown by the change in intensity to the microtubule tip. EB3 shows the greatest affinity to the microtubule, and EB1 the weakest. All three EB proteins have a significant effect on the growth speed of the microtubule, with the order of the increase in growth speed correlating to the order in affinity. EB3 causes the greatest effect to an increase in growth speed and EB1 the least. The same trend is true for the shrinkage rate, catastrophe frequency and the dynamicity of the microtubule. EB3 has a significant affect on the shrinkage rate of the microtubule, and a 10 fold increase in catastrophe frequency over control. EB3 and EB1 both increase the rescue frequency of the microtubule while EB2 has a little effect. All three proteins caused an decrease in the percentage of time the microtubule spent in a paused state, and an increase in the percentage of time spent in a growth state.

EB3s high affinity to the microtubule correlates to its ability in having a potent effect on the microtubule dynamics. Whether the other two EBs would have a similar effect on microtubule dynamics if the tip intensities were matched is unknown. For EB2 it is unlikely as it has little effect on rescue frequency whilst EB1 and EB3 both show an effect. EB3 shows a paradoxical effect on microtubule dynamics by both increasing growth speed, which should increase the size of the GTP cap stabilising the microtubule. Conversely,

EB3 also increases catastrophe frequency which is evident of a destabilising effect on the microtubule.

A.2 Differences between EB protein binding profiles in the cellular environment

Lower eukaryotes express only one EB protein (Straube et al., 2003; Rehberg and Gräf, 2002; Beinhauer et al., 1997), while mammalian cells have three EB homologues: EB1 is ubiquitously expressed, but EB2 and EB3 are differentially regulated (Su and Qi, 2001; Straube and Merdes, 2007). The three different EB proteins have also been shown to have differential cellular functions (Ferreira et al., 2013; Komarova et al., 2005; Straube and Merdes, 2007). This raises the possibility that specific cellular functions of EB1, EB2 and EB3 are conferred by differential MT binding properties of EB proteins themselves. To test this idea, MT plus end localisation of EB1, EB2 and EB3 in interphase cells was carefully investigated.

To do this, C2C12 and RPE1 cells were fixed and simultaneously stained with specific EB1, EB2 and EB3 antibodies, Figure A.1.A. Line-scans along the MT end were aligned and averaged using the pixel closest to the mean location of the first half-maximum intensity values for EB1 and EB3 as reference point, Figure A.1.B. To exclude any effects due to different properties of fluorophores and chromatic aberration, data was averaged from experiments using different combinations of secondary antibodies. EB1 and EB3 show a similar shaped curve with a half-maximal width of about 1 μm. Interestingly, the EB1 peak was found to be located closer to the MT tip than the EB3 peak with a mean difference of 145 nm (p=8.8x10-4, paired t-test). The positional difference holds true in different cell types, as illustrated by data from mouse myoblasts (C2C12) and human retinal pigment epithelial cells (RPE1), Figure A.1.C. EB2 localised to a several micron wide region with a broad peak 400-700 nm distal from the reference point, consistent with previous findings Komarova et al. (2009). Depletion of individual EB proteins did not significantly alter the peak locations of any of the EBs. Instead the amount of the other EB proteins bound to the microtubule was affected, Figure A.1.D. In some cases, an increase

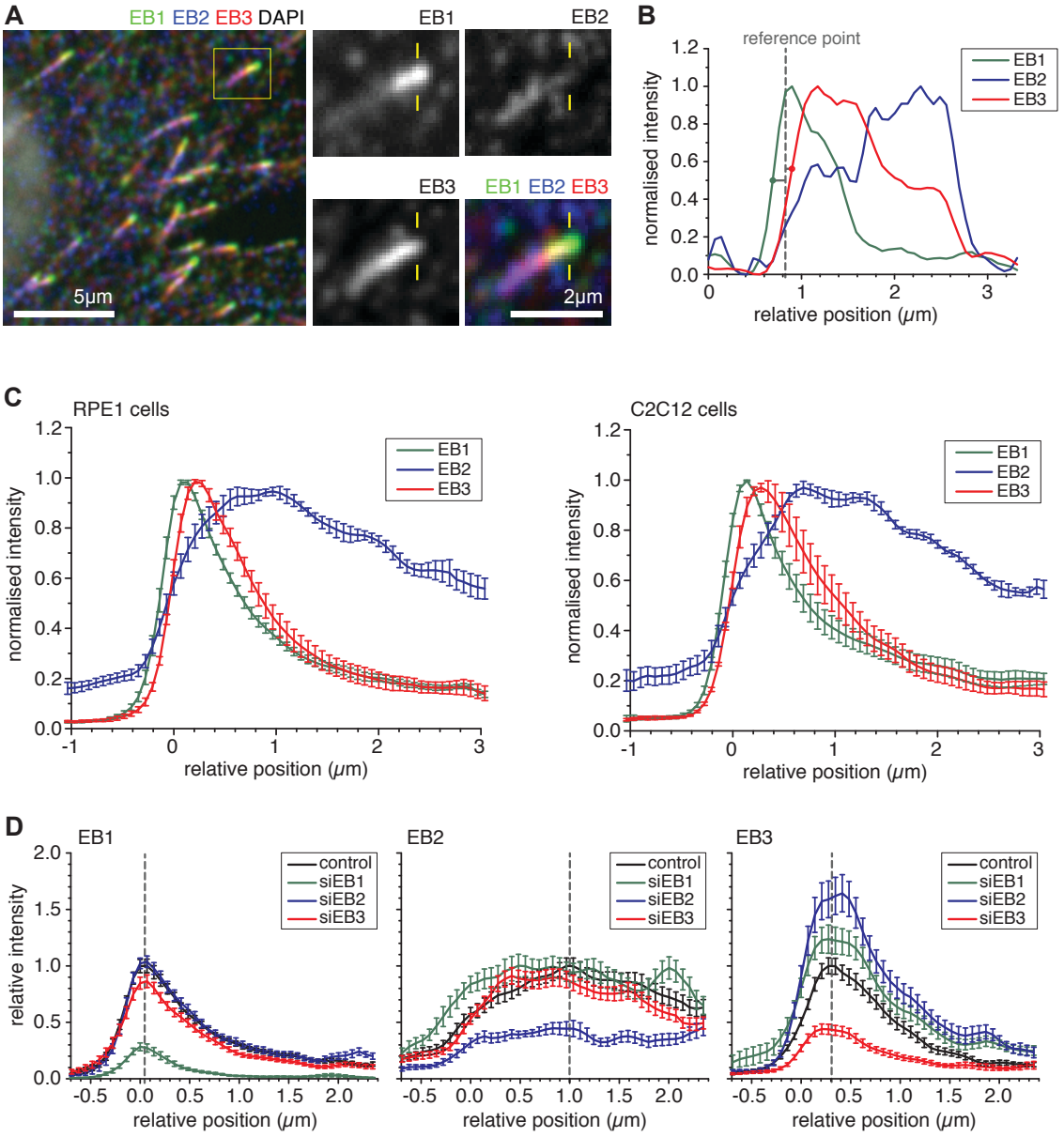

Figure A.1: **EB1, EB2 and EB3 localise sequentially to the microtubule end.** (A) Immunolocalisation of EB1, EB2 and EB3 in C2C12 cells. (B) Line profile of EB1, EB2 and EB3 along the microtubule shown in zoomed section in A. Microtubule plus end is on the left. Intensity values were normalised for each protein. (C) Averaged line profiles of EB1, EB2 and EB3 in different cell types. Data from different microtubules were aligned at the midpoint between the first half-maximal values for EB1 and EB3 (position = 0 μm). Averaged values show data from 4-6 experiments using different combinations of fluorophores to exclude chromatic shift artifacts. n 50 lines from 5 cells per experiment. Error bars represent SD. (D) Averaged line profile of EB1, EB2 and EB3 in RPE1 cells treated with control, EB1, EB2 and EB3 siRNA as indicated. Data shown are from one representative experiment and normalised to the peak intensity in control RNAi. Error bars represent SEM.

in the binding of a not-targeted EB protein was observed. This suggests that EB proteins have limited competion for binding sites at the MT tip. The absence of a localisation shift following depletion suggests that competition with each other is not sufficient to explain the differences in MT tip localisation observed.

A.3 Affinity of EB proteins to different nucleotide substrates

The three EB proteins are though to recognise the microtubule in a nucleotide dependent manner, (Maurer et al., 2012, 2011). EB1 and its S. pombe homologue Mal3 preferentially bind to microtubule lattices composed entirely of tubulin bound to GTP mimics, GMP-CPP (Guanosine-5'-(α,β-methyleno)triphosphate) and GTPγS (Guanosine-5'-(γ-thio)-triphosphate) (Maurer et al., 2012, 2011; Zanic et al., 2009; Buey et al., 2011). To determine whether the different EBs have different nucelotide preferences, the binding affinity of EB1, EB2 and EB3 to different tubulin substrates was calculated. In order to accurately assess the affinities to the different substrates relative to each other, specialised seeds that contained both GMP-CPP and GTPγS were created GMP-CPP seeds were created as normal, and following polymerisation, pelleted, resuspended in a reaction mix containing GTPγS equilibrated tubulin and left to polymerise for an hour. To differentiate between the GMP-CPP and GTPγS regions on the seed, each nucleotide was equilibrated with a different chemically labelled tubulin, GMP-CPP was equilibrated with HiLyte 647™-labelled tubulin, and GTPγS with X-rhodamine-labelled tubulin.

These barcode nucleotide seeds were used in the standard assay with 12 μM GTP-tubulin, Figure A.3. A range of concentrations (50 nM (EB3 only), 100 nM, 200 nM 400 nM, 600 nM, 800 nM and 1.2 μM) was used for each EB; EB1-GFP, EB2-GFP, and EB3-GFP. Using the modified seeds with dynamics microtubules on a TIRF microscopy it was possible to simultaneously observe EB binding to four different tubulin substrates, Figure A.2 A-B. The four substrates are MT lattices with GMP-CPP, GTPγS, GDP tubulin, and the tips that are a mix of GDP/Pi and GTP tubulin, Figure A.2 A-B.

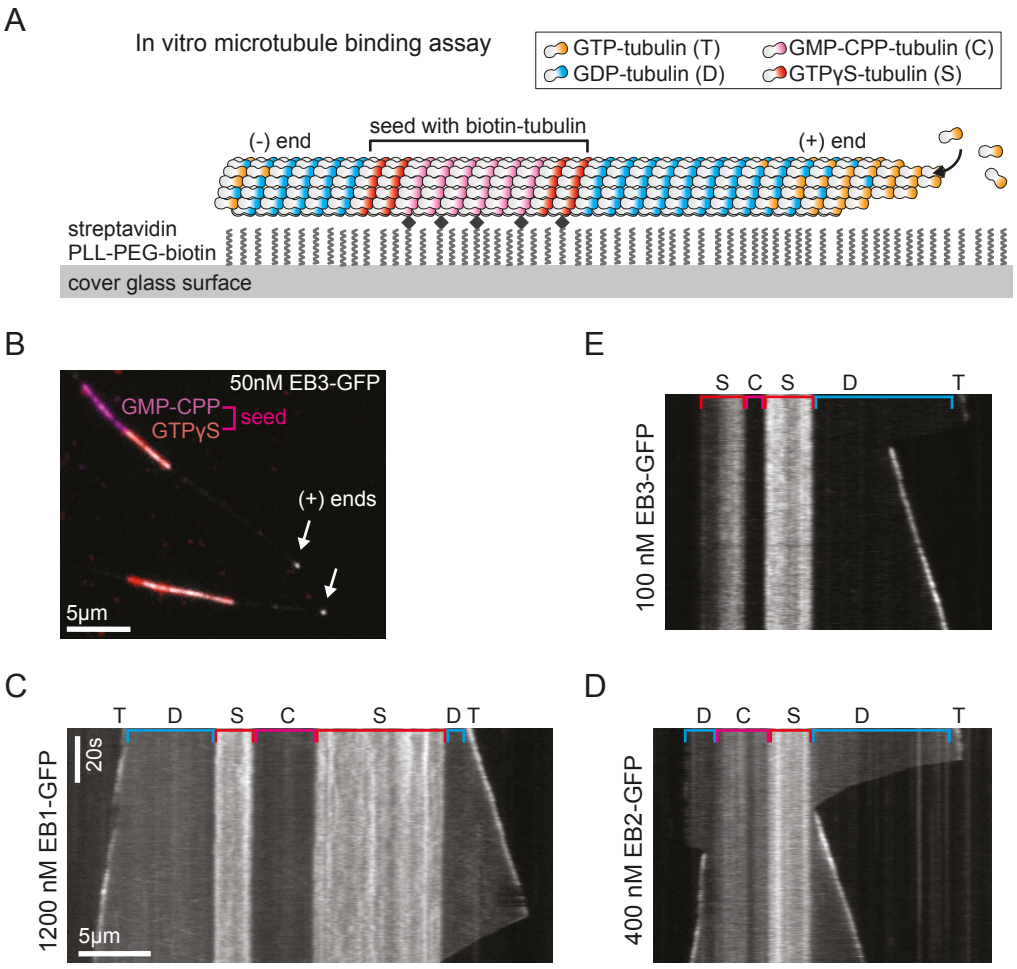

Figure A.2: **Affinity of EB proteins to different nucleotide lattices examples:** (A) Representation of TIRF microscope dynamic microtubule assay. Creation of a microtubule containing 4 different nucelotide substrates. Standard GMP-CPP microtubule seeds are extended with GTP-γS before being placed in a standard dynamics assay chamber. For visual purposes GMP-CPP is equilibrated with Alexa 640 tubulin, and GTP-γS with X-Rhodamine label tubulin. (B) Example microscope image showing a dynamic end growing away from a two-colour seed. (C-E) Example kymographs from TIRF images showing the difference in affinity to the different substrates.The different concentrations of EB1-GFP, EB2-GFP and EB3-GFP have been selected that show comparable plus tip labelling. Different substrates are indicated with single-letter codes as in A.

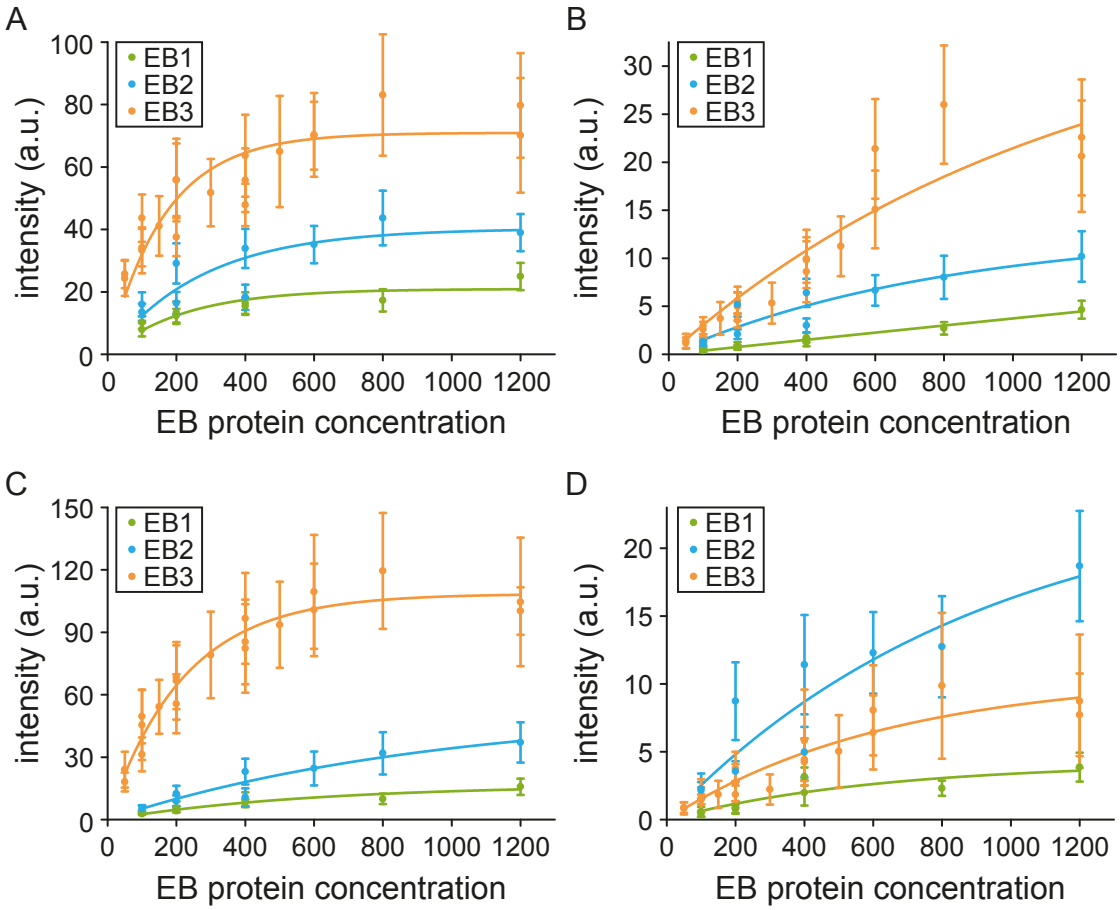

Figure A.3: **Affinity of EB proteins to different nucleotide lattices:** (A-D) Protein concentration dependent binding curves for EB1-GFP, EB2-GFP and EB3-GFP on four different microtubule substrates: (A) Microtubule tips; (B) GDP tubulin; (C) GTPγS tubulin; (D) GMP-CPP tubulin. Intensity measured as fluorescence intensity from TIRF image sequences. Note that GMP-CPP and GTP-γS substrates contain labelled tubulin, which reduces available binding sites to about 70%.

Under the conditions and concentrations used saturation was only observed with EB3-GFP binding to GTP-tubulin and GTPγS-tubulin, Figure A.3A and C. By assuming similar binding capacity to each substrate for the other combinations, it is possible to use the slope of the binding curves as an indication relevant binding affinity. Using this assumption EB3 has the highest affinity to the GTP-tubulin, GDP-tubulin and GTPγS-tubulin, followed by EB2 and then EB1. However, this is not the case for GMP-CPP tubulin as it is preferentially bound to by EB2, with EB3 and EB1 showing less affinity, Figure A.3. These results back up the endogenous levels of EBs measured in cells, as they demonstrate that EB3 has the highest affinity to microtubule tips, and EB1 the weakest affinity.

Chapter B

Paper: CLASPs are Required for Proper Microtubule Localization of End Binding Proteins

As part of my PhD I was asked to get involved in a collaboration looking at the interaction between EB proteins and CLASP. Within the cellular environment, when CLASP proteins are depleted, EB3 localisation is changed. Instead of being localised at the microtubule tip, EB3 is now dispersed along the microtubule lattice. It was discovered that it was the TOG2, MT binding, domain that was sufficient to restore normal EB localisation within cells. Neither the EB binding domain or other EB associating proteins were required for restoring normal EB localisation. To see whether this was an inherent ability of CLASP proteins it was decided to test this whether the same effect was observable in vitro. For carrying out in-vitro plus tip tracking assays the Straube lab was asked to help out.

Obtaining the correct imaging conditions, and concentrations of proteins required significant trial error and was a joint effect between myself and Daniel Roth. Chamber creation and imaging of two of the repeats used in the paper, and the analysis was mine. Daniel Roth and Anne Straube imaged the first repeat. 600 nM EB1-ΔT -GFP (EB1(1-139)-GCN4-GFP) was added to dynamic microtubules (13 μM tubulin) nucleated of HiLyte 647™-labelled GMPCPP-tubulin seeds. 30 nM CLASP2 or CLASP storage buffer was added to the dynamic imaging chambers to allow for comparison between control (buffer) and CLASP2 chambers. Analysis was conducted by background subtracting the raw images using a rolling ball. From the background subtracted images, kymographs were created to include background, tip, lattice and GMP-CPP seed. From these kymographs, growth regions were identified. For each growth region the average

EB1 intensity was measured at the tip (line width of 3), at the lattice (rectangular ROI), and for the background (rectangular ROI). The average intensity before the tip was subtracted as background. The resulting values for lattice and tip intensity were then used to generate lattice to tip ratios.

It was also discovered that CLASP depletion led to an increase in the number of GTP islands on the microtubule lattice. From these results Grimaldi et al. (2014) concluded that CLASP is responsible for removing GTP islands and any resulting conformation changes from the microtubule lattice. This removes the binding sites that EB1 recognises on the microtubule lattice, and EB1 binding is removed from the MT lattice. As such CLASP is required for proper localisation of EB proteins to microtubule tips within cells.

Developmental Cell
Short Article

CLASPs Are Required for Proper Microtubule Localization of End-Binding Proteins

Ashley D. Grimaldi,[1] Takahisa Maki,[2] Benjamin P. Fitton,[4] Daniel Roth,[4] Dmitry Yampolsky,[1] Michael W. Davidson,[3] Tatyana Svitkina,[5] Anne Straube,[4] Ikuko Hayashi,[2] and Irina Kaverina[1,*]
[1]Department of Cell and Developmental Biology, Vanderbilt University Medical Center, Nashville, TN 37232, USA
[2]Department of Medical Life Science, Yokohama City University, 1-7-29 Suehiro, Tsurumi, Yokohama 230-0045, Japan
[3]National High Magnetic Field Laboratory and Department of Biological Science, Florida State University, Tallahassee, FL 32310, USA
[4]Centre for Mechanochemical Cell Biology, Warwick Medical School, University of Warwick, Coventry CV4 7AL, UK
[5]Department of Biology, University of Pennsylvania, Philadelphia, PA 19104, USA
*Correspondence: irina.kaverina@vanderbilt.edu
http://dx.doi.org/10.1016/j.devcel.2014.06.026

SUMMARY

Microtubule (MT) plus-end tracking proteins (+TIPs) preferentially localize to MT plus ends. End-binding proteins (EBs) are master regulators of the +TIP complex; however, it is unknown whether EBs are regulated by other +TIPs. Here, we show that cytoplasmic linker-associated proteins (CLASPs) modulate EB localization at MTs. In CLASP-depleted cells, EBs localized along the MT lattice in addition to plus ends. The MT-binding region of CLASP was sufficient for restoring normal EB localization, whereas neither EB-CLASP interactions nor EB tail-binding proteins are involved. In vitro assays revealed that CLASP directly functions to remove EB from MTs. Importantly, this effect occurs specifically during MT polymerization, but not at preformed MTs. Increased GTP-tubulin content within MTs in CLASP-depleted cells suggests that CLASPs facilitate GTP hydrolysis to reduce EB lattice binding. Together, these findings suggest that CLASPs influence the MT lattice itself to regulate EB and determine exclusive plus-end localization of EBs in cells.

INTRODUCTION

Microtubules (MTs) are inherently polar structures polymerized from GTP-tubulin heterodimers, which incorporate at the growing MT plus end. Plus-end tracking proteins (+TIPs) are a diverse group of conserved MT-associated proteins (MAPs) that specifically localize to the dynamic tips of MTs (Schuyler and Pellman, 2001). +TIPs are ideally positioned to regulate MT dynamics and many important MT-based processes. Of the +TIPs, end-binding proteins (EBs) are notable in their ability to autonomously recognize a transient feature at plus ends with great specificity (Bieling et al., 2007). In mammalian cells, there are three EB family members: EB1, EB2, and EB3. EB1 and EB3 are well studied and are similar in their structure, localization, and behavior, whereas EB2 is more divergent (Buey et al., 2011; Komarova et al., 2009). Recent work has revealed that EBs localize to MT tips by sensing the nucleotide-state, as well as the specific conformation, of tubulin at MT plus ends (Maurer et al., 2011, 2012; Zanic et al., 2009). The majority of +TIPs require binding to the EB tail region, via various localization signals (SxIP, Honnappa et al., 2009; or CAP-Gly, Weisbrich et al., 2007), to achieve their specific comet-like localization (Akhmanova and Steinmetz, 2008); for this reason, EBs are considered the master regulators of the MT +TIP network.

Within this network, CLASPs are a unique class of +TIPs that exhibit two specific MT localizations. CLASPs support MT growth by binding plus ends and promoting rescues (Akhmanova et al., 2001; Mimori-Kiyosue et al., 2005). CLASPs also stabilize MT subsets by binding along the MT lattice, for example pioneer MTs at the leading edge (Wittmann and Waterman-Storer, 2005) and Golgi-derived MTs (Efimov et al., 2007; Miller et al., 2009). In mammalian cells, there are two redundant CLASP family members, CLASP1 and CLASP2, which rely on EB interactions (via the basic/SxIP region) to localize to MT tips (Mimori-Kiyosue et al., 2005). In fission yeast, although CLASP associates with EB1, its stabilizing effect on MTs is independent of other +TIPs suggesting that CLASP directly regulates MTs (Bratman and Chang, 2007). Of note, CLASPs also independently bind tubulin heterodimers and associate with the MT lattice through their TOG (tumor-overexpressed gene) domains (Al-Bassam et al., 2007, 2010). Here, we report evidence that CLASPs are crucial determinants of proper EB localization at MTs in cells.

RESULTS

EB Proteins Localize to the MT Lattice in CLASP-Depleted Cells

Although it is well established that EBs are the master regulators of the MT +TIP network, it is unknown whether other +TIPs regulate EB localization at MTs. Strikingly, we found that, upon depletion of CLASP1 and CLASP2 (herein referred to as CLASPs), endogenous EB1 (Figures S1A and S1B available online), and EB3 (Figures 1A and 1B) both bind along the MT lattice in addition to their tip localizations. This dramatic change is quantified by line scan analysis of EB fluorescence intensity along MTs (Figure 1H). CLASP-dependent EB redistribution was observed in multiple cell types and is therefore not cell type specific: A7r5 (Figures 1A, 1B, S1A, and S1B), RPE1 (Figures 2A and 2B),

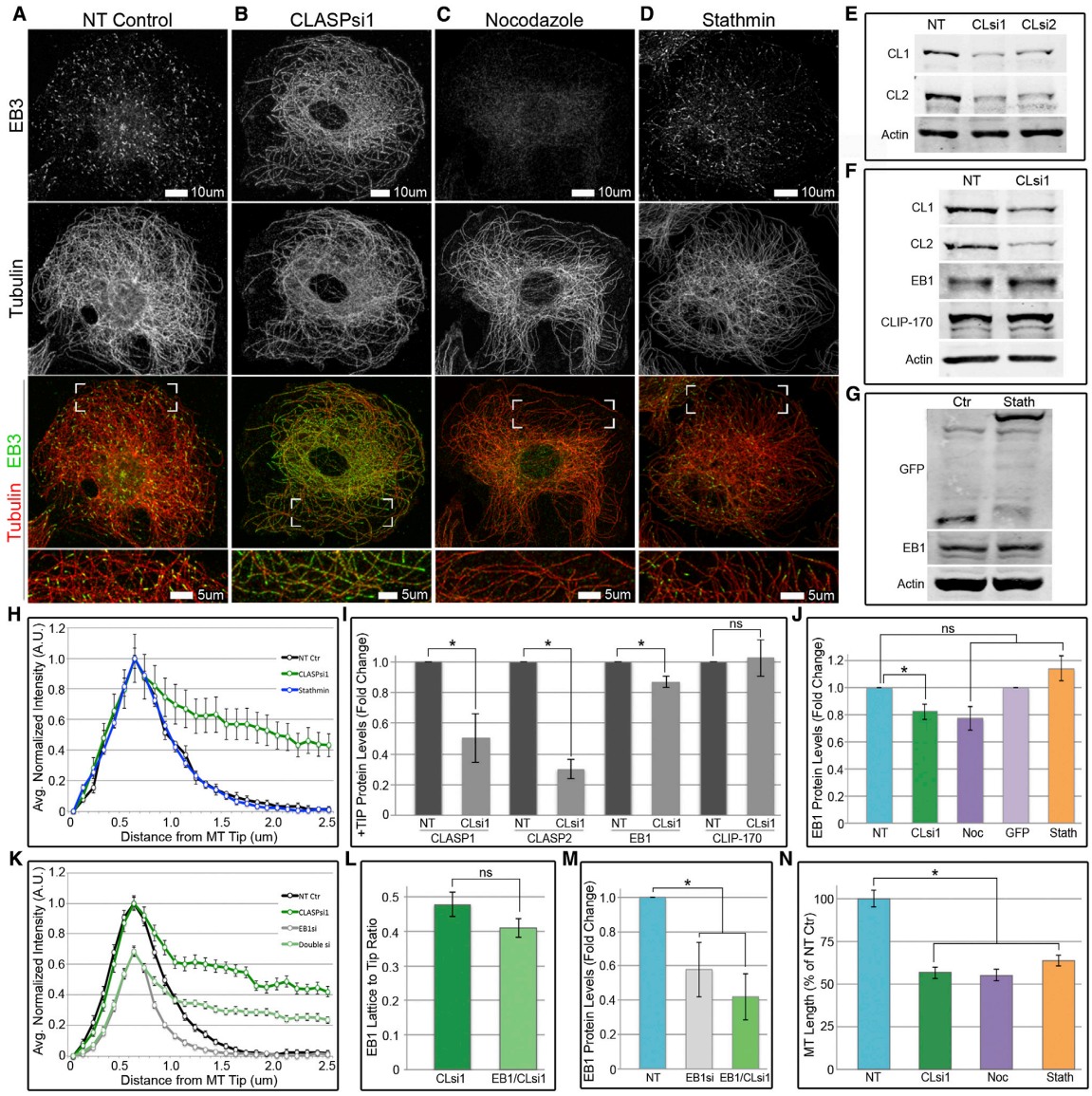

Figure 1. Localization of EB Proteins at Microtubules Is Altered in CLASP-Depleted Cells

(A–D) Immunofluorescence images of A7r5 cells stained for α-tubulin (red) and EB3 (green). (A) EB3 localizes to MT plus ends in NT control cells. (B) EB3 coats the MT lattice, in addition to its plus-end localization, in CLASP-depleted cells. (C) EB3 does not significantly localize to the lattice in Nocodazole-treated cells. (D) EB3 localizes to MT plus ends in GFP-stathmin expressing cells. Boxed corners indicate zoom region. White box represents scale bar.

(E) Western blot of CLASP1 and CLASP2 depletion by two different siRNA combinations. Actin as loading control.

(F) Western blot showing no change in EB1 and CLIP-170 protein levels upon CLASP-depletion. Actin as loading control.

(G) Western blot showing no change in EB1 protein levels upon GFP-stathmin expression compared to GFP-control. Actin as loading control.

(H) Line scans showing distribution of EB3 at MTs in NT control (black), CLASP-depletion (green), or GFP-stathmin (blue). Based on data similar to (A), (B), and (D). Line scan and L:T ratio values are normalized mean intensities ± SEM (n = 50, two independent experiments).

(I) +TIP levels by western blot analysis in NT control and CLASP-depletion. Graph is normalized mean ±SEM in three independent experiments.

(J) EB1 levels by western blot analysis in NT control, CLASP-depletion, Nocodazole treatment, and GFP-control or GFP-stathmin expression. Graph is normalized mean ± SEM in three independent experiments.

(K) Line scans showing distribution of EB1 at MTs in NT control (black), CLASP-depletion (green), EB1 partial depletion (gray), or EB1/CLASP double depletion (light green). Line scan and L:T ratio values are normalized mean intensities ± SEM (n = 50, two independent experiments).

(legend continued on next page)

MEF, COS-7, HeLa, B16-F1, and Caco-2 (Figure S2) are shown in this study. Interestingly, depletion of CLASP1 or CLASP2 individually (Figure S1J) resulted in partial redistribution of EB1 and EB3 (herein referred to as EBs) along the MT lattice (Figures S1D–S1I); a combination of siRNAs against both CLASPs was used for all subsequent CLASP-depletion experiments (Figure 1E).

Because overexpression of EBs results in lattice decoration, it is in principle possible that an increased EB-to-MT ratio causes the enhanced EB lattice binding observed. Endogenous levels of EB1 protein did not increase upon CLASP-depletion (Figures 1F and 1I), but MT number decreased because CLASP-depletion alters MT dynamics (Akhmanova et al., 2001; Mimori-Kiyosue et al., 2005). However, in cells briefly treated with nocodazole to decrease MT number (Figures 1C and 1N), no significant EB3 lattice relocalization was observed (Figure 1C). Also, cells expressing GFP-stathmin, which sequesters free tubulin dimers and decreases MT number (Figures 1D and 1N), did not show significant EB3 lattice binding (Figures 1D and 1H). Total MT length did not significantly differ between CLASP-depleted, nocodazole-treated, and GFP-stathmin-expressing cells (Figure 1N). Moreover, the number of EB3 plus ends upon CLASP depletion and GFP-stathmin expression did not statistically differ (Figure S2L). Importantly, in both nocodazole treatment and GFP-stathmin expression, EB1 protein levels did not differ from NT control (Figures 1G, 1J, and S1K).

To further confirm that EB lattice binding in CLASP-depleted cells is not an artifact of an increased EB-to-MT ratio, we performed a partial depletion of EB1, either alone or in addition to CLASP depletion (Figures 1M and S1M). For single depletion of CLASPs, the lattice-to-tip ratio (L:T) was 0.48 ± 0.03 (Figure 1K); similarly, upon double depletion of EB1 and CLASPs, this ratio was 0.41 ± 0.03 (Figure 1L). This difference was not statistically significant indicating that, regardless of the amount of EB protein, CLASP depletion has the same effect on EBs. Thus, altered EB localization in cells lacking CLASPs is not a result of an increased EB-to-MT ratio.

+TIP Proteins Relocalize with EBs in CLASP-Depleted Cells

We next sought to determine whether CLASP influenced the localization of other +TIP families at MTs, or if CLASP regulation of EB was specific. We screened CLASP-depleted cells for localization of representative proteins from the major +TIP families: CAP-Gly, SxIP, and EB-independent. The CAP-Gly proteins, CLIP-170 and p150^{Glued}, relocalized to the MT lattice upon CLASP depletion and were indistinguishable from lattice-bound EBs (Figures 2, S3A, and S3B). Endogenous levels of CLIP-170 protein did not increase upon CLASP depletion (Figures 1F and 1I). The SxIP proteins, GFP-SLAIN2 (Figures S3C and S3D) and the minimal EB-binding domain of dystonin (GFP-Dst-EBBD; Figures S3E and S3F) relocalized to the lattice upon CLASP depletion in a similar manner. An exception was another SxIP protein, APC, which did not change localization upon CLASP depletion (Figures S3G and S3H), possibly due to its regulation by a large number of factors (Kita et al., 2006). Similarly, chTOG did not relocalize to the MT lattice (Figures S3I and S3J); this is likely explained by the capacity of chTOG to track MT tips independently of EBs (Brouhard et al., 2008).

To examine whether CLASPs directly regulate CAP-Gly protein localization at MTs, or if these proteins simply follow EBs to the lattice, we took advantage of a previously described approach. It has been shown that a C-terminal GFP tag on EB occludes binding of CLIP-170 to the EEY/F tail of EBs; therefore, expression of EB3-GFP in cells displaces CLIP-170 from MT plus ends (Lomakin et al., 2009; Skube et al., 2010). We observed that EB3-GFP, similar to endogenous protein, relocalizes to the MT lattice in CLASP-depleted cells (Figures 2F and 2K). Interestingly, upon CLASP-depletion in cells expressing EB3-GFP, CLIP-170 did not relocalize to the MT lattice (Figures 2D, 2F, and 2K). We further designed an Emerald-EB3 construct, which interacts normally with CLIP-170 and allows for correct CLIP-170 plus-end localization (Figure 2G). In CLASP-depleted cells, both Emerald-EB3 and CLIP-170 significantly relocalize to MT lattices (Figures 2H and 2L). These experiments reveal that CLIP-170 interaction with the C terminus of EBs underlies its lattice binding in CLASP-depleted cells. Together with relocalization of GFP-Dst-EBBD, which cannot be recruited by factors other than EBs (Honnappa et al., 2009), these data suggest that both CAP-Gly and SxIP proteins likely follow EBs to the lattice rather than being independently regulated by CLASPs.

TOG2 Region of CLASP, but Not EB Binding, Is Required to Restore Normal EB Plus-End Localization

To determine which CLASP domains are instrumental for the mechanism of CLASP-dependent EB regulation, we tested the capacity of various CLASP mutants (Figures 3 and S4) to rescue EB localization. CLASPs have three main protein-interacting regions: The TOG/TOG-like domains confer MT binding (Al-Bassam et al., 2007; Patel et al., 2012), whereas the basic/SxIP region dictates EB binding (Mimori-Kiyosue et al., 2005; Patel et al., 2012), and the C terminus mediates CLASP dimerization and interactions with protein partners (Akhmanova et al., 2001; Efimov et al., 2007; Lansbergen et al., 2006). For this study, the TOG-like domains of CLASP2 will be referred to as TOG2 and TOG3, as in (Leano et al., 2013). As expected, re-expression of CLASP2 in CLASP-depleted cells rescued EB3 plus-end localization (Figures 3D and 3O).

Intriguingly, a CLASP construct with mutated EB-binding motifs readily rescued EB plus-end localization (Figures 3E and 3O), indicating that CLASP-EB interactions are not involved in the observed phenomenon. To confirm this conclusion, we utilized an artificial dimer of the EB3 MT binding domain, EB3-N-LZ-GFP (Komarova et al., 2009), which lacks the CLASP-interacting

(L) EB1 L:T ratio in CLASP-depletion and EB1/CLASP double depletion based on (K). Line scan and L:T ratio values are normalized mean intensities ± SEM (n = 50, two independent experiments).
(M) EB1 levels by western blot analysis in NT control, EB1 partial depletion, and EB1/CLASP double depletion. Graph is normalized mean ± SEM in three independent experiments.
(N) Average total MT length in NT control, CLASP-depletion, Nocodazole treatment, and GFP-stathmin expression. Based on data similar to (A–D).
See also Figures S1 and S2.

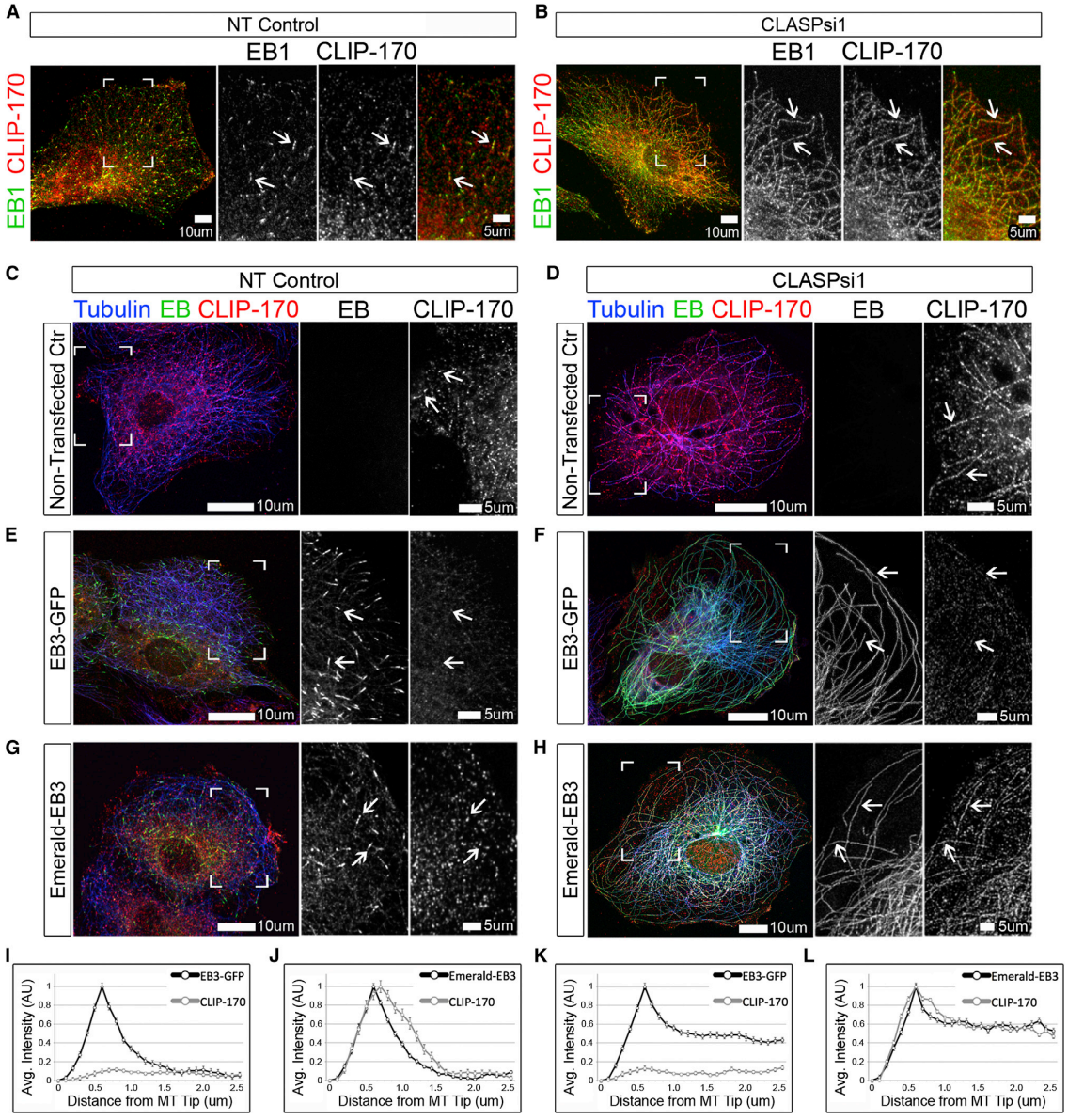

Figure 2. CAP-Gly Proteins Follow EBs to the Microtubule Lattice in CLASP-Depleted Cells

(A and B) RPE cells stained for EB1 (green) and CLIP-170 (red). (A) EB1 and CLIP-170 localize to MT plus ends in NT control cells. (B) EB1 and CLIP-170 relocalize to the lattice in CLASP-depleted cells. Boxed corners indicate zoom region. White box represents scale bar. Immunofluorescence. Values are normalized mean intensities ± SEM (n = 50, two independent experiments).

(C–H) A7r5 cells expressing EB3 (green), and stained for CLIP-170 (red) and α-tubulin (blue, pseudocolored). (C) CLIP-170 localizes to MT plus ends in untransfected NT control cells, (D) CLIP-170 coats the lattice in CLASP-depleted cells. (E) In NT control cells expressing EB3-GFP, EB3-GFP localizes to MT plus ends, while CLIP-170 localization to plus ends is reduced. (F) In CLASP-depleted cells expressing EB3-GFP, EB3-GFP relocalizes to the MT lattice, whereas lattice-bound CLIP-170 is reduced. (G) In NT control cells expressing Emerald-EB3, Emerald-EB3 and CLIP-170 localize to plus ends. (H) In CLASP-depleted cells expressing Emerald-EB3, Emerald-EB3 and CLIP-170 coat the lattice. Boxed corners indicate zoom region. White box represents scale bar. White arrows represent EB/CLIP-170 characteristic localization, CLIP-170 displacement, or EB/CLIP-170 lattice relocalization, respectively. Immunofluorescence. Values are normalized mean intensities ± SEM (n = 50, two independent experiments).

(I–L) Line scans showing distribution of CLIP-170 (gray) at MTs in cells expressing either EB3-GFP or Emerald-EB3 (black). Based on data similar to (E)–(H). See also Figure S3.

EB tail region. EB3-N-LZ-GFP localized along the MT lattice in CLASP-depleted cells (Figure 3R), indicating that CLASPs influence EB localization without a contribution from: (1) CLASP-EB interaction or (2) binding of other proteins to the EB tail domain, such as another MAP that might recruit EB to the lattice when CLASPs are not present. Together, these data support a model in which CLASPs alter MTs themselves to restrict EB-MT interactions to MT tips.

Further rescue experiments with CLASP mutant constructs revealed that the TOG2 domain, but not the TOG3 domain of CLASP, was required for regulation of EB (Figures 3F–3H, 3O, and 3P). Importantly, the TOG2 domain of CLASP has been reported to mediate strong MT interactions (Patel et al., 2012). The monomeric TOG2 domain alone was not sufficient to restore EB plus-end localization (Figures 3L and 3P); although, truncated CLASP mutants containing TOG2 plus an additional MT-interacting region (TOG3 or the Ensconsin MT-binding domain [EMTB]) were sufficient for CLASP-dependent regulation of EBs (Figures 3I, 3J, 3N, and 3O). In addition, TOG2 directly linked to the C terminus of CLASP rescued EB localization (Figures 3M and 3O), possibly because the C-terminal domain weakly interacts with MTs (Wittmann and Waterman-Storer, 2005) or promotes MT binding via dimerization (Al-Bassam et al., 2010; Patel et al., 2012). Nevertheless, the C-terminal domain of CLASP was not strictly required to rescue EB localization (Figures 3I and 3O), which reveals that CLASP does not bind its cellular partners for regulation of EB at MTs. Together, these mutant studies demonstrate that the TOG2 domain of CLASP is necessary to restore EB localization. Accordingly, we suggest that CLASP influences the MT lattice itself to promote normal EB plus-end distribution.

CLASP Modulates Microtubule Affinity and EB Localization In Vitro

To address whether CLASPs independently regulate EB localization at MTs, we performed in vitro MT plus-end tracking assays. For these experiments, we analyzed the capacity for CLASP2 to remove a minimal EB1 construct, EB1-N-LZ-GFP, from the lattice. In the absence of CLASP, this minimal EB1 construct clearly decorated MT lattices in addition to its plus-end recruitment (Figures 4A and 4B) with an L:T of 0.185 ± 0.001 (Figure 4D). Copolymerization with CLASP2 resulted in significant reduction of lattice binding (Figures 4A and 4C) resulting in a ratio of 0.136 ± 0.001 (Figure 4D). Thus, CLASP independently modulated EB1-N-LZ-GFP lattice localization in vitro. Confirming our results in cells, these data indicate that the observed effects are due to CLASP interactions with MTs, rather than a CLASP-EB interaction, because the minimal EB1 construct lacks the CLASP-interacting region.

To quantitatively analyze the effect of CLASP on EB binding, we determined EB affinity for MTs in vitro. GDP-MTs were polymerized from GTP-tubulin in the presence or absence of CLASP2 then incubated with varying concentrations of EB3-GFP prior to cosedimentation. Hyperbolic fit shows EB3-GFP has lower affinity for GDP-MTs copolymerized with CLASP2 compared to GDP-MTs alone (Figures 4E and 4I). Consistent with our data in cells, a CLASP2 mutant unable to bind to EBs (IP12-ΔC) similarly reduced EB3-GFP affinity (Figures 4F, 4I, and 4O).

To test whether CLASPs function during MT polymerization, we examined EB3-GFP affinity for GDP-MTs that were first assembled then incubated with CLASP2; importantly, EB3-GFP affinity for these MTs did not significantly differ from GDP-MTs alone (Figures 4G and 4I). This reveals that CLASPs must be present during MT polymerization in order to regulate EB affinity for MTs.

Interestingly, the use of GTPγS, a slowly hydrolyzable GTP analog (experimental model for the natural GDP-P_i state EBs recognize) eliminated the difference between MTs polymerized with and without CLASP. As in previously published reports (Maurer et al., 2011), EB3-GFP displayed higher affinity for GTPγS-MTs than GDP-MTs (Figures 4H and 4I). Copolymerization of GTPγS-MTs with CLASP2 did not significantly reduce EB3-GFP affinity (Figures 4H and 4I). This result indicates that CLASPs recognize or modify a particular tubulin and/or MT conformation to regulate MT-affinity and localization of EBs, possibly via altering the GTP-state.

GTP-Tubulin Content at the MT Lattice Is Increased in CLASP-Depleted Cells

Because EBs have higher affinity for MTs formed from GTP-tubulin analogs compared to GDP-tubulin (Maurer et al., 2011, 2012; Zanic et al., 2009), redistribution of EBs to the MT lattice could be explained by a change in GTP-tubulin content after CLASP-depletion. To explore this hypothesis, we took advantage of the recently described hMB11 antibody, which is thought to recognize GTP-tubulin in cells (Dimitrov et al., 2008). Currently, it is not clear whether hMB11 recognizes GTP-tubulin conformation (or GDP-P_i) or a more general GTP-tubulin-like structural feature. In NT control cells, hMB11 highlights MT tips and occasional lattice patches, known as GTP-tubulin remnants (Figure 4J). In CLASP-depleted cells, GTP-tubulin content was significantly increased: hMB11 lattice patches were more abundant and extended along whole MTs in regions (Figures 4K and 4L).

Consistent with previous findings (Dimitrov et al., 2008), the pattern of GTP-tubulin lattice remnants in CLASP-depleted cells was nonhomogenous (Figure 4M); interestingly, it closely resembled the speckle-like lattice distribution of EBs upon CLASP-depletion (Figure 4N). Unfortunately, due to hMB11 antibody restrictions, we were unable to costain for EB and GTP-tubulin at MTs; as an alternative, we used computational modeling to determine whether EB1 lattice speckles and GTP-tubulin remnants are similar in size and distribution along MTs. Image processing was applied to compensate for differences in contrast between EB1 and GTP-tubulin (see Supplemental Experimental Procedures). EB1 and GTP-tubulin speckles, although not identical, had similar distribution characteristics (Figures S4N and S4O); thus, these patterns could, in principle, indicate the same lattice regions. Therefore, we propose that EB lattice binding may be the result of increased GTP-tubulin content along MTs in CLASP-depleted cells, and that the speckle-like appearance of EB staining reflects uneven distribution of GTP-tubulin remnants at the lattice. These experiments reveal a possible mechanism for relocalization of EBs to the MT lattice in CLASP-depleted cells, via recognition of increased GTP-tubulin content, or another hMB11-recognized lattice feature.

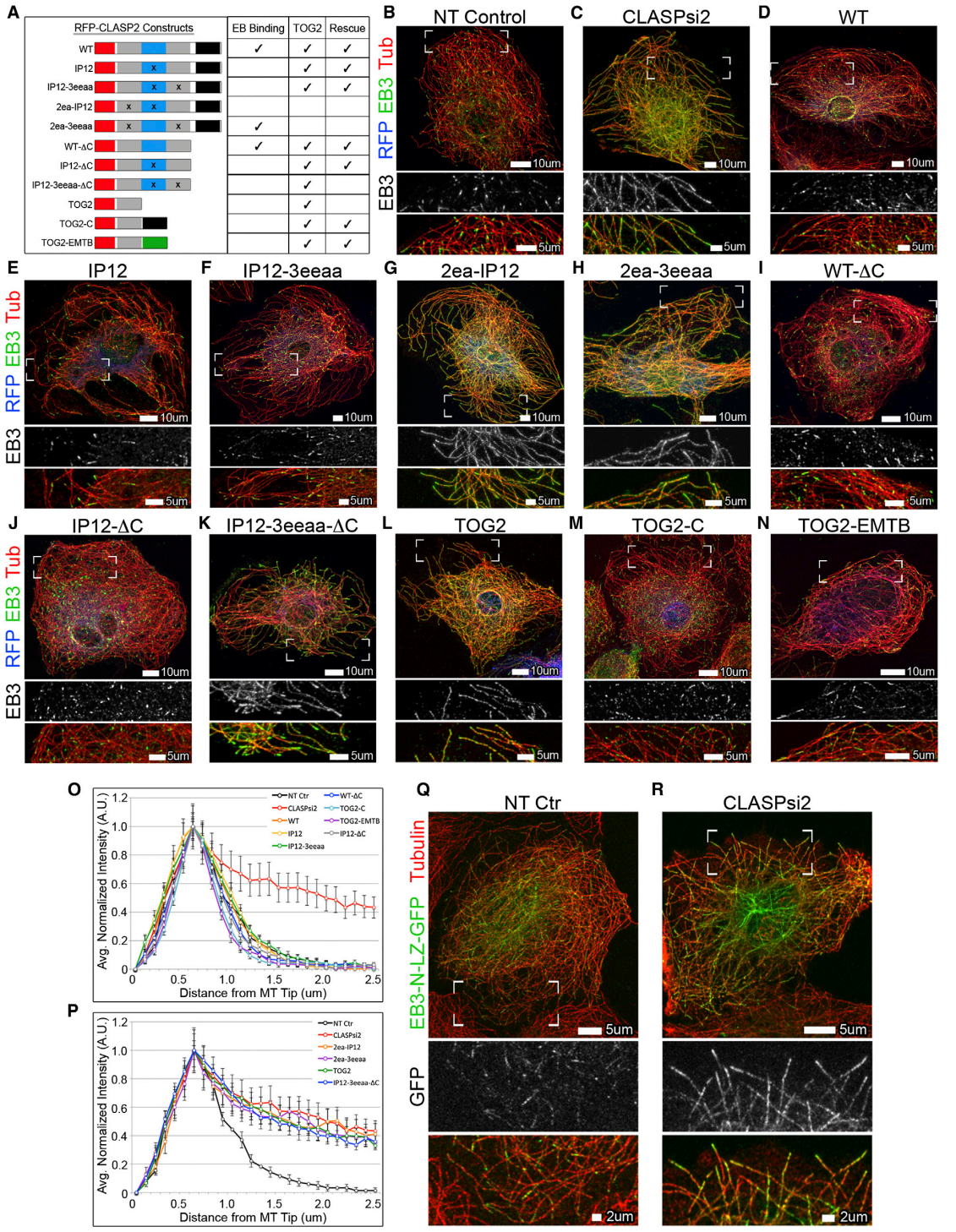

(legend on next page)

DISCUSSION

Our study has uncovered a regulatory mechanism for the localization and MT affinity of EBs. Our data indicate that, when CLASPs bind a MT, they influence the lattice itself to reduce EB binding, thereby promoting EB plus-end distribution. This regulation likely occurs during MT polymerization, setting up the nucleotide state sensed by EB for tip localization (Maurer et al., 2012; Zanic et al., 2009). Specifically, we show that GTP-tubulin content is increased at the lattice of CLASP-depleted cells and thus propose that high-affinity EB binding sites within the lattice are likely GTP-tubulin remnants. Because it is unclear what the hMB11 antibody recognizes, our findings in CLASP-depleted cells may indicate that MT lattice structure is altered to more closely resemble MT tips.

These findings add another level of complexity to existing evidence on the regulation of EB interactions with MTs. Whereas CLASPs clearly act as prominent regulators of EB localization, EBs are still enriched at plus ends, in addition to their lattice localization, in CLASP-depleted cells. In addition, in vitro, EBs autonomously track MT plus ends and are not enriched at the lattice at physiological concentrations, despite CLASPs not being present (Bieling et al., 2007). In our assays, a higher concentration of EB, which binds the lattice, displayed decreased lattice localization in the presence of CLASP leading to restricted EB binding to MT tips. It is likely that whereas GTP hydrolysis does not strictly require CLASPs, this important process is hindered in their absence both in cells and in vitro.

There are unknown differences in the lattices of MTs polymerized in cells and in vitro (McEwen and Edelstein, 1980; Wade and Chrétien, 1993). Indeed, a recent study demonstrates that MT properties in vitro only resemble those in cells when additional cellular proteins are present; Interestingly, they found that another TOG-containing MAP, XMAP215, influences EB behavior via an allosteric interaction though MTs (Zanic et al., 2013). In our study, the effect of CLASP on EB localization is TOG-domain dependent. Thus, we suggest a similar model in which CLASP allosterically regulates EB localization: as an MT polymerizes, CLASPs likely alter the MT lattice, behind the tip, thus restricting high-affinity EB-binding sites to the plus end, for example by promoting GTP-hydrolysis. Alternatively, because CLASP binds tubulin dimers (Al-Bassam et al., 2010), CLASPs may prime GTP-tubulin dimers for efficient hydrolysis upon lattice incorporation. Either mechanism would lead to increased GTP-tubulin content at MTs and enhanced EB lattice binding if misregulated.

Another potential mechanism of CLASP-dependent regulation of EB involves steric hindrance. In this scenario, under physiological conditions, CLASPs would bind the lattice during MT polymerization and remain associated with GTP-tubulin remnants, thereby blocking potential EB recruitment to these sites (and antibody recognition). In this model, CLASPs would bind MTs in a way that prevents EB-lattice interactions. Moreover, this type of MT association should be different from CLASP association with already polymerized MTs observed under overexpression conditions, in which EB is artificially recruited to MTs (Mimori-Kiyosue et al., 2005). The presence of mini bundles along the MT lattice in CLASP-depleted cells could also explain EB lattice localization; however, MT bundling in CLASP-depleted cells was not detected (Figure S4P).

Because GTP-tubulin remnants are proposed to be sites of MT rescue, it is interesting that in CLASP-depleted cells MTs undergo low rescue frequency. If our model of increased GTP-tubulin content is correct, this may reflect that the absence of a strong rescue factor like CLASP leads to inefficient rescues even in the presence of multiple GTP-tubulin remnants. In the steric hindrance model, the number of GTP-tubulin remnants would not differ in CLASP-depleted cells, and low rescue activity would be explained by the absence of CLASP at these sites.

However, existing evidence leans toward the model of allosteric EB regulation by CLASPs rather than the steric hindrance model, because typically only low amounts of CLASPs are observed at the MT lattice. Furthermore, a recent study on the effects of γ-tubulin depletion reported an increase in GTP-tubulin remnants and a similar EB distribution at MT lattices (Bouissou et al., 2014). Because γ-tubulin is a major factor defining consistency in MT structure, we hypothesize that the lattice structure in γ-tubulin depleted cells is changed, and as a result, EB lattice affinity is altered. This finding supports the idea that a structural change in MT lattices would result in EB recruitment.

Figure 3. TOG2 Domain of CLASP Is Necessary to Restore Normal EB Plus-End Localization

(A) Schematic representation of CLASP2 rescue constructs. Red represents RFP tag, gray represents MT-binding domains (TOG2 and TOG3), blue represents EB-binding region (basic/SxIP), black represents C terminus, green represents MT-binding domain of Ensconsin (EMTB). Construct capacity to bind EB and rescue EB localization is shown.

(B) EB3 localizes to MT tips in NT control cells. Immunofluorescence. Boxed corners indicate zoom region. White box represents scale bar.

(C) EB3 extensively coats the lattice, in addition to plus-end localization, in CLASP-depleted cells. Immunofluorescence. Boxed corners indicate zoom region. White box represents scale bar.

(D–N) A7r5 cells expressing various RFP-CLASP2 rescue constructs (pseudo-colored blue) stained for endogenous EB3 (green) and α-tubulin (pseudo-colored red). (D–F, I, J, M, N) CLASP-depleted cells expressing WT (D), IP12 (E), IP12-3eeaa (F), WT-ΔC (I), IP12-ΔC (J), TOG2-C (M), or TOG2-EMTB (N) rescue constructs all restore normal EB3 plus-end localization. (G, H, K, L) CLASP-depleted cells expressing 2ea-IP12 (G), 2ea-3eeaa (H), IP12-3eeaa-ΔC (K), or TOG2 (L) rescue constructs were not sufficient to restore normal EB3 localization. EB3 binds along the lattice. Immunofluorescence. Boxed corners indicate zoom region. White box represents scale bar.

(O and P) Line scan analysis for constructs that rescue EB3 plus-end localization (O) or constructs unable to rescue (P). Line scan values are normalized mean intensities ±SEM (n = 50, two independent experiments).

(Q and R) A7r5 cells expressing minimal MT-binding region of EB3, EB3-N-LZ-GFP (green), and stained for α-tubulin (red). EB3-N-LZ-GFP localizes to MT tips in NT control cells (Q) and relocalizes to the lattice in CLASP-depleted cells (R). Immunofluorescence. Boxed corners indicate zoom region. White box represents scale bar.

See also Figure S4.

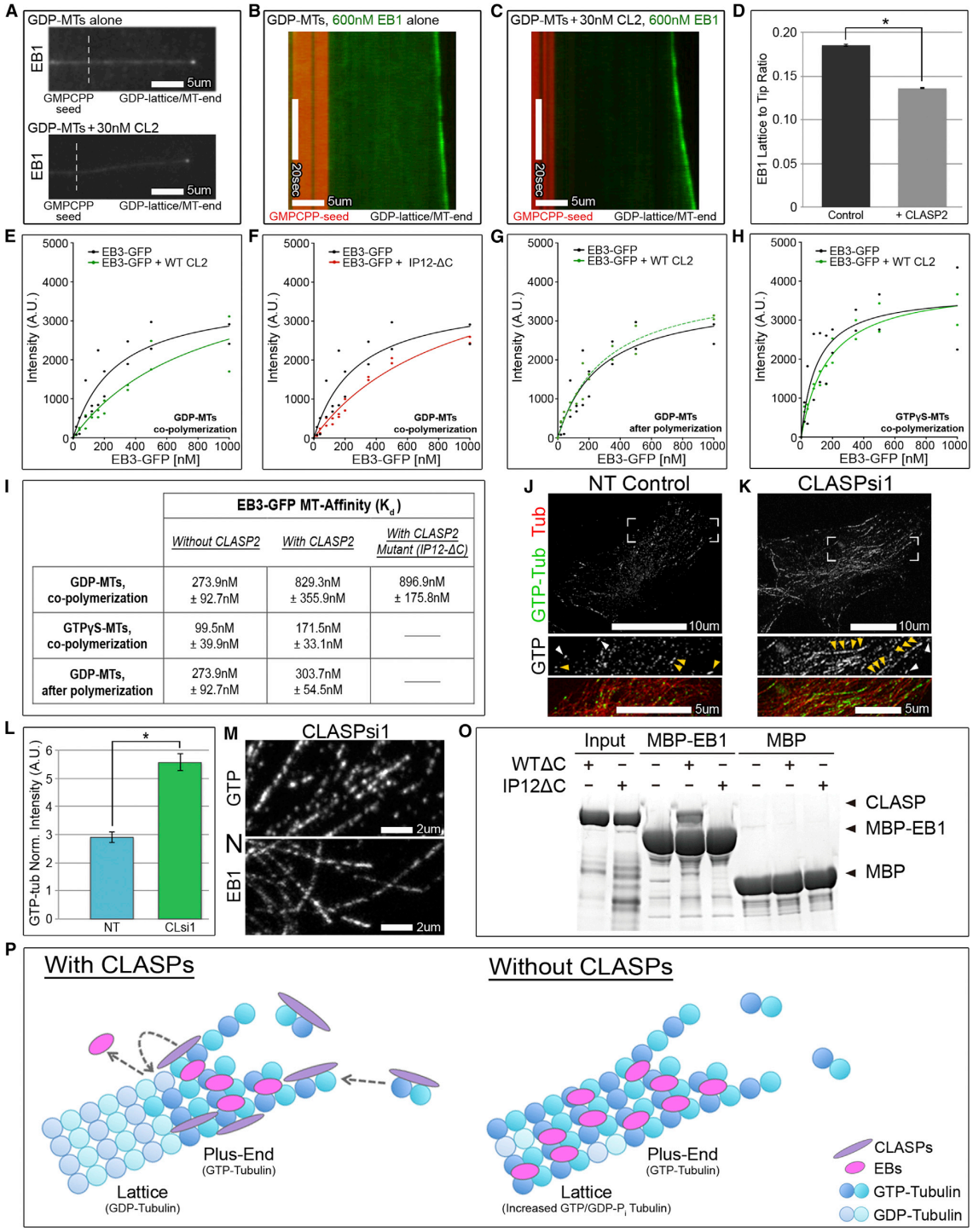

(legend on next page)

In conclusion, our findings have revealed functions for CLASPs, have uncovered an additional regulatory mechanism for EB tip tracking, and have major implications for understanding establishment of the +TIP network at MT plus ends.

EXPERIMENTAL PROCEDURES

Cells

A7r5 cells (ATCC) were maintained in low glucose (1 g/l) Dulbecco's modified Eagle's medium (DMEM), without phenol red. hTert-RPE1 cells (Clontech) were maintained in DMEM/F12, which was supplemented with 500 ug/ml G418 for an mCherry-tubulin RPE stable line (R. Ohi, Vanderbilt University, TN). HeLa (R. Ohi, Vanderbilt University, TN), MEF (A. Kenworthy, Vanderbilt University, TN), COS-7 (A. Kenworthy), and B16-F1 cells (M. Tyska, Vanderbilt University, TN) were maintained in DMEM. Caco-2 cells (M. Tyska) were maintained in DMEM supplemented with 20% fetal bovine serum (FBS). All cells were grown with 10% FBS (unless indicated) and in 5%CO_2 at 37°C. Cells were plated on fibronectin-coated glass coverslips 72 hr prior to experiments.

Antibodies

Mouse monoclonal primary antibodies: anti-α-tubulin (DM1A, Sigma); anti-EB1 (BD Transduction), anti-$p150^{Glued}$ (BD Transduction). Rabbit polyclonal primary antibodies: anti-α-tubulin (Abcam); anti-EB3 (A. Akhmanova); anti-CLIP-170 (A. Akhmanova); anti-chTOG (L. Cassimeris); anti-APC (R. Coffey). A recombinant human primary antibody, hMB11, against GTP-MTs (F. Perez) was also used. Secondary antibodies: Alexa488, Alexa568, or Alexa647-conjugated highly cross-absorbed goat anti-mouse, anti-rabbit, or anti-human (Invitrogen/Molecular Probes). For +TIPs/MT staining, cells were fixed in methanol (5 min, −20°C). hMB11 staining was done according to Dimitrov et al., 2008.

In Vitro MT-Affinity and MT Plus-End Tracking Assays

For in vitro MT-affinity assays, 20 uM tubulin was polymerized alone or with 150 nM CLASP2 or IP12ΔC in BRB80 buffer (80 mM K-Pipes [pH 6.8], 2 mM $MgCl_2$, 1 mM EGTA) supplemented with 1 mM GTP and 140 mM KCl. Samples were incubated at 37°C for 30 min, and stabilized with taxol (30 uM). For GTPγS-MTs, 1 mM GTPγS was used to polymerize MTs for 2 hr. After centrifugation at 35°C for 20 min at 60,000 rpm, supernatant was removed and MT pellets were incubated with EB3-GFP (0–1,000 nM) for 5 min at room temperature (RT). For experiments where CLASP was added after polymerization, 150 nM CLASP2 was incubated with MT pellet for 5 min at RT prior to EB3-GFP addition for another 5 min. MTs were pelleted again, then supernatants and pellets were analyzed with Coomassie.

For in vitro MT plus-end tracking assays, preformed Hilyte647-labeled GMPCPP-MT seeds were attached to PLL-PEG-50% biotin-passivated coverslips via biotin-streptavidin linkers. Using TIRF, dynamic MTs and 600 nM EB1-N-LZ-GFP were observed in the presence of 13 uM tubulin in assay buffer: 50 mM KCl, 1 mM GTP, 0.6 mg/ml κ-casein, 0.2% methyl cellulose, 4 mM dithiothreitol, 0.2 mg/ml catalase, 0.4 mg/ml glucose oxidase, and 50 mM glucose in MRB80 (80 mM PIPES [pH 6.8] with KOH, 1 mM EGTA, 4 mM $MgCl_2$), with 30 nM CLASP2 or equal volume buffer control.

Statistics

All quantitative data were collected from experiments performed in at least duplicate and are expressed as mean ± SEM generated in Excel. Student's t test (two-tailed, unpaired) was performed to determine statistical difference between groups. A p value <0.05 was considered statistically significant.

SUPPLEMENTAL INFORMATION

Supplemental Information includes Supplemental Experimental Procedures and four figures and can be found with this article online at http://dx.doi.org/10.1016/j.devcel.2014.06.026.

ACKNOWLEDGMENTS

We thank the Kaverina, Tyska, Ohi, and Lee laboratories for insightful discussions as well as Nadia Efimova and Changsong Yang for help with the platinum replica experiments. We are grateful to A. Akhmanova, L. Cassimeris, F. Perez, and R. Coffey for reagents. This study was supported by NIH grant GM078373 (to I.K.), AHA grant-in-aid 13GRNT16980096 (to I.K.), AHA pre-doctoral fellowship 12PRE12040153 (to A.D.G.), and Scientific Research grant-in-aid 22570190 (to I.H.). B.P.F. is supported by EPSRC-funded MOAC Doctoral Training Centre. A.S. is a Lister Institute Research Prize Fellow. This collaboration has benefited from a Strategic Partnership Grant from the University of Warwick (to A.S.) and a Marie Curie Cancer Care program grant (to A.S.).

Received: December 11, 2013
Revised: April 18, 2014
Accepted: June 27, 2014
Published: August 11, 2014

REFERENCES

Akhmanova, A., and Steinmetz, M.O. (2008). Tracking the ends: a dynamic protein network controls the fate of microtubule tips. Nat. Rev. Mol. Cell Biol. *9*, 309–322.

Akhmanova, A., Hoogenraad, C.C., Drabek, K., Stepanova, T., Dortland, B., Verkerk, T., Vermeulen, W., Burgering, B.M., De Zeeuw, C.I., Grosveld, F., and Galjart, N. (2001). Clasps are CLIP-115 and -170 associating proteins

Figure 4. CLASP Modulates Microtubule Affinity of EB and Promotes GTP Hydrolysis at Microtubules In Vitro

(A–C) in vitro MT plus-end tracking assays. (A) Localization of 600 nM EB1-N-LZ-GFP to GDP-MTs grown from GMPCPP seeds. (B and C) Kymographs of MTs (shown in A). EB1-N-LZ-GFP alone (B) or in the presence of 30 nM CLASP2 (C). Red represents GMPCPP-seed, green represents EB1, CLASP2 and tubulin are unlabeled. (B and C) White box represents scale bar.

(D) EB1-N-LZ-GFP L:T ratio based on kymographs similar to (B) and (C); n = 87 for control, n = 93 for CLASP, two independent experiments. Values are normalized mean intensities ± SEM.

(E–H) EB3-GFP binding curves for MTs: GDP-MTs copolymerized with 150 nM CLASP2 (E), GDP-MTs copolymerized with 150 nM IP12-ΔC (EB-binding mutant) (F), GDP-MTs with 150 nM CLASP2 added after polymerization (G), or GTPγS-MTs copolymerized with 150 nM CLASP2 (H). Intensities of MT-bound EB3-GFP as a function of EB concentration with corresponding hyperbolic fit. (E–G) Intensities and binding curves (solid black line) for EB3-GFP bound to GDP-MTs same for each graph.

(I) Derived dissociation constants (K_d). Analysis performed over two independent experiments. K_d are ±SE.

(J and K) RPE cells stained for GTP-tubulin (hMB11, gray/green) expressing mCherry-tubulin (red). (J) In NT control cells, hMB11 localizes to MT tips and at GTP-tubulin remnants. (K) In CLASP-depleted cells, lattice decoration by hMB11 is increased compared to NT control. Immunofluorescence. Boxed corners indicate zoom region. White arrowheads represent MT tips, yellow arrowheads represent GTP-tubulin remnants, white box represents scale bar.

(L) GTP-tubulin intensity in NT control and CLASP-depleted cells. Based on data similar to (J) and (K). Values are normalized mean intensities ± SEM (n = 20, 2 independent experiments).

(M and N) Zoomed images highlight speckled nature of GTP-tubulin (M) and EB1 (N). Immunofluorescence. White box represents scale bar.

(O) Coomasie showing CLASP (WTΔC and IP12ΔC) pull-down by maltose-binding protein (MBP)-EB1. MBP as negative control.

(P) Model for CLASP-dependent regulation of EB localization at MTs. EB nucleotide-state sensing and EB-CLASP interactions are not shown. Purple represents CLASP, pink represents EB, dark blue represents GTP-tubulin, light blue represents GDP-tubulin. Grey arrows indicate possible mechanisms of CLASP function.

involved in the regional regulation of microtubule dynamics in motile fibroblasts. Cell *104*, 923–935.

Al-Bassam, J., Larsen, N.A., Hyman, A.A., and Harrison, S.C. (2007). Crystal structure of a TOG domain: conserved features of XMAP215/Dis1-family TOG domains and implications for tubulin binding. Structure *15*, 355–362.

Al-Bassam, J., Kim, H., Brouhard, G., van Oijen, A., Harrison, S.C., and Chang, F. (2010). CLASP promotes microtubule rescue by recruiting tubulin dimers to the microtubule. Dev. Cell *19*, 245–258.

Bieling, P., Laan, L., Schek, H., Munteanu, E.L., Sandblad, L., Dogterom, M., Brunner, D., and Surrey, T. (2007). Reconstitution of a microtubule plus-end tracking system in vitro. Nature *450*, 1100–1105.

Bouissou, A., Vérollet, C., de Forges, H., Haren, L., Bellaïche, Y., Perez, F., Merdes, A., and Raynaud-Messina, B. (2014). γ-Tubulin ring complexes and EB1 play antagonistic roles in microtubule dynamics and spindle positioning. EMBO J. *33*, 114–128.

Bratman, S.V., and Chang, F. (2007). Stabilization of overlapping microtubules by fission yeast CLASP. Dev. Cell *13*, 812–827.

Brouhard, G.J., Stear, J.H., Noetzel, T.L., Al-Bassam, J., Kinoshita, K., Harrison, S.C., Howard, J., and Hyman, A.A. (2008). XMAP215 is a processive microtubule polymerase. Cell *132*, 79–88.

Buey, R.M., Mohan, R., Leslie, K., Walzthoeni, T., Missimer, J.H., Menzel, A., Bjelic, S., Bargsten, K., Grigoriev, I., Smal, I., et al. (2011). Insights into EB1 structure and the role of its C-terminal domain for discriminating microtubule tips from the lattice. Mol. Biol. Cell *22*, 2912–2923.

Dimitrov, A., Quesnoit, M., Moutel, S., Cantaloube, I., Poüs, C., and Perez, F. (2008). Detection of GTP-tubulin conformation in vivo reveals a role for GTP remnants in microtubule rescues. Science *322*, 1353–1356.

Efimov, A., Kharitonov, A., Efimova, N., Loncarek, J., Miller, P.M., Andreyeva, N., Gleeson, P., Galjart, N., Maia, A.R., McLeod, I.X., et al. (2007). Asymmetric CLASP-dependent nucleation of noncentrosomal microtubules at the trans-Golgi network. Dev. Cell *12*, 917–930.

Honnappa, S., Gouveia, S.M., Weisbrich, A., Damberger, F.F., Bhavesh, N.S., Jawhari, H., Grigoriev, I., van Rijssel, F.J., Buey, R.M., Lawera, A., et al. (2009). An EB1-binding motif acts as a microtubule tip localization signal. Cell *138*, 366–376.

Kita, K., Wittmann, T., Näthke, I.S., and Waterman-Storer, C.M. (2006). Adenomatous polyposis coli on microtubule plus ends in cell extensions can promote microtubule net growth with or without EB1. Mol. Biol. Cell *17*, 2331–2345.

Komarova, Y., De Groot, C.O., Grigoriev, I., Gouveia, S.M., Munteanu, E.L., Schober, J.M., Honnappa, S., Buey, R.M., Hoogenraad, C.C., Dogterom, M., et al. (2009). Mammalian end binding proteins control persistent microtubule growth. J. Cell Biol. *184*, 691–706.

Lansbergen, G., Grigoriev, I., Mimori-Kiyosue, Y., Ohtsuka, T., Higa, S., Kitajima, I., Demmers, J., Galjart, N., Houtsmuller, A.B., Grosveld, F., and Akhmanova, A. (2006). CLASPs attach microtubule plus ends to the cell cortex through a complex with LL5beta. Dev. Cell *11*, 21–32.

Leano, J.B., Rogers, S.L., and Slep, K.C. (2013). A cryptic TOG domain with a distinct architecture underlies CLASP-dependent bipolar spindle formation. Structure *21*, 939–950.

Lomakin, A.J., Semenova, I., Zaliapin, I., Kraikivski, P., Nadezhdina, E., Slepchenko, B.M., Akhmanova, A., and Rodionov, V. (2009). CLIP-170-dependent capture of membrane organelles by microtubules initiates minus-end directed transport. Dev. Cell *17*, 323–333.

Maurer, S.P., Bieling, P., Cope, J., Hoenger, A., and Surrey, T. (2011). GTPgammaS microtubules mimic the growing microtubule end structure recognized by end-binding proteins (EBs). Proc. Natl. Acad. Sci. USA *108*, 3988–3993.

Maurer, S.P., Fourniol, F.J., Bohner, G., Moores, C.A., and Surrey, T. (2012). EBs recognize a nucleotide-dependent structural cap at growing microtubule ends. Cell *149*, 371–382.

McEwen, B., and Edelstein, S.J. (1980). Evidence for a mixed lattice in microtubules reassembled in vitro. J. Mol. Biol. *139*, 123–145.

Miller, P.M., Folkmann, A.W., Maia, A.R., Efimova, N., Efimov, A., and Kaverina, I. (2009). Golgi-derived CLASP-dependent microtubules control Golgi organization and polarized trafficking in motile cells. Nat. Cell Biol. *11*, 1069–1080.

Mimori-Kiyosue, Y., Grigoriev, I., Lansbergen, G., Sasaki, H., Matsui, C., Severin, F., Galjart, N., Grosveld, F., Vorobjev, I., Tsukita, S., and Akhmanova, A. (2005). CLASP1 and CLASP2 bind to EB1 and regulate microtubule plus-end dynamics at the cell cortex. J. Cell Biol. *168*, 141–153.

Patel, K., Nogales, E., and Heald, R. (2012). Multiple domains of human CLASP contribute to microtubule dynamics and organization in vitro and in Xenopus egg extracts. Cytoskeleton (Hoboken) *69*, 155–165.

Schuyler, S.C., and Pellman, D. (2001). Microtubule "plus-end-tracking proteins": The end is just the beginning. Cell *105*, 421–424.

Skube, S.B., Chaverri, J.M., and Goodson, H.V. (2010). Effect of GFP tags on the localization of EB1 and EB1 fragments in vivo. Cytoskeleton (Hoboken) *67*, 1–12.

Wade, R.H., and Chrétien, D. (1993). Cryoelectron microscopy of microtubules. J. Struct. Biol. *110*, 1–27.

Weisbrich, A., Honnappa, S., Jaussi, R., Okhrimenko, O., Frey, D., Jelesarov, I., Akhmanova, A., and Steinmetz, M.O. (2007). Structure-function relationship of CAP-Gly domains. Nat. Struct. Mol. Biol. *14*, 959–967.

Wittmann, T., and Waterman-Storer, C.M. (2005). Spatial regulation of CLASP affinity for microtubules by Rac1 and GSK3beta in migrating epithelial cells. J. Cell Biol. *169*, 929–939.

Zanic, M., Stear, J.H., Hyman, A.A., and Howard, J. (2009). EB1 recognizes the nucleotide state of tubulin in the microtubule lattice. PLoS ONE *4*, e7585.

Zanic, M., Widlund, P.O., Hyman, A.A., and Howard, J. (2013). Synergy between XMAP215 and EB1 increases microtubule growth rates to physiological levels. Nat. Cell Biol. *15*, 688–693.